

**THESE**

**Présentée**

**à**

**L'Université de Strasbourg  
pour l'obtention du grade de:**

**Docteur**

**Discipline: Science de la Terre et de l'Univers  
Spécialité: Géophysique**

**Seyfallah BOURAOUI**

**Time Series Analysis of SAR Images using  
Persistent Scatterer (PS), Small Baseline (SB)  
and Merged Approaches in Regions with Small Surface  
Deformation**

**Soutenue le 02 juillet 2013**

<b>Directeur de Thèse</b>	Pr. Meghraoui Mustapha	IPG Strasbourg, France
<b>Rapporteur Externe</b>	Pr. Stramondo Salvatore	INGV Rome, Italy
<b>Rapporteur Externe</b>	Dr. Briole Pierre	ENS Paris, France
<b>Rapporteur Interne</b>	Pr. Masson Frederic	IPG Strasbourg, France
<b>Examineur</b>	Dr. Çakir Ziyadin	ITU Istanbul, Turkey



This work is dedicated to all my family and to my parents  
Anissa and Said in particular



# Acknowledgements

It is with great pleasure that I present my sincere thanks to all those who helped me to complete this work.

I would like to thank all the jury for accepting to review my work.

My sincere thanks also go to Ziyadin Cakir with whom I worked closely throughout this thesis and the valuable assistance for its development. I thank him very much for his availability and his valuable advice and especially the training month that I spend in his Laboratory in Turkey at the beginning of my thesis. Thank you Pacha Ziyadin.

My sincere thanks go to all the resarchers who accept to take part of the jury oh my PhD thesis: Pr. Stramondo Salvatore, Dr. Briole Pierre, Pr. Masson Frederic, Dr. Çakir Ziyadin.

My sincere thanks go to Fawzi Doumaz and Salvatore Stramondo from the Istituto Nazionale di Geofisica e Vulcanologia (INGV, Rome) with whom I worked in InSAR, Cartography and especialy the DEMs generation. I would like to extend my thanks to his family and to all INGV team. I am grateful to Rachid Bougdal who introduced me to the natural hazards of Haoud Berkaoui and Constantine landslides.

I wish to thank Dr. David Sandwell for the exchange and assistance for GMTSAR InSAR processing on Windows system.

I wish to also thank Yves Rogister, Jacques Hinderer, Jérôme van der Woerd, Noel Gourmelen, Antoine Schlupp for discussions and their precious help.

I also thank Mrs. Rabia Seray from the Algerian Ministry of Higher Education and Scientific Research for the funding provided for this thesis and especially for her confidence.

I thank Mr. Ibrahim Zeroual (INSA and University of Oran) for his help at the beginning of my thesis. Thank you very much.

Special thanks to my PhD student colleagues and Postdocs at the IPGS Abeer Al-Ashkar, Esra Cetin, Mohamed El-Gabry, Elise Kali, Silke Schmidt, Romy Schlogel and Karim Marakchi. Thank you very much.

Many thanks to my parents, my sisters and brothers for their support and their encouragements during the three years of my thesis.

The figures in this thesis have been plotted using readhgt for SRTM-3 providing by François Beauducel IPGP, Matlab and the generic mapping tools (GMT, Wessel and Smith, 1998). The ERS SAR data were provided by the European spatial agency (ESA) under project

C1P 2532. Softwares used in this study are: ROI-PAC (Rosen et al., 2004), Doris (Kampes et al., 2006), StaMPS (Hooper, 2008), and Snaphu (Chen et al., 2000).

## **Table of Contents**

**Acknowledgments**

**5**

<b>I. Summary</b>	<b>11</b>
<b>II. Résumé</b>	<b>15</b>
<b>III. Introduction</b>	<b>19</b>
<b>Chapter I: Basic Principles of Conventional InSAR and New InSAR Processing Generations PS-InSAR, Small Baseline and Merged Methods</b>	<b>23</b>
1. Introduction	25
2.1. Synthetic Aperture Radar Interferometry: Methods and techniques	25
2.1.1. Principles of SAR image acquisition:	25
2.1.2. Characteristics of SAR images:	26
2.2. Conventional InSAR technique limits	34
2.3. Multi-temporal InSAR	35
2.3.1. Permanent Scatterers (Persistent Scatterers, PS)	35
2.3.2. Small Baseline (SBAS)	38
2.3.3. Merged Permanent Scatterers and Small Baseline	40
<b>Chapter II: Monitoring Ground Deformation in the Haoud Berkaoui Oil Field (Sahara, Algeria) Using Time Series Analysis of SAR Images</b>	<b>43</b>
Summary	46
1. Introduction	47
2. The collapse of OKN32 and OKN32bis wells and geologic context	48
3. InSAR data and processing	52
3.1. Differential InSAR results	56
3.2. MT-InSAR processing and results	58
4. Modeling	66
5. Discussion and Conclusion	70
Acknowledgments	71
References	72
	<b>99</b>
<b>Chapter III: Monitoring Landslide in the Urban Area of Constantine (Northeast Algeria) using Advanced Merged PS-SB Insar Analysis</b>	
Summary	101

1. Introduction	103
2. Constantine Landslides Description	105
3. Constantine Geology	108
4. InSAR analyses	111
5. Conclusion	125
Acknowledgment	126
References	126
<b>Chapter IV: Postseismic (Interseismic) Deformation in the El Asnam Fault Region (Algeria): Results From Merged PS-InSAR and Small Baseline Methods</b>	<b>129</b>
Summary	131
1. Introduction	133
2. Tectonic setting	134
3. InSAR Analyses	137
3.1 Chelif basin-scale deformation using time series analysis	142
4. Modeling	148
5. Conclusion	150
References	151
<b>Chapter V: Postseismic Surface Deformation Associated with the Mw 6.4, 24 February 2004 Al Hoceima (Morocco) Earthquake using Time Series Analysis of SAR Images</b>	<b>155</b>
1. Introduction	157
2. InSAR Analysis	159
3. Modeling	175
4. Disussion and conclusion	177
References	177
General conclusion	179
List of All references	185
<b>Appendix</b>	<b>195</b>
<b>GMTSAR Processing: Application to the Surface Deformation of A</b>	

**Moderate Mw 5.7 Seismic Event (1999 Ain Temouchent Earthquake,  
Northwest Algeria)**

Summary	<b>201</b>
1. Introduction	<b>201</b>
2. Seismotectonic Context	<b>207</b>
2. GMTSAR systems	<b>207</b>
3. InSAR data analysis	
4.1. A new program for automatic fringe counting	
4.2. A new Graphical User Interface (GUI) for GMTSAR	
5. Discussion	
References	
Houd Berkaoui additional models	
Article 1: A system to Detect Residential Area in Multispectral Satellite Image	
Résumé	
Articile-2: The Study of the Bay of Mount Saint-Michel by Using Graph Theory in The Analysis of Satellite Images	
Résumé	



# I. Summary

This thesis aims at the study of small to large surface deformation that can be detected using the remote sensing interferometric synthetic aperture radar (InSAR) methods. The new developments of InSAR processing techniques allow the monitoring of surface deformation with millimeter surface change accuracy. Conventional InSAR use a pair of SAR images (“Master” and “Slave” images) in order to measure the phase difference between the two images taken at different times. The uncertainties in measurements using the conventional InSAR due to the atmospheric delay, the topographic changes and the orbital artifacts are the handicaps of this method. The idea of InSAR method is to measure the phase difference between two SAR acquisitions. These measurements refer to the ground movement according to the satellite position. In an interferogram the red to blue colors refer to the pixel movement towards or away from the satellite position in Line-Of-Sight (LOS) direction. In the 2000’s, Radar spacecraft have seen a large number of launching missions, SAR acquisitions and InSAR applicability have seen an explosion in different geophysical studies due to the important SAR data and facility of data accessibility. This SAR-mining needs other type and generation of InSAR processing.

In 2001, Ferretti and others introduced a new method called Permanent Scatterer InSAR (PS) that is based on the use of more than one Slave image in InSAR processing with the same Master image. This method allows enhancing the LOS signal for each pixel (PS) by using the best time and/or space-correlated signal (from amplitude and/or from phase) for each pixel over the acquisitions. A large number of algorithms were developed for this purpose using the same principle (variants). In 2002, Berardino et al developed a new algorithm for monitoring surface deformation based on the combination of a stack of InSAR results from SAR couples respecting small baseline (SB) distance. Nowadays, these two methods represent the existing time series (TS) analysis of SAR images approaches. In addition, StaMPS software introduced by Hooper and others, in 2008 is able to combine these two methods in order to take advantages from both of these TS approaches in terms of best signal correlation and reducing the signal noise errors. In this thesis, the time series studies of surface changes associated to different geophysical phenomena will have two interests: the first is to highlight the PS and SBAS results and discuss the reliability of obtained InSAR signal with comparison with the previous studies of the same geophysical case or observations in the field and in the second time, the combined method will also validate the results obtained separately with different TS techniques. The validation of obtained signal is assured by these two steps: Both of PS and SBAS methods should give

relatively the same interferograms and LOS-displacement signal (in term of sign and values), in addition these results will be compared with the previous studies results or with observations on the field.

In this thesis, the InSAR techniques are applied to different case-studies of small surface deformation: 1) A subsidence in an oil-well area, 2) landslides in an urban area, and 3) slow deformation across fault zones in earthquake areas. In order to study the small deformation I use the two algorithms (PS and SBAS) incorporated in StaMPS software (Hooper, 2008) and developed further in the merged method for all the case studies. The used open access softwares for StaMPS are Roi-pac to align the SAR images and Doris to perform interferograms.

The conductive ligne of this thesis is to demonstrate the ability to measure small surface deformation that cannot be measured effectively using conventional InSAR due to uncertainties and difference in wather conditions, satellite position, topographic changes and other noise, in addition how to correct the obtained LOS signal from both time series methods using the combined method.

The question to answer when we use InSAR techniques is the quality in term of validity of the obtained LOS signal in other word how can we be sure about the interferogram results and what is their geophysical interpretation and associate phenomena. This thesis will try to give answers to these questions by analysing surface changes associate to differents geophysical and natural hazard phenomena in desertic place, montagns, and cities with humain concentration. In addition, several researchers have demonstrated that PS method is not able to measure changes in city, however, in case of Constantine landslide, using the PS approach, I have a good signal quality.

This thesis contains six chapters and one appendix presenting compliments of works:

**1-** After an introduction that presents the context of case studies and previous works using the InSAR techniques, the first Chapter consists in the description of the different InSAR processing methods, the obtained results and their limitations.

**2-**The second chapter is on the *“Monitoring of Ground Deformation in the HaoudBerkaoui Oil Field (Sahara, Algeria) Using Time Series Analysis of SAR Images”*. In this chapter, we presentthe surface displacement (sinkhole and the subsidence) during eight years (1992 to 2000) and the study of the Haoud Berkaoui oil field area, using seventeen ERS-SAR images. A well (OKN32) collapse occurred in 1978 and large crater was formed with 320-m diameter and ~80-m depth.

I apply PS-SB and merged methods for times series analysis to retrieve the deformation map and study the time series evolution in order to delimits the subsidence area. I obtain 1.5

mm/yr of subsidence rate and also estimate the subsidence evolution by studying the direction of the surface deformation over time. The results of this chapter are submitted to the journal Natural Hazards.

3-The third chapter, is about the “*Monitoring Landslide in The Urban Area of Constantine (Northeast Algeria) Using Advanced Merged PS-SB InSAR Analysis*”. In this chapter, I study eight years of surface deformation associated with the well known landslide areas located in the Constantine city (Algeria). I use PS-SB and merged methods and obtain the combined multi-temporal rate of  $\sim 1.2$ mm/yr of subsiding area. In addition, I developed the merged method and obtain  $\sim 3.15$  mm/yr rate of landslide movement.

4- The chapter four is about “*The Postseismic and interseismic deformation across the El Asnam fault (Algeria) from Merged PS-InSAR and Small Baseline methods*”. In this chapter, I investigate surface displacement along the 36-km-long and NE trending El-Asnam thrust fault (NW Algeria) responsible of two large earthquakes (Ms 6.7 in 1954 and Ms 7.3 in 1980) using methods of time series analysis. I characterize two tectonic blocks that limit the earthquake area but parallel to the El Asnam fault, with an uplifted (positive LOS) and a subsided area (negative LOS) of slow deformation. The persistence of the surface deformation more than 40 years after the large Mw 7.3 earthquake is discussed in comparison with the seismic cycle of this active zone of northern Algeria.

5- In chapter 5, I describe recent results on the postseismic surface deformation associated with the  $M_w$  6.4, 24 February 2004 Al Hoceima, Morocco, earthquake using time series analysis of SAR images. The analysis of ERS SAR images from 1992 to 2000 and ENVISAT SAR images from 2000 to 2010 shows a clear signal of surface deformation in the area of coseismic surface faulting. A discrepancy in the location of the coseismic and postseismic surface deformation indicates a complex fault structure with possible branching of seismic ruptures at depth. The characteristics and persistence of the postseismic deformation is discussed and a model of faulting geometry at depth is proposed to explain the relationships with the surface deformation.

A chapter of conclusion presents the main results of this work and the advantage and limitations in the use of InSAR techniques for small surface deformation.

In appendix I present chapter given a description of the open access GMTSAR (Generic Mapping Tools SAR; Sandwell, 2011) for InSAR analysis: “*GMTSAR Processing: Application to the surface deformation of a moderate seismic event in northwest Algeria (Mw 5.7, 1999 AinTemouchent earthquake)*”. Here, I apply GMTSAR to the same data sets used in (Belabbes et

al., 2009) in order to compare the results. In addition, I have developed a new algorithm to count automatically the number of fringes and a new GUI (Graphical User Interface) is proposed. In comparison with the previous work, our results show an additional fringe in the earthquake area that indicates a total 14.3 cm LOS surface displacement. Other models are presented to explain the Haoud Berkaoui case study and two articles treating the optical remote sensing applications.

### **Publication in Journals**

- 2011 Bouraoui, S. A system to detect residential area in multispectral satellite images. IJCSI International Journal of Computer Science Issues, Vol. 8, Issue 6, No 2, November 2011.
- 2013 Bouraoui, S. The Study of the Bay of Mount Saint-Michel by Using Graph Theory in the Analysis of Satellite Images. IJCSI International Journal of Computer Science Issues, Vol. 10, Issue 1, No 3, January 2013. ISSN (Print): 1694-0784 | ISSN (Online): 1694-0814.

### **Meeting & Abstracts**

- 2010 Bouraoui, S. La Télédétection Satellitaire : La Détection Des Quartiers Résidentielle Dans Des Images De Télédétection Optiques De Très Haute Résolution. La Fête De La Science, LSIIT, Strasbourg 2010.
- 2010 Bouraoui, S. A System To Detect Residential Area In Multispectral Satellite Images, Image And Vision Computing New Zeland (IVCNZ), 8-9 Nov. 2010. (Abstract)
- 2011 Bouraoui, S. l'Etude De L'apporté De La Théorie Des Graphes A La Classification Non Supervisée Et La Classification Supervisée Pour L'analyse De La Baie Du Mont Saint-Michel A Partir Des Images Satellitaires. ICC Paris France, 3-8 July 2011.
- 2011 Bouraoui, S. A Multitemporal InSAR Methods Incorporating Both Persistent Scatterer And Small Baseline Approaches For Study Surface Deformation: Sinkhole Of Haoud Berkaoui Area. JDD, Strasbourg, France. 2011. (Abstract)
- 2012 Bouraoui, S., Cakir, Z., Bougdal, R. And Meghraoui, M. MT-Insar Monitoring Of Ground Deformation Around The Haoud Berkaoui Sinkhole (SE Algeria), Abstract: EGU2012-3344, Advanced Methods In Landslides Research I: Remote Sensing And Geophysics. Vienna, Austria, 22-27 April 2012. (Abstract)

- 2012 Bouraoui, S., Meghraoui, M., Bougdal, R. and Cakir,Z.Monitoring Ground Deformation in the Haoud Berkaoui Oil Field (Sahara, Algeria) Using Time Series Analysis of SAR Images. Invited seminar. INGV, Rome. 6 juillet 2012.
- 2012 Bouraoui, S.L'apport de la Télédétection Satellitaire dans l'Observation l'Etude des Sciences de la terre: L'Utilisation des Images Satellitaires Optiques. Les Doctoriales d'Alsace, Centre international de Mittelwihr 2012.(Poster)
- 2012 Bouraoui, S.,Meghraoui, M., Bougdal, R. and Cakir,Z.Monitoring Ground Deformation in the Haoud Berkaoui Oil Field (Sahara, Algeria) Using Time Series Analysis of SAR Images. WEGENER, Strasbourg. France.17-20 Sep. 2012. (Abstract)
- 2012 Meghraoui, M., Bouraoui, S.,Bougdal, R. and Cakir,Z.Of Ground Deformation In The Haoud Berkaoui Oil Field (Sahara, Algeria) Using Time Series Analysis Of SAR Images. American Geophysical Union. San Francisco, USA. 3-7 Decembre 2012.(Abstract)
- 2012 Bouraoui, S.,Meghraoui, M.,Doumaz., F. Postseismic And Interseismic Deformation Across The El Asnam Fault (Algeria) From Merged PS-InSAR And Small Baseline Methods. American Geophysical Union. San Francisco, USA. 3-7 Decembre 2012.(Abstract)
- 2013 Bouraoui, S.,Meghraoui, M., Doumaz, F. Postseismic deformation in the El Asnam fault region (Algeria): Results from merged PS-InSAR and Small Baseline methods **(solicited)**.Geophysical Research Abstracts. Vol. 15, EGU2013-5976, 2013.EGU General Assembly.Vienna Austria. 07- 12 April 2013. (Abstract)

## II. Résumé

Cette thèse porte sur l'étude de la déformation de surface (petite et grande déformation) pouvant être détectée en utilisant la méthode de l'interférométrie « InSAR » pour le traitement des images SAR (Synthetic Aperture Radar, bande C :  $\lambda = 5.6$  cm) et signal associé à synthèse d'ouverture. Les nouveaux développements des techniques de traitement InSAR permettent le suivi de la déformation en surface avec une précision de l'ordre millimétrique. Les traitements dits conventionnels de l'InSAR utilisent une paire d'images SAR (« Maître » et « Esclave ») afin de mesurer la différence de phase entre les deux prises de la même scène d'image à des moments différents. Les incertitudes dans les mesures obtenus à partir du traitement conventionnel de l'InSAR sont nombreuses : la décorrélation dans le signal en raison du délai du à l'atmosphère, la contribution topographique et les positions orbitales sont les handicaps majeurs de cette technique.

En 2001, Ferretti et al. ont introduit une nouvelle méthode appelée Permanent Scatterer (PS-InSAR) également connue sous le nom de Persistent Scatterer. Pour cette méthode, nous utilisons une série d'images, dont une dite esclave pour construire des interférogrammes avec la même image dite « Maître ». Cette méthode permet d'améliorer le signal de visé (LOS) en terme de corrélation pour chaque pixel (PS) en utilisant les meilleurs réflecteurs donnant une corrélation maximale (à partir de l'amplitude et/ou la phase) dans le temps et dans l'espace. Un grand nombre d'algorithmes a été élaboré à cet effet en utilisant le même principe (des variantes) décrit auparavant. En 2002, Berardino et al. publient un nouveau algorithme développé pour le suivi de la déformation en surface en se basant sur les interférogrammes produits à partir des couples d'image SAR ayant une petite séparation spatiale (SBAS) de la ligne de base.

Dans cette thèse, les techniques InSAR sont appliquées pour différents cas d'étude allant de la petite déformation en surface telle que: 1) Un affaissement dans une zone de puits de pétrole, 2) des glissements de terrain dans une zone urbaine, et 3) la déformation lente à travers les zones de failles des zones sismiques. Afin d'étudier la petite déformation j'opte pour l'utilisation des deux algorithmes (PS et SBAS) dit de traitement multi-temporelle de l'InSAR incorporés dans le logiciel StaMPS (Hooper, 2008). Ainsi, j'ai pu calculer la méthode de combinaison ou hybride entre PS et SBAS et ce, pour toutes les études de cas présentées dans cette thèse. Par ailleurs, certains logiciels en libre accès sont utilisés tout au long de cette thèse tel que, Roi-pac (Rosen et al., 2004) pour aligner les images SAR ainsi que Doris (Kampes et al., 2003) pour calculer interférogrammes à partir de images SAR.

Cette thèse contient sept chapitres:

1 - Après une introduction qui présente le contexte d'études des cas et des travaux précédents en utilisant les techniques InSAR, le premier chapitre consiste en la description des différentes méthodes de traitement InSAR, en détaillant les aspects fondamentaux et leurs limites.

2 - Le deuxième chapitre porte sur le suivi et la surveillance de la déformation dans le champ pétrolier de Haoud Berkaoui (Sahara, Algérie) engendré par un puits de prospection mettant en contact les eaux souterraines avec une couche de sel. Le puits OKN32 s'est effondré produisant en 1978 un grand cratère visible en surface avec un diamètre de 320 m et une profondeur de ~80 m. Le cratère formé suite à l'incident et la dissolution de la couche de sel ainsi que l'évolution de la subsidence sont étudiés par le suivi spatio-temporel MT-InSAR à partir de dix-sept images ERS-SAR. Dans ce chapitre, nous calculons le déplacement en surface à l'aide des images SAR qui couvrent une période de huit ans (1992-2000), accompagné d'une modélisation pour expliquer l'origine du phénomène. J'applique les deux méthodes de suivi-temporel PS-SB ainsi que la méthode hybride pour produire la carte de déformation permettant d'étudier l'évolution des séries chronologiques afin de délimiter la tendance de propagation de la zone de subsidence. J'ai obtenu une vitesse de subsidence de 1.5 mm/an durant les huit ans. Les résultats de ce chapitre sont soumis au journal « Natural Hazards ».

3 - Le troisième chapitre est consacré au suivi de l'évolution des glissements de terrain dans la zone urbaine de Constantine (Algérie au nord) en utilisant les deux approches PS-SB et celle hybride pour l'analyse des images SAR de 1992 à 2000. Après une identification des zones de glissement à l'aide des observations de terrain (Bougdal, 2007), l'application des méthodes Mt-InSAR permet d'obtenir une vitesse moyenne des glissements de ~ 1.2 mm/an dans la zone d'étude. En outre, j'ai développé une méthode de fusion PS-SB avec laquelle j'ai obtenu la vitesse de ~ 3.15 mm/an de glissement de terrain.

4 - Le chapitre quatre porte sur la déformation postsismique et intersismique de 1997 à 2000 à travers la faille d'El Asnam (Algérie) à partir des méthodes MT-InSAR. J'étudie ici le déplacement en surface le long de zone de faille de chevauchement d'El-Asnam (36-km de long), de direction NE, et responsable de deux grands tremblements de terre de 1954 (Mw 6.7) et 1980 (Mw 7.3), en utilisant les méthodes PS, SBAS et hybride. Les résultats montrent deux grands blocs tectoniques avec une limite entre une zone de soulèvement (LOS positif) et une zone de subsidence (LOS négatif) parallèle à la faille El Asnam, avec un déplacement total annuel de 30.2 mm. 40 ans après le séisme majeur de Mw 7.3, la persistance de la déformation en surface est discutée en comparaison avec le cycle sismique de cette zone active du nord de

l'Algérie.

6 - Dans le chapitre 5, je décris les résultats récents sur la déformation de surface postsismique associée au séisme de 2004 (Mw 6.4) d'Al Hoceima (Maroc), en utilisant une analyse de séries temporelles d'images SAR. L'analyse des images SAR ERS 1992-2010 montre un signal clair de la déformation de surface dans la zone épacentrale. Une différence dans la localisation de la déformation de la surface cosismique et postsismique indique une structure complexe de la faille avec la possibilité d'avoir un branchement de la rupture sismique en profondeur. Les caractéristiques et la persistance de la déformation postsismique est discutée et un modèle de failles géométrie en profondeur est proposé pour expliquer les relations avec la déformation de surface.

Un chapitre de conclusion présente les principaux résultats de ce travail avec les avantages et limitates dans l'utilisation des techniques InSAR pour la petite déformation de surface.

En annex, je present un chapitre dicrivant l'utilisation de GMTSAR (Sandwell, 2011 ; code source en libre accès) et son application à la détection d'une déformation de surface de faible amplitude liée au séisme de Ain Temouchent de 1999 (Mw 5.7) au Nord de l'Algérie. J'applique ici GMTSAR aux même jeux de données SAR utilisé dans (Belabbes et al., 2009) afin de comparer les deux résultats. De plus, j'ai développé un nouvel algorithme pour compter automatiquement le nombre de franges de la déformation cosismique ainsi qu'une interface graphique (Graphical User Interface) pour faciliter l'utilisaion de GMTSAR. En comparaison avec le travail précédent mené dans cette zône, nos résultats montrent une frange supplémentaire dans la zône épacentrale qui indique 14.3 cm de déplacement de surface dans la direction du LOS. Deux modèles sont présentés dans le cas de l'études de Haoud Berkaoui. Deux articles portant sur le traitement des images optiques sont ainsi presnete dans le cade de l etudes par le biais de la teledetection.

### III. Introduction

The purpose of this thesis is the study of small to large surface deformation that can be detected using the remote sensing interferometric synthetic aperture radar (InSAR) methods. The recent developments of InSAR processing techniques allow the monitoring of surface deformation with millimeter surface change accuracy (Cakir et al., 2006; Hooper, 2012). Conventional InSAR and D-InSAR consist in the use of a pair of SAR images (“Master” and “Slave” images) in order to measure the phase difference between the two images taken at different times. Indeed, InSAR has been used in several studies concerning seismically active regions in North-Africa (Cakir et al., 2006; Belabbes, 2008; Akoglu et al., 2006). The coseismic surface deformation in the LOS direction for moderate or large earthquakes ( $M_w > 5.5$ ) is relatively well constrained through the succession of fringes (mainly for band C). Although, the North African arid and semi-arid areas (with good coherency) generally allows the visibility of a certain amount ( $> 1$  fringe) of surface deformation, the uncertainties in measurements due to the atmospheric delay, the topographic contribution and the orbital error, added the temporal and geometric deccorelations constitute a serioushandicapthat affects the resulting interferogram and interpretation. Hence, small and/or slow deformation or creeping hardly visible at the surface requires a better constraint of measurements and related uncertainties.

To overcome these problems, the InSAR technique called Multi-Temporal (MT-InSAR) also known as time series analysis of SAR images has been developed. Two approaches exist nowadays: Ferretti et al. (2000, 2001) introduce the Permanent Scatterer InSAR (PS) based on the use of more than one slave image in InSAR processed with the same master image. This InSAR approach deals with the selection of the reflector elements for each pixel that present the small phase variation over the considered time period. Each selected PS is the sum of the contributed wavelets for one pixel, and with high correlation (for amplitude and phase) in time and in space. A large numbers of algorithms were developed for this purpose using the same principle (variants). The second method has been initially developed by Berardino et al. (2002) using a new algorithm for monitoring surface deformation respecting the small baseline separation between different SAR-pairs (SBAS or SB). Nowadays, these MT-InSAR techniques can be combined or merged as in the StaMPS algorithm of Hooper (2008). More recently, Ferretti et al. (2011) added a new method called SqueeSAR aiming to combine the results from processing PS and DS (Distributed Scatterer)

In this thesis, the InSAR techniques are applied to different case-studies of small surface deformation: 1) A subsidence in an oil-well area, 2) landslides in an urban area, and 3) slow deformation across fault zones in earthquake areas. These three subjects presumably present evidence of surface deformation with mm to cm amount of displacement. In order to measure the small deformation I proceed by using i) the two MT-InSAR algorithms (PS and SBAS) and ii) the Merged method (PS-SB), both incorporated in StaMPS software for all the case-studies. The used open access softwares for StaMPS are Roi-pac to align the SAR images and Doris to perform interferograms.

After an introduction that presents the rationale of the chosen subject and InSAR approach, a second chapter details the basic principles of the Conventional Synthetic Aperture Radar InSAR with their limitations and shows the fundamentals of InSAR processing generations PS-InSAR, Small Baseline and Merged methods. In parallel and for comparison I also present the conventional InSAR techniques and D-InSAR, and discuss their limitations. A first example of small surface deformation with subsidence, next to a sinkhole since 1978, in the Haoud Berkaoui oil field area (Sahara, Algeria) is presented in chapter three; this is also an article submitted to the journal Natural Hazards.

The second case-study deals with well-known landslide areas located in the Constantine city (Algeria); the mapping of surface deformation using PS-SB and merged methods locate the main landslides and indicate their sense and rate of movement. A comparison with field studies shows the spatial and temporal resolution of InSAR methods in determining landslide hazards.

The transition to regions of earthquake activity is done through the application of the open access GMTSAR (Generic Mapping Tools SAR; Sandwell, 2011) to a moderate earthquake in northwest Algeria (Mw 5.7, 1999 Ain Temouchent earthquake) and related small deformation (initially 4 fringes determined from a previous study). In this section, I present a new algorithm that counts automatically the number of fringes and a new GUI (Graphical User Interface). This part is moved to the Appendix.

Chapter five shows how with MT-InSAR algorithms (PS and SBAS) a slow surface deformation is determined in the El Asnam region, the site of Ms 6.7 in 1954 and Ms 7.3 in 1980; here, even 33 years after the large earthquake I advocate that the observed deformation can be postseismic or interseismic. Furthermore in chapter seven, I describe the postseismic surface deformation associated with the  $M_w$  6.4, 24 February 2004 Al Hoceima, Morocco, earthquake using time series analysis of SAR images. The characteristics and persistence of the postseismic deformation is discussed and a model of faulting geometry at depth is proposed to explain the relationships with the surface deformation.

Finally, a conclusion presents the main results of this work and the advantage and limitations in the use of InSAR techniques for small surface deformation.



## **Chapter I**

# **Basic Principles of Conventional InSAR and New InSAR Processing Generations PS-InSAR, Small Baseline and Merged Methods**



# 1. Introduction

Time series analysis marks the second generation of the Synthetic Aperture Radar Interferometry (InSAR) processing methods. In this chapter, I present the fundamental principles of InSAR processing technique, after that I discuss their limitations, which have been the reason for the appearance of new powerful InSAR techniques. Nowadays, there are two approaches of time series analysis: persistent scatterer (PS, Ferretti et al., 2001) and small baseline (SBAS, Berardino et al., 2002). After a general introduction on the SAR interferometry, I give here the fundamental principles of these two approaches accompanied by the merging method incorporated in StaMPS/MTI (Hooper, 2008).

## 2.1 Synthetic Aperture Radar Interferometry: Methods and techniques

Airborne and spaceborne remote sensing systems may be divided into two categories according to the sensor type: 1) The Synthetic Aperture Radar (SAR) family which is an active remote sensing system, and 2) the optical systems (e.g., SPOT-5, QuickBird satellites) endowed by optical sensors called passive systems.

Unlike the optical systems, radio detection and ranging (Radar) systems have the advantage to operate in all weather conditions because they are based on radio and microwave frequencies that are able to penetrate the clouds and provide images where pixels record the electrical and geometrical properties of the surface reflectors in the line of sight of the satellite.

In geophysics, scientists are interested in natural events that imply surface changes such as earthquakes, volcanic eruption, glacier surges and landslides. Therefore, remote sensing techniques were developed in particular for the understanding of natural hazards.

### 2.1.1 Principles of SAR image acquisition:

The Radar (RAdio Detection And Ranging) technique was developed in the 20<sup>th</sup> century for its ability to determine physical parameters (size, roughness or the displacement) of an illuminated object using the range and backscatter intensity from two-way travel time of the electromagnetic pulse. In 1978, NASA launched the first SAR space-borne SEASAT satellite for ocean studies (Fu et al., 1982). The frequent use of InSAR began in late 20<sup>th</sup> and InSAR became an indispensable remote sensing technique that can be applied for the studies of different geophysical areas and especially for natural phenomena. Goldstein et al. (1993) and (Massonnet

et al., 1993) presented the first InSAR analysis performing map of surface deformation of ice stream in Antarctica. SAR was firstly used for exploring the planetary surfaces. Conventional InSAR use two-pass in this sense, there are similarity between conventional InSAR and the stereoscopy methods, especially to detect changes on the earth surface (Hanssen, 2001; Simons et al., 2007). The InSAR technique using two acquisitions on a single platform is called ‘cross-track’, ‘single-track’ or ‘single-pass’ interferometry. (Richman, 1971; Zisk, 1972) present initially the first studies using principle of InSAR to study Earth remote sensing. Goldstein and Zebker (1987) improve the InSAR method by developing the new technique called “along-track” interferometry that is able to detect surface movement from different time-lapse SAR acquisition. The large applicability of InSAR in geophysical domains was with the launch of the European Space Agency (ESA) ERS-1 satellite providing a large quantity of SAR data with side-looking geometry (Figure 1).

The resolution of SAR image is defined as the minimal distance for two objects on the ground to be distinguished, which depends on properties of the antenna (length, width and angle of incidence), the satellite altitude and duration of the emitted pulse. The launch of ESA satellite ERS-1 mission ended on 10-03-2000 and the ERS-2 mission was retired on 05-09-2011, which enabled the use of satellite images especially in surface deformation associated with large shallow earthquakes.

### **2.1.2 Characteristics of SAR images:**

As the aircraft / spacecraft platform carrying the SAR instrument moves, the beam footprint scanned along the cross-track direction, and pulses or radar waveforms are transmitted at the pulse repetition frequency in the cross-track and azimuth dimension (Figure 1). As a consequence, objects that are close to the antenna (i.e. near range) return an echo before those that are farther away. Pulse repetition frequency (PRF) used to acquire a series of backscatter each of the beam footprints along the cross track scan length. For each scan, a two-dimensional image is constructed with pixels in the along-track direction resolved by range gating and pixels in the cross-track direction resolved by the aperture size; the PRF rate and raw data recorded by SAR system is focused to form an image. Using 2-D matched pulse compression in range and azimuth directions after merging echoes in the flight direction synthesizes a large antenna aperture. Bandwidth in flight direction contains a Doppler effect associated with the variation in the sensor movement relative to Earth (Hanssen, 2001).

In SAR image, each pixel has both amplitude and phase values; the amplitude value record the radar brightness “speckle effect” in range direction, the backscattered energy of the pulse informs about the radar contribution of that pixel (figure 2). Radar mapping using SAR signal processing enables us to remotely image a target respecting a high resolution reaching meters. The first processing step for SAR is to produce the single look complex (SLC) image of the raw image represented in 2-D array containing complex numbers recording the brightness and the phase each scatterers on the ground respecting the azimuth and the range direction of the SAR-platform.

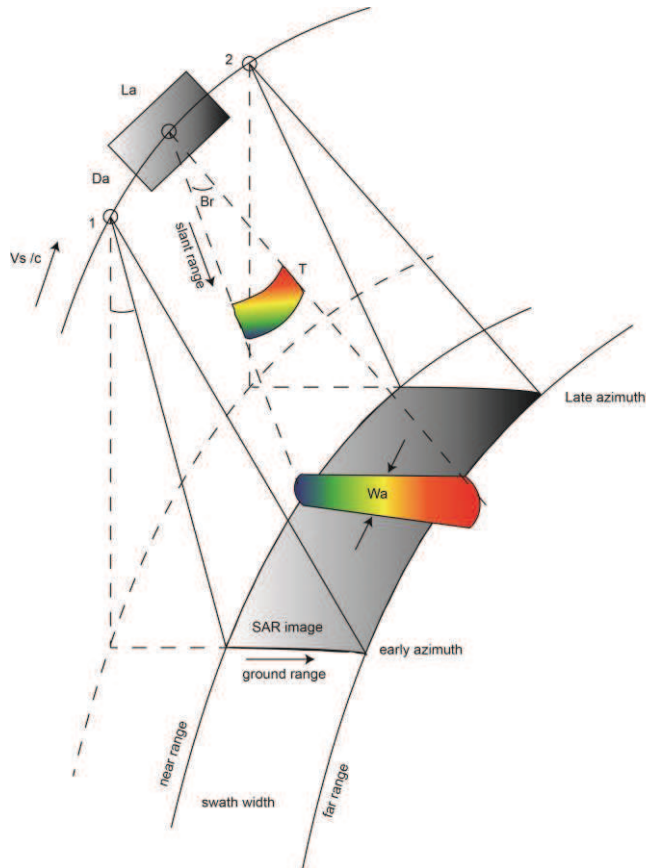


**Figure 1:** Typical synthetic aperture radar imaging system geometry from Hanssen (2001). The common image geometry mode illuminates footprint area with the strip-map mode, recently, there is modern phased-array used with ScanSAR and spotlight SAR mode. 1 and 2 indicate respectively the first and second SAR acquisition as well as the Orbital positions 1 and 2.

SAR systems are divided into two families according to their look angle and track direction. Ascending and descending tracks are used for single looking radar system. The combined ascending and descending acquisitions in InSAR processing allows avoiding problems as shadow and layover and has a complete vision of the study area in term of displacement in LOS (Line Of Sight) and give ability to construct the 3-D displacement component as shown in

Figure 2. In addition, The SAR system acquisition illuminates the same scatterer more than one time using the aperture antenna property and the combination of information from many pulses.

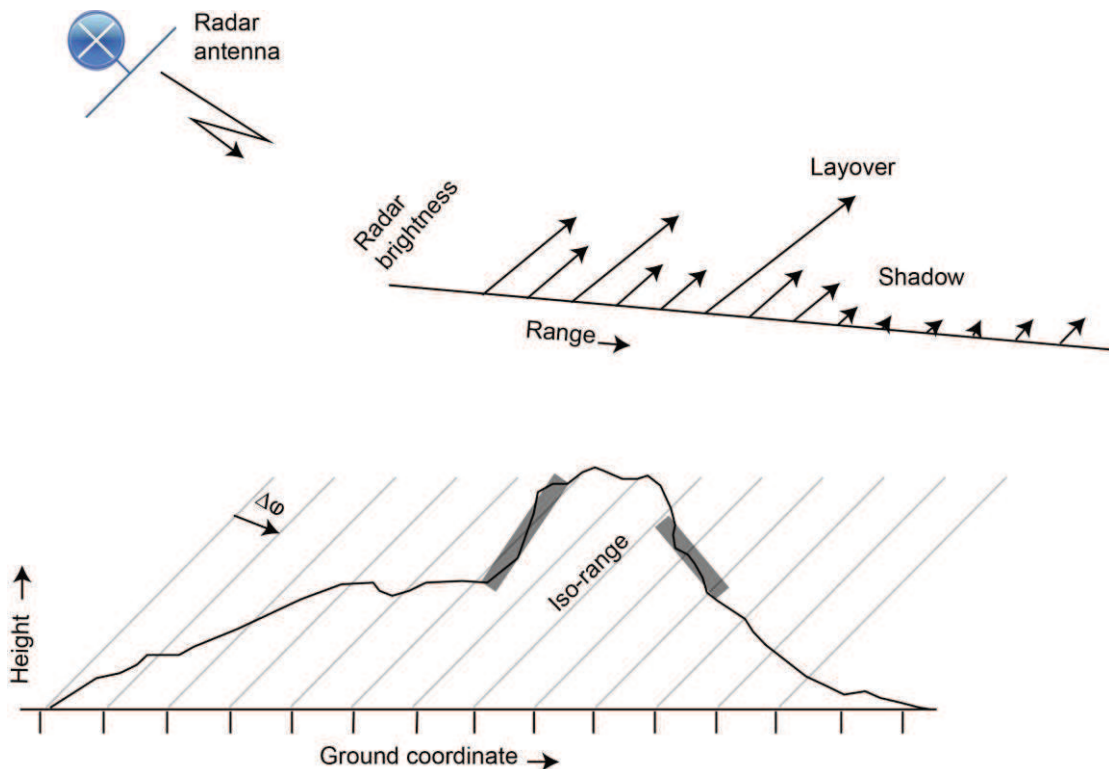


**Figure 2:** The 3-D vision is simplified into two dimensions in conventional SAR imaging. After image formation, the radar return is resolved into an image in range-azimuth coordinates. This panel shows a profile of the terrain at constant azimuth, with the radar flight track into the page. The profile is cut by curves of constant range, spaced by the range resolution of radar, defined as  $\Delta\rho = c/2\Delta f_{BW}$ , where  $c$  is the speed of light ( $\sim 2.9979 \times 10^8$  km/s) and  $\Delta f_{BW}$  is the range bandwidth of the radar. The backscattered energy from all surface scatterers within a range resolution element contributes to the radar return for that element.

Interferometry works when two images are acquired over the same area at different times, by the same sensor or different sensors with similar characteristics (Figure 3). The difference in phase interference between the two images is obtained by multiplying the complex conjugate of the second image (Slave) after a resampling by the first image (Master). These two SAR images are almost obtained with marginally different two-imaging geometries, and the Slave image (the second SAR image) must be coregistered and resampled to match the Master (the first) SLC image geometry (Zebker et al., 1986). The interferogram is obtained by multiplying respectively the phase and the amplitude of the SLC Master image with the corresponding conjugate and co-registered Slave image for each element phase and amplitude.

In order to illustrate some interferograms results I also used GMTSAR which is an InSAR processing software (<http://topex.ucsd.edu/gmtsar/>, see chapter 5) that can be applied to different SAR images (ALOS data, Envisat data and ERS data). Some illustrations in Figure 3 a, b and c show the resulting interferogram obtained with GMTSAR and (d) with Roi-pac of HaoudBerkaoui (see chapter 3) using two ERS-SAR images recorded in C-band ( $\lambda / 2 = 2.83$  cm) gives one cycle of phase difference. In Figure 3 d, the interferogram using 1992-06-04 and 2000-05-07 SAR images with the color palette represents the interferogram phase modulo  $2-\pi$  phase modulo  $2-4$ , and 2000-05-07 SAR images with the color palette represents the phase with the same results but with one or less than a complete fringe.

Both SAR platform ERS-1/2 and Envisat ASAR use C-band wavelength 5.66 cm making the combination in the use of this two SAR platforms possible in order to produce interferograms and also other SAR processing type. ALOS SAR platform using the PALSAR sensor use the L-band with wavelength 23.6 cm (Figure 3).

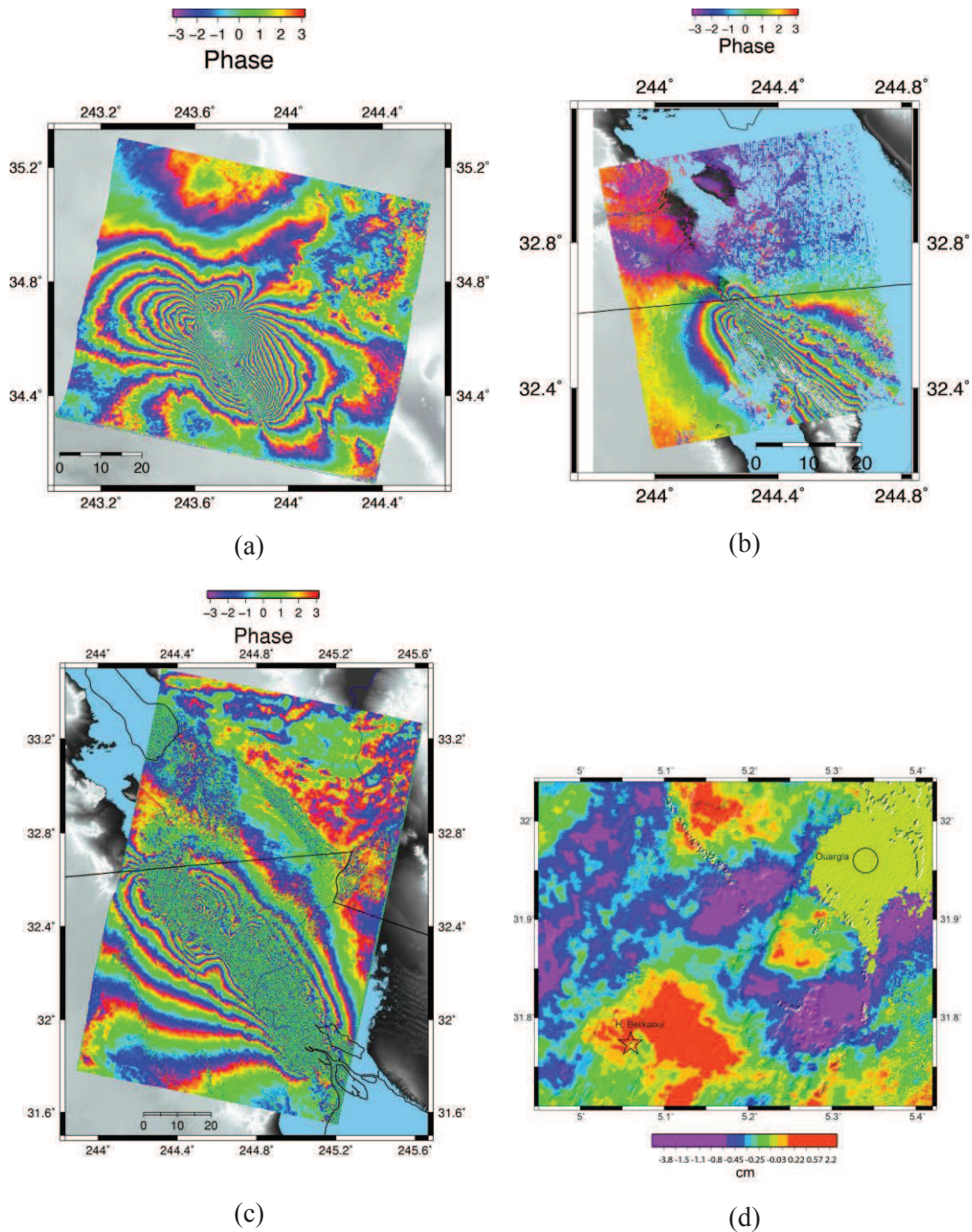


**Figure 3:** Examples illustrating four interferograms with surface changes obtained for three earthquake events and a surface subsidence. (a) Hector Mine California earthquake, 16th of October 1999 (Mw 7.1) using GMTSAR processing of two-ERS-2 SAR images of (e2\_127\_2907\_23027 and e2\_127\_2907\_23528, see chapter 5). (b) Baja California earthquake, 4 April 2010 (Mw 7.2) using GMTSAR processing of two-ALOS SAR images of (2009-1-25 and 2010-12-4). (c) El Major-Cuppacah earthquake, 4 April 2010 (Mw 7.2) using GMTSAR processing of two-Envisat SAR images of (2010-02-12 and 2010-8-7). (d) Descending Interferogram obtained for HaoudBerkaoui area using Roi-pac (Bouraoui et al., 2013).

In Figure 1, the difference in phase 1 and phase 2 between the two SAR acquisitions forming the interferogram (IFG) is associated to the difference in path length between the SAR platform and the target during the two time acquisitions. In fact, this difference is expressed in the line of sight (LOS) direction. Phase difference associated to the ground deformation is composed of the topographic and displacement constituents (the component we need to be extracted); in addition, the signal noise ratio contains the atmospheric component delay, the orbital artifact (or known as difference in baseline between the two SAR acquisitions) and the noise due to the material characteristics:

$$\Phi_{\Delta t_i} = \Phi_{topo,\Delta t_i} + \Phi_{def,\Delta t_i} + \Phi_{atm,\Delta t_i} + \Phi_{orb(base),\Delta t_i} + \Phi_{noise,\Delta t_i} \quad (1)$$

Where:  $\Delta t_i$  is the time interval separating the two SAR acquisitions for interferogram.  $\Phi_{topo,\Delta t_i}$  is due to the changes in topography.  $\Phi_{atm,\Delta t_i}$  is due to the atmospheric delay (The cloud and ionosphere introduce delay parameter to the phase penetrating them). Notice that the topographic component is static in time, however,  $\Phi_{topo,\Delta t_i}$  changes over the time, because the interferograms have different perpendicular baselines  $B_{\perp,i}$ .  $\Phi_{def,\Delta t_i}$  is due to the ground changes.

In order to simplify the InSAR phase difference, we may consider as negligible the decorrelation effects due to the atmospheric delay, the topographic changes or the orbital contribution (the change associated to the difference in length between Acquisition-1 to the target and Acquisition-2 to the target in term of line-of-sight -LOS- as illustrated in Figure 1). We may obtain:

$$\phi_I = \phi_1 - \phi_2 = -\frac{4\pi}{\lambda}(r_2 - r_1) = -\frac{4\pi}{\lambda} \Delta r \quad (2)$$

Where:  $\phi_1$  and  $\phi_2$  are respectively phase of SAR-1 and phase of SAR-2.  $\Delta r$  is the difference between path lengths from the acquisition-1 and the acquisition-2 to the target.

Spaceborne geometries respecting baseline  $B < 1\text{km}$ , and  $D$  the distance between the illuminated target at time  $t_1$  and  $t_2$  respectively, and assuming the same imaging geometry we obtain:

$$\phi = \frac{4\pi}{\lambda}(-(I_1, B) + (I_1, D)) \quad (3)$$

The complete formula describes InSAR phase difference between two SAR images taken for the same area in different time as in Rosen et al. (1996):

$$\phi = -\frac{4\pi}{\lambda} B \cos(\theta_0 - \alpha) \frac{z}{r_0 \sin \theta_0} + \frac{4\pi}{\lambda} \delta r_{disp} \quad (4)$$

Where  $\delta r_{disp}$  is the surface displacement between two imaging times in the LOS direction and  $z$  is the topographic height above the reference surface (the topography file used as reference, i.e SRTM file). This equation of phase difference is also sensitive to change in topography between two SAR acquisitions and used to generate map of displacement or topography. The atmospheric delay is one of the noises known in InSAR processing, which varies in space and time along the radar propagation path. In two-pass InSAR, the atmospheric delay has minor effect in the results. However it is much important in the repeat-pass InSAR systems (Rosen et al., 2000; Zebker et al., 1994).

The topographic artifact can be subtracted from the LOS signal of the interferogram using known digital elevation model (DEM) as described in Massonnet et al. (1993), thus allowing the phase unwrapping. The phase unwrapping can be seen as optional if the LOS signal after InSAR interferometry is less than one fringe (Figure 3d). In general it is seen as  $2\pi$ -modulus of absolute phase signal. We use filters before starting the unwrapping of phase in order to reduce the noises affecting negatively the final results (topography or surface displacement).

All phase unwrapping algorithms work when the phase signal is continuous and the unwrapped image produces multiples of  $2\pi$ . The interferometric phase is determined modulo  $2\pi$  from the wrapped image and the map have non continuous phase. Phase unwrapped algorithms came to solve this phenomena, and obtained a continuous interferometric map taking into account the phase difference between the neighboring pixels. The differential InSAR processing systems have the similar processing steps order as shown in Figure 4. The InSAR systems can be divided into six steps that are: SAR focusing, Coregistering and resampling the Slave image(s), calculate the phase difference and estimate the correlation, remove the topography (using external DEM or GPS files), filtering the interferometry, phase unwrapping, geocoding (georeferencing), post-processing (plot, modeling, ...etc., Figure 4).

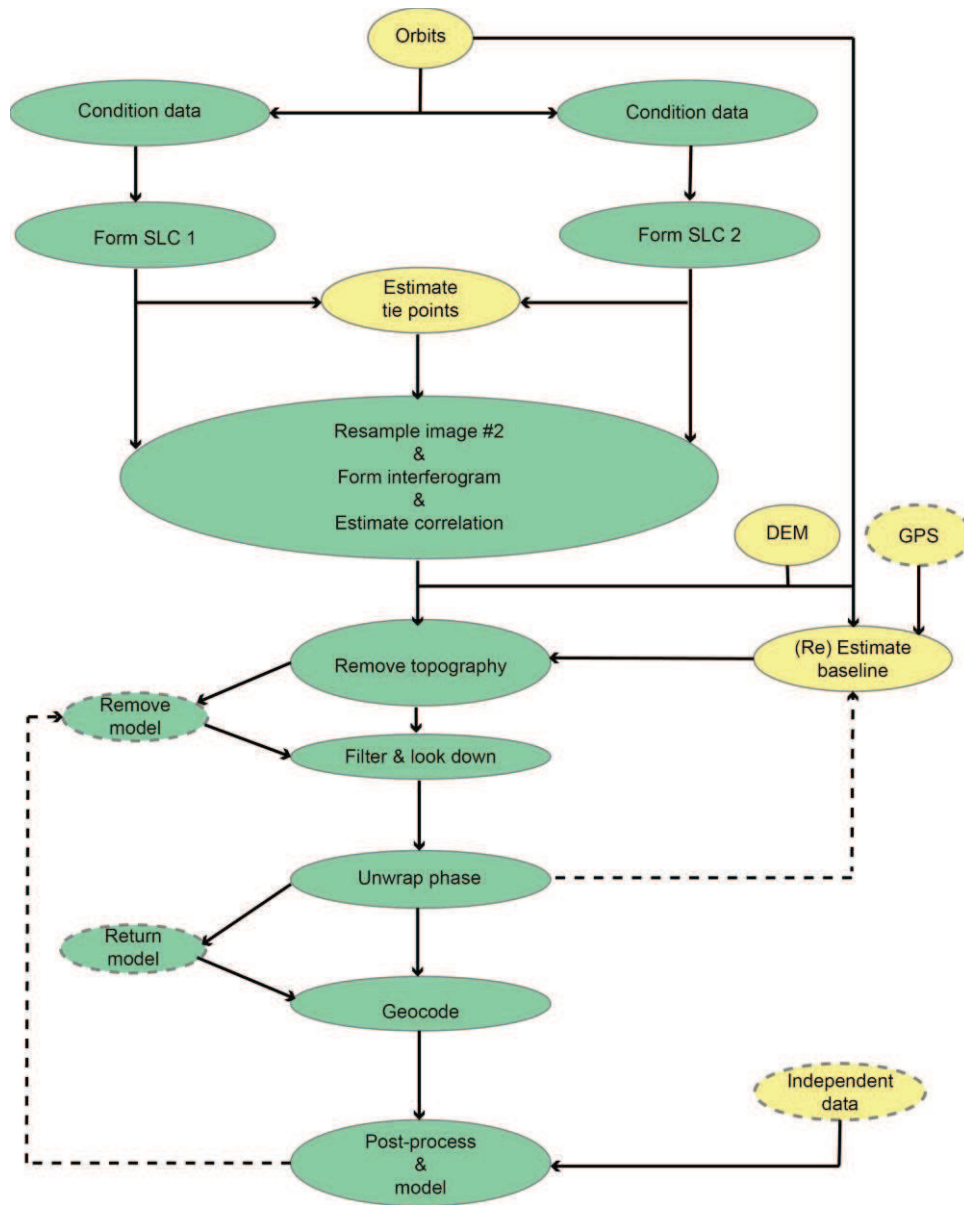


**Figure 4:** Flowchart of standard InSAR2-pass and differential InSAR processing as described in ROI-PAC software suite (Rosen et al., 2004). Yellow ellipses represent non-image data and the dashed arrow indicates optional iteration, dashed ellipses indicate optional procedure. The green ellipses indicate the main processing steps or component (from raw data to images output).

To study ground deformation, the term to take into consideration and that should be extracted from the formula (1) is  $\phi_{def, \Delta t_i}$ . Therefore, the other terms of this formula are considered as noise.  $\phi_{orb (base), \Delta t_i}$  and  $\phi_{topo, \Delta t_i}$  can be estimated and removed using respectively precise orbit information with a spherical model for the Earth's surface, and a digital elevation model (DEM), commonly using DEM from the Shuttle Radar Topography Mission (SRTM; Farr et al., 2007). This InSAR method called Differential interferometry (D-InSAR; Massonnet et al., 1993) is now considered as conventional InSAR.

## 2.2 Conventional InSAR technique limits

The differential InSAR technique are the more adopted remote sensing method used by the geophysical community to study earthquake deformation. This is mainly due to their applicability to different geophysical measurements going from small-scale to large-scale displacement with sub-centimeter accuracy. D-InSAR has been applied for measuring ground deformation due to volcanic (Hooper et al., 2012), co-seismic (Cakir et al., 2006; Akoglu et al., 2006), post-seismic slip (Ryder et al., 2007; Cakir et al., 2003), movement of glaciers (Gourmelen et al., 2011), fault creeping (Cakir et al., 2005). The measured deformation using D-InSAR is related to the quality of the signal correlation that can be limited by changes in scatterers property with time. Temporal decorrelation (Zebker et al., 1992) due to the dielectrically changes in the scatterers property (vegetation, water, or other phenomena) limits the use of conventional InSAR to regions having a waterless condition as in desertic areas (see also the Haoud Berkaoui case-study in Chapter 3.). In addition, interferometric phase decorrelation has another source due to the geometry of the SAR acquisitions known as the difference in incidence angles that have a big impact with large baseline separating the two SAR images (Zebker et al., 1992); this is also true with changes in the squint angle of the spacecraft that cause change in the SAR Doppler frequencies. The first step to remove or avoid this deccorelations factors, we use filtering methods and condition to imitate and help in the choice of the suitable SAR pairs to be processed respecting a small baseline and also short time in order to reduce the temporal and geometric deccorelation effects. The atmospheric delay  $\phi_{atm,\Delta t_i}$  is one of the most difficult signal contribution to be estimated. The signal signature can be seen as a variation in the atmospheric conditions involving a variation in the signal propagation after and before cloud penetration. This variation is compared and very soon correlated with the topographic contribution. For this reason, as the time separating the two (or more) SAR image acquisitions is important (more that one month), the time uncorrelation due to the atmospheric delay is more important and difficult to be integrally removed using the conventional D-InSAR processing system.

In order to enhance the interferogram results and reduce the temporal uncorrelation, new techniques are applied based on the use of interferograms stacking and their combined information. This method is commonly called Multi-Temporal InSAR methods (MT-InSAR).

## 2.3 Multi-temporal InSAR

Conventional InSAR processing involve decorrelation of the interferometric signal caused by the difference in orbital position between the two SAR acquisitions, topography changes, atmospheric delay (ionosphere), atmospheric condition changes. In addition, the changes in dielectrical characteristics of scatterers favor the presence of temporal and geometric (baseline) decorrelations presented in conventional D-InSAR interferograms. Using DELFT orbital precision data (Sharoo and Visser, 1998) we can estimate and remove the orbital error  $\phi_{orb (base), \Delta t_i}$ . The atmospheric and topographic errors are correlated and to attenuate these decorrelations phenomena the Multi-temporal processing also known as time series analysis aims to reduce the signal decorrelation and residuals with the processing of multiple SAR images over the same track in order to get the best signal-to-noise ratio and then obtain the best phase signal correlation matrix. Nowadays, there are two MT-InSAR classes: Persistent Scatterer (PS) and Small BASline (SBAS) methods. Each of these two methods gives temporal solution to the uncorrelated phenomena based on the principle of dominant reflectivity of centers of permanent scatterers. MT-InSAR use one set of images (for phase values) and the reflected signal from each element in the ground (depending on it is resolution) is obtained with the sum of all individual wavelets reflected by the scattering centers of each elements (See Figure 5).

### 2.3.1 Permanent Scatterers (Persistent Scatterers, PS)

Persistent scatterer InSAR (PS) (Ferretti et al., 2000, 2001; Kampes, 2005; Hooper et al., 2004; van der Kooij et al., 2006) marks the second generation of InSAR processing systems that belong to the family of time series analysis and MT-InSAR techniques. PS was developed to give solutions to the conventional InSAR decorrelation especially those due to temporal and geometric effects (Ferretti et al., 2001). The errors due to spatial and temporal variations cause the temporal and spatial phase errors producing disconnected areas in space and time (Hooper, 2006). This makes the interpretation of geodetic measurements from interferograms difficult and sometimes ambiguous by reducing the signal-to-noise ratio (SNR). Man-made structures can be used as corner reflectors and reference to calibrate the InSAR system due to their coherent phase center. The principle of permanent reflector method is to identify points (scatterers) from a series of InSAR images that preserve their coherence (in term of signal backscattered) in time and space. These scatterers will form a connected network from their phase measurements (Hooper, 2006). The interferometric phase distribution ranging between  $[\pi -\pi]$ , to improve the phase

signal, one of the existing solutions is to choose the dominant element from the interferometric phase by statistical estimations from the brightness of each reflector and the dominant signal with its corresponding dominant scatterer. This method guarantees that the obtained signal is less affected by the decorrelations phenomena using the one signal of the dominant scatterer for each pixel to perform the time series evolutions of the studied phenomena. The chosen pixels have invariance in their amplitude values and/or their phase values over a set of PS SAR images. Note that the variance correlates with the brightness of the non-selected scatterers of the same pixel. In fact, as their brightness raises, the variance of the pixel grows. The signal-to-clutter ratio (SCR) is obtained in this case by measuring the ratio between the echo of the dominant scatterer and to the sum of echoes from the other reflectors of the same pixel. The aim of using the PS method is to separate the noise signals and extract the signal of deformation ( $\phi_{def,\Delta t_i}$ ) from formula 1.

In order to remove from the interferograms the phase contribution due to the topography and the imaging geometry  $\phi_{topo,\Delta t_i}$ , PS use the flattening correction. The principle is to suppose that all scatterers are in the WGS-84 projection system of the digital elevation model (DEM) in radar coordinate and calculate the topographic contribution and then remove it. Most common way is to use the SRTM data (Farr et al., 2007). Following Kampes (2006), the DEM error is estimated from the phase signal using:

$$\phi_{topo,\Delta t_i} = \frac{4\pi}{\lambda} B_{\perp}(\theta) \frac{\Delta h \sin(\theta)}{r} \quad (5)$$

Where:  $r$  is the distance from the satellite to the pixel on the ground.  $\theta$  is the look angle of the satellite.  $B_{\perp}$  is the perpendicular baseline.

Where  $r$  is the distance from the satellite to the pixel on the ground,  $\theta$  is the look angle of the satellite, and  $B_{\perp}$  is the perpendicular baseline.

One of the typical characteristics of the SAR images is the range and azimuth resolutions. Using the time series methods, these two parameters belong to dominant scatterer positions in the pixel. We may then estimate the error in the range and in azimuth position of sub-pixel as following (Kampes, 2006):

$$\phi_{\epsilon,\Delta t_i} = \frac{4\pi}{\lambda} B_{\perp}(\theta) \frac{\epsilon \cos(\theta)}{r} \quad (6)$$

$$\phi_{v,\Delta t_i} = \frac{2\pi}{\delta} \Delta F_{DC} \omega \quad (7)$$

Where  $\varepsilon$  indicates the distance between the dominant scatterer and the center of the pixel,  $v$  is the velocity of the satellite,  $\omega$  the azimuthal offset component of the dominant scatterer from the center of the pixel,  $\Delta F_{DC}$  the difference in the Doppler centroid frequencies between the Master and Slave SAR images. Hooper (2006) considers the phase signal due to the atmospheric delay  $\phi_{atm,\Delta t_i}$  as a long wavelength observed from the unwrapped phase which characterizes a significant gradual variation in space.

PS are therefore obtained from SAR images that are less affected by noises due to the atmospheric delay, topographic artifact, and orbital error and also from the scatterer noise in addition to the scatterer signal models. PS algorithms have two scattering signal models that are, the constant signal model and the Gaussian signal model. The probability distribution functions (PDFs) are calculated for each SAR pixel respectively from their amplitude and phase.

Ferretti et al. (2001) propose a signal model:  $z_i = g + n_i$  ( $i = 1, \dots, K + 1$ ) where  $g$  is the complex reflectivity taken as  $g = 1$ ,  $n_i$  represents the noise sources and  $K + 1$  the number of used SAR data. The amplitude of the SAR signal after Ferretti et al. (2001) is given by:

$$f_A(a) = \frac{a}{\sigma_n^2} I_0\left(\frac{ag}{\sigma_n^2}\right) e^{-(a^2+g^2)/2\sigma_n^2} \quad a > 0 \quad (8)$$

Where  $I_0$  is the modified Bessel function. The complex circular Gaussian noise variance  $\sigma_n^2$  is given for real and imaginary signal parts. The SNR is given by:

$$SNR = g/\sigma_n \quad (9)$$

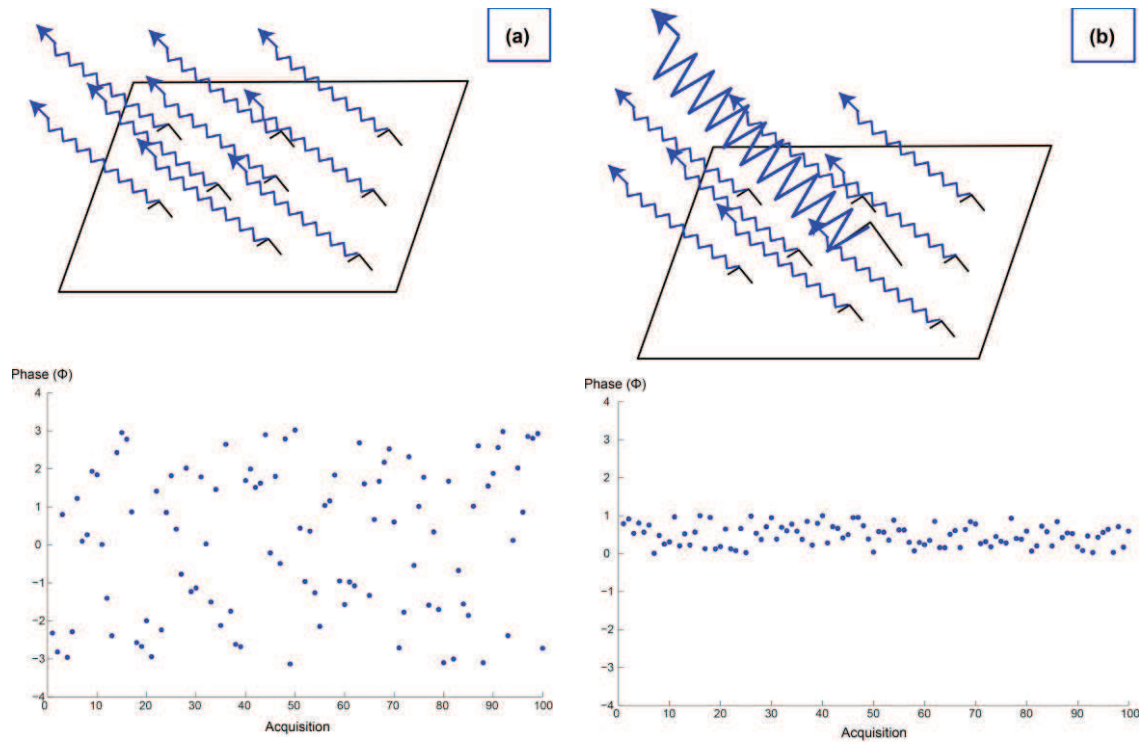


**Figure 5:** InSAR phase simulations for 100 iterations over the same reflected elements (pixel). (a) Shows the phase of one-pixel ranging between  $[\pi -\pi]$  with very dispersing signal values for a distributed scatterers contributions. (b) Presents the persistent scatterer response in one-pixel obtained with the sum of the contributed wavelets scattered verifying that the phase acquisition value for all 100 acquisitions is the best correlated with the best response similarity value (small phase variation). (Hooper, 2006)

Nowadays, PS-InSAR algorithms have been implemented with different variations and the most known are: The Stanford Method for PS (StaMPS) package (Hooper, 2006), the DePSI system from the Delft University (Kampes., 2006), Permanent Scatterers<sup>TM</sup> of the Tele-Rilevamento Europe (TRE), the Interferometric Point Target Analysis of GAMMA (IPTA; Werner et al., 2003), the GENESIS-PSI (Adam et al., 2003) of the DLR (German Aerospace Center), the Spatio-Temporal Unwrapping Network (STUN; Kampes., 2006).

### 2.3.2 Small Baseline (SBAS)

The small Baseline (SBAS) method (Berardino et al., 2002; Lanari et al., 2004) is one of the differential synthetic aperture radar interferometry (DIFSAR) algorithms for studying temporal evolution of ground deformation characterized by the small baseline separation between the SAR pairs used to generate interferograms (Sandwell et al., 1998; Berardino et al., 2002; Schmidt and Burgmann, 2003). This algorithm aims to limit the spatial decorrelation taking into account the spatial and the temporal information from the SAR data (Berardino et al., 2002). The generation

of time series is the principle of MT-InSAR algorithms.

The small baseline processing method was introduced for the first time by Sandwell et al. (1998) and defined as an InSAR staking method. This method is able to calculate the average velocity (mean-velocity) by measuring the average displacements obtained with the set of interferograms respecting a short baseline. The SBAS algorithm relates the different SAR acquisitions having a short baseline (short spatial separation) in order to generate series of interferograms under some circumstances: By reducing the spatial separation between SAR images, we reduce the decorrelations especially due to the large baseline separation and obtain correlated inteferograms. Figure 6 gives the flow chart of the SBAS algorithm after Berardino et al. (2002).

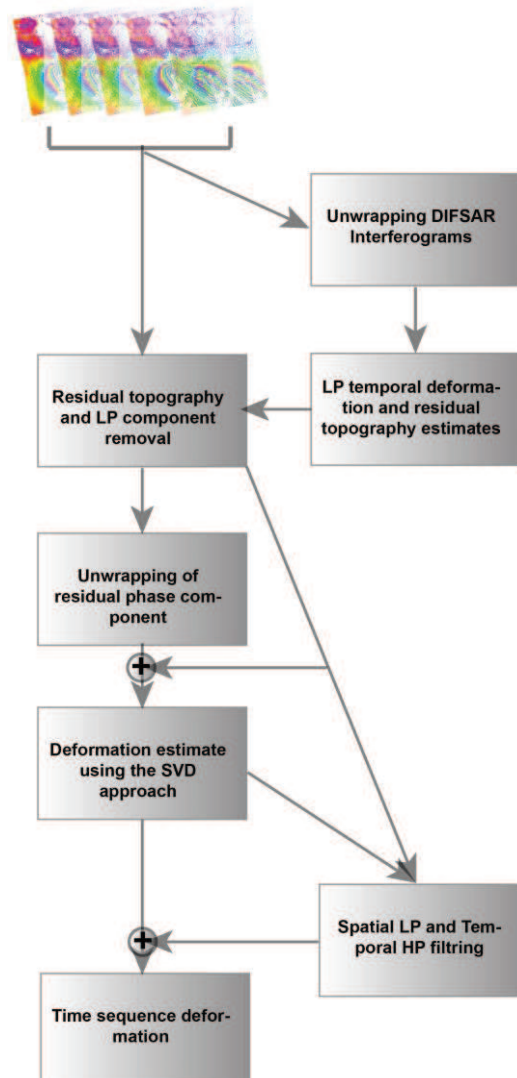


**Figure 6:** diagram describing the SBAS algorithm after (Berardino et al., 2002).

After InSAR processing, the interferometric phase distribution ranges between  $[\pi -\pi]$  (wrapped phase). In order to improve the phase signal quality, one of the existing solutions from MT-InSAR algorithms is to measure the average value of the scatterers for each pixel, by taking into account the neighbored reflectors value. This method can attenuate the exhibited large random phase difference observed in time and takes into account the average from all scatterers of each averaged elements.

After Berardino et al. (2002), SBAS algorithm works as shown in Figure 6. Considering  $N + 1$  SAR images, the topographic phase component removal is obtained by:

$$\Delta\phi_j(x, r) = \frac{4\pi}{\lambda} [d(t_2, x, r) - d(t_1, x, r) ] \quad (13)$$

Where  $(x, r)$  are the pixel coordinates in azimuth and in range, respectively.  $d(t_1, x, r)$  and  $d(t_2, x, r)$  are the cumulative deformations at  $t_1$  and  $t_2$  measured in LOS.

The SBAS algorithm uses series of SAR to perform interferograms having a short baseline separation. These interferograms obtained with the conventional D-InSAR method are used as inputs to calculate the unwrapping stage, from which we estimate the topographic contribution and extract the low-pass (LP) temporal deformation that will be subtracted from the wrapped interferograms modulo- $2\pi$ . After extraction of the residual topographic contribution and LP component from the wrapped interferograms, they will be considered as residual phase and be unwrapped. The next step is to apply spatial and temporal filtering to the unwrapping residual file that contains the temporal deformation and the topographic phase residual. Finally, the inversion of the stack of interferograms is assured using the singular value decomposition (SVD) method.

### 2.3.3 Merged Permanent Scatterers and Small Baseline

Since the appearance of MT-InSAR methods (PS and SBAS), several software solutions have been developed. The Stanford Method for Persistent Scatterers (StaMPS) (Hooper, 2008) is the only software package that incorporates both PS and SBAS algorithms. In addition, StaMPS/MTI proposes a combined method from both of PS and SBAS results. StaMPS uses i) ROI-pac (Rosen et al., 2004) in order to focus the raw SAR data, ii) Doris (Kampes., 2006) to perform interferograms from SLC images and iii) SNAPHU (Statistical-Cost, Network-Flow Algorithm for Phase Unwrapping ) (Hooper et al., 2007) for 3D unwrapping. StaMPS PS algorithm use the information from SAR amplitude dispersion (Ferreti et al., 2001) with

threshold value of  $\sim 0.4$  in order to select the candidate scatterers. According to (Hooper, 2008) the pixels of filtered phase that exhibit a small decorrelation in short time and are denoted as slowly-decorrelating filtered phase (SDFP), are selected by the SBAS method. The merged method selects pixel from the PS and SDFP groups that are in coincidence to improve the spatial sampling of the signal. The used PS algorithm from Hooper (2007) requires a minimum constraint of five SAR data. In order to have the possibility to process large areas, Hooper (2007) proposes to divide the whole area into small patches (in azimuth and in range) and process InSAR for each of them separately. The final map will be reconstituted from the processed patches.

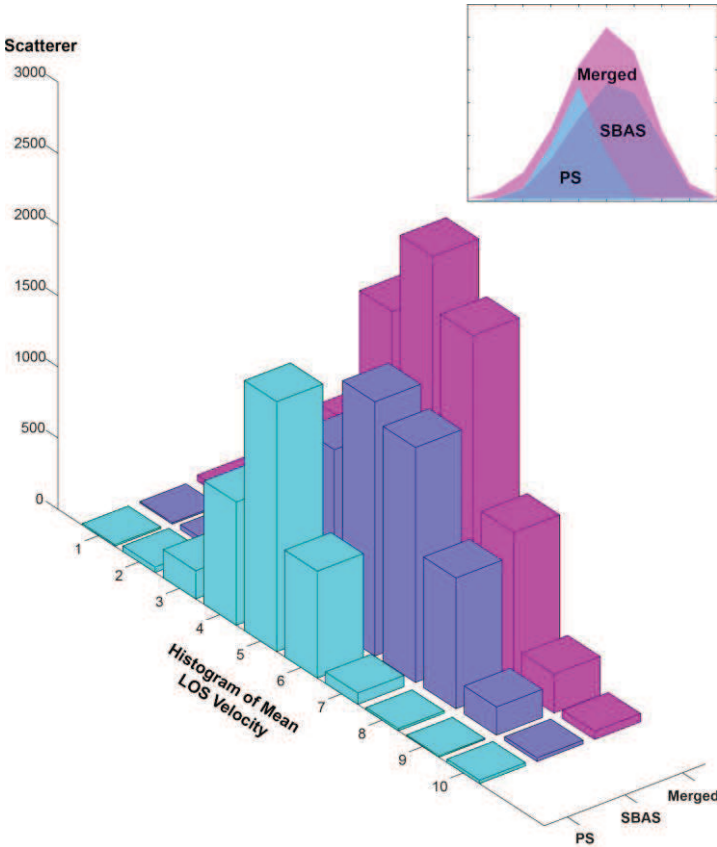


**Figure 7:** comparison between the number of scatterer obtained and there velocity values achieved using Persistent Scatterer (PS) method, Small Baseline (SB) method and Merged (PS-SBAS) method.

The model used in StaMPS SB is based on the use of single-look images to identify single-look SDFP pixels. SBAS maximizes the interferograms correlation by minimizing the time separation, the space separation and the Doppler between the chosen SAR pairs. The processing consists in a threshold value to construct the network connecting all the chosen SAR

image pairs without rupture in the connectivity. Using an amplitude dispersion index as in Ferretti et al. (2001) the pre-selection of the SDFP candidates imposes the threshold value of 0.6.

After Hooper (2008), the amplitude difference dispersion for Gaussian model is given by:  $D_{\Delta A} = \sigma_{\Delta A} / \mu_A$ , where  $\sigma_{\Delta A}$  is the standard deviation difference between Slave amplitude and Master amplitude, and  $\mu_A$  is the mean amplitude. A bandpass filter is used to estimate the spatially correlated contribution of neighbored pixels. An estimation of the coherence magnitude is given by (Hooper, 2008):

$$\gamma_x = \frac{1}{N} \left| \sum_{i=1}^N \exp\{\sqrt{-1}(\psi_{x,1} - \tilde{\psi}_{x,1} - \Delta \hat{\vartheta}_{\theta,x,i}^u)\} \right| \quad (14)$$

Where:  $\psi_{x,1}$  is the pixel x from the wrapped phase in the interferogram (i),  $\tilde{\psi}_{x,1}$  is the spatially correlated,  $\hat{\vartheta}_{\theta,x,i}^u$  is the spatially uncorrelated and N interferograms numbers.

The pixels model that uses Gaussian for interferometric phase  $\psi_\phi$  is given by (Just et al., 1994):

$$PDF(\psi_\phi) = \frac{1 - |\rho|^2}{2\pi} \frac{1}{1 - |\rho|^2 \cos^2(\psi_\phi - \psi_0)} \quad (15)$$

The combination between PS-SBAS calculates the equivalence from SBAS interferograms to PS single Master interferogram. When pixel has both PS and SB values, the system set to the pixel the mean values from the phase and the amplitude obtained by PS and SBAS algorithms. The Merged method have two highlights, it increase the number of obtained scatterer and also increase the SNR (Hooper, 2008). For example, in the case of the landslide of Constantine (see chapter 4) the pixels distribution obtained with StaMPS merged method is shown by Figure 7.

According to (Hooper, 2008), The merged pixels are obtained by measuring the mean of both PS and SBAS sets of results for each pixel and SNR is defined by:

$$\widehat{SNR} = \frac{1}{\gamma_x^{-1} - 1} \quad (16)$$

In Chapter 4 (Landslide in Constantine), I show a merged method obtained not with the mean values between SBAS and PS pixels but for each merged pixel, the value is obtained from the maximum summe of both signal (PS and SBAS).

## **Chapter II**

# **Monitoring Ground Deformation in the Haoud Berkaoui Oil Field (Sahara, Algeria) Using Time Series Analysis of SAR Images**



# **Monitoring Ground Deformation in the Haoud Berkaoui Oil Field (Sahara, Algeria) Using Time Series Analysis of SAR Images**

Seyfallah Bouraoui (1)

Mustapha Meghraoui (1)

Rachid Bougdal (2)

Ziyadin Cakir (3)

*(1) IPG Strasbourg, CNRS-UMR 7516, France*

*(2) FSTGAT, USTHB, Algeria*

*(3) Dept. of Geology, ITU, Turkey*

Submitted to Natural Hazards  
January 2013

## Summary

We investigate the surface displacement in the Haoud Berkaoui (Algerian Sahara) area, a locus of an oil well accident since 1978, using an advanced times series analysis of SAR images. The Haoud Berkaoui area also includes numerous wells that served for oil extraction starting from 1970s. Among all wells, OKN32 and OKN32bis collapsed due to dissolution of evaporator rocks inducing rapid ground subsidence and eventually a spectacular 320-m-diameter crater and ~80-m-depth as per today. We apply the Merged method between the Small Baseline (SB) and the Persistent Scatterer (PS) InSAR methods to retrieve deformation maps and displacement time series from C-band ESA-SAR images (17 images of ERS-1 and ERS-2) acquired between 1992 and 2000. Our analysis delimits the subsidence area and shows an average 1.5-mm/yr subsidence located around the OKN32 (oil well) and in the direction of Ouargla city. We also evaluate the possible propagation and the direction of subsidence by studying the spatial temporal variation of subsidence together with the distribution of the other oil wells in the same area. An elastic model with volume decrease is calculated to relate the surface subsidence with the dissolution-collapse at depth. The study of this oil field incident helps in the understanding of the subsidence process and mitigation of further underground collapse that may affect neighboring urban areas.

**Key words:** Sinkhole, Subsidence, Underground Dissolution, Merged InSAR Time Series, Surface Deformation.

# 1. Introduction

Land subsidence caused by accidental contact between a salt layer and a deep aquifer is one of the most important problems in geological hazards. The major cause of the land subsidence is due to the exploitation of underground fluids, involving water aquifers layers, gas or oil from deeper reservoirs or wells. Examples of land subsidence are primarily described in regions with groundwater extraction, minefields, and oilfield exploitation taking place in different locations worldwide (e.g., San Joaquin Valley (California), Houston (Texas), Phoenix (Arizona), Venice (Italy), Saint-Nicolas (France), Holle (Congo), Restrof (USA); Bernard Feuga., 2009). In Algeria, (Akretche et al., 1992) report on the Haoud Berkaoui oil field incident and provide a description of the catastrophic crater history and occurrence since 1978 in the Sahara region (Figs. 1 and 2). Their study also discusses the used methods (gravity, topography, seismic and resistivity profiles) to monitoring the oil well collapse and subsequent crater structure. However, the surface deformation and related subsidence near the crater is not well delimited and its evolution poorly known.

The land subsidence occurs in particular when large amounts of ground water have been withdrawn from certain types of stratigraphic succession of fine-grained sediments. As a consequence, the land subsidence induces surface deformation that can be observed and measured from field investigations and remote sensing images. The study of satellite images by radar interferometry can be used to measure surface change due to sinkholes collapse and earth subsidence since the early 1990s (Gibson et al., 2002; Closson et al., 2005). Using SAR interferograms, (Snieder et al., 2007) showed up to 3 to 5 cm land subsidence over ~5-km-wide area and different localized features affecting the western margin of the Bakersfield (California) oil field. However, major issues in InSAR technique are related to temporal and geometrical decorrelations that make interferogram results difficult to interpret (Ferretti et al. 2001). The atmospheric artifacts, orbital error, topographic effect, and noise signal in the captor registration add to the difficulty in the analysis of interferograms. New widely used techniques as SB-InSAR and PS-InSAR provide solutions for temporal and geometrical decorrelation and atmospheric artifacts in most of complex case studies (Bianchi and Ferretti, 2006; Hooper, 2007).

In this paper, we first present the local geologic and morphological context of Okn32 and Okn32bis, and field observations in order to explain the water eruption and crater formation. The analysis of SAR images (ERS-1 and ERS-2) from 1992 to 2002, allows us to quantify the

surface deformation related with the local dissolution at depth. The succession of interferograms obtained from 17 SAR images shows the area of subsidence located in the oil wells area. The modeling of local deformation using a half-elastic inversion is proposed to explain the physical characteristics of the incident causing the subsidence. The superficial damage caused to two wells can be observed nowadays in Haoud Berkaoui and therefore, we discuss its origin and a possible forecast of an induced environmental catastrophe.

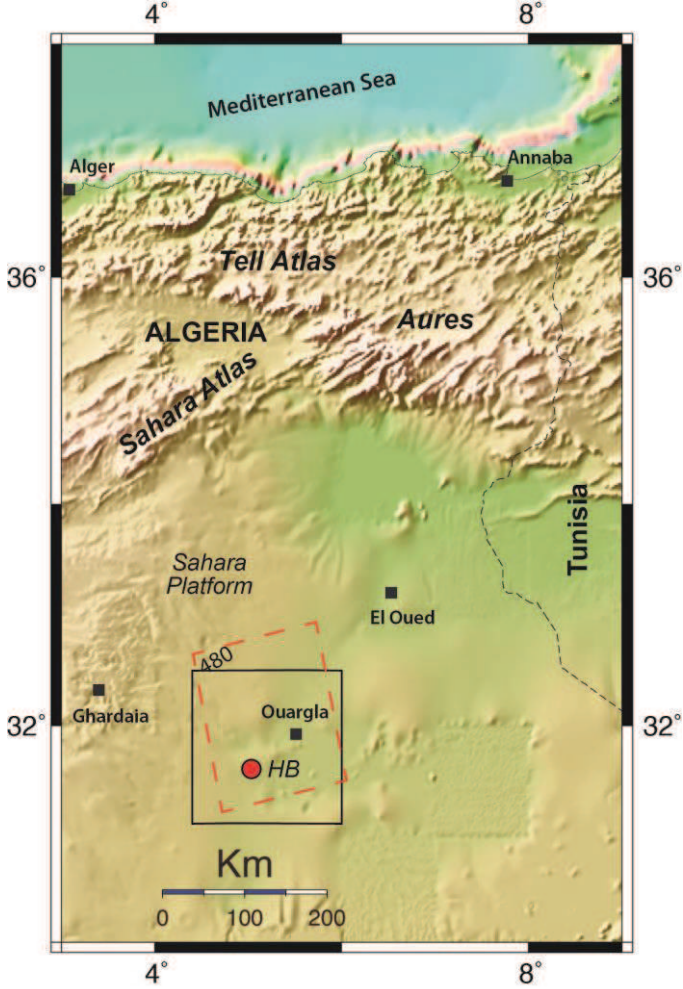


**Fig. 1.** Location of the study area in Ouargla region and Haoud Berkaoui (HB) oil field (box) in the Sahara platform of Northeast Algeria. Dashed squares indicate the frame of ERS SAR images. The morphology and bathymetry are from global data of GEBCO\_08 grid (Smith and Sandwell, 1997).

## 2. The collapse of OKN32 and OKN32bis wells and geologic context

The Haoud Bekaoui is an active oil field extraction located 30 km southwest of Ouargla city, northeast of the Algerian Sahara desert (Fig. 1). Several wells were installed in the region to

exploit oil natural resources, and among them the drilling of OKN32 in January 1978 (Fig. 2). The Haoud Berkaoui oil field is situated on a monoclinical structure of outcropping and gently west dipping Upper Cretaceous units (Figs. 3 and 4). The upper 2000 m stratigraphic log shows from bottom (Fig. 4): 1) 1400-m-thick succession of clay and limestone units from Neocomian to Turonian, 2) 600-m-thick Senonian units made of ~200-m-thick saline deposits overlaid by ~250-m-thick of anhydrite covered by ~150-m-thick carbonate, and 3) ~40-m-thick Mio-Pliocene sandy-clay (Sonatrach, 2004). In February 1978, OKN32 oil well has accidentally exposed aquifer eruptions that belong to the well-known continental sandstone deposit (Albo-Barremian). This drilling has been monitored afterward by the Sonatrach petroleum company that tried repeatedly to stabilize the collapse and stop the spreading of the subsidence area. Indeed, soon after the drilling the two oil fields Okn32 and Okn32bis, 80 m distance from each other, were badly damaged in this incident, causing an important environmental and ecologic impact in the region.

The oil well collapse formed a cavity crater or sinkhole showing 80-m-depth and 320 m in diameter that expands from year to year (Fig. 5). It is surrounded by 0.25 to 0.30 m wide and ~50-m-deep cracks visible at the surface. According to previous studies made by Sonatrach (unpublished reports, Hocine et al., 2008), the collapse of oil wells is caused mainly by the interaction between the ~200-m-thick lower Senonian salt layers and pressurized (50°C) Albo-Barremian fossil water (Akretche et al., 1992). An important collapse episode of OKN32 oil drilling occurred in October 1986, despite many attempts since 1978 to stabilize the collapse by tubing to protect against aquifer eruptions and pollution. Fossil water rises through the ~200-m-thick salt layer and to the surface at 300 m<sup>3</sup>/hr and a temperature of over 50°C at a speed of 1 to 1.5 m/sec. The hot and pressurized water that induces the gradual dissolution of salt units is at the origin of an expanding large cavity located at 450 to 650-m-depth (Fig. 4). In May 1991, a concentric and meter-wide crack system was formed at 600 m from the crater center. Hence, the underground collapse chamber may increase from 300-400 m to 600 m in diameter or larger if the dissolution process will continue in the future (Fig. 4).

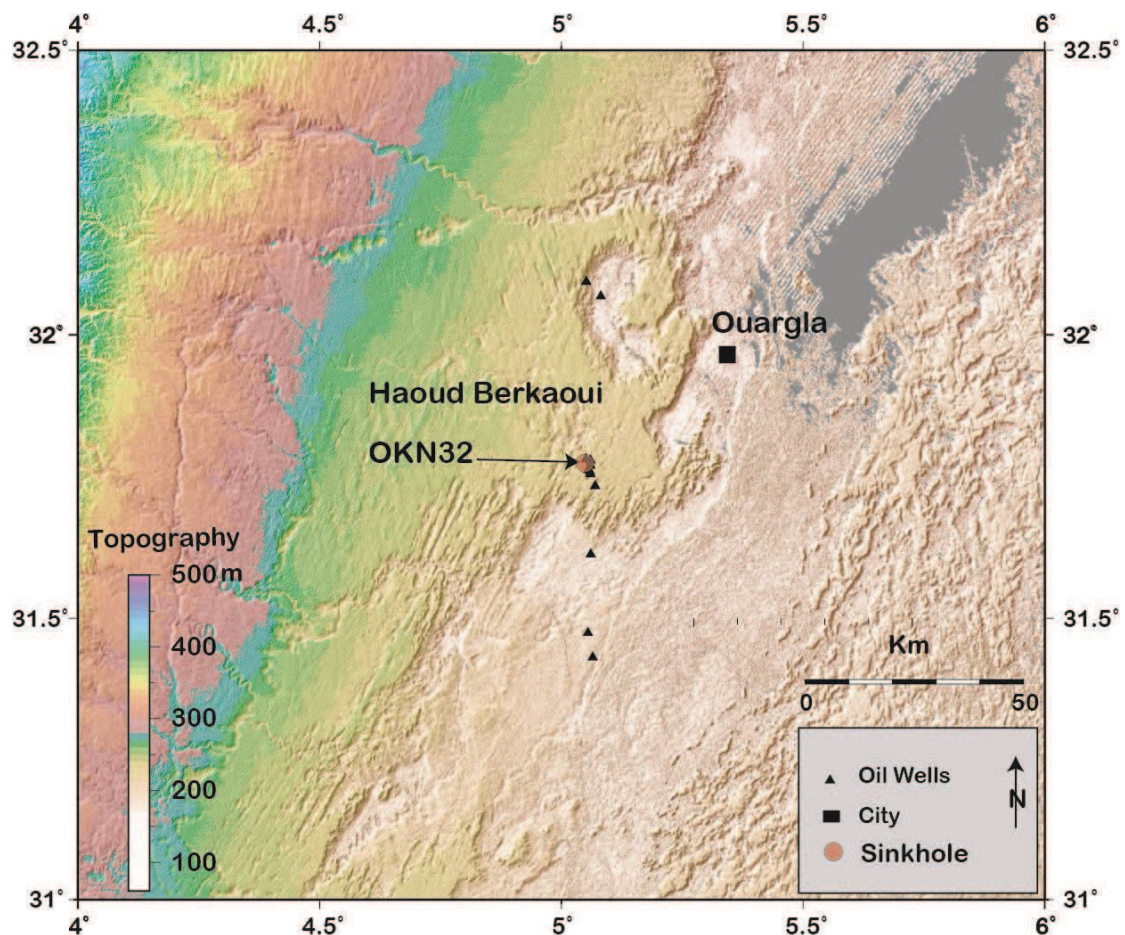


**Fig. 2.** Morphology of the Haoud Berkaoui oil field south west of Ouargla city. The sinkhole position is indicated with a circle. Oil wells distributions (triangle) are from Sonatrach (1995). Topographic data from SRTM 90 m resolution (Farr and Kobrick, 2007).

The impact of this disaster is at least in four levels: 1) the environmental pollution of the water table by the rise to the surface of the fossil water through the salt layer, 2) the crater damage zone diameter increasing and crack expansion of the sinkhole area, 3) the possible increase and spreading of the subsidence area to the nearest wells and Ouargla city, and 4) the economical loss due to the collapse of two oil wells and damage to the neighboring oil wells. This latter point is critical taking into account that Haoud Berkaoui constitutes ~50% of the total oil production of Algeria, complemented by the nearby Hassi Messaoud oil field for a total of 211 980 km<sup>2</sup> explored area (Razon, 1999). The size and amplitude of this catastrophe requires a detailed study that includes satellite geodesy and radar interferometry that provide high-resolution measurements of surface deformation.

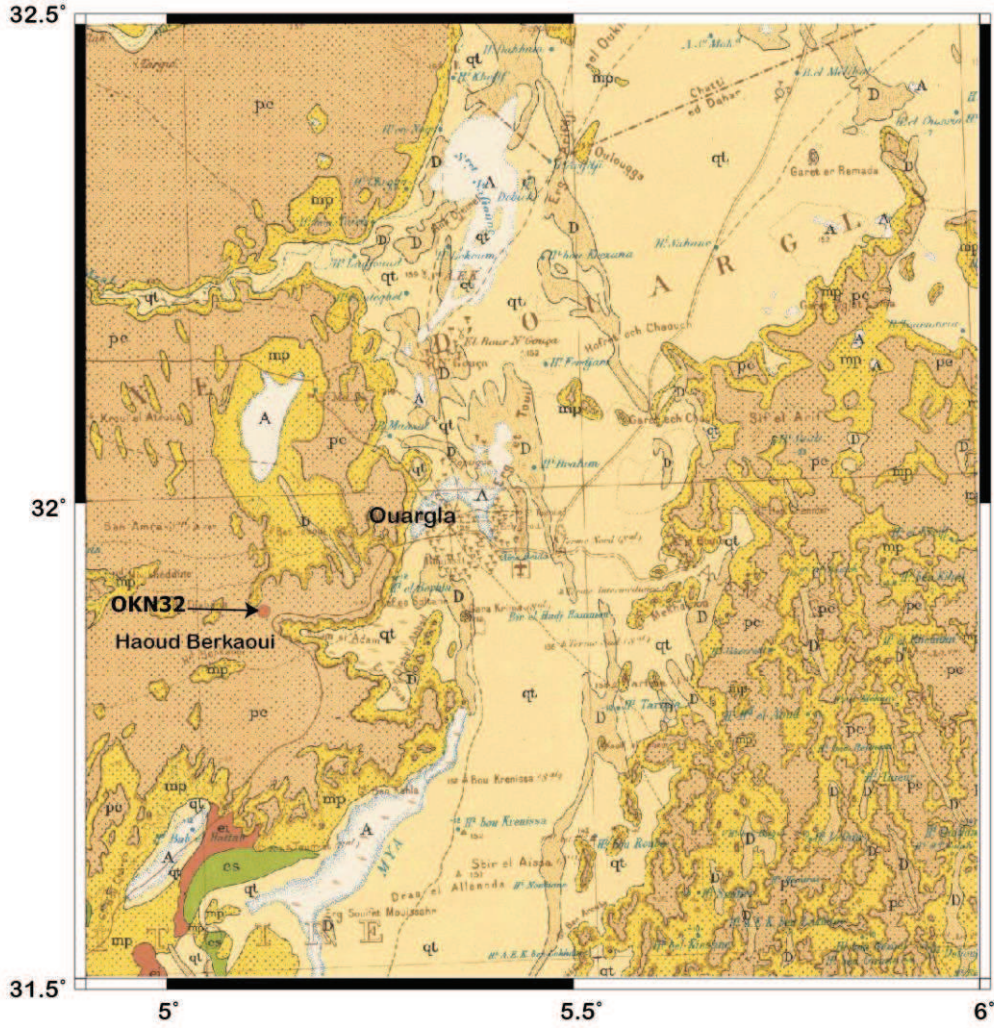


**Fig. 3.** Geological map of Ouargla region and Haoud Berkaoui oil field site (Service de la Carte Géologique, Algérie, 1952). A: Modern alluvial units; D: Recent dunes; qt: Quaternary continental units; pc: Continental Pliocene; mp: Marine Pliocene; ei: Marine lower Eocene; cs: Marine lower Cretaceous.

In order to better understand the well collapse and subsidence, Fig. 6 illustrates a laboratory experiment that indicates the effect of dissolution at depth on the surface topography. The dissolved saline layer at Haoud Berkaoui is submitted to a lithostatic pressure  $p(z)$  at 400 m depth that can be described as follow:

$$p(z) = p_0 + g \int_0^z \rho(z) dz$$

Where:  $p_0 = 101325$  Pa (0.1 bar) is the atmospheric pressure (at the surface),  $g = 9.806 \text{ m}\cdot\text{s}^{-2}$  is the gravity acceleration,  $\rho = 2 \text{ g}\cdot\text{cm}^3$  is the average density for the sedimentary pile including

saline layer at depth at  $\sim 50^\circ \text{C}$ . The estimated  $p(z) = 1000 \text{ g/cm}^2 + 980.6 \text{ cm/s}^2 * 2 \text{ g/cm}^3 * 4 * 10^4 \text{ cm} = 7.84 \text{ Kbar}$ .

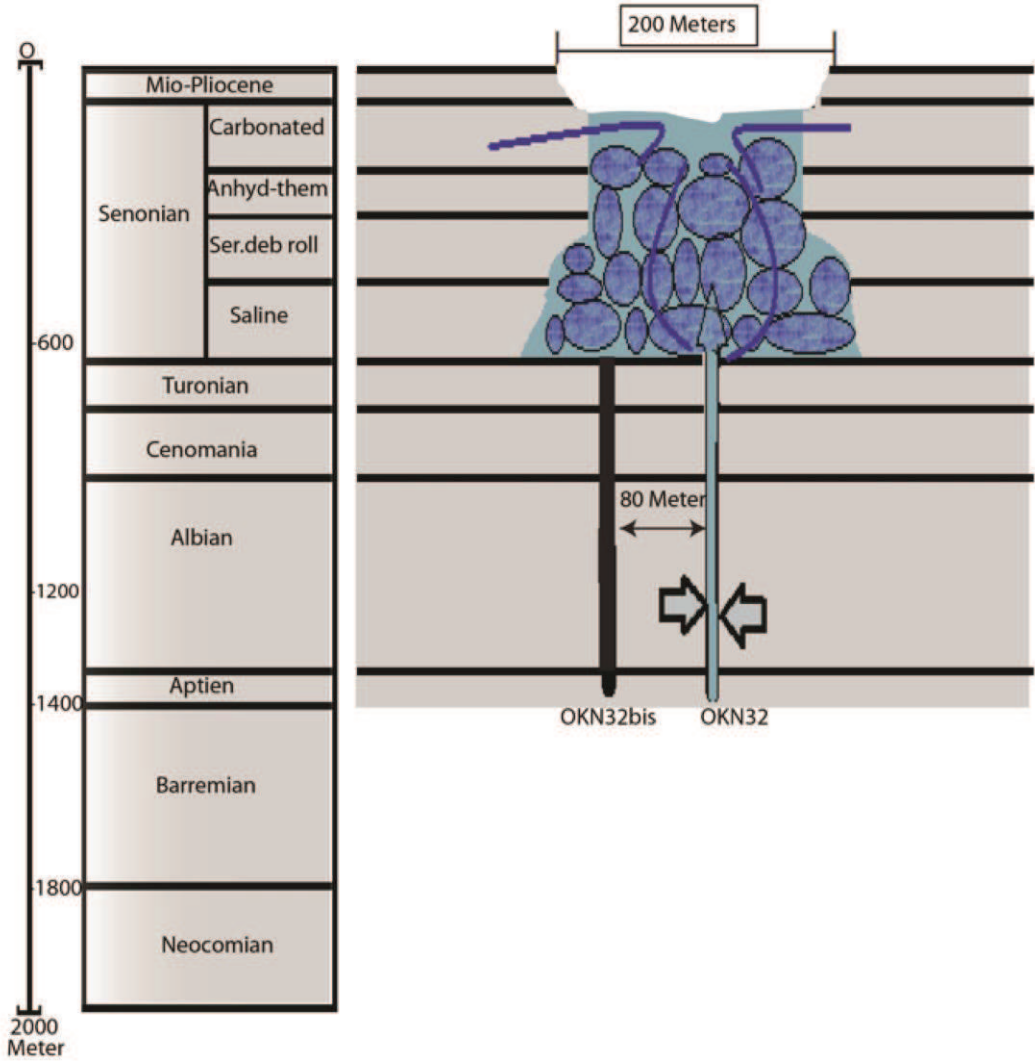


**Fig. 4.** Oil wells OKN32 and OKN32bis and the stratigraphic log with the schematic illustrated collapse. The Albian hot water that flows within the lower Senonian saline layer is responsible of the well collapse generating a crater with a 200 m diameter.

### 3. InSAR data and processing

The InSAR technique is based on high-frequency electromagnetic wave emissions used in remote sensing and geodesy to generate maps of surface deformation at sub-centimeter accuracy or high-resolution digital elevation models (DEM) from the Radar wave phase differences (Hanssen, 2001). The method has been widely and successfully used to measure and

study surface deformation due to several natural hazards phenomena such as glacier movements (Goldstein et al., 1993; Zhen Li et al., 2009), earthquakes (Massonnet and Feigl, 1998), volcanoes (Amelung et al., 2000), human activity (Gabriel et al., 1989, Carnec et al., 1996), and landslides (Castañeda et al., 2009). The precision of InSAR measurements are, however, affected by decorrelation phenomena, phase contributions due to atmospheric water vapor and ionospheric effects, the internal dielectric modifications, relief in the topography, sensitivity to technical effects, and uncertainties in the position of the satellites (orbit errors; Hanssen, 2001, Hooper et al., 2007):

$$\phi_{\text{int}} = W\{\phi_{\text{defo}} + \phi_{\text{atmos}} + \Delta\phi_{\text{orbit}} + \Delta\phi_{\text{topo}} + \phi_{\text{noise}}\}$$

Where:  $W\{ \}$  is the wrapping operator,  $\phi_{\text{defo}}$  is the phase change in the line-of-sight (LOS) direction,  $\phi_{\text{atmos}}$  is the atmospheric delay difference between passes,  $\Delta\phi_{\text{orbit}}$  is the orbit error,  $\Delta\phi_{\text{topo}}$  is the DEM error (look angle error),  $\phi_{\text{noise}}$  is the phase noise (due to variability in scattering characteristics).

In our study, the observed sinkhole and land subsidence is a consequence of the human activity. In order to study subsidence in Haoud Berkaoui area, we have used 17 SAR images acquired by ERS-1 and ERS-2 satellites of the European Space Agency (ESA) between 1992 and 2002 in the descending mode, Track: 480 Frame: 2961 (Fig. 1). Atmospheric artifacts and topographic residuals are expected to be insignificant as the study region is a desert with fairly flat topography, resulting in high coherency in interferograms. The raw ERS SAR data were processed with the ROI-PAC software (Rosen et al., 2000) using precise orbits obtained from Delft University (Scharoo and Visser, 1998) the SRTM 3 arc-second (~90 m) digital elevation data for the removal of topographic contribution (Farr et al., 2007).

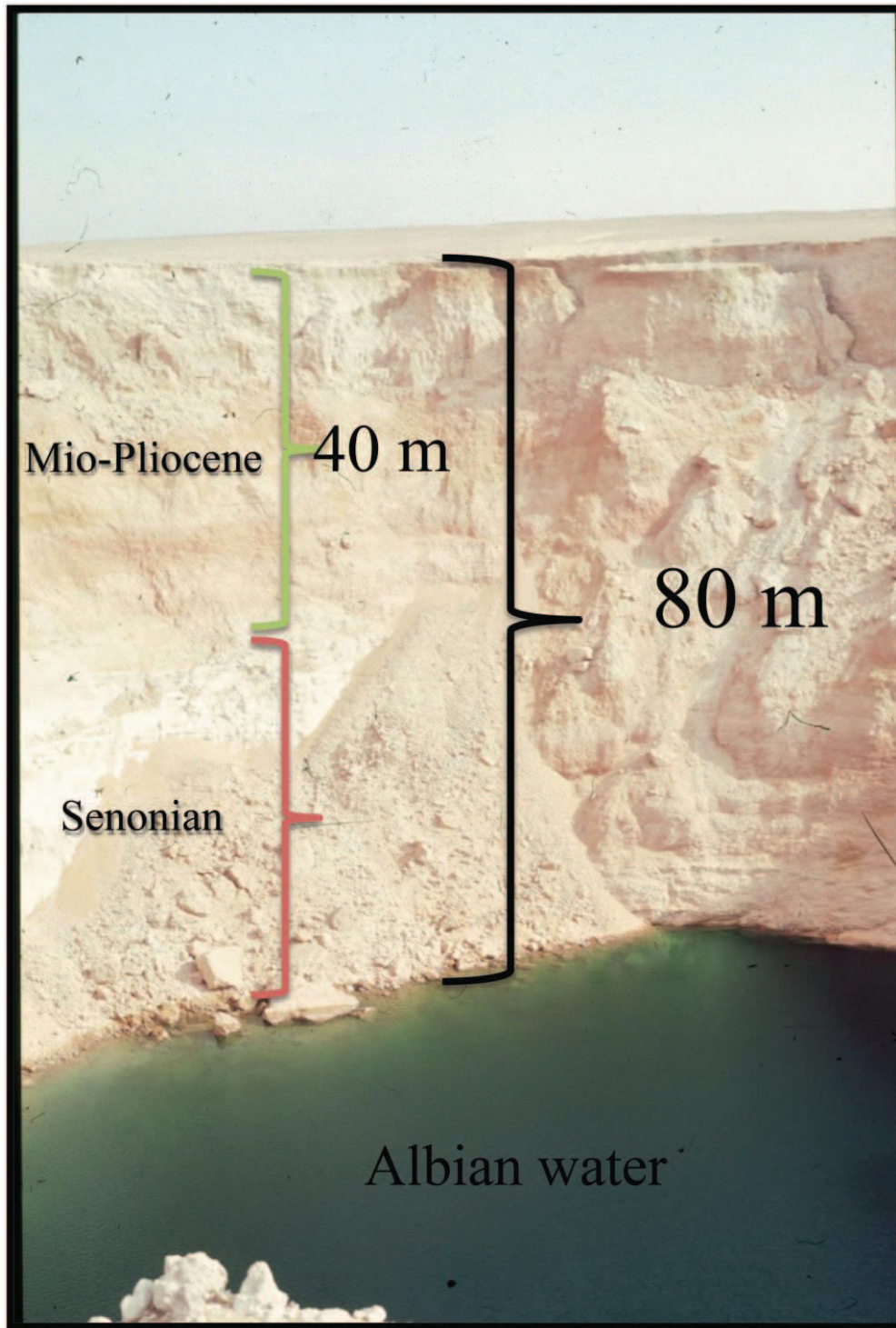


**Fig. 5.** Southeast view of the Haoud Berkaoui crater filled by water. The crater appeared in 1978 following an oil well prospection.

In order to adequately exploit the InSAR data, we first use classical differential InSAR method by generating and analyzing all possible differential interferograms to detect an observable signal of deformation. In the second step, we use several time series techniques in order to overcome possible atmospheric effects and spatiotemporal evolution of subsidence.

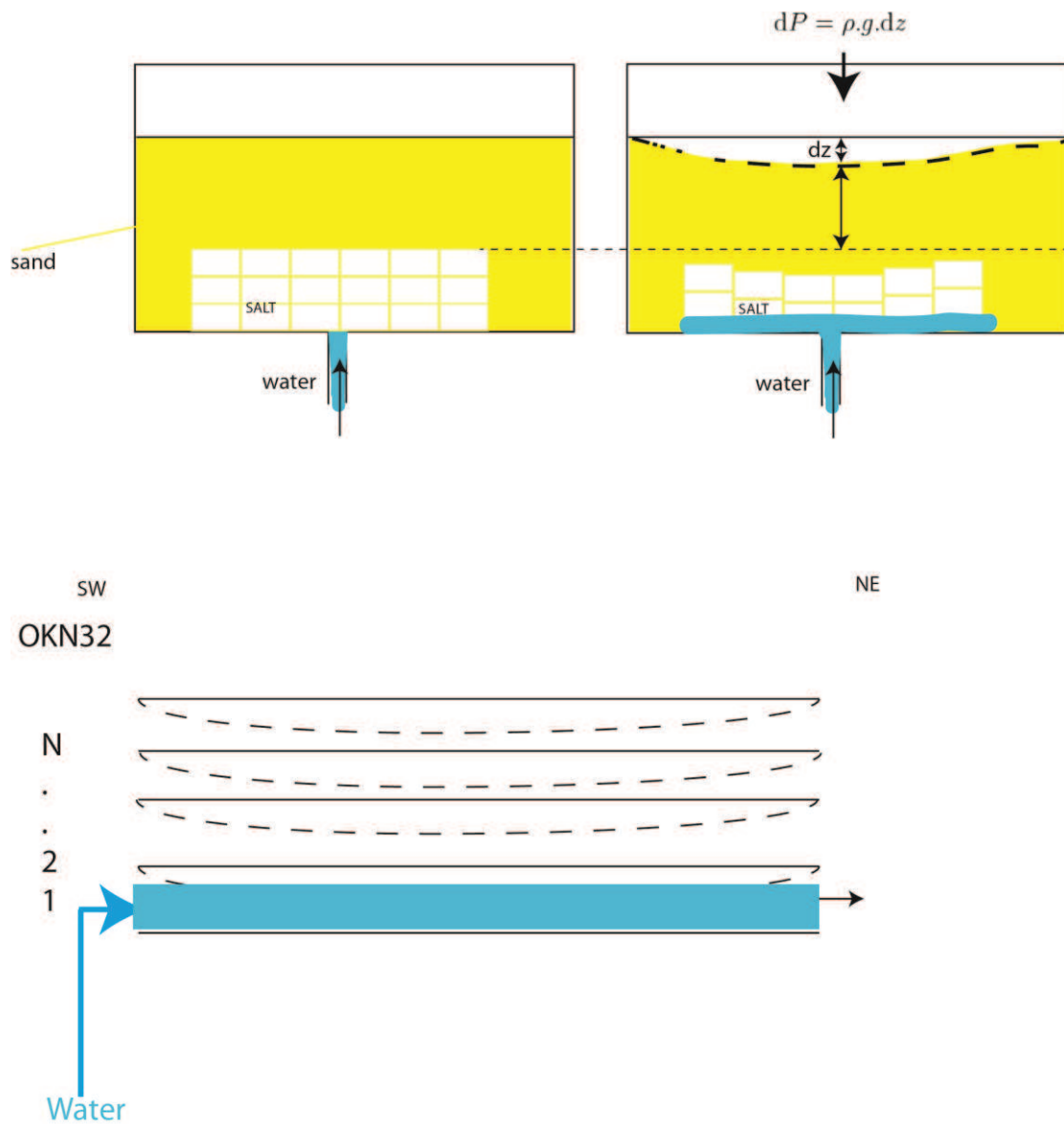


**Fig. 6.** Scenario of salt layer dissolution (introduction of the water) made in cube and covered by salt layer. (a) Gives the initial stat. (b) describe the final stat of the experience, showing dz according to thelithostatic pressure of the saline water.

### 3.1. Differential InSAR results

136 interferograms with relatively short baselines (450 m) were calculated from ERS SAR images. Of these, 38 interferograms provided usable data to analyze surface subsidence. (Fig. 8) shows two of these interferograms constructed from orbits dated 1992-06-06 and 1995-11-04, and 1995-09-30 and 2000-05-07, showing subsidence reaching 33 mm over an area of  $\sim 64 \text{ km}^2$ . The subsidence calculated between 1992-09-17 and 1995-11-04 SAR images is  $12 \pm 4 \text{ mm}$ , while between 1993-07-29 and 1995-09-30 SAR images the deformation is  $7.8 \pm 4 \text{ mm}$ . Finally, the average of all interferograms gives  $4.1 \pm 4 \text{ mm/year}$  subsidence rate, with the maximum signal east and northeast of the sinkhole. Although, the DInSAR analysis of Haoud Berkaoui roughly documents the subsidence area and evolution from 1992 to 2000, this method needs to be complemented with more accurate reflector signals and time series evolution (Permanent Scatterers) of the surface deformation. In the second stage of data exploration, we therefore use the Multi-temporal InSAR (MT-InSAR) techniques since temporal and geometrical decorrelation limitations due to diverse phenomena cause significant phase delay that affects the legibility of resulting interferograms that can be misinterpreted as surface change.

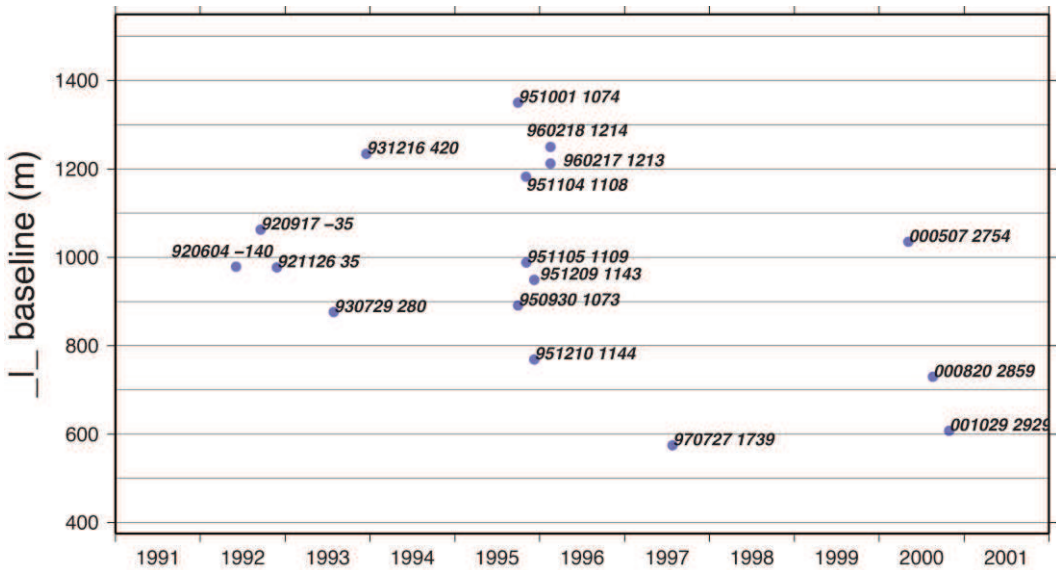


**Fig. 7.** Perpendicular baselines and date of acquisition of 17 ERS SAR images used in our study. The satellite image acquisition spans a period of more than eight years (from 1992/06/04 to 2000/10/29).

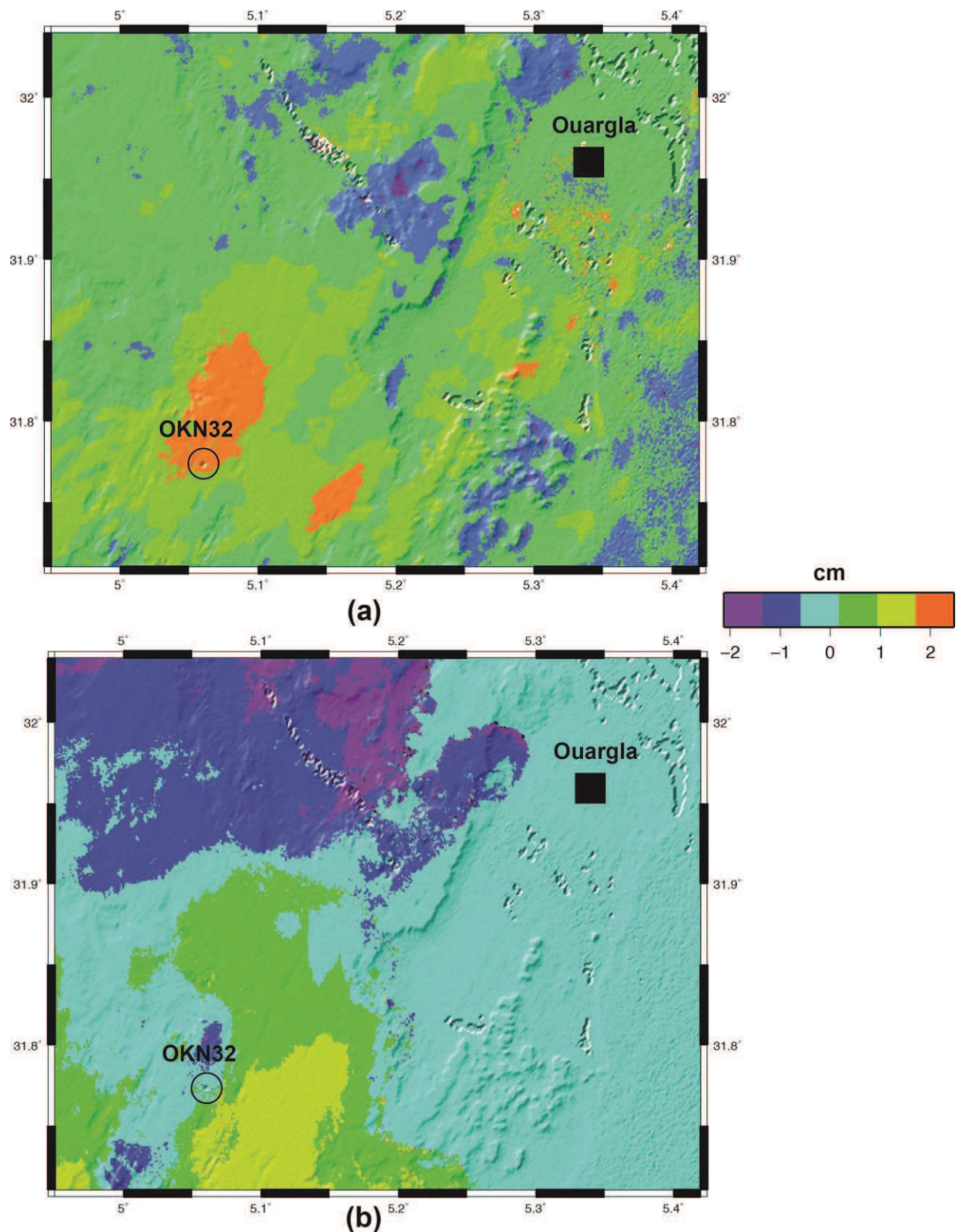


**Fig. 8.** (a) Interferogram from C-band ERS SAR data displaying the subsidence deformation (in red patch, away from satellite) measured between 1992\06\04 and 2000\10\29 and reaching 2.2 cm. (b) Interferogram displaying the subsidence deformation measured between 1995 and 2000. The Haoud Berkaoui crater at OKN32 is shown southwest of Ouargla city. there are no fringes. The question is: Does this differomation in LOS direction ( $\geq 1$  cm) is obviously bound to subsidence ?

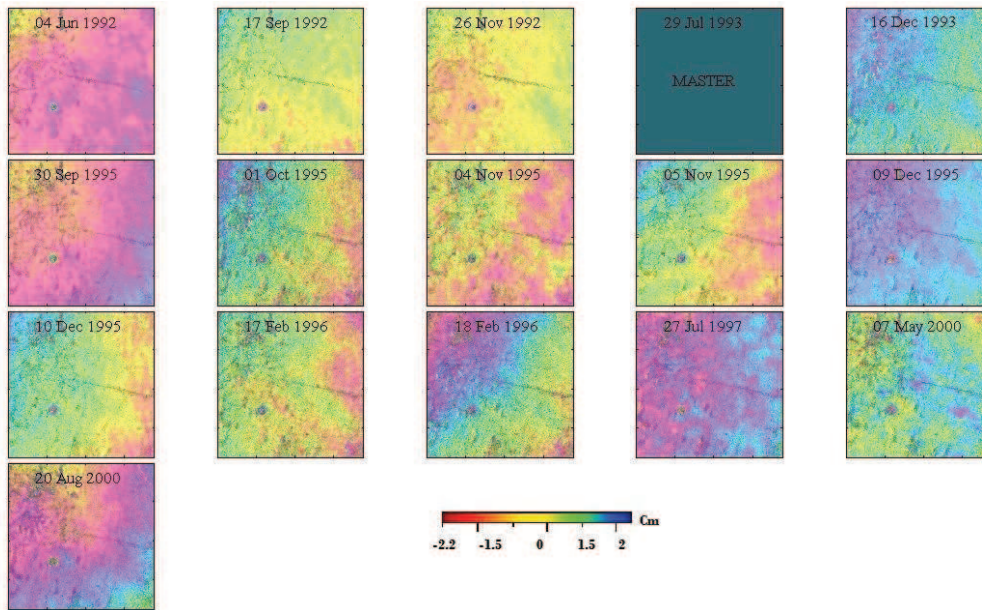


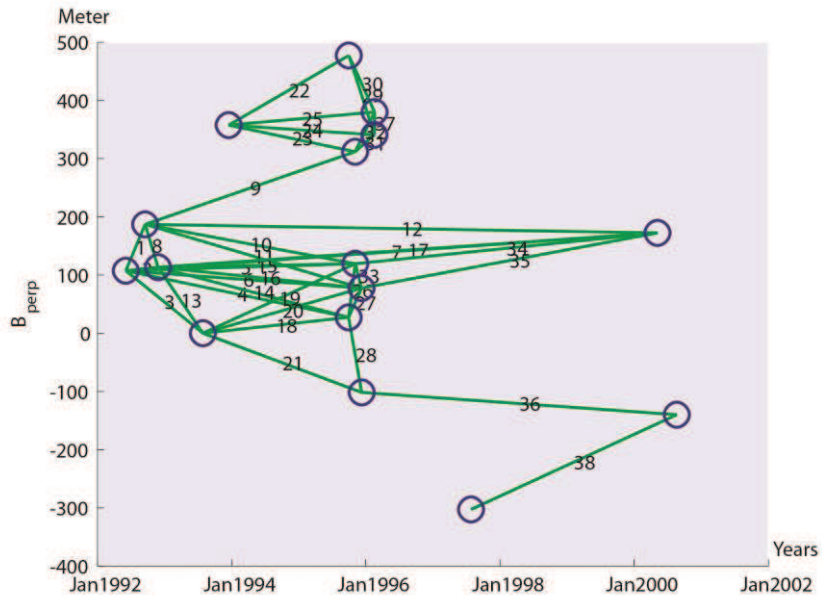
**Fig. 9.** All interferograms extracted from the same SAR master image of 29 July 1993 and relative slave images. The master image is chosen based on minimizing perpendicular, Doppler and temporal baselines (Hooper et al., 2007).

### 3.2. MT-InSAR processing and results

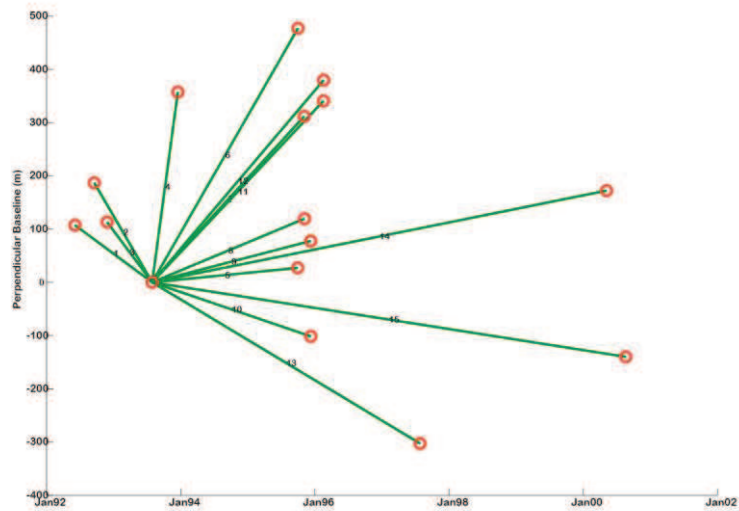
MT-InSAR techniques involve the processing of multiple acquisitions in time on the same SAR frame. Currently, there are two broad categories of MT-InSAR techniques: 1) Persistent scatterer (PS) methods including those that identify pixels based primarily on their phase variation in time (Ferretti et al., 2001; Kampes, 2005) and those that use primarily correlation of their phase in space (Hooper et al., 2004; van der Kooij et al., 2006), and 2) small baseline (SB) methods (Berardino et al., 2002; Schmidt and Burgmann, 2003).

PS-InSAR is developed by Politecnico di Milano (POLIMI) and TRE (a POLIMI spin-off) to exploit characteristics of radar scattering and atmospheric decorrelation and measure surface displacement in otherwise non-optimum conditions. PS-InSAR can resolve surface displacement of individual features at a level of about 0.5 mm/year using all data collected over the target area by a SAR satellite. The atmospheric phase contributions are spatially correlated within a single SAR scene, but tend to be uncorrelated on time scales of days to weeks. Conversely, surface motion is usually strongly correlated in time. In our study, the surface subsidence is usually steady over periods of months and sometimes years (8 Years in our case; (Fig. 9)), and thus atmospheric effects can be estimated and removed by combining data from long time series of SAR images (1992 – 2000 for ERS-1 and ERS-2 data), averaging out the temporal fluctuations. Radar scatterers that are only slightly affected by temporal and

geometrical decorrelation are used, allowing exploitation of all available images regardless of imaging geometry. In this sense the scatterers are permanent, because persistent over many satellite revolutions.



(a)



(b)

**Fig. 10.** Perpendicular baseline ( $B_{\text{perp}}$ ) versus time plot of SAR images in (a) The baseline approach and (b) the persistent scatterer approach. Circles represent SAR images and arcs lines indicate the interferograms that are formed. Perpendicular baseline refers to the component of the satellite separation distance that is perpendicular to the look direction, and is proportional to the difference in look angle.

SB-InSAR technique on the other hand minimizes the perpendicular, temporal and Doppler baselines for maximizing the correlation of generated interferograms and increasing the number of observable ground points by identifying natural reflectors (scatterers) whose characteristics viewed from different angles remain stable in time (Berardino et al., 2002). Permanent Scatterers are found on the basis of pixel phase correlations for a given time frame (Ferretti et al., 2001; Colesanti et al., 2005; Hooper, 2008). Hence, multiple acquisitions in the same track over long time periods (over 8 years in this case) are used to analyze spatiotemporal evolution of surface deformation with high accuracy.

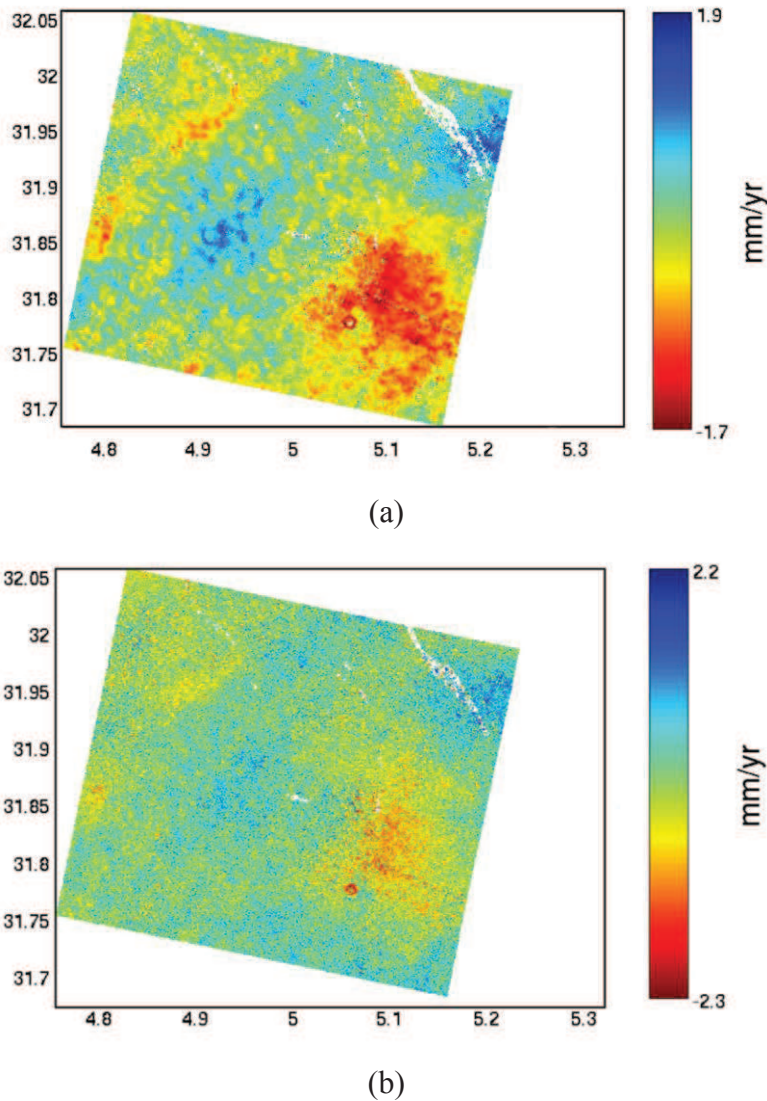


**Fig. 11.** Mean LOS velocity results obtained by using (a) Small Baseline method and (b) Persistent Scatterer method over an 8-year period with LOS rate change between -2 to 2 mm.

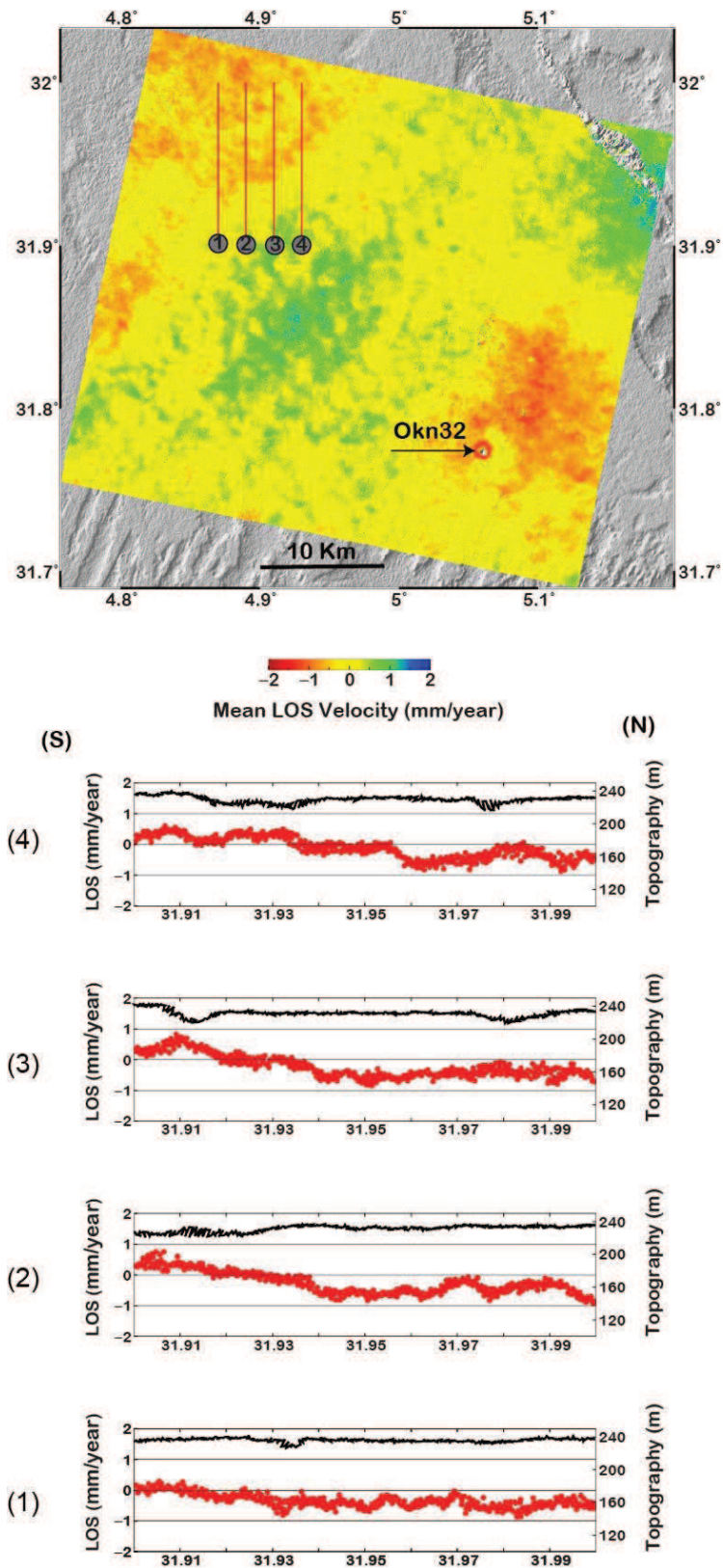


**Fig. 12.** Mean LOS velocity obtained by combining PS and SB InSAR results. The map view displays two main red patches in the OKN32 well region about 50 km NW of OKN32. Four profiles across the latter region show the correlation between the topography (black scatters) and mean LOS signal (red scatters) that indicates the absence of ground deformation.

We use the SB and PS InSAR techniques incorporated in StaMPS/MTI [Stanford Method for Persistent Scatterers / Multi-Temporal InSAR, (Hooper, 2008)] software package, using the DORIS software (Kampes and Usai, 1999) for calculating interferograms and ROI-PAC for focused the SAR images. We calculate 38 interferograms using 17 ERS image with baselines less than 200 m (Figs. 7 and 9). We show in (Fig. 10a and 10b) respectively the interferometric data pairs selected for the SB methods and for the PS method. We obtained 15 interferograms for the PS processing method and 38 interferograms calculated with the SB SAR network. As shown in (Figs. 11a and 11b), mean line of sight velocity (LOS) fields deduced from the PS and SB methods provide comparable results of subsidence pattern where the crater can be clearly distinguished. The positive signal is viewed in the blue area and considered as the zero reference of PS. The subsidence signal, however, reaches -2.3 mm/yr using the PS method (Fig. 11b) while for SB method the subsidence rate attains -1.7 mm/yr.

A LOS velocity field obtained by combining the PS and SB results using StaMPS is shown in (Fig. 12) (Hooper, 2008). The circular pattern along the rim of the sinkhole crater is still conspicuous in the LOS velocity map. Profiles across a region relatively far (~20 km) from the sinkhole areas shown in (Fig. 12) reveal the atmospheric effects correlated with topography as the LOS velocities mimic very well the topography (i.e. the mirror effect; Cakir et al., 2003). The profile crossing the sinkhole shows sharp change in subsidence rate around the sinkhole (profile 1 in Fig. 13). The sharp change indicates relatively rapid subsidence of the crater rim reaching to 1.5 mm/y. The red area (negative LOS direction, Figs. 12 and 13) represents the subsided area, obtained from merged (PS-SB) method of time series analysis of SAR images acquired between 1992 and 2000. The 64-km<sup>2</sup> extents of red area that includes the OKN32 well and sinkhole crater (Lat. 31.77 and Long. 5.06) are estimated as a square of 8 km size inferred from the different patches of PS-SB scatterer. The area of maximum LOS distribution visible in (Fig. 13) corresponds to a flat plateau of continental Pliocene (lacustrine limestones, see Fig. 4) with no change of soil dielectric parameters that would affect the coherency. The subsidence area starts from the sinkhole and OKN32 well location at the origin of the ground deformation and extends to the east and northeast in the direction of Ouargla city (Figs. 11a and 11b).

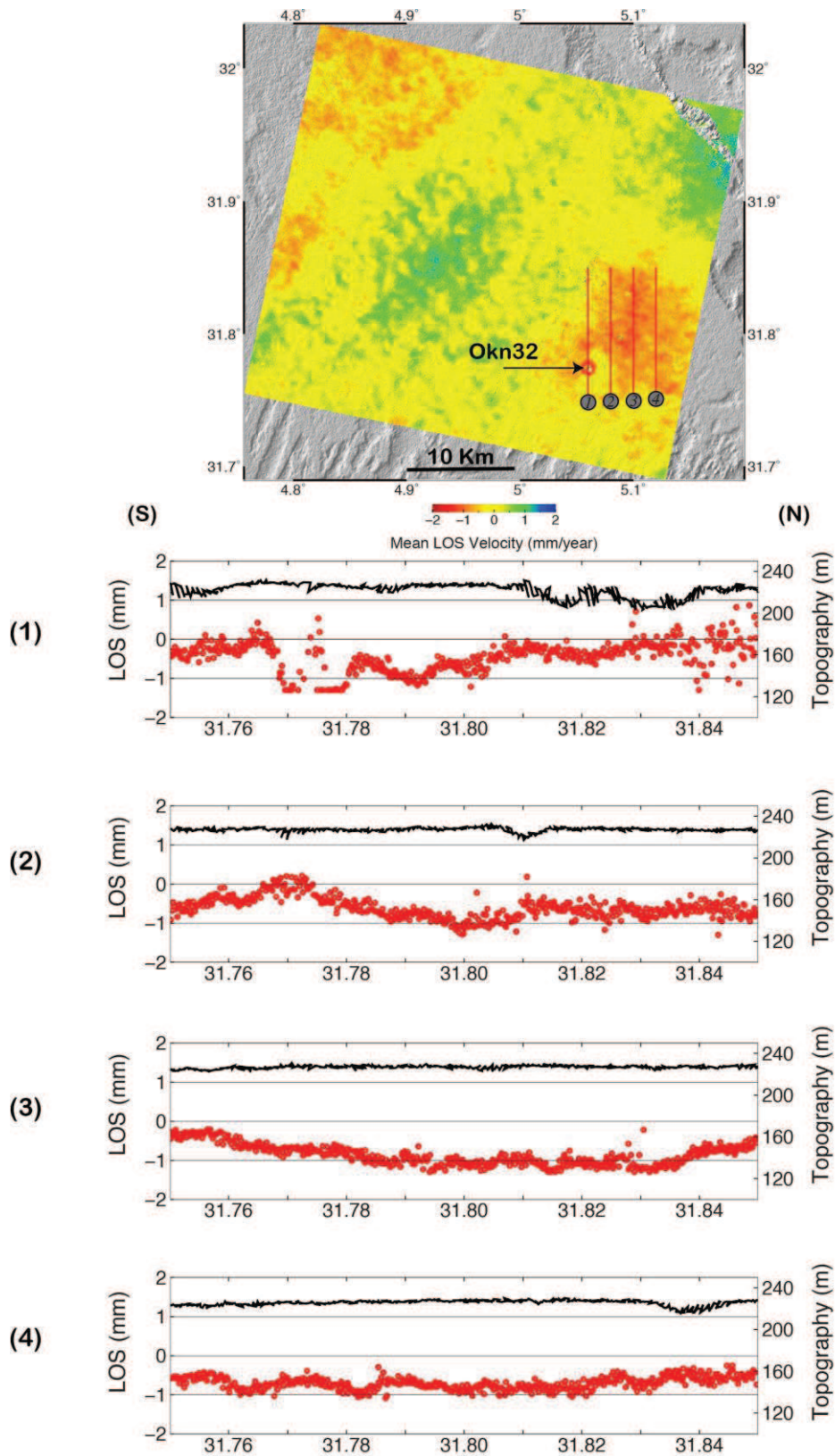


**Fig. 13.** Mean LOS velocity over 8-year period with LOS rate change between -2 to 2 mm. Profiles across the red zone (next to OKN32 Oil well) and the subsidence region also crosses the crater (profile 1). The comparison between the topography (black scatters) and the mean LOS (red scatters) indicates a clear discrepancy due to the ground deformation

A profile of (Fig. 13) crosses Haoud Berkaoui area as well as the sinkhole in particular (profile 1) with a clear mean LOS rate signature (see longitude interval 31.77 to 31.78). In all profiles, the topographic and mean LOS signals are clearly distinct reaching  $1.5 \pm 0.5$  mm/yr subsidence rate (Fig. 13). Profiles 2, 3 and 4 crosses the subsided area situated at the east of the sinkhole and the profile 1, with maximum deformation as shown by the LOS values and indicates with the topography. A prominent LOS signal appears in profiles 3 and 4 as they cross the region of maximum deformation, including the crater structure. Moreover, we observe in profile 1 a sudden increase of velocity (from  $\sim 0$  to  $-1.3$  mm/yr.) when crossing the central section of crater with nearly no surface changes at the border. The subsidence is clearly visible further east and northeast thanks to the LOS signal reaching  $-1.3$  mm/yr of surface rate change in profile 3.

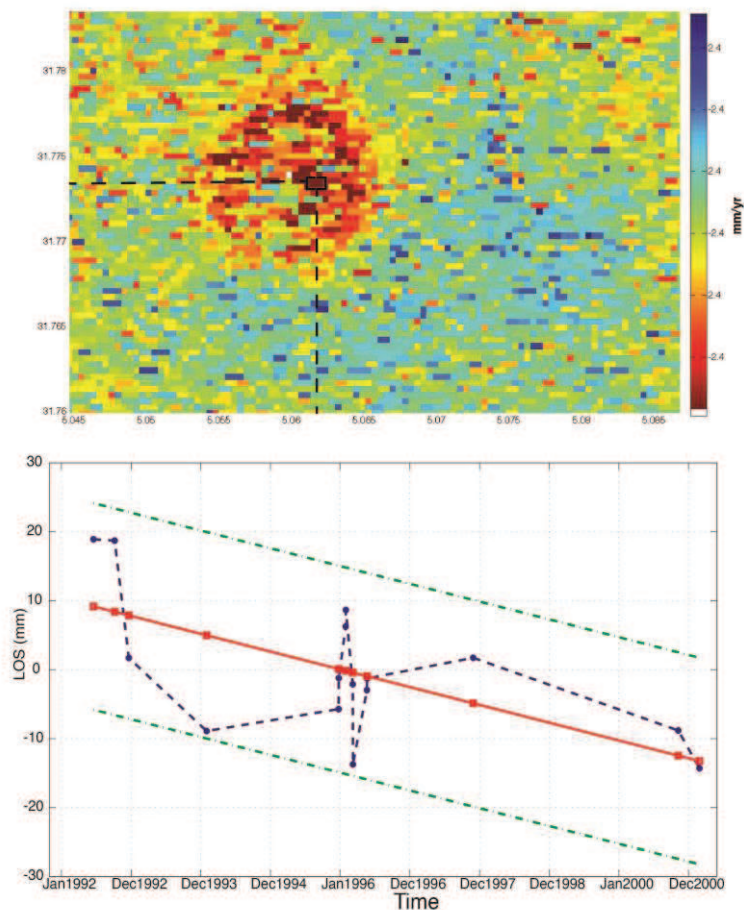


**Fig. 14.** (a) MT-InSAR time series in the OKN32 crater. b) The plot of time series evolution for a single pixel yields  $F(t) = -1.5t + 7.67281$  with  $1.5$  mm/yr subsidence velocity in the LOS. The cross is the LOS value per year, red square is the mean displacement per year, and red line is the regression function that constrains the subsidence velocity. Green dashed lines illustrate maximum and minimum velocity function obtained from all selected PS.

To visualize the temporal evolution by PS, we plot the time series of several PSs chosen in the subsidence area and the crater (Fig. 14a). As an example, the scatterer located in the crater (Lat. 31.77 and Long. 5.06) indicates an area with maximum continuous surface deformation (Fig. 14a). Furthermore, the subsidence northeast spreading from the crater confirms the surface change and evolution determined using the InSAR interferograms (see paragraph 3.1 above). The time series analysis gives access to the  $F(t) = -1.5t + 7.647$  of the subsidence evolution as (Fig. 14b).

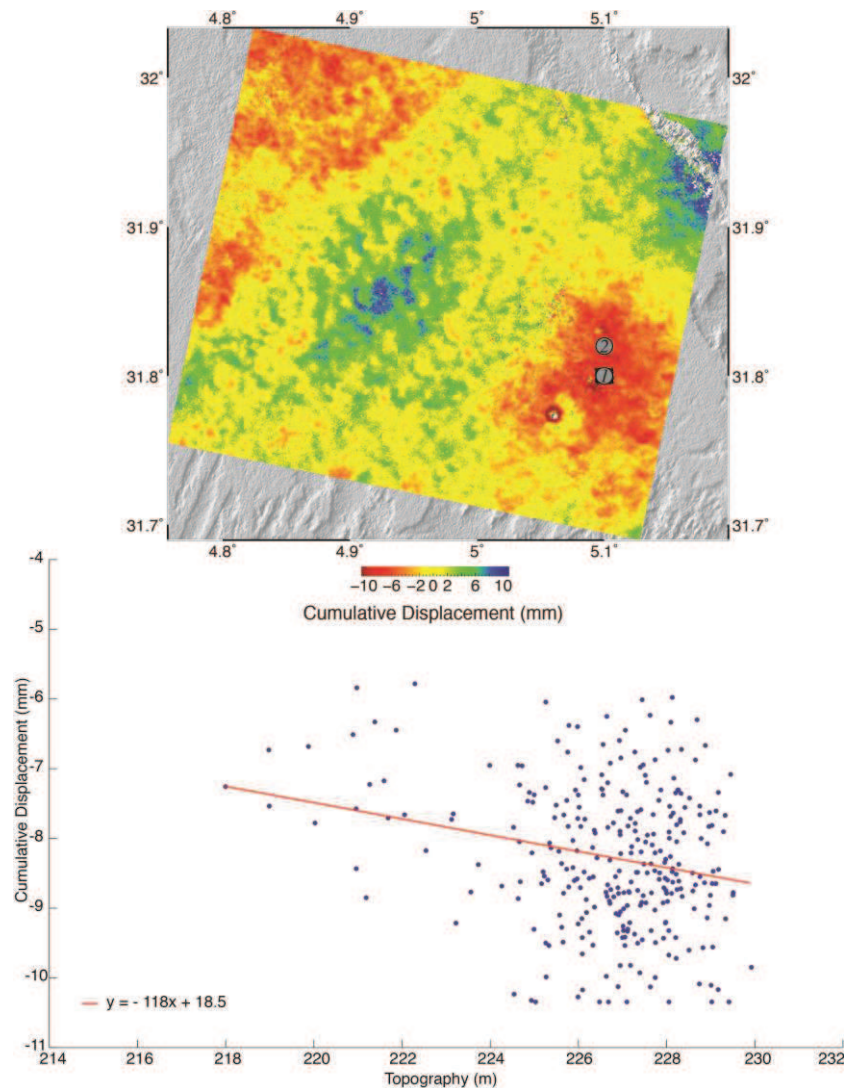


**Fig. 15.** (a) Two patches for comparing the cumulative displacement and their associated topography chosen from the maximum values in the subsidence area in the cumulative displacement map. (b) Plot of the cumulative displacement and the topography of these two patches in order to study the possible correlation between these two signals. The fit function gives:  $f(x) = -118.15x + 18.502$  and the  $R^2 = 0.05397$ .

The final LOS signal can include small topographic contribution and in order to enhance the processing results, we reduced the phase contribution due to any spatially-correlated look angle (SCLA) error (Hooper, 2008), using StaMPS/MTI software. This error can be temporarily subtracted from the wrapped phase before unwrapping step, which is improved, by subtracting the atmosphere and orbit error (AOE) phase obtained from the master image and applied from all interferograms (Hooper, 2008). We choose two patches from the maximum of cumulative displacement map (Fig. 15a) and we compare these values with their associated topography. The idea is that if we still have (AOE) in the final signal, we should have correlation between the topography value and the total displacement of each pixel. (Fig 15b) plotted the assimilation between the cumulative displacements with their associated topography value. The fit function measured in this case indicates a negative correlation (decorrelation) expressed by:  $y = -118x + 18.5$ ,  $R^2 = 0.054$ .

## 4. Modeling

Several models are used for the study of sinkholes and subsidence based on geomorphic mechanisms and surface change data (Frumkin et al., 2001). The ground deformation in the Haoud Berkaoui area is constrained by two aspects: 1) The saline layer dissolution process by a pressurized and hot fossil water circulation at ~400-m-depth, and 2) the lithostatic pressure and associated subsidence visible at the surface and induced by the Upper Senonian and Mio-Pliocene unit above the saline layer.

*Dissolution:* The subsidence is a direct consequence of the dissolution from which we infer quantitative parameters based on geological and physical characteristics (Bernabé et al., 2003). Taking into account that the intensive dissolution process of the saline layer develops within an area near the sinkhole, the related parameters are: ground water circulation, dissolution, and permeability described as:

$$N = N_0(\varphi/\varphi_0)^n$$

Where  $N_0$  and  $\varphi_0$  are the initial permeability and porosity,  $N$  and  $\varphi$  are the current permeability and porosity, respectively;  $n$  is an empirical constant in the range  $> 5$  depending on the sediment content (Bernabé et al., 2003). From field observations and previous reports (Sonatrach, 1998), the water saturation for NaCl content is equal to 360g/l at 50°C, the considered surface area is

about  $8 \text{ km}^2$  and the salt layer is between 450 and 620-m-depth from which we infer 170 m thickness; hence, the considered total volume exposed to the dissolution is:

$$V = 64 * 10^6 \text{m}^2 * 170 \text{ m} = 108 * 10^9 \text{ m}^3$$

We suppose also that all salt grains have similar molecular size, and the volumetric mass of NaCl is given by  $\rho = \frac{m}{v}$  ( $m$  being the mass and  $v$  the volumetric mass). Knowing that the Albian water flow at the OKN32 well is about  $300 \text{ m}^3/\text{h}$  (Sonatrach, 1998), we may estimate the necessary injected water to saturate the  $108 * 10^9 \text{ m}^3$  saline volume. The NaCl saturation level being reached at  $360 \text{ g/l}$ , a total  $3 * 10^8 \text{ l}$  of injected water is necessary for the saturation of the saline layer, which may have occurred in  $\sim 113$  years. Hence, the estimated saline volume dissolved since the OKN32 accident in 1978 (until 2000 according to the latest acquired ERS SAR images) is  $21.026 * 10^9 \text{ m}^3$ ; this amount of dissolved saline in saturated circulating Albo-Barremian water may represent the estimated amount of subsidence.

*Subsidence:* We consider in our model the warping of a plane surface at depth representing the subsidence due to the lithostatic pressure and presumably located above the saline layer. The warping is modeled by means of two dislocations, dipping in opposite sense, and with opening mechanism that illustrates the subsidence (Figs. 16a and 16b).

The total subsidence estimated at the Earth's surface during the observation period is modeled in an inverse approach using the Poly3D software. The deformation of sedimentary units is modeled as a horizontal plane that bears a lithostatic pressure due to the dissolved volume of the saline layer (see the previous paragraph) at  $\sim 600 \text{ m}$  of depth. The Poly3D software is a boundary element computer program based on a three-dimensional polygonal element, and displacement discontinuity with applications to fractures, faults, and cavities in the earth crust (Thomas, 1993). The polygonal element may represent some portions, or all, of the subsidence area across which the discontinuity in displacement is assumed constant. Constructed with triangular elements, the modeled horizontal plane is  $17 \times 17 \text{ km}$  in size encompassing the sinkhole and the region to the northeast. We model the warping of the horizontal plane as triangular grids in dislocation taking into account the merged PS-SB means resulting file and its spatial distribution. Therefore, we assume that subsidence is directly the result of volume loss due to the dissolution of the saline layer at depth, which is approximated with a total negative opening of  $6 \text{ m}$  (cumulative opening for all cells that corresponds to the best fit model using Mode I deformation crack; Davidson et al. 1983; Jordan et al., 2000).

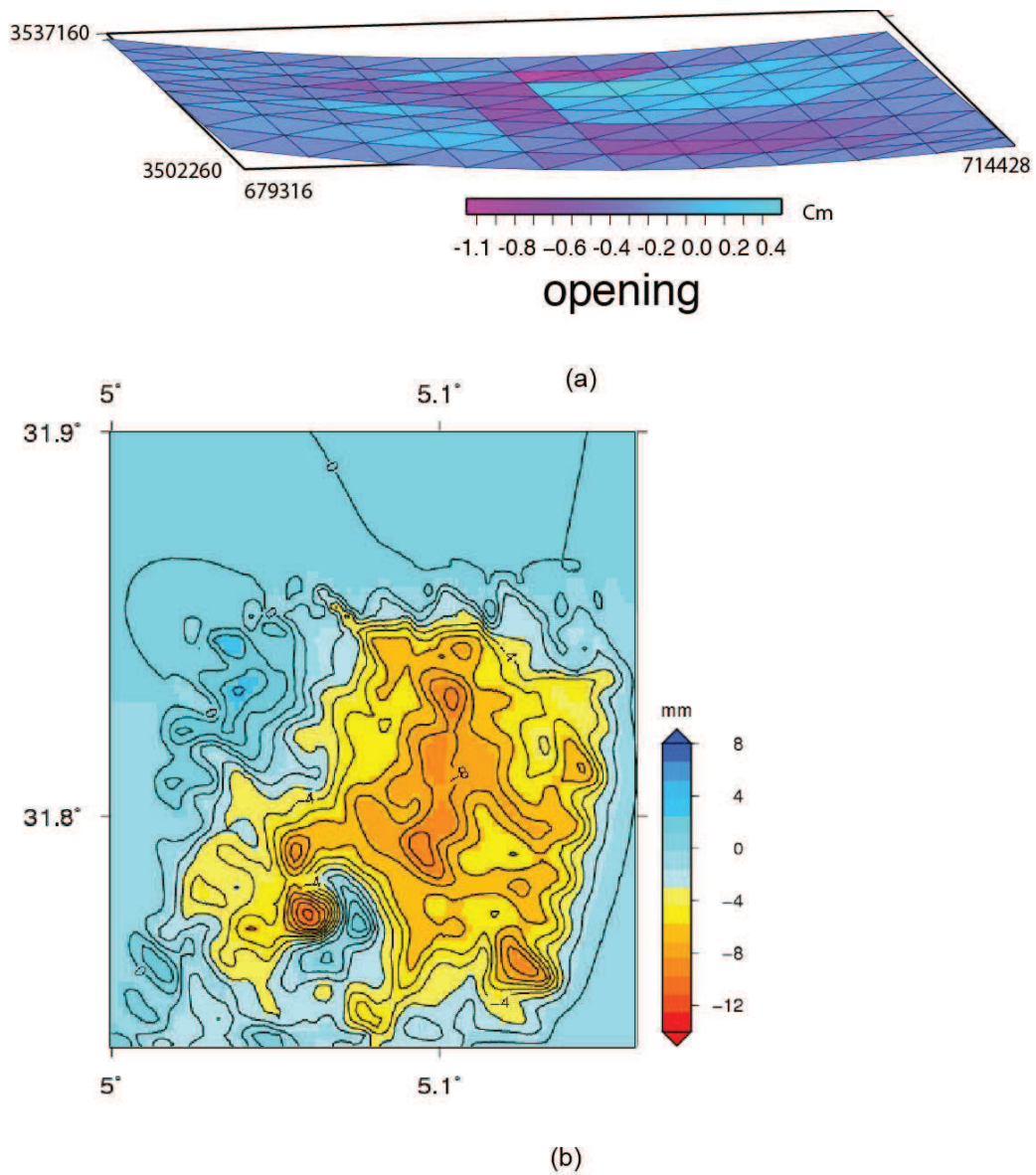


**Fig. 16.** (a) Modeling of the dissolution and subsiding stratigraphic plane by means of two opposite planes. The opening mechanism for each triangular element of the Poly3DInv program illustrates the amount of subsidence. (b) The inversion model using the merge PS results and related parameters of (Table 1) show the distribution of ground deformation with up to 8 cm subsidence comparable to the results shown in (Fig. 12c) Observed LOS velocity field.

Young Modulus (E)	(Top, bottom) Plane	Poisson ratio ( $\nu$ )	Shear modulus ( $\mu$ )	Lame parameter ( $\lambda$ )
40.0	(0, -100) m	0.250	16.0	32000.0
40.0	(-100, 0) m	0.250	16.0	32000.0
40.0	(0,100) m	0.250	16.0	16.0

**Table 1:** Physical parameters of geological units involved in the subsidence phenomena (see text for explanation).

According to the observed depth of salt layer, the 64 km<sup>2</sup> subsidence area can be considered as a warped surface that we model as two 2.4° opposite dipping planes over 8 km distance (Figs. 16a and 16b) describes the final inversion model of the warped and stable area. Comparing the observations and the model shown in (Figs. 12a and 16b), the observed pattern and amplitude of surface subsidence is well reproduced by the model. The model presented in (Fig. 16b) is the best fit model obtained using minimum Gaussian error between the model and the data and different modeling parameters such as (see (Table 1)).

The ground deformation indicates 3.68 cm cumulative mean subsidence with a negative signal indicating movements away from satellite over 8 years in the LOS range. The inverse model presented in (Fig 16b) is tested after several changes of physical parameters (Table 1) to obtain the best-fit solution. The best-fit solution is illustrated by the linear relationship between the Merged MT-InSAR (cumulative LOS signal) and model shown in (Fig. 17), using 8 years of ERS SAR data. Using a poly fit function with a least squares equation,  $y = 1.08t$  ( $t = 8$  years) regression function is obtained with correlation factor  $R^2 = 0.78$  (Fig. 17).

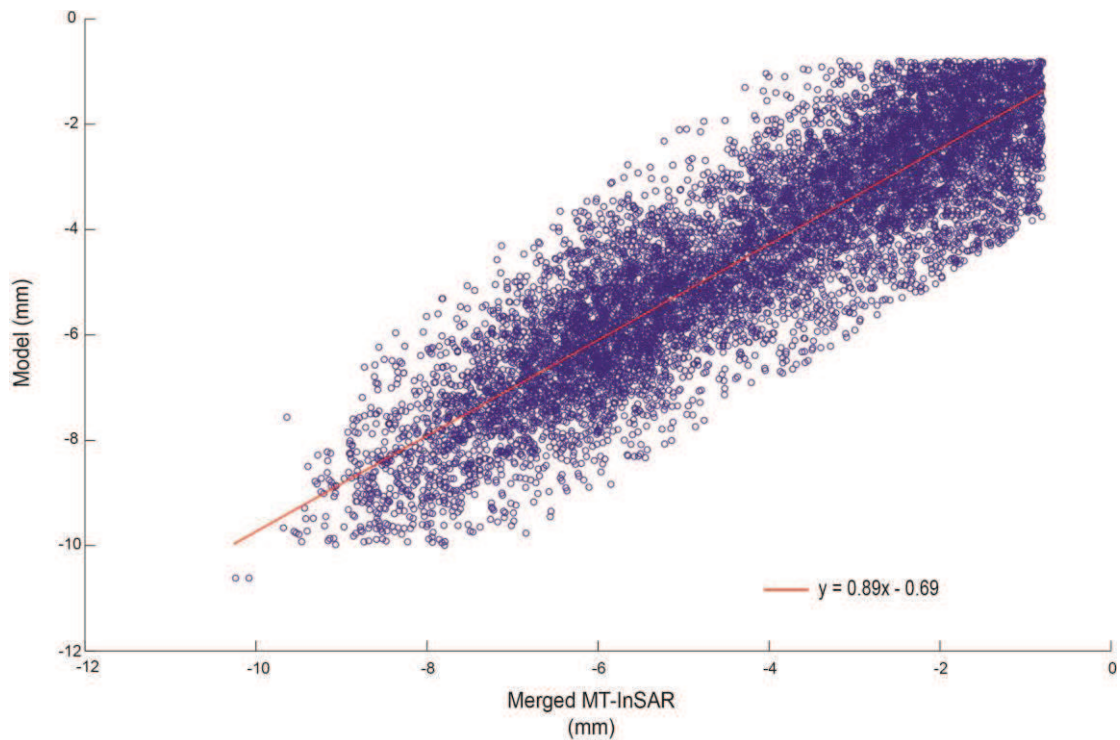


**Fig. 17.** Plot of Merged PS-SB MT-InSAR cumulative data versus the modeled displacement over the 8-year period. The regression line shows 78 % correlation factor and confirms the validity of the subsidence model.

## 5. Discussion and Conclusion

The study of Haoud Berkaoui subsidence area is presented using InSAR remote sensing methods for small but perceptible ground movement monitoring. The Multi-Temporal InSAR (SB and PS) method and related times series analysis gives a spatial and temporal variation of the ground deformation. The 17 ERS SAR images analysis consists in 136 possible interferograms that provide ~80 exploitable interferograms, from which we obtain an average 1.5 mm/year in the LOS direction over an area of ~64 km<sup>2</sup>. The ground subsidence is interpreted as a result of the ~400-m-thick lithostatic pressure on the 170-m-thick dissolved saline layer. Deep-water circulation and saline layer dissolution, responsible of the subsidence are evaluated to reveal an estimated  $21.026 * 10^9$  m<sup>3</sup> of saline volume dissolved since the OKN32 accident in 1978. We observe that the subsidence area propagates from the oil well OKN32 position in the northeastern direction and to Ouargla city located at about 30 km.

The monitoring of land subsidence caused by gas/oil extraction using InSAR was addressed in several works. The land subsidence and sinkhole hazard was widely studied using

the repeat-pass interferometry technique (Gidson and al., 2002; Alsop, 2011). Using the DInSAR technique in the Los Angeles Basin (California), Bawden et al. (2001) found that from 1997 to 1999 the Wilmington and the Salt Lake oil fields underwent an episodic subsidence rate of 28 mm/yr and 11 mm/yr, respectively. The evolution of sinkhole fields due to underground dissolution near the Dead Sea coast in Jordan reveal an accurate (Closson et al., 2005). Although the rate of subsidence may vary depending on case studies worldwide, the rate of ground deformation is in the order of a few mm/yr. In Haoud Berkaoui, we observe that the rate of ground deformation reaches 1.5 mm/yr and the total amount of subsidence is 21 mm between 1992 and 2000. In our study, the use of PS and SB techniques gives not only an accurate estimate of the rate of ground deformation but also a global vision of the area of subsidence and its evolution.

The impact of such catastrophic event since the first collapse in 1978 and related conversion of oil drilling into water well has created serious environmental problems. The analysis of interferograms obtained from SAR images (taken between 1992-06-04 and 2000-05-07), reveals a continuous subsidence and its migration towards the city of Ouargla (see (Figs. 8a and 8b) for Differential InSAR, and (Figs. 11a, 11b and 12) for respectively PS, SB and merged methods). The distance between Ouargla city and the subsidence area gets apparently shorter passing from about 28 km in 1992 to about 20 km in 2000. If the rate of dissolution and northeastern propagation of subsidence including the enlarged of the city are constant, the ground deformation may reach the city in about 40 years (in ~2050).

Our study encompassing the whole Haoud Berkaoui oilfield and the determination of the affected region and its spatial and temporal evolution may help in the understanding of the underground dissolution phenomena and related environmental consequences. We believe that further studies are now needed using for instance Envisat data from 2002 to 2010 and further actions must be taken before the oil field situation can cause serious and sometimes irreversible damage.

## **Acknowledgements**

S B (PhD student) benefited during this study with a scholarship from the Algerian Government (MESRS, Algiers). We thank A. Hooper for providing access to StaMPS software tools. The ERS SAR data were provided by the European spatial agency (ESA) under project C1P 2532.

## References

- Akretche, S., Okbi, L. (1995). Historique de l'incident d'Okn 32, à la partie du nord du Sahara algérien, in Land subsidence, Proceedings of the land subsidence meeting, The Hague, IAHS Publ. 234 p.
- Amelung, F., Oppenheimer, C., Segall, P. and Zebker, H. (2000). Ground deformation near Gada 'Ale volcano, Afar, observed by radar interferometry. *Geophys. Res. Letters* 27(19): doi: 10.1029/2000GL008497. issn: 0094-8276.
- Alsop, G.I., and Marco, S. (2011). Soft-sediment deformation within seismogenic slumps of the Dead Sea Basin. *J. of Struct. Geology* 33, 433-457.
- Bawden, G., Thatcher, W., Stein, R.S., Hudnut, K.W., and Peltzer, G. (2011). Tectonic contraction across Los Angeles after removal of groundwater pumping effects, *Nature* 412, 812-815.
- Berardino, P., G. Fornaro, R. Lanari, and E. Sansosti. (2002). A new algorithm for surface deformation monitoring based on small baseline differential SAR interferograms, *IEEE Trans. Geosci. Remote Sens.* 40, 2375 – 2383.
- Bernabé, Y., Mok, U., Evans, B. (2003). Permeability–porosity relationship in rocks subjected to various evolution processes. *Pure and Applied Geophysics* 160, 937–960.
- Feuga, B. (2009). Les effondrements dus à l'exploitation du sel, *Geosciences* 9, 86-95.
- Bianchi, M., and Ferretti, A., 2006, Land deformation monitoring using satellite radar data processed with the Permanent Scatterers Technique (POLIMI PS Technique), *Tele-Rilevamento Europa*, 30 p., Milano.
- Çakir, Z., A. Barka, J-B.deChabalier, R. Armijo, B. Meyer. (2003). Kinematics of the November 12, 1999 (Mw=7.2) Düzce earthquake deduced from SAR interferometry, *Turkish Journal of Earth Sciences* 12, 105-118.
- Carnec, C., Massonnet, D. and King, C. (1996). Two examples of the use of SAR interferometry on displacement fields of small spatial extent, *Geophys. Res. Letters* 23(24): doi: 10.1029/96GL03042. issn: 0094-8276..
- Castañeda, C., Gutiérrez, F., Manunta, M. and Galve, J.P. (2009). DInSAR measurements of ground deformation by sinkholes, mining subsidence and landslides, Ebro River (Spain), *Earth Surface Processes and Landforms* 34, 1562-1574.

- Closson, D., AbouKaraki, N., Klinger, Y. & Hussein, M.J. (2005). Subsidence Hazards Assessment in the Southern Dead Sea Area, Jordan, *Pure and Applied Geophysics*, 162, 2, 221-248, ISSN 0033-4553.
- Colesanti C., Le Mouelic, A., Bennani, M., Raucoules, D., Carnec, C., Ferretti, A. (2005). Detection of mining related ground instabilities using the Permanent Scatterers Technique – a case study in the east of France, *International Journal of Remote Sensing* 26, 1, 201-207,.
- Davidson D. L. and Lankford. J. (1983). Mixed-mode crack opening in fatigue, *Materials Science and Engineering* 60, 3, 225-229.
- Farr, T. G., and Kobrick, J. (2007). The Shuttle Radar Topography Mission, *Rev. Geophys.* 45, RG 2004, doi : 10.1029/2005RG000183.
- Ferretti A., Prati C., Rocca F. (2001). Permanent Scatterers in SAR Interferometry, *IEEE Trans. on Geoscience and Remote Sensing* 39, 1, 8-20.
- Frumkin, A., Magaritz, M., Carmi, I., and Zak, I. (1991). The Holocene climatic record of the salt caves of Mount Sedom, Israel, *The Holocene* 3, p. 191-200.
- Gabriel, A. K., Goldstein, R. M., and Zebker, H. A. (1989). Mapping small elevation changes over large areas, differential radar interferometry. *J. Geophys. Res.* 94 (B7), 9183-9191.
- Gibson, J. J. (2002). Short-term evaporation and water budget comparisons in shallow arctic lakes using non-steady isotope mass balance, *Journal of Hydrology* 264, 247-266.
- Goldstein, R. M., H. Engelhardt, B. Kamb, and R. M. Frolich. (1993). Satellite radar interferometry for monitoring ice sheet motion : Application to an Antarctic ice stream. *Science* 262, 1525-1530.
- Hanssen, R. F. (2001). *Radar Interferometry: Data interpretation and error analysis*, Kluwer Academic Publishers, Dordrecht, 308 p.
- Hilley G. E., Bürgmann, R., Ferretti, A., Novali F., and Rocca, F. (2004). Dynamics of Slow-Moving Landslides from Permanent Scatterer Analysis, *Science* 304, 1952-1955.
- Hocine F., Belhadj A. M., Ouarzeddine M., Haddoud A., and Belhadj A. A. (2008). Suivi des failles et du cratère de Haoud Berkaoui sud Algérie par images radar ERS1/ERS2, XIèmes Journées Scientifiques du Réseau Télédétection de l'AUF, 276-279, Madagascar.
- Hooper, A. and Zebker, H. (2007). Phase Unwrapping in Three Dimensions with Application to InSAR Time Series, *J. Optical Soc. of America.* 24, 2737-2747.
- Hooper, A. (2008). A multi-temporal InSAR method incorporating both persistent scatterer and small baseline approaches, *Geophys. Res. Letters* 35, L16302, doi:10.1029/2008GL034654.

- Hooper, A. (2009). A Statistical-Cost Approach to Unwrapping the Phase of InSAR Time Series, Proceedings FRINGE Workshop, ESA-Frascati (Italy).
- Lundgren, P., Usai, S., Sansosti, E., Lanari, R., Tesauro, M., Fornaro, G., and Berardino, P. (2001). Modeling surface deformation observed with synthetic aperture radar interferometry at Campi Flegreicaldera, *J. Geophys. Res.* 106, 19355–19366.
- Massonnet, D., and Feigl, K.L. (1998). Radar interferometry and its application to changes in the Earth's surface. *Reviews of Geophysics* 36, 441-500.
- Muller, J. R. and Martel S. J. (2000). Numerical Models of Translational Landslide Rupture Surface Growth, *Pure appl, geophys* 157, 1009-1038.
- Razon, B., 1999, L'effondrement d'un forage réalisé par Total en 1978 menace de polluer les eaux de Ouargla, l'un des plus anciens oasis sahariens. Magazine Don Quichotte de la Mancha, juillet-aout, Paris.
- Rosen, P.A., Hensley, S., Joughin, I.R, Li, F.K., Madsen, S.N., Rodriguez, E., Goldstein, R. M. (2000). Synthetic Aperture Radar Interferometry, *Proc. IEEE*.
- Scharoo, R. and Visser, P. (1998). Precise orbit determination and gravity field improvement for the ERS satellites, *J. Geophys. Res.* 103, 8113–8127.
- Schmidt, D. A. & Burgman, R. (2003). Time-dependent land uplift and subsidence in the Santa Clara valley, California, from a large interferometric, synthetic aperture radar dataset, *J. geophys. Res.* 108, 8534–8543.
- Service de la carte géologique, Algérie. (1952). Carte géologique de l'Algérie (1 :500 000), Agence Nationale de la Géologie (ANGCM), Ministère de l'Energie et des Mines, Alger.
- Smith, W. H. F., and Sandwell, D. T. (1997). Global sea floor topography from satellite altimetry and ship depth soundings. *Science*, 277,1, 956-1,962.
- Snieder, R.; Hubbard, S.; Haney, M.; Bawden, G.; Hatchell, P.; Revil, A., and DOE. (2007). Geophysical Monitoring Working Group, Advanced noninvasive geophysical monitoring techniques, *Annu. Rev. Earth Pl. Sc.* 35, 653-683,
- Sonatrach. (1995). Suivi de l'évolution de l'effondrement d'Okn 32. Rapports internes (1990, 1992, 1994, 1995), Division Ingénierie et Production, Direction Regional Haoud Berkaoui.
- Sonatrach. (1998). Le cratère d'effondrement du puits OKN 32, Service Technique, Rapport Puits 17, Division Ingénierie et Production, Direction Regional Haoud Berkaoui.
- Thomas, A. L. (1993). POLY3D, A Three-Dimensional, Polygonal Element, Displacement Discontinuity Boundary Element Computer Program With Applications to Fractures, Faults, and Cavities in the Earth's Crust, M.S. Thesis, Stanford University, Stanford, CA.

- Thompson, A., J.M. Moran, and G.W. Swenson. (1986). *Interferometry and Synthesis in Radio Astronomy*, Wiley-Interscience, New York, 528 p.
- van der Kooij, M., Hughes, W., Sato, S., and Poncos, V. (2006). Coherent target monitoring at high spatial density, Examples of validation results, Eur. Space Agency Spec. Publ., SP-610.
- Wessel, P. and Smith, H.F. (1998). New improved version of the Generic Mapping Tools Released, EOS Trans. AGU79, p. 579.
- Zhen Li, Xinwu Li, Huadong G., Huanyin Y. and Quan C. (2009). Sub-Canopy Soil Moisture Inversion Using Repeat Pass Shuttle Imaging Radar C Polarimetric Synthetic Aperture Radar Interferometric Data, *J. Appl. Remote Sens.* 3, 033553; Doi:10.1117/1.3256001.
- Zebker, H.A., and R.M. Goldstein. (1986). Topographic mapping from interferometric SAR observations, *J. Geophys.Res.* 91, 4993-4999.



## **Chapter III**

# **Monitoring Landslide in the Urban Area of Constantine (Northeast Algeria) using Advanced Merged PS-SB Insar Analysis**



## Summary:

We investigate eight years of land subsidence in Constantine urban area (Northeast Algeria) using a merged method of Persistent Scatterer (PS, Ferretti et al., 2001) and Small Baseline (SB, Berardino et al., 2002) for time series analysis of SAR images. The ground surface deformation in Constantine area is measured using 58 C-band ERS-1 and ERS-2 SAR images acquired between 20-Jun-1992 and 19-Dec-2000. Eight important landslide patches appear in this region according to the description given by (Bougdal, 2007) as it follows: Patch 1 : Belouizdad, Kitouni and Kaidi. Patch 2: Chabet el Merdja involving residential areas of Sotraco, Boudraa, Zaouche, Boussouf. Patch 3: from the bridge of Sidi Rached until the Constantine railway station and in the left bank of the Rhumel river. Patch 4: The left bank of Oued El Mellah river and neighborhood of Ben Chergui stream. Patch 5: The ruptures at the right bank of Rhumel near the Mentouri University. Patch 6: La Poudriere. Patch 7: Slope of Bardo. Patch 8: Zouaghi plateau crossed by the road of Massinissa. Bougdal (2007) also describes land subsidence that takes place very often near the bridge of Sidi Rached. The present study gives a spatial evolution description of landslides that relies on the height precision and time series of the InSAR technique. PS-InSAR and Small Baseline methods are used together in order to infer the resulting time dependent LOS signal from which we extract the best spatial and temporal correlated LOS signal using the merged method.

The combined multi-temporal InSAR method of PS-SB is incorporated in StaMPS/MTI (Stanford Method for Persistent Scatterers/Multi-Temporal InSAR) software package (Hooper., 2008), which is one of the best InSAR techniques applied in terrains and man-made structures. ROI\_PAC (Repeat Orbit Interferometry PACkage; Rosen, P. A et al., 2004) is used for the focusing of the raw data and Doris (Delft Object-oriented Radar Interferometric Software) (Bert M Kampes et al., 2003) for interferogram formation. Landslide is a classical example of surface deformation that highlights the importance of InSAR time series analysis and their combination with local geology and geomorphology. In our study, we produce a velocity map of land subsidence from 1992-2000. This map can be used in order to make a probabilistic model of land displacement taking into account several parameters such as: the average LOS velocity, the slope of each morphological structure, and the condition of neighbor pixels. We also use the Fuzzy K-means classification in order to estimate the potential of land subsidence in the area according to these parameters. Finally, the Mamdani fuzzy algorithm is used as well in the assessment of the land subsidence susceptibility.



# 1. Introduction

Among natural hazards, landslides in urban areas may cause large damage with numerous victims (Sidle et al., 2006). Synthetic Aperture Radar (InSAR) with 2-repeat passes geodetic technique is widely used for monitoring surface deformation. InSAR very often combined with GPS data, have been successfully used to study landslides (Singhroy et al., 2007; Riedel et al., 2008; Yin et al., 2010). Recently, Nikolavea et al., (2012) tested a comparison between conventional InSAR and time series methods using ALOS PALSAR (L-band) SAR data to analyse landslides of central Georgia. Interferograms were produced and analysed using DORIS and subsequently SBAS and PS methods developed in StaMPS (Hooper, 2008). Constantine is one of the most important cities (840 000 Habitants in 2010) situated in northeast Algeria (36.35° Lat., 6.6° Long.; Figure 1). Called town of bridges, Constantine is facing for over three decades, serious landslide hazards affecting its urban area and related constructions. Recent extensive building constructions and the confusing urban planning accentuated the vulnerability of the city. In addition, several economic and geostrategic projects recently programmed (especially the great east-west highway and the tramway installation) can be damaged after landslide movements.

For all these reasons, it is important and mandatory to study and produce map of the existing and possible hazardous areas in order to reduce the risks in the city. Several districts affecting the man made constructions caused by landslides are recorded in the last decades (Machane et al., 2008). According to Benazzouz (2002), the landslide vulnerability area spread over 120 hectares and covers 15,000 buildings and about 100,000 people.

Guemache et al. (2011) provide a local study of the Constantine landslide at Sidi Rached Bridge. They document the causes of this feature and emphasize five factors controlling the failure process: geomorphology, geology, human activities, climate and seismicity. Bougdal (2007) presents geological and morphological studies of the landslides in the Constantine agglomeration. Based on detailed field observations he describes 9 areas of instable zones affecting the urban area and produces a map with 7 classes describing the status of the zones with reasons to avoid man made constructions.

In this study, I describe 9 patches of landslide area previously identified by Bougdal (2007) based on observations and measurements using InSAR techniques. The aim of this study is to show the ability of InSAR technique to measure and follow the evolution of such phenomena with relatively high resolution. Times series analysis used in this study is with

double issues: the first describes the landslide patches location and delimitation, the second gives the space/time evolution of each patch showing the average velocity of each patch.

In section 2, I describe in detail the landslide areas and the local geology of Constantine region is presented in section 3. In section 4, I present the used InSAR time series analysis and related merged PS-SB methods for monitoring ground deformation with high resolution. In section 5, I draw some conclusions from this work and discuss future works.

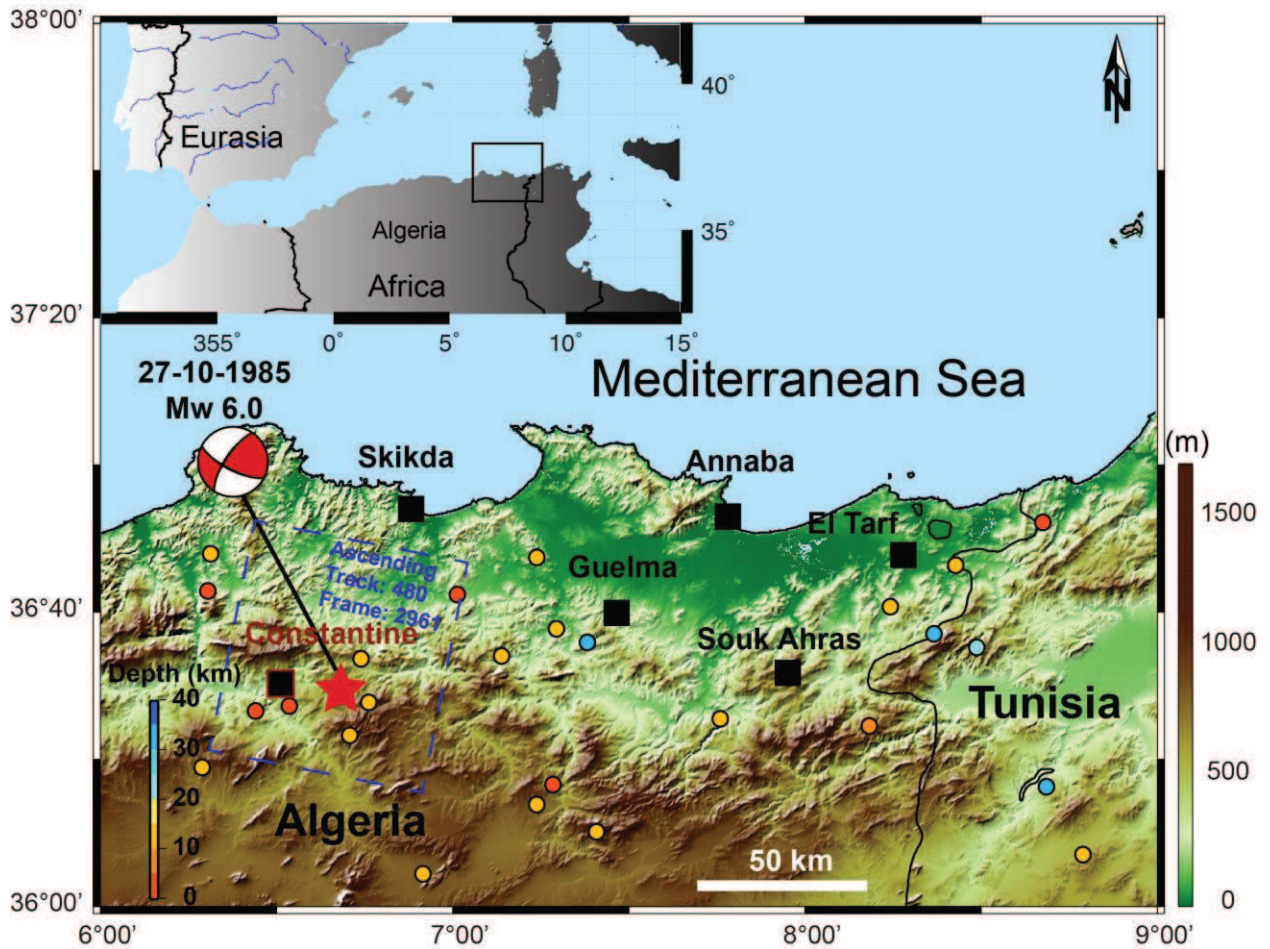


**Figure 1:** Location of the study area as shown in the inset of Northern Algeria. The seismicity is from the 1984-1996 ISC catalogue of worldwide earthquake; the study area also shows a shaded relief topographic map of Constantine obtained from SRTM 3+ (Farr and Kobrick, 1998). , The focal mechanism solution of the largest recorded event in the region (27-10-1985, Mw 6.0) is from Global CMT Harvard and the red star shows the mainshock location by CSEM.

## 2. Constantine Landslides Description

Among many landslide sites located inside the agglomeration of Constantine city, Belouizdad has the greatest concern because of its location in an urban zone with high-density population (Figure 2). Its large extension (over 30-ha of instable land) and the intensity of the disorders and damage affecting the constructions. The complexity of Constantine landslides are also linked with the rapidly changing slopes reaching 25%. The topographic slope is one of the principal factors to take into account in the location and landslide directions. These landslides take place on steep slopes as for example the Kitouni, Maquis, Kaidi, Aouinet el Foul and up the Rhumel River.

Figure 2 shows the principal location of major landslides of the Constantine city according to Bougdal., (2007). There are 9 principal landslide areas in the urban area of Constantine described as follows:

- 1- Landslides located in Belouizdad, Kitouni and Kaidi (Red area number 4 in Figure 2) indicating an area of  $\sim 232440 \text{ m}^2$ .
- 2- The landslide of Chabet el Merdja involving Sotraco, Boudraa, Zaouche, Boussouf areas (Red area number 2 in Figure 2) covering an area of  $\sim 1000000 \text{ m}^2$ .
- 3- Landslide in the right bank of the Rhumel River including the Sidi Rached bridge and until the Constantine gas station (Red area number 3 in Figure 2) affecting an area of  $\sim 232864 \text{ m}^2$ .
- 4- Landslides observed on the right bank of the El Mellah River including the residential area of Ben Chergui (Red area number 5 in Figure 2) indicating an area of  $\sim 82940 \text{ m}^2$ .
- 5- The landslide surface ruptures observed in the right bank of the Rhumel River that affect the University of Mentouri (Red area number 6 in Figure 2) indicating an area of  $\sim 110547 \text{ m}^2$ .
- 6- The recent landslides observed in the Poudriers zone (Red area number 1 in Figure 2) affecting an area of  $\sim 243941 \text{ m}^2$ .
- 7- Landslides observed in the Bardo area (Red area number 8 in Figure 2) indicating an area of  $\sim 66300 \text{ m}^2$ .
- 8- Landslides recorded in the Massinissa and Zouaghi areas (Red area number 9 in Figure 2) indicating an area of  $\sim 1250536 \text{ m}^2$ .

Landslides observed on the right bank of the Poudriers and the Rhumel rivers (Red area number 7 in Figure 2) indicating an area of  $\sim 33043 \text{ m}^2$ .

The total surface of all 9 landslides areas reaches  $\sim 3252611 \text{ m}^2$  representing  $\sim 0.15 \%$  of the total surface of Constantine city ( $2197000000 \text{ m}^2$ ). In his work, Bougdal. (2007) used the archived geological and geotechnical mapping data of landslide areas of Constantine, and

presents investigations by coring samples of 25 – 90 m-depth, piezometers and inclinometers. GPS network and topographic leveling were installed in this area for monitoring the landslides.

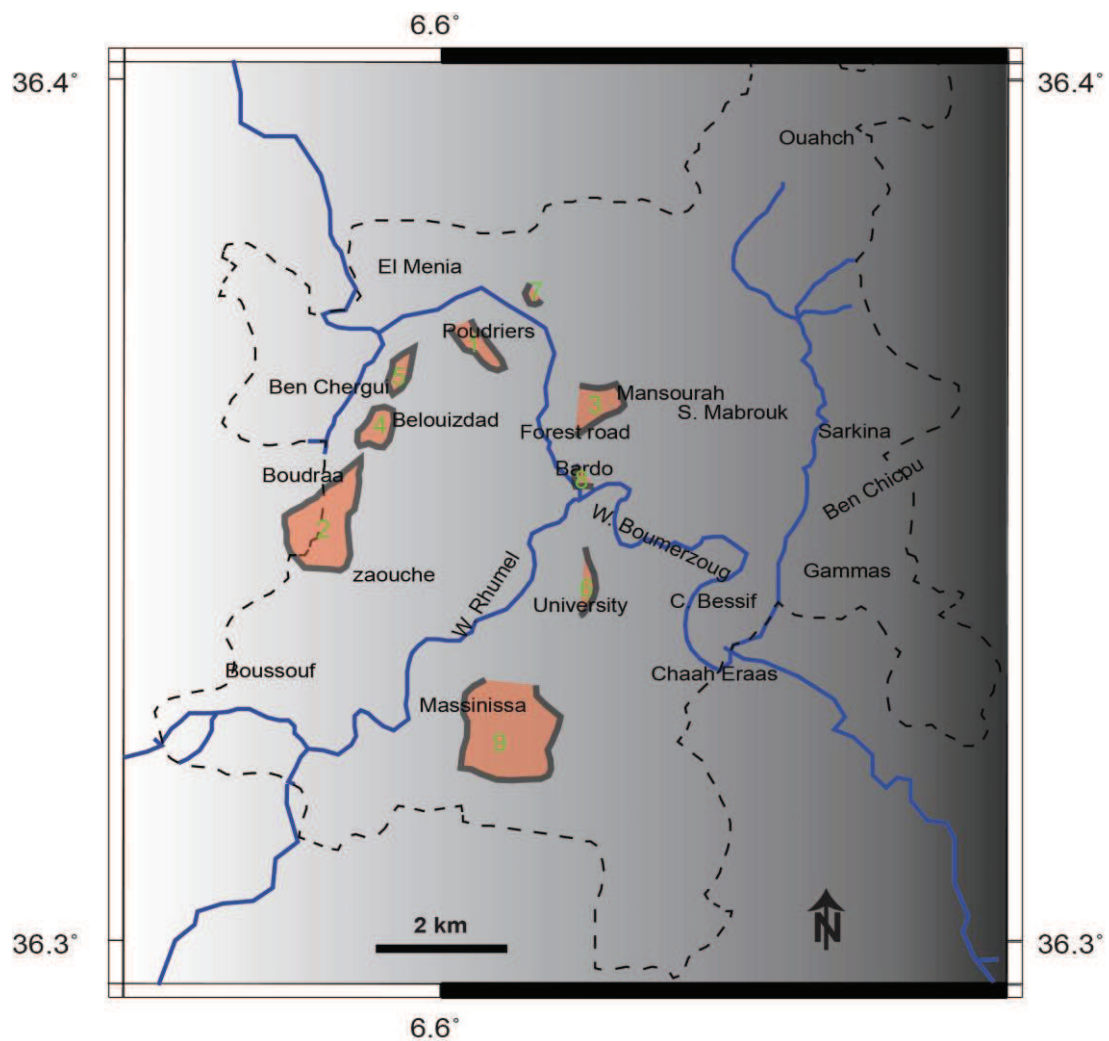


**Figure 2:** Principal landslides location found after geological investigations in the Constantine city according to (Bougdal, 2007). The numbered landslide areas are indicated in red color shapes. Following Bougdal (2007), there are 9 major landslide areas affecting the urban zone of Constantine.

The detailed map of the landslide locations is presented on the shaded topography from SRTM used for all InSAR processing (Figure 2). The map shows the location and the shape of the landslide areas in the city of Constantine.

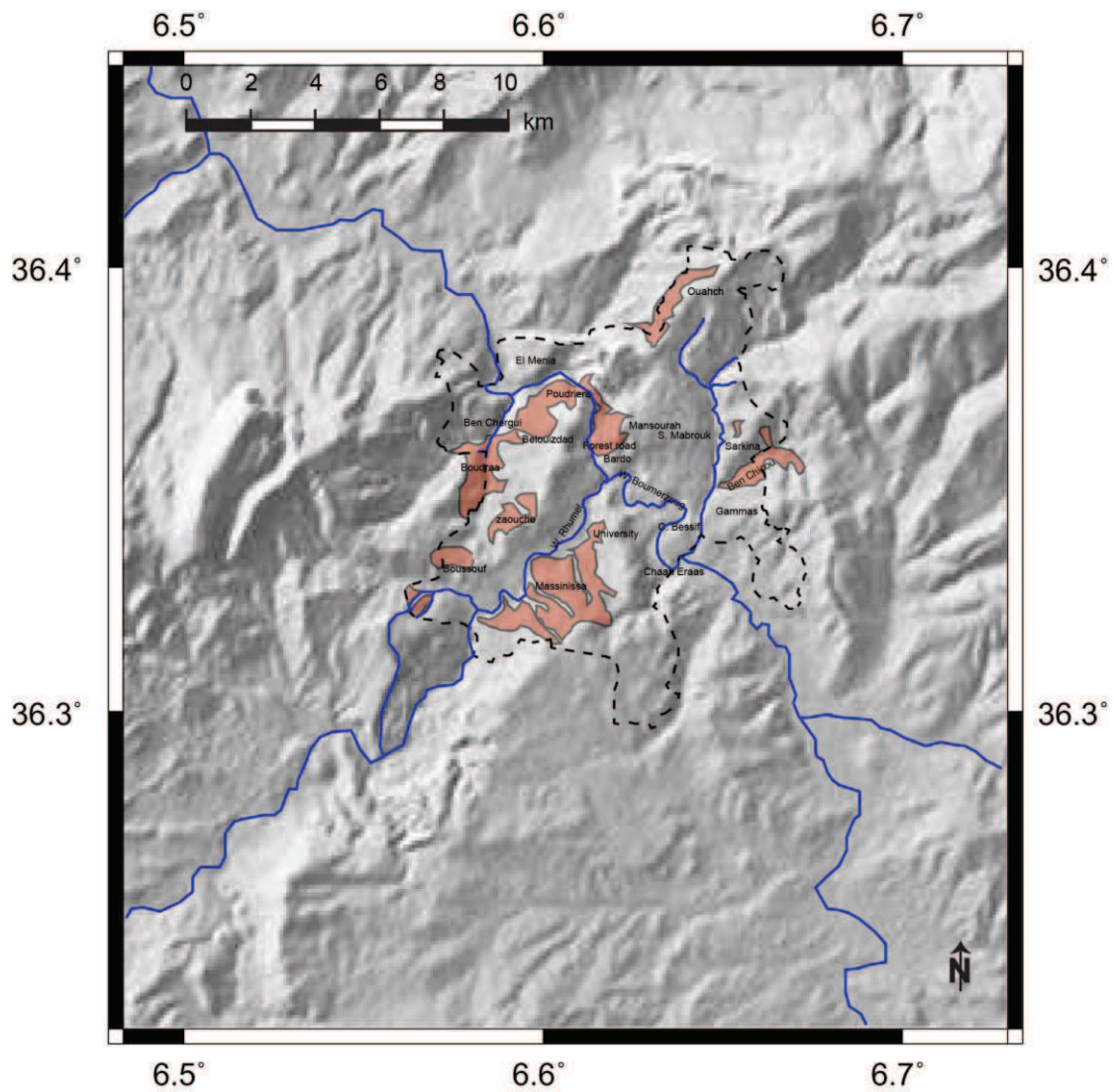


**Figure 3:** Active landslides areas in Constantine large urban area according to Bougdal et al., (2007) on the shaded topography (SRTM 3 arc.sec.; Farr and Kobrick, 1998). The dashed lines indicate the administrative delimitation of Constantine city and the blue lines indicate Rhumel and Boumerzoug rivers.

### 3. Constantine Geology:

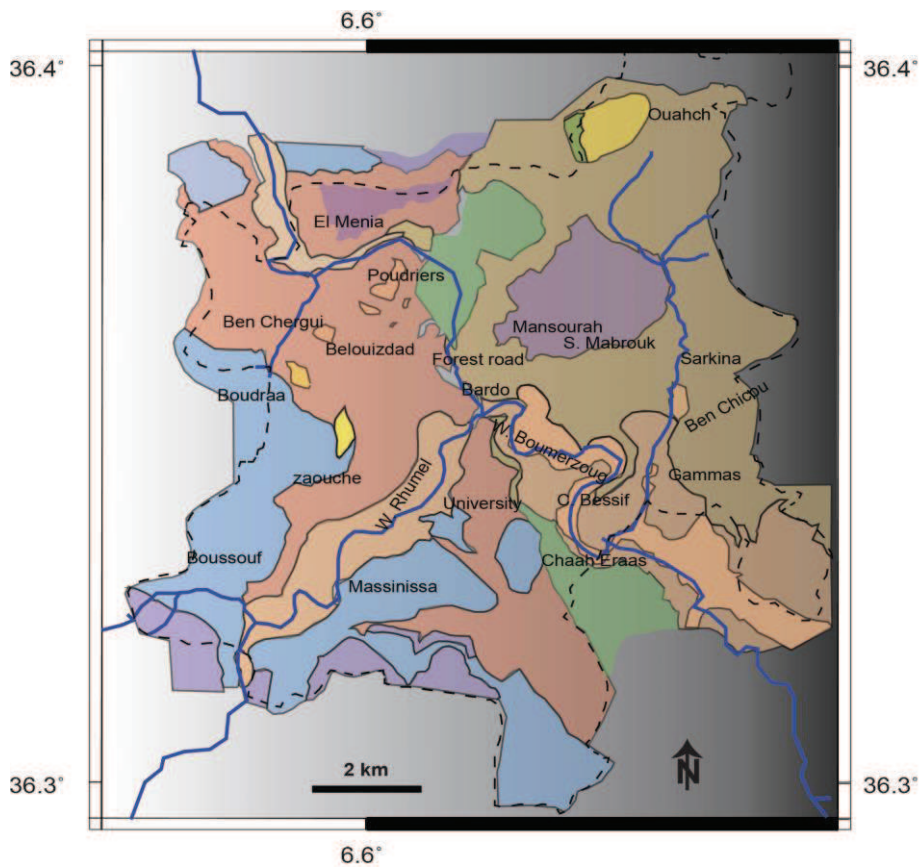
In Constantine area, we can distinguish eight main geological formations (Figure 4): (1) Quaternary lacustrine limestone, especially at the El Mansourah and Sidi Mabrouk, on the north-part of El Menia and the southern side of Constantine city. (2) Marl and gypsum of the middle to upper Miocene located in the left border of the city and in the left part of Boudraa and Boussouf

and the center of Massinissa. (3) Quaternary low terrace (T2) located on the two sides and along the Rhumel and Boumerzoug rivers. (4) The middle to upper Miocene made of conglomerate and red sandstone located mainly on the western side of the map involving Belouizded, Ben Chergui, El Menia, the University of Mentouri and the southwest of Chaah Eraas. (5) A Cenomanian-Turonian neritic limestone, situated in the center-north and center-south of the map of Constantine, including east of Poudriers and the south part of Chaah Raas. (6) Middle to upper Miocene, situated on both sides of the Boumerzoug River starting from Bardo and upstream. (7) Old and high Quaternary terrace (T1) which is one of the largest geological formations covering almost all the Easter part of the city. (8) Quaternary silty slope deposits, located in particular near the mountainous area of Djebel Ouahch and North of Zaouche.

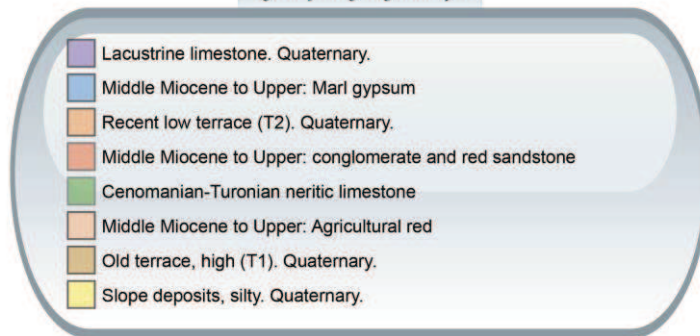
Field investigations and geological map of Bougdal (2007) indicate that landslides are associated to 4 types of geological structures: a) Miocene unit with gray marl and red clays, b) Mio-Pliocene intercalated clays in conglomerates, c) Cretaceous marly limestone (nappe complex), and d) river embankments. Fissures, ruptures and tilted houses are observed at different landslide locations in the Constantine city area. In his detailed account of surface deformation, Bougdal (2007) reports 0.5 to 1 m vertical offset on a 200 m-long rupture in the Boudraa landslide area. Landslides and related surface deformation are clearly related to Neogene and Quaternary clay and marl units and their water content. Field observations in landslide areas are decisive, but their comprehensive study and understanding of their evolution require the contribution of remote sensing techniques.

The Constantine area being with limited vegetation cover, the geological and geomorphological conditions favor the analysis using SAR interferometry. Hence, the continuous monitoring of surface deformation by remote sensing and using the MT-InSAR techniques become recommendable for the evaluation of landslide hazard in the city.

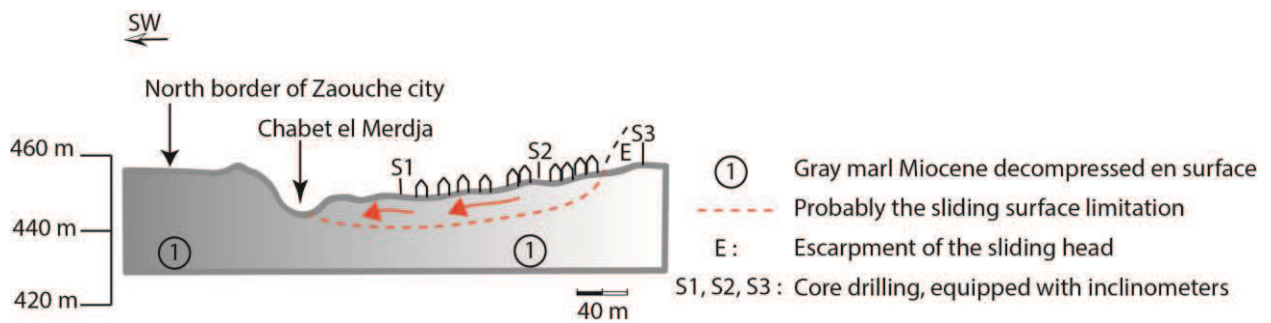
Previous study (Bougdal, 2007) of Constantine landslides was using core drilling equipped with inclinometers to analysis the impact of the geology and the slope for the intensive of slided areas and their characteristics. Figure 4.b shows example of geological cup of Boudraa slide area with the dashed line indicates the probably slided area, according to the slope direction and the geology of the region combined with observation data at field.



legend of the geological map



(a)



(b)

**Figure 4:** (a) Geological map of Constantine (Bougdal, 2007). Eight main geological formations cover the Constantine city and neighboring areas. (b) Geological cup of Boudraa slide area.

## 4. InSAR analyses:

In comparison with other geodetic techniques (conventional triangulation and leveling, GPS), the Synthetic Aperture Radar interferometry (InSAR) is a microwave remote sensing technique that can be used to generate sub-centimeter maps of surface deformation (Hanssen, 2001). However, the decorrelation in the Radar Line Of Sight (LOS) signal due to the topographic, atmospheric and orbital contributions may not be successfully removed using conventional InSAR method based (see also chapter I). The Differential SAR Interferometry (D-InSAR) enables the measurement of surface changes with millimeter accuracy. D-InSAR method also uses two SAR images in the processing of phase signal where the DEM error can be removed using a precise topographic file. Similarly, the orbital error can be also corrected using the orbital precision file. Nevertheless, the atmospheric delay remains complicated to remove, a solution is the use of time series analysis based on the processing of a large number of SAR images (Chapter I).

In our study, the observed landslides in the Constantine city appear to be very active implying important consequences in buildings of the urban area. In order to identify and follow the evolution of the landslide areas, we have used 36 SAR images acquired by ERS-1 and ERS-2 satellites of the European Space Agency (ESA) between 1992 and 2002 in the descending mode, (Track: 480, Frame: 2961; Figure 1). A high coherency of interferogram results is obtained using Gaussian filtering. The raw ERS SAR data were processed with the ROI-PAC software (Rosen et al., 2000), the orbital correction was made using precise orbits obtained from Delft University (Scharoo and Visser, 1998) and the DEM (digital elevation data) topographic contribution is removed using SRTM 3 arc-second (~90 m resolution; Farr and Kobrick, 1998).

As a first step for the analysis of surface deformation, I use PS-InSAR based on the same one master in the calculation of all interferograms. The choice of the master image is based on minimizing the perpendicular, Doppler and temporal baselines (Hooper et al., 2007). Persistent Scatterer (PS) InSAR is an extension to the conventional InSAR techniques, which addresses the problems of signal decorrelation and atmospheric delay (Hooper., 2006; see also Chapter I). Pixels are selected on the basis of their noise characteristics, controlled by the maximum acceptable percentage of selected pixels having random phase. The wrapped phase of the selected pixels is corrected for spatially-uncorrelated look angle (DEM) error. The displacement map is calculated according to the same master SAR image, which minimizes the better the perpendicular, Doppler and temporal baseline, using the PS algorithm incorporated in StaMPS software (Hooper, 2008). The results of the PS method will be approved after data processing

using the The Atmospheric and Orbital Estimation (AOE) and removing this contribution from the final resulting LOS signal.

Figure 5 shows all interferograms obtained for the Constantine area using the PS method, with the same Master SAR image of 08-JUL-1997. The LOS ranges are in the ERS C-band wavelength.

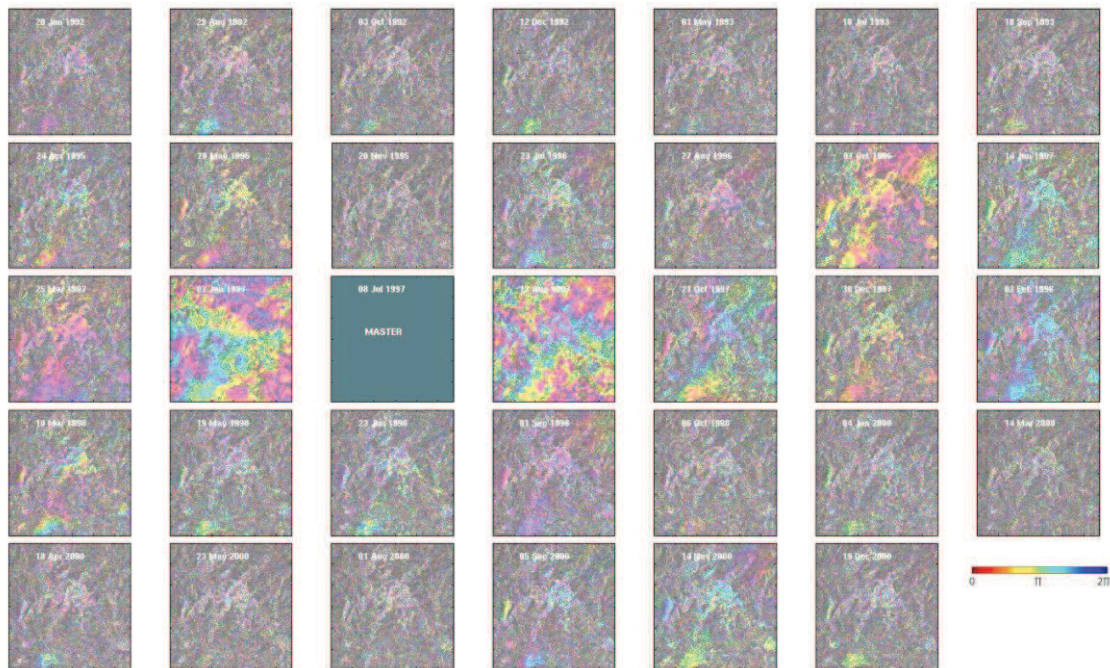


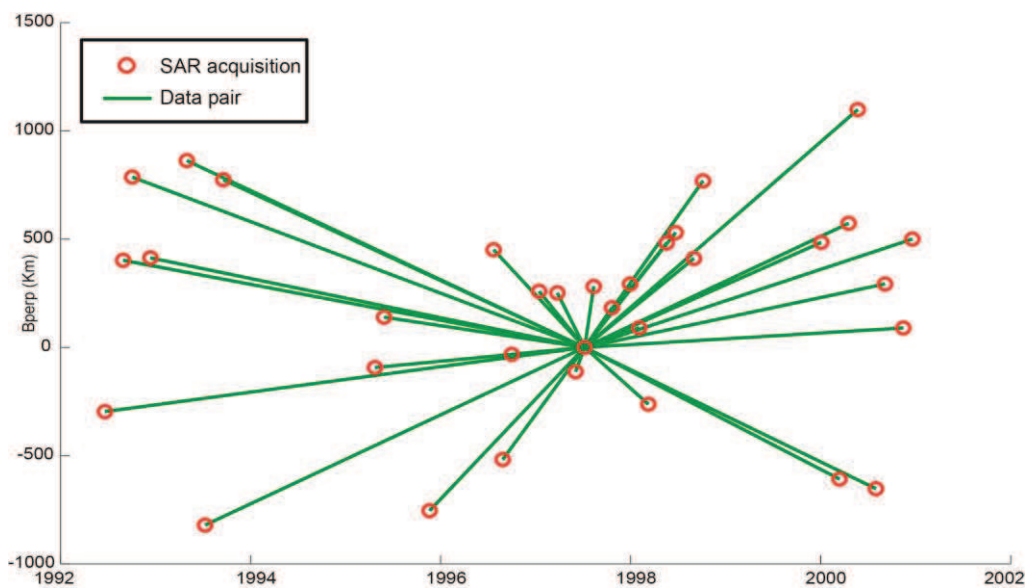
**Figure 4:** The SAR Master image taken on 08-JUL-1997 used to process PS-InSAR. The presented 33 interferograms are from 1992 until 2000. The best coherence interferograms are those of 1997. Each color fringe represents 2.8 cm of displacement in the LOS; the phase of the selected pixels has been filtered using an adaptive phase filter (Goldstein and Werner, 1998).

The PS-InSAR algorithm gives a temporal evolution of the landslide in Constantine over 8 years using a multiple SAR image acquisitions (Figure 6 a). Setting the amplitude dispersion higher in the processing parameter can increase the number of initial PS candidates. The used unwrapping method in processing is the phase unwrapping in three dimensions (Hooper et al., 2007). There is a big concentration of PS pixels in the agglomeration of Constantine due to the high LOS signal and the coherence between the SAR phase images. The Master SAR image is from July season, the land has almost no vegetation cover and the dielectric changes of the pixel characteristics are respected in the selection of the Master SAR image. Figure 6 b gives the mean velocity of surface change from PS-InSAR algorithm, where most permanent scatterer indicates that pixels are moving in the LOS direction (far from the

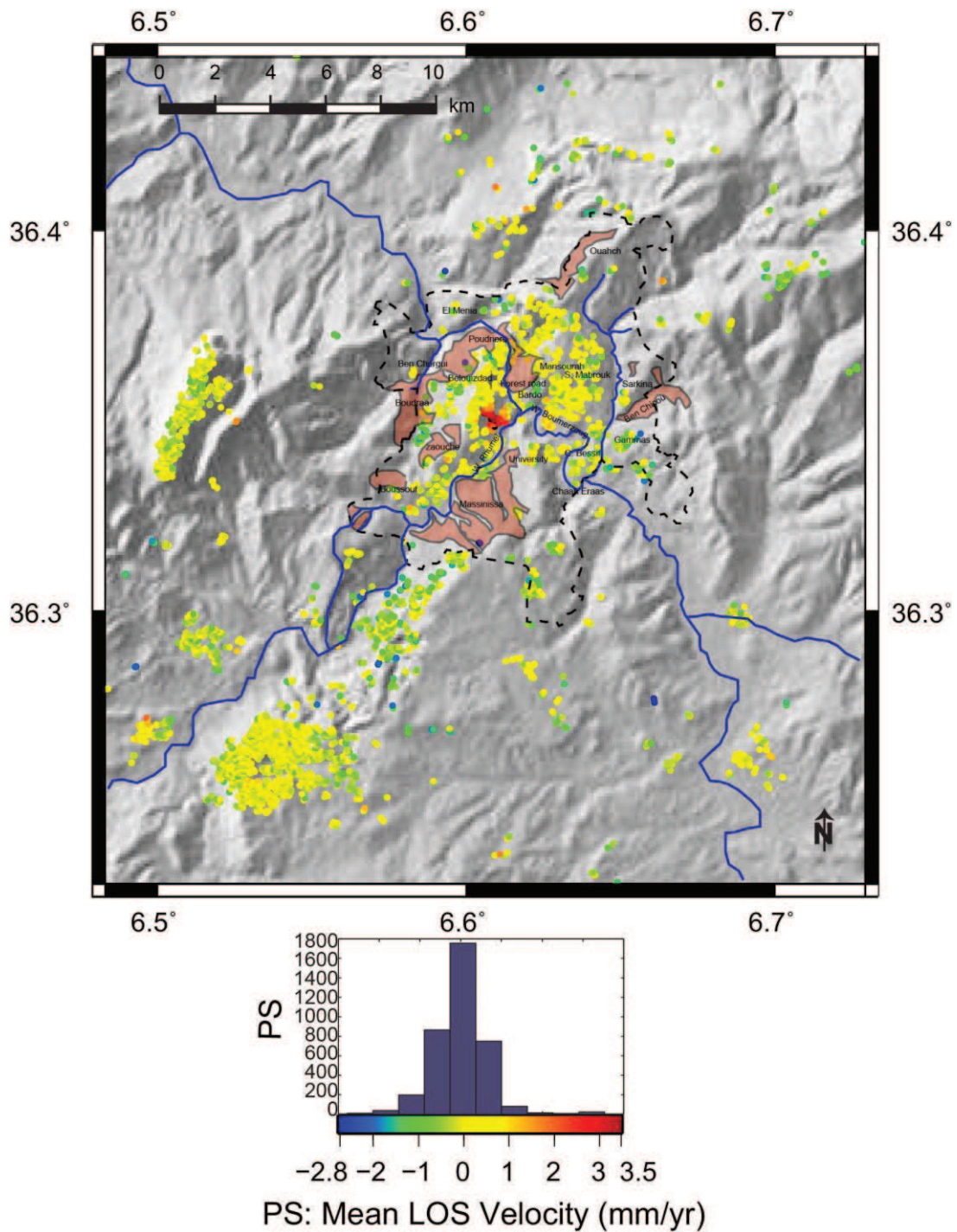
satellite). Hence, the obtained mean LOS velocity of landslide movement ranges from -2.8 to 3.5 mm/yr for total of 6.3 mm/yr.

In a second step of the study, I use the Small Baseline (SB) algorithm of StaMPS software for time series analysis of SAR images. The SB method is based on the calculation of conventional InSAR interferograms from a network of SAR images with small baseline distance (Chapter I). In order to reduce the unwrapping errors, I estimate the spatially correlated look angle (SCLA) due to spatially correlated DEM error and subtract the atmosphere and orbit error (AOE) phase of the master image. The signal decorrelation is minimized by forming interferograms only between images separated by a short time interval and with a small difference in look and squint angle (Figure 7 a).

Figure 7 b shows a map of the mean velocity ranging from -2.8 to 3.5 mm/yr. This result comes to confirm our first result obtained with PS algorithm (-2.8 to 3.5 mm/yr, see above).

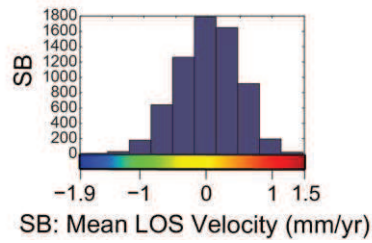
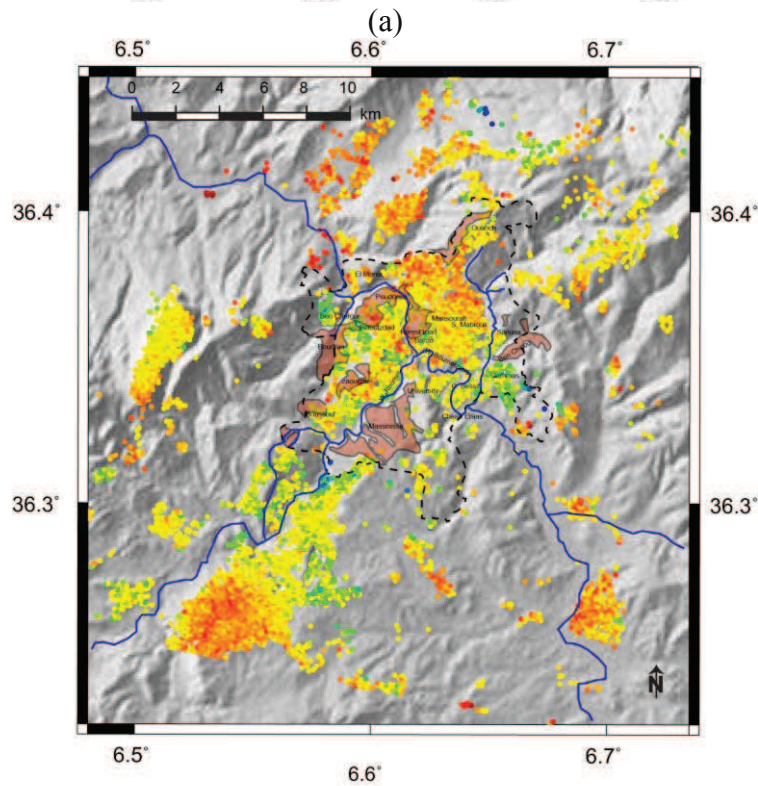
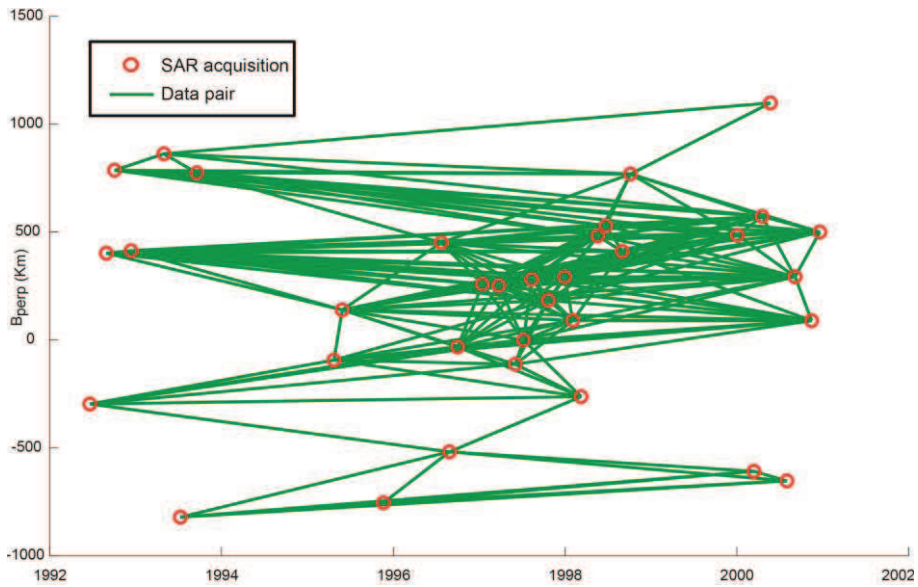


(a)



(b)

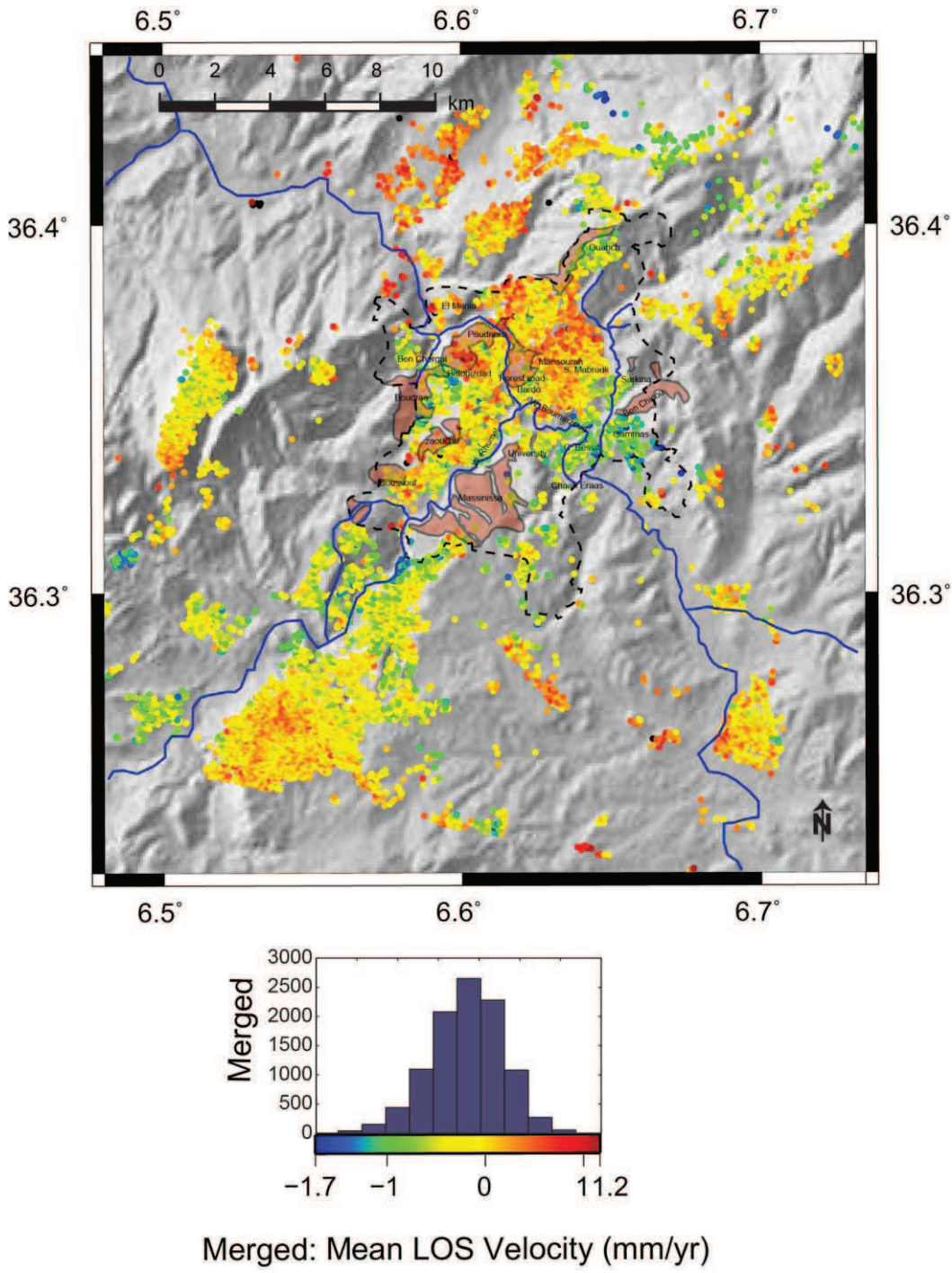
**Figure 5:** (a) The interferometric data pairs selection from PS-InSAR StaMPS method. (b) Mean Velocity map from C-band ERS SAR PS-InSAR results. The most significant Mean velocity is in blue and red colors situated in the Constantine agglomeration (Center of the Map). The mean velocity map ranges (-2.8 3.5) mm/yr. The PSs are plotted on topography in shaded relief.



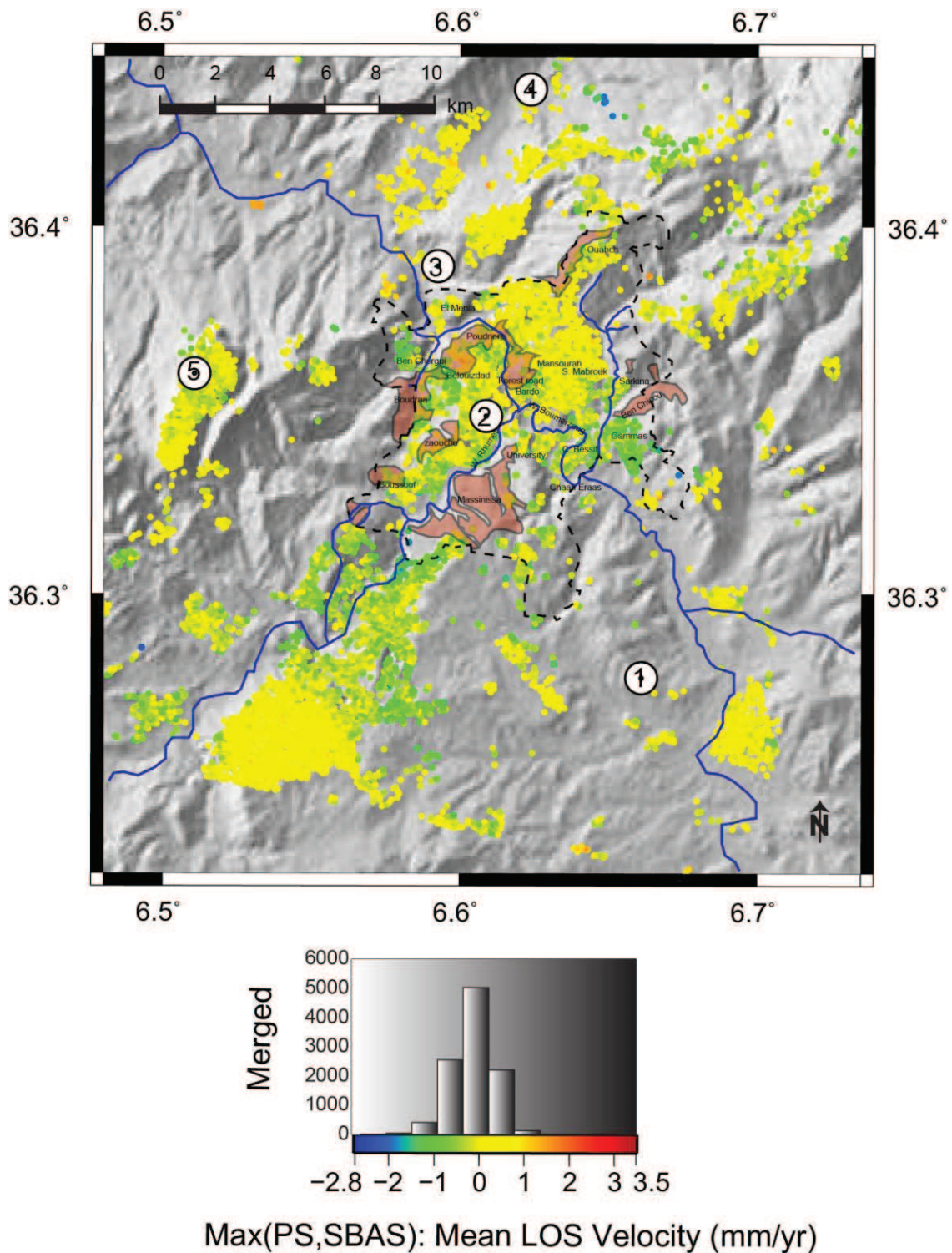
(b)

**Figure 6:** (a) The interferometric pairs selected using SBAS StaMPS method. (b) Mean Velocity map from C-band ERS SAR SBAS results. The most significant Mean velocity is indicated in blue and red colors situated in the Constantine agglomeration (Center of the Map). The mean velocity map ranges (- 1.9 1.5) mm/yr. The SBAS selected Scatterers are plotted on topography in shaded relief. The result is obtained after removing the AOE.

Pixels selected by both PS and SB methods can be combined in the called Merged technique (Figure 8). The result is obtained after removing the AOE.



(a)



(b)

**Figure 7:** (a) StaMPS Merged PS-SBAS results given more coherent signal. The standard merged method obtains results oriented more to SBAS approach. The mean velocity map ranges (- 1.7 1.2) mm/yr.

Map of mean velocity obtained with Merged method (PS+SB) incorporated in StaMPS/MTI, are plotted against the map proposed by (Bougdal, 2007) in order to compare our

results with the results obtained in this study. The result is obtained after removing the AOE. The distribution of the majority of scatterer or in correlation with the non-building area indicated in this study. Some new area has also big velocity value that is located in the center of the agglomeration of Constatine and over Belouizdad, Kitouni, Kaidi, Rhumel and the bridge of Sidi Rached.

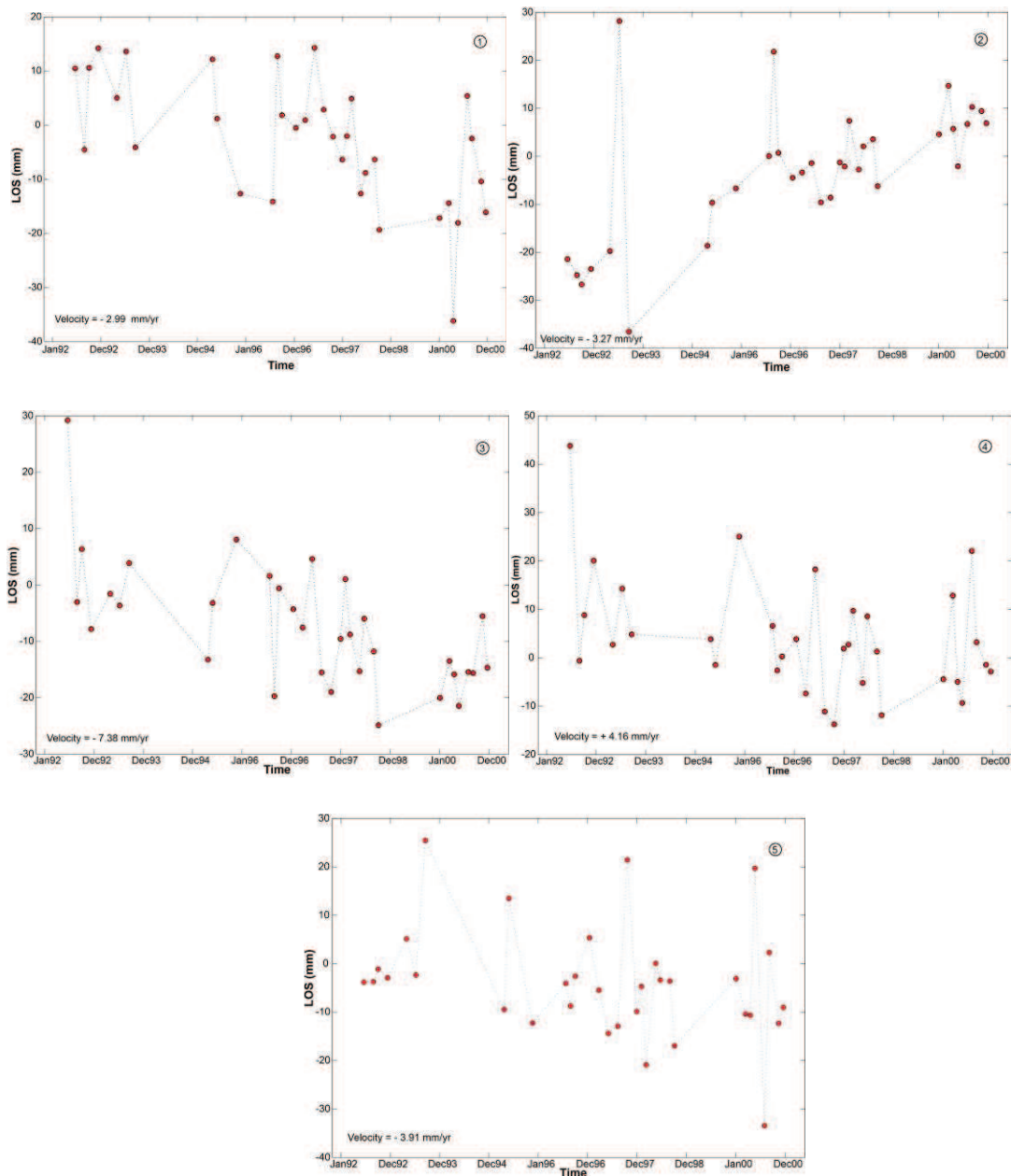


**Figure 8:** Fives time series of InSAR LOS data (red circles) from five selected reflectors shown by numbers in Figure 8b and using my proposed merged method. Except for site 2, most of reflectors indicate a negative surface change (i.e., movement away from satellite).

## 4.1 Surface sliding measurement:

Using three parameters, we can plot the direction and displacement on surface of the sliding pixels, taking into account that for each pixel we can have more than one scatterer. Following the slope direction, the surface displacement quantity is obtained from the maximum merged InSAR results and the look angle for each pixel.

We calculate the slope from the SRTM file of Constantine city (3D topography) with the help of contour file to lead the processing following this formula for each pixel:

A	B	C
D	E	F
G	H	i

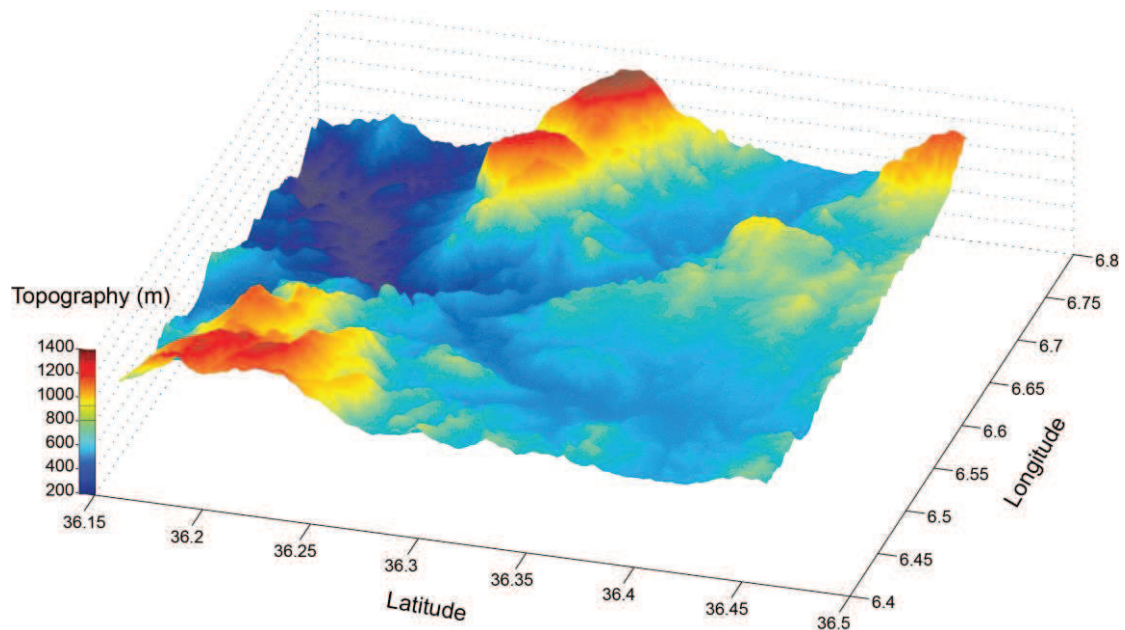
**Table 1:** Eight neighbors of the pixels (e) used to calculate the slope value between them and the pixel (e).

$$\frac{\Delta z}{\Delta x} = \frac{1*(g-a)+2*(h-b)+1*(i-c)}{\sum Sp} \quad (1)$$

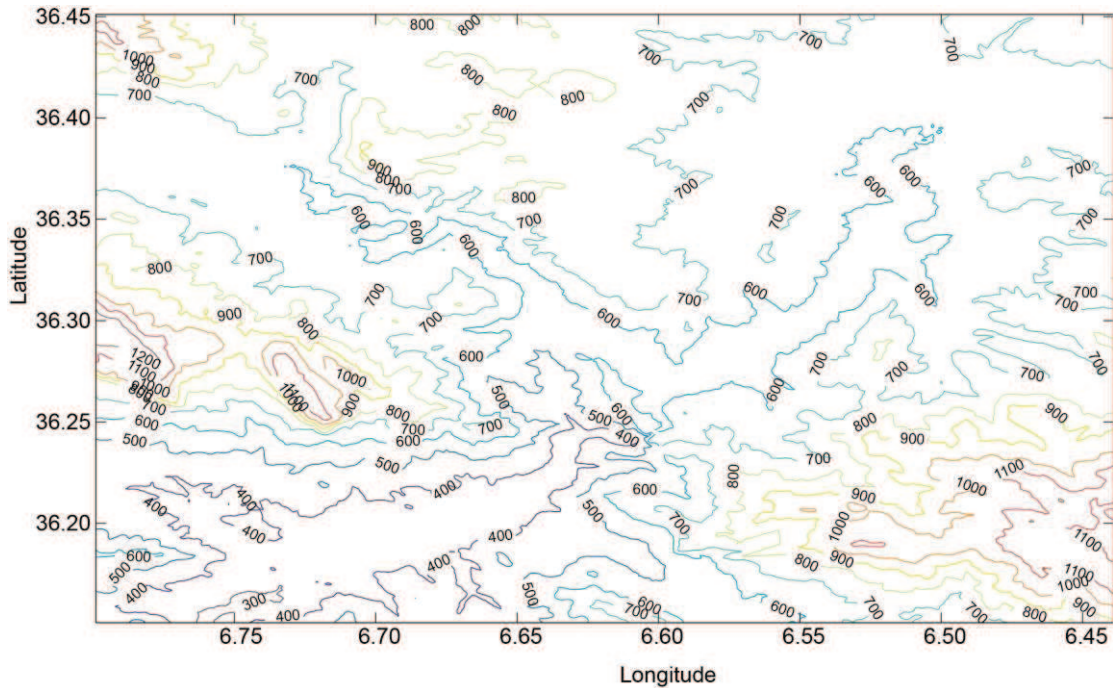
$$\text{WithSp}_{(e,d)} = \frac{\text{abs}(\text{altitude}(e)-\text{altitude}(d))}{\text{abs}(\text{Longitude}(e)-\text{Longitude}(d))} \quad (2)$$

$$\frac{\Delta z}{\Delta y} = \frac{1*(c-a)+2*(f-d)+1*(i-g)}{\sum Sp} \quad (3)$$

$$\text{Slop}_a = \sqrt{\left(\frac{\Delta z}{\Delta x}\right)^2 + \left(\frac{\Delta z}{\Delta y}\right)^2} \quad (4)$$



(a)



(b)

**Figure 9:** (a) 3D view of the SRTM topographic file of Constantine city using Matlab. (b) The contour file helped to calculate the final slope map.

I calculate  $Slop_b$  file by normalizing the contour file [0 1] using:

$$Slop_b = \text{Contour} / \text{Max}(\text{Contour}) \quad (5)$$

The final Slop file obtained with this formula:

$$\text{Slop} = \text{atand}(\sqrt{\text{Slop}_a^2 * \text{Inv}(\text{Slop}_b)}) \quad (6)$$

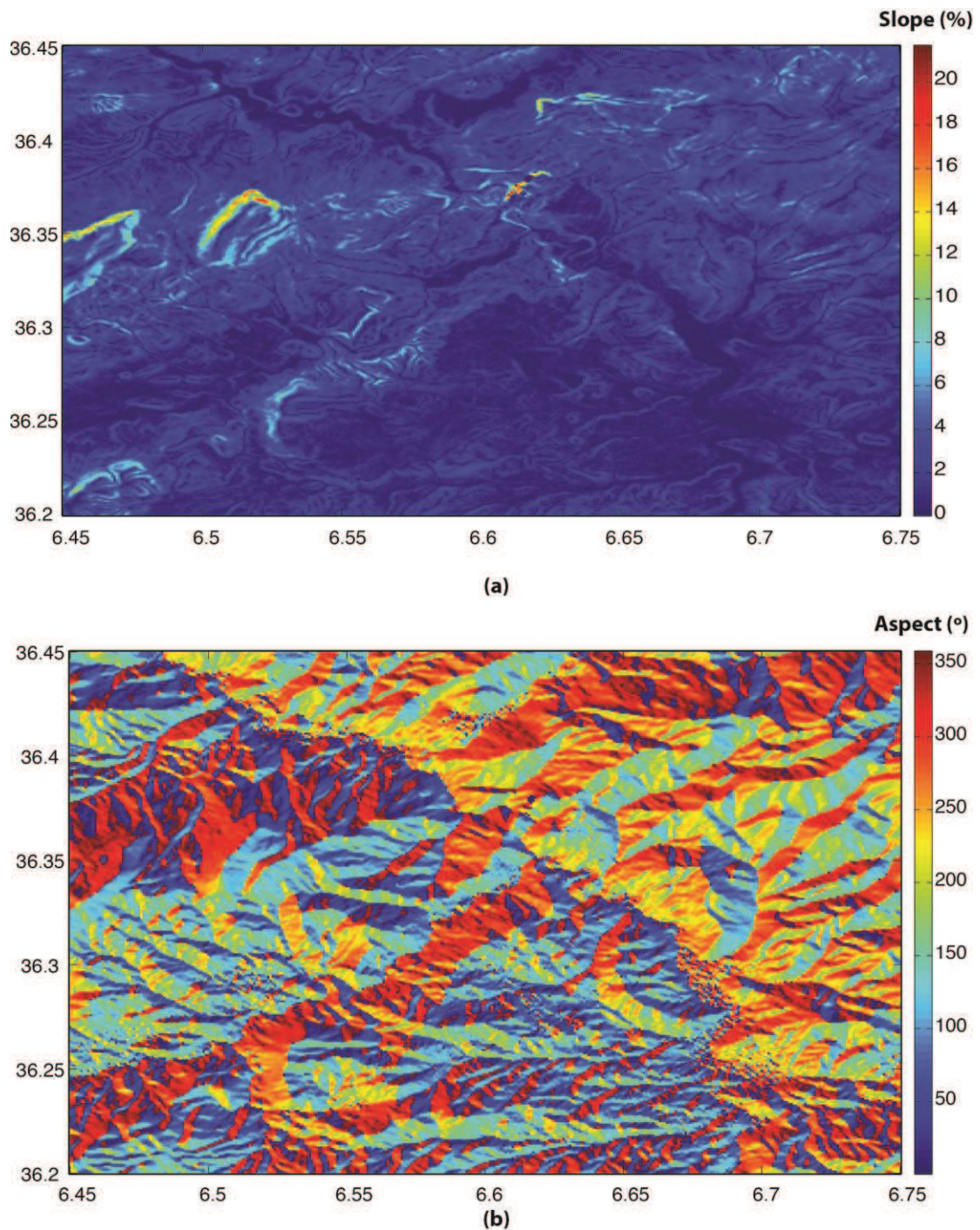


**Figure 10:** (a) The final Slope map of Constantine area is obtained using matlab code from the SRTM 3 arc.sec file and the contour file of the study area. (b) The values of aspect map characterize the horizontal direction to which the slope of topographical units look. Using the slope map with the merged InSAR mean LOS velocity for each pixel according to the satellite look-angle, we calculate the direction and the value of the horizontal pixel movement.

In order to well interpret the landslide movements in the Constantine area as obtained from the MT-InSAR merged method, I use the slope map from the SRTM file (3D topography) and with the help of a contour file processing (Figures 8, 9 and 10).

Look angle changes for each pixel according to the range position. Using the ERS SAR configuration as fellow:

```

pixel_size_range = 12.5; %in m
pixel_size_azimuth = 12.5;%in m
Range_strart = 250000; %in m
Sat_altitude = 785000; %in m
image_range = 100; % in km
imgae_azimuth = 102.5;% in km
pixels_range = 8000; % pixels in range
pixels_azimuth = 8200; % pixels in azimuth
look_angle = zeros(pixels_range,1);
for j = 1:pixels_range
    look_angle(j,1) = atand(((j * pixel_size_range) + Range_strart)/Sat_altitude);
end

```

The positive LOS values indicate that the scatterer is moving in LOS direction (far from Satellite) and the negative LOS values indicate that the scatterer is moving to the satellite position. This information will help to plot the LOS vector of scatterer on ground using the track direction of the satellite and the look angle for each pixel. This projection on the ground of the LOS victor taking anto account the LOS sign have a hemisphere vector solutions in term of direction ( $\pm 180^\circ$  in plan parallel to the track of the satellite; Figure 11a). There is multitude of solutions respecting the sign of LOS in 2D ground plan going from that satellite track  $0^\circ$  to  $\pm 180^\circ$ . We can give one solution assuming that the maximum displacement is in sin of look angle plan and gided by the slope direction and the quantite of displacement on ground is obtained by multiplying the absolue LOS value by sinus of look angle (Figure 11a).

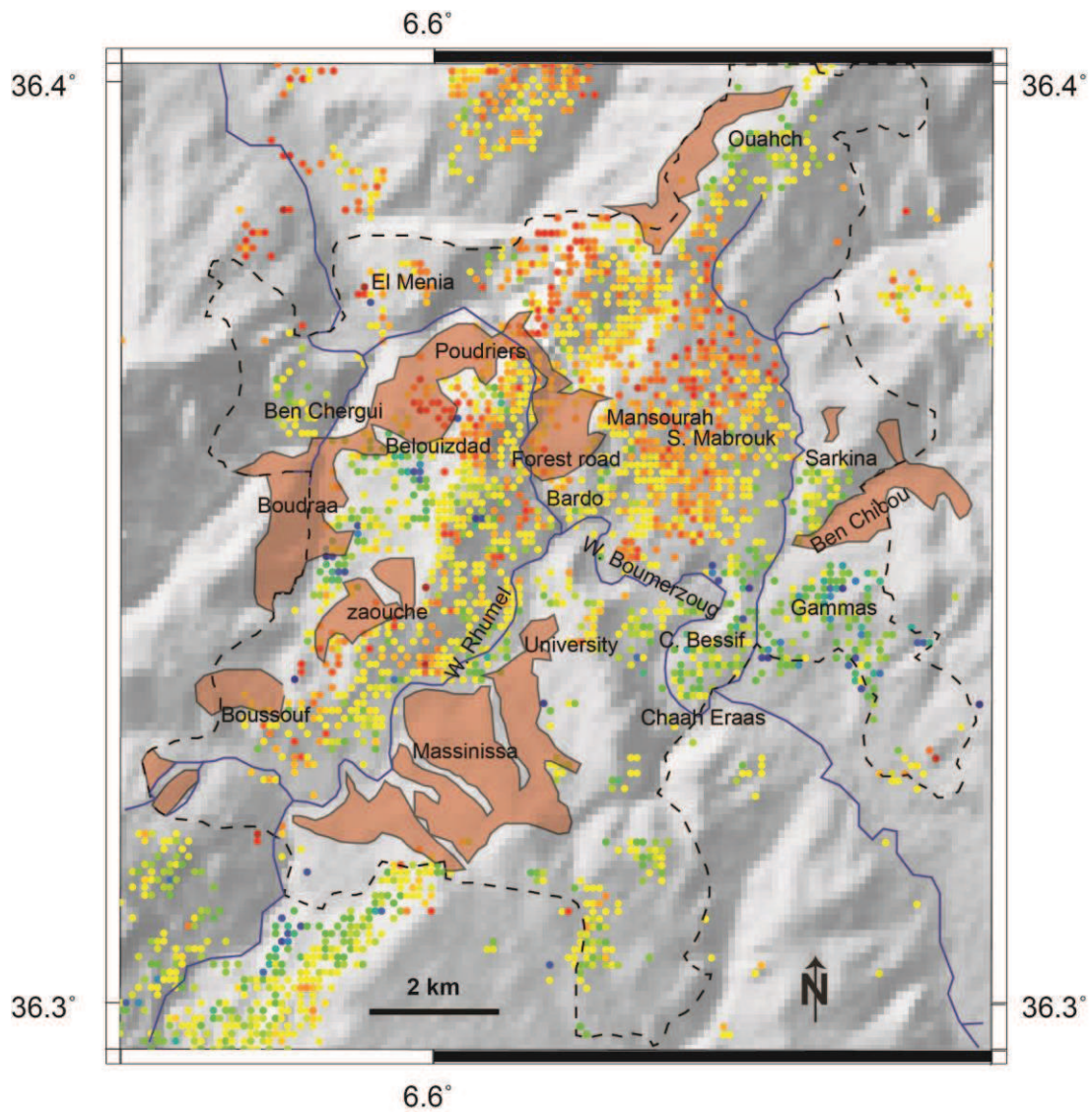
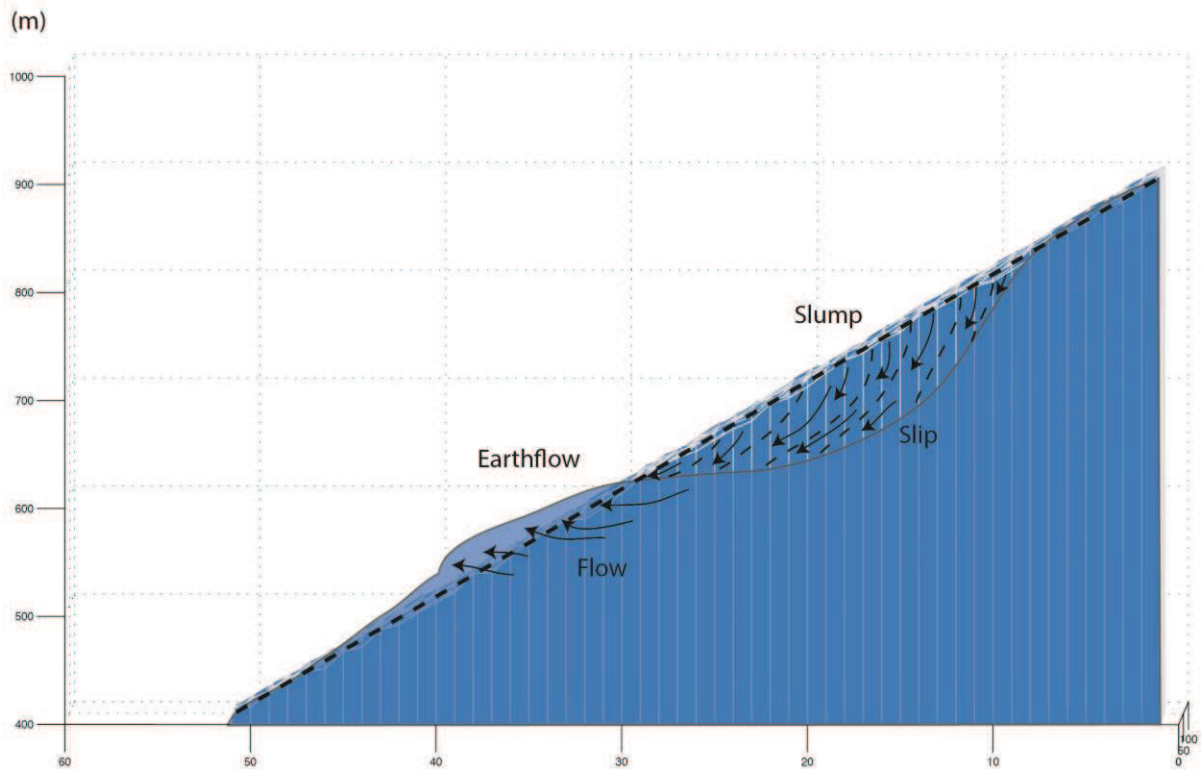
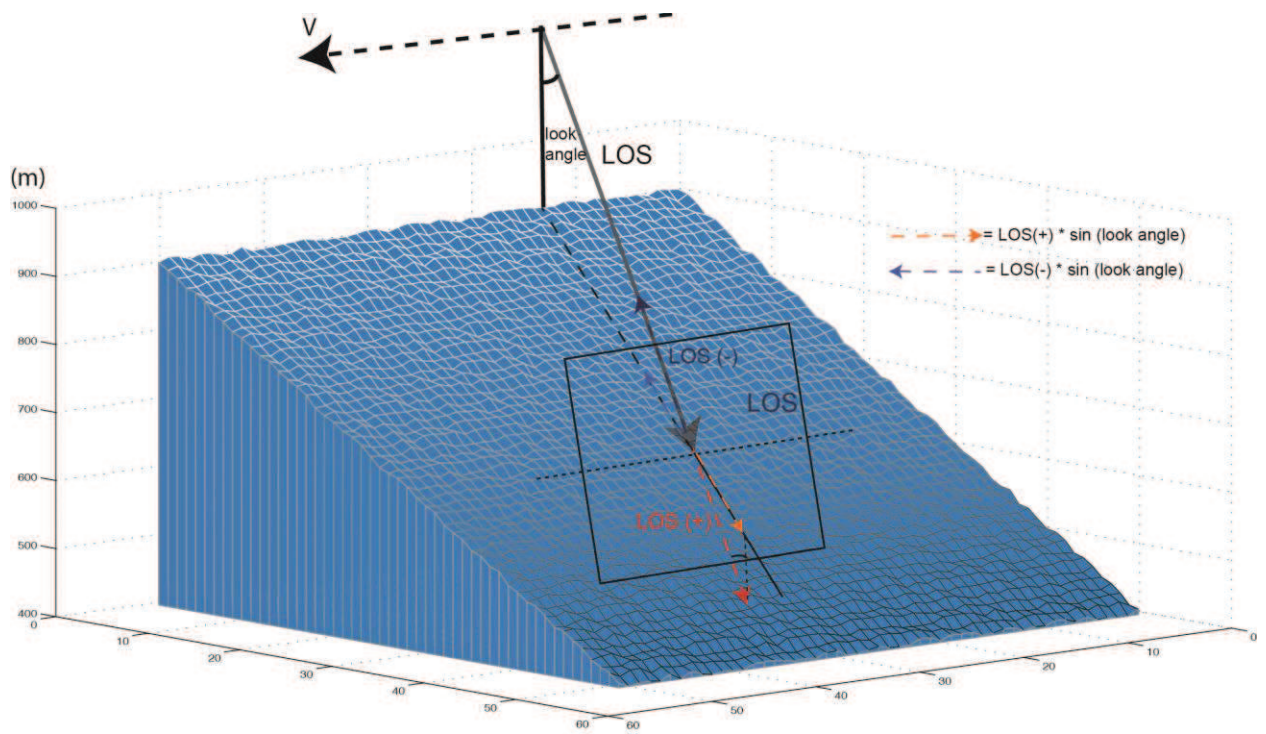
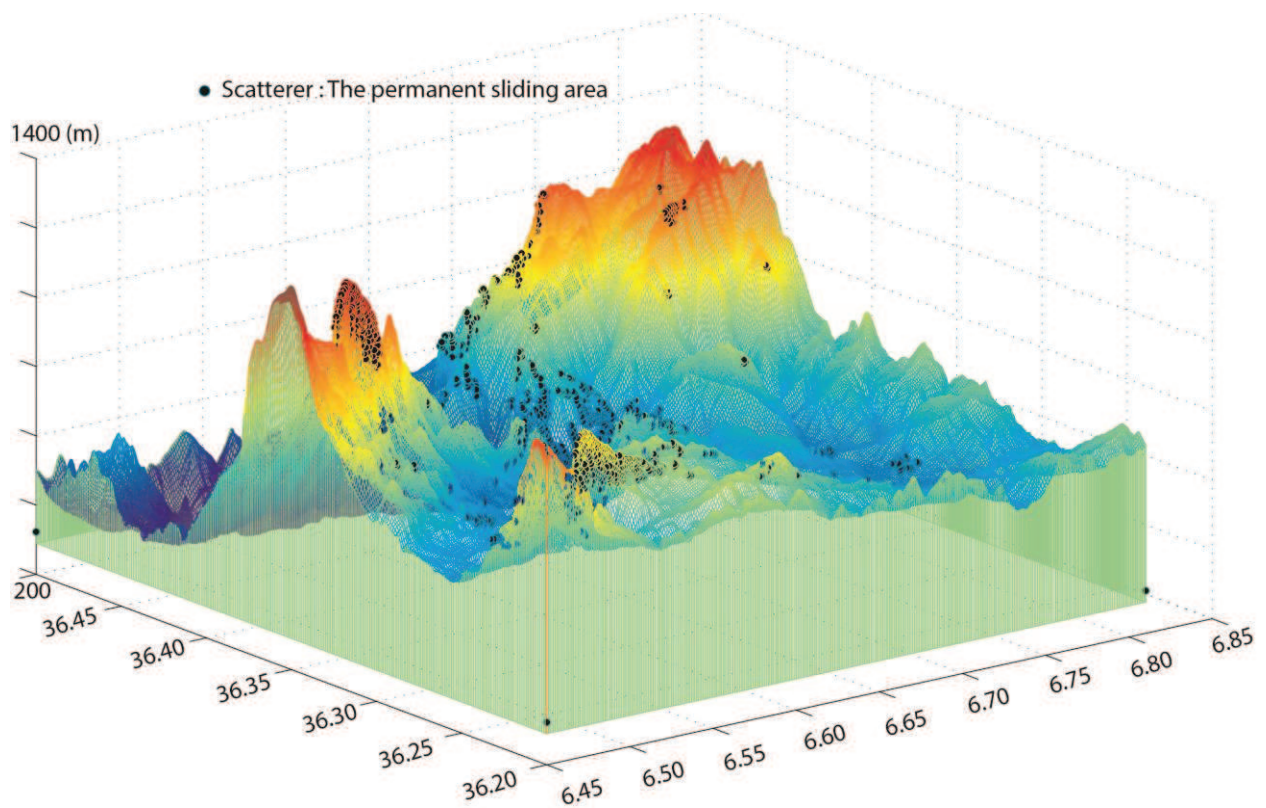


**Figure 11:** Zoom in the merged PS-SB resulting file to show the correspondence between the observed results after (Bougdal et al., 2007) and the results of merged method. The shaded topography is from SRTM 3 arc sec.

We calculate the final landslide horizontal (at the surface) component for each pixel with their direction according to the slope value and the horizontal component of the mean velocity vector (Figure 11b) taking into account the track direction of the satellite (descending) and the horizontal LOS vector value (Figure 11a). We obtain maximum means landslide value at the surface of  $\sim 0.9$  mm/year. We calculate the cumulate surface displacement from the cumulate LOS of eight years of study using the same process used to calculate (Figure 11b), we obtained the maps showing in (Figure 12a and Figure 12b).



(a)



(b)

**Figure 12:** (a) LOS geometric according to their sign and the slope direction with the complex landslide characteristics are used to obtain the slide velocity and direction on ground. (b) Black circle indicates the permanent (according to the permanent scatterer with the studied period) sliding areas obtained with the merged means velocity file that show the distribution of the selected scatterer and the intensity of the landslide in each study area.

The projection of the on the surface is done using the maximum Mean LOS from both of PS and SBAS methods and the slope value for each scatterer of each pixel.

The obtained result is also compared with the active landslide map proposed by Bougdal et al., 2007 (Figure 13). In all cases, the results obtained with InSAR coincide with those of the observations in the field, at the exception, Massinissa area is not totally covered by scatterers which can have explanation that this area is not active anymore. The choice of both of PS and SBAS methods and the merged method (Figure 14) is necessary in this case of study due to the small LOS signal obtained with InSAR and the difficulty in the processing and analysis of such signal especially in an urban area.

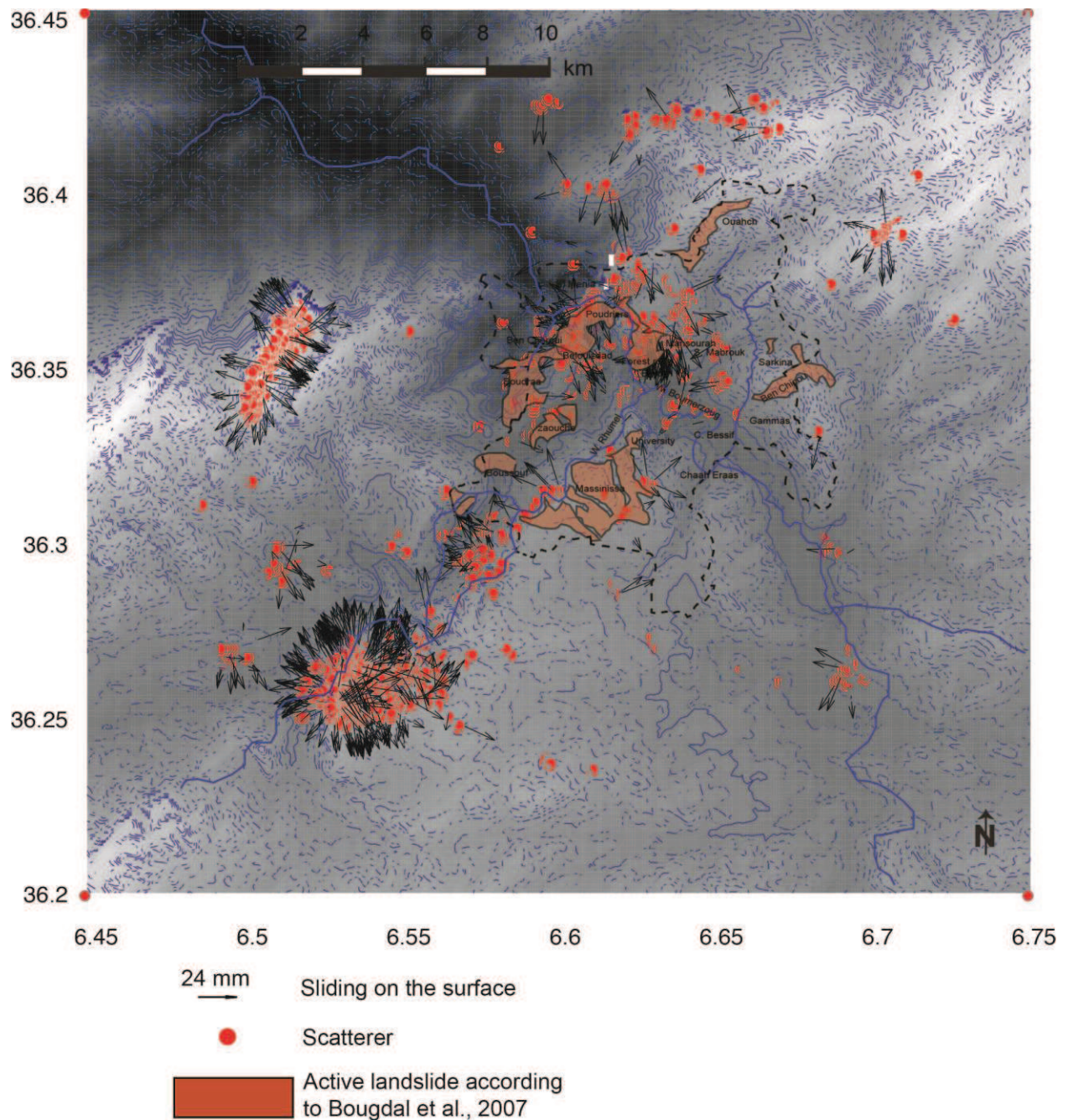


**Figure 13:** (a) The horizontal landslide displacement obtained with the eight years cumulative PS-SB file show the direction and the value of the landslide for each pixel. The red circles indicates the scatterer location, the black arrow indicate the direction and the value of the displacement en the surface following the slope. The red areas are the mapped sliding areas after Bougdal et al., 2007.

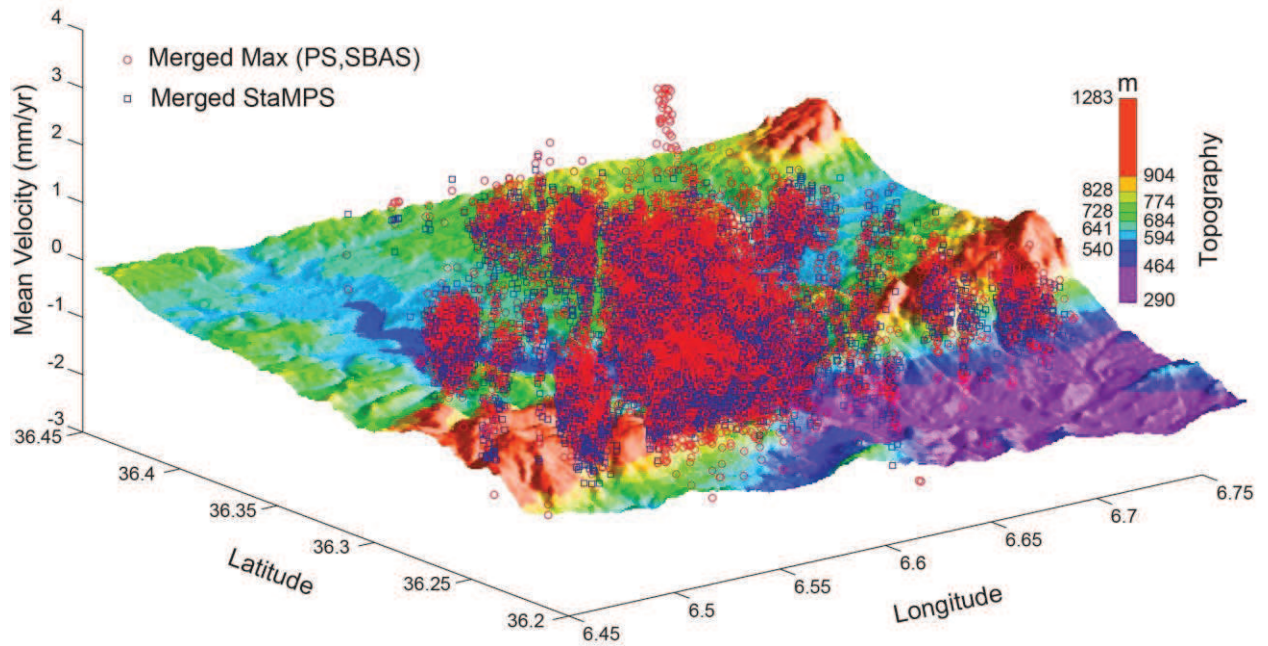


**Figure 14:** Comparing the merged method obtained from MTI-StaMPS software for this study (blue scatterer) and merged method based on the maximum scattering values between PS and SBAS methods (red scatterer) plotted on 3D shaded SRTM 3 arc second topographic file.

## 5. Conclusion

The MT-InSAR method is applied to the Constantine landslides, for 8 years interval, and a time series for the displacement field was retrieved that is consistent with field observations. Our study shows more details in landslide locations accompanied by the mean velocity reaching 6.3 mm/yr and an average cumulative displacement of about 5 cm in 8 years, in the LOS direction. The landslide locations and related surface deformation obtained from the merged PS-SB InSAR method are compared to the field observations and mapping (Bougdal, 2007). Our study highlights the importance of the combined MT-InSAR algorithm in order to estimate the zones of maximum deformation in the urban city of Constantine.

Some differences appear, however, between the MT-InSAR analysis and mapping of surface deformation, and the field mapping provided by Bougdal (2007). As shown in Figures 8 a and b, 12 and 14 a, the Massinissa zone does not show any reflector with displacement. Although the field mapping indicates a clear contour of the landslide area, Bougdal (2007) observe that this landslide shows only slow movement with respect to other areas. The long-term slow movement may explain the absence of surface deformation in the Massinissa zone during the eight years of SAR images (1992 to 2000). However, these differences may also be due to

the time window at which the images are collected and the stability of reflectors. The average cumulative amount of 5 cm in 8 years of surface LOS deformation may appear quite low in comparison of the visible damage in the field. However, landslides may also show areas of maximum displacement next to a zone of minimum deformation in a short distance.

The urban growth of the Constantine city includes large infrastructure projects (highways, extensive building for lodging, public buildings, etc.). It is of utmost importance that the monitoring of landslide hazards by InSAR techniques includes built reflectors that may guarantee the InSAR measurements with regards to the possible fluctuations of landslide movements.

### **Acknowledgement:**

The ERS 1 and 2 images were obtained through the European Space Agency (ESA) C1P-2532 project. Focused SAR images were obtained using the ROI\_PAC software package developed by the Jet Propulsion Laboratory. The interferometric processing was performed using the Doris software package developed by Delft University of Technology. Time series analysis was done using StaMPS software developed by (Hooper., 2008). Most figures were prepared using GMT tools (Wessel and Smith, 1998).

### **References:**

Benaissa A., Cordary D., Giraud A., (1989) Les mouvements de terrain dans la zone urbaine de Constantine (Algérie), Bull. Int. Assoc. Eng. Geol. 40, 85-90.

Benazzouz, M.T., 2002. Les Caractéristiques géomorphologique des glissements de terrain à Constantine (Algérie): Risques et aménagement, In: Proc. Symp. "Geomorphology: From Expert Opinion To Modeling", Strasbourg, France, April 2002, pp. 87-94.

Berardino, P., G. Fornaro, R. Lanari, and E. Sansosti. A new algorithm for surface deformation monitoring based on small baseline differential SAR interferograms, IEEE Trans. Geosci. Remote Sens., 40(11), 2375 – 2383. 2002.

Bougdal, R., Urbanisation et mouvements de versants dans le contexte géologique et géotechnique des bassins néogènes d'Algérie du Nord, Thèse de Doctorat es-Sciences, FSTGAT-USTHB, 194 p, 2007.

Farr, T.G. and Kobrick, M., The Shuttle Radar Topography Mission; a global DEM, Geological Society of America, 1998 annual meeting. Geological Society of America (GSA), Geological Society of America (GSA), 359, 1998.

Ferretti, A., C. Prati, and F. Rocca., (2001) Permanent scatterers in SAR interferometry, *IEEE Trans. Geosci. Remote Sens.* 39(1), 8–20. Goldstein, R. M., and C. L. Werner., (1998) Radar interferogram filtering for geophysical applications, *Geophys. Res. Lett.* 25(21), 4035–4038.

Guemache M. A., Chatelain J. L., Machane D., Benahmed S., Djadia L. (2011). Failure of landslide stabilization measures: The sidi Rached viaduct case (Constantine, Algeria), *Journal of African Earth Sciences* 59, 349-358.

Hooper, A., A multi-temporal InSAR method incorporating both persistent scatterer and small baseline approaches, *Geophys. Res. Lett.*, 35, L16,302, doi:10.1029/2008GL03465, 2008.

Hooper, A., and H. Zebker, Phase unwrapping in three dimensions with application to InSAR time series, *J. Opt. Soc. Amer. A*, 24, 2737–2747, 2007.

Hooper, A. J., Persistent scatterer radar interferometry for crustal deformation studies and modeling of volcanic deformation, Ph.D. thesis, Stanford University, 2006.

Kampes, B. M., R. F Hanssen and Z. Perski., Radar interferometry with public domain tools, In Third International Workshop on ERS SAR Interferometry, 'FRINGE03', Frascati, Italy, 1-5 Dec 2003, page 6 pp., 2003.

Machane, D., Bouhadad, Y., Cheikhounis, G., Chatelain, J.-L., Oubaiche, E.H., Abbes, K., Guillier, B., Bensalem, R., (2008). Examples of geomorphologic and geological hazards in Algeria. *Nat. Hazards* 45, 295–308.

Nikolaeva, E. and Walter, T. R. (2012) Comparison of InSAR two-pass and time series methods for analyzing landslides in central Georgia, Caucasus. *Geoscience and Remote Sensing Symposium (IGARSS), 2012 IEEE International*.7573 – 7576. doi: 10.1109/IGARSS.2012.6351909

Rosen, P. A., S. Henley, G. Peltzer, and M. Simons, Updated Repeat Orbit Interferometry Package Released, *Eos Trans. AGU*, 85(5), 47.2004.

Riedel, B. and Walther, A. (2008) InSAR processing for the recognition of landslides. *Adv. Geosci.*, 14, 189–194.

Sidle, R. C. and Ochiai, H., (2006) *Landslides- Processes, Prediction and Land Use*, AGU Books Board, Washington, 312 pp.,.

Singhroy V., Coutre R., Alasset P.-J. and Poncos V. (2007). InSAR monitoring of landslides on permafrost terrain in Canada, *Proc. IGARSS*, pp.2451 -2454.

Wessel, P. and Smith, H.F., 1998, New, improved version of the Generic Mapping Tools Released, *EOS Trans. AGU*, 79, 579.

Yueping Y., Wamo Z., Yuping L., Jialong Z., Xiaochun L. (2010) Integration of GPS with InSAR to monitoringof the Jiaju landslide in Sichuan, China. *Landslides*.7:359–365 DOI 10.1007/s10346-010-0225-9.

## **Chapter IV:**

# **Postseismic (Interseismic) Deformation in the El Asnam Fault Region (Algeria): Results From Merged PS-InSAR and Small Baseline Methods**



## Summary

We investigate the surface displacement along the 36-km-long and NE trending El-Asnam thrust fault (NW Algeria) responsible of two large earthquakes (Ms 6.7 in 1954 and Ms 7.3 in 1980) using Stamps/MTI advanced time series analysis of C-band ERS SAR images acquired between 1997 and 2000. Previous leveling measurements of geodetic benchmarks conducted from 1986 to 1991 show a significant post seismic deformation with  $5.1 \pm 1.9$  mm/yr uplift rate and  $9.6 \pm 1.4$  mm/yr slip rate of the northwestern block (Lammali et al., 1997; Bezzeghoud et al., 1995). The processed 9 SAR images (ERS1 and ERS2) are based on the combination of PS-SB methods using Stamps, the 3-arc/sec SRTM topographic data, and filtering in order to remove topographic contribution, atmospheric delay and control the Doppler centroid difference. The semi-arid landscape of the El Asnam (nowadays Chlef) region provides favorable image coherency for interferometric SAR processing. The application of Persistent Scatterer (PS) and Small baseline (SB) InSAR approaches reveal significant surface changes across the fault zone. Five NW-SE trending profiles across the fault zone are plotted to compare the cumulative LOS displacement on both sides of the fault. In all cases, the fault is located at zero-LOS value separating the tow blocks, the uplifted (positives LOS) area from the subsided area (negative LOS). The earthquake fault area limits two distinct zones, with LOS values reaching 30.4 mm cumulative displacement corresponding to 16.2 mm (uplift) on the hanging block and -14.2 mm (subsidence) on the footwall block. We then extract the vertical and horizontal components (uplift and NNW-SSE shortening) from the LOS and obtain 0.6 mm/yr and 0.4 mm/yr, respectively.



# 1. Introduction:

Spatial techniques provide very powerful tools in the study of surface deformation on the long and short-term basis. Interferometry radar (InSAR) is one of the used spatial methods because of its ability to acquire data independently of the daylight (active captor) or the weather condition. InSAR produces and uses the wave to illuminate and detect a remote object. In this chapter, I study the postseismic and interseismic surface deformation along the NE trending, 36-km-long El-Asnam (NW Algeria) thrust fault responsible of two large earthquakes (Figure 1). The first earthquake was in 1954 (Ms 6.7) and the second was in 1980 (Ms 7.3) as among the largest events that occurred along the North Africa plate boundary.

33 years after the second earthquake of 1980, this study aims to detect and measure the existence of postseismic displacement using advanced InSAR processing methods from 9 C-band SAR images (ERS1 and ERS2) acquired between 1997 and 2000. One of the assumptions of a significant postseismic deformation is that the fault is still active and the fault strains are accumulating since 33 years. One may also note that the interseismic period between the first large event of 1954 and the second of 1980 is 26 years in comparison with the 33 years post-1980 period, helping to understand and predict the characteristics of the seismic cycle in the El Asnam area.

Several field studies of the 1980 El Asnam earthquake were performed in order to document the 36-km-long surface faulting and related reverse (thrust) rupture offsets with an average 2.5 m vertical slip on three fault segments (Figure 2; Yielding et al., 1981; Philip and Meghraoui, 1983). Ruegg et al., (1982) did geodetic measurements of the vertical and horizontal movements by the combination of geodetic network and a leveling profile (along the railway crossing the fault) 8 months after the El Asnam earthquake. With the leveling method they obtain ~ 5 m uplift in the northwestern block of the fault, 1 m of depression in the SE and ~ 2.5 m shortening. Bezzeghoud et al., (1995) observe from historical levelling data a significant 1.34 m vertical uplift from a leveling line on the NE fault segment. They also recalculate the faulting mechanism of both 1954 and 1980 earthquakes at El Asnam by modeling their associated vertical movement, which suggest two different but parallel faults for the 1954, and the 1980 seismic events.

Furthermore, a continuous measurement of leveling lines across the fault was also performed from 1986 to 1991 showing a significant postseismic  $5.1 \pm 1.9$  mm/yr uplift of the northwestern fault block, with a relatively stable southeastern block (Dimitrov et al., 1987; Lammali et al., 1997). An even larger postseismic deformation with  $9.6 \pm 1.4$  mm/yr slip rate is inferred by the authors for the northeast fault section (Lammali et al., 1997).

Spatial geodesy and especially the InSAR techniques have been successfully used to study the surface deformation associated with earthquakes worldwide (Massonet and Feigl, 1998; Wright et al., 2003; Sudhaus et al., 2009). In Algeria, Belabbes (2008) did the first comprehensive InSAR analyses using ERS (1 and 2), Envisat and Radarsat images applied to three major earthquake areas (1994 Mascara – Mw 5.7, 1999 Ain Temouchent – Mw 5.7, and 2003 Zemmouri – Mw 6.8). He also proposed the modeling of surface deformation associated with the large 1980 El Asnam earthquake, accompanied by a simulation of InSAR fringes indicating an uplift reaching the Mediterranean coastline.

In chapter 2, I presented the advantages of the new InSAR methods called time series analysis, and their ability to remove the signal artifacts. The merged PS-SBAS method (Hooper., 2008) is here applied to study and detect the El Asnam postseismic deformation given the best signal/noise ration and increases of the InSAR signal correlation. An inversion model based on the cumulative postseismic deformation detected by the merged InSAR method is proposed taking into account the El Asnam fault ruptures parameters as in Philip and Meghraoui (1983) coseismic and postseismic uplift along the 36-km-long fault rupture (Ruegg et al., 1982; Lammali et al., 1997).

## **2. Tectonic setting:**

The El Asnam (Algeria) earthquake of 10/10/1980 ( $M_s = 7.3$ ) occurred in the Chelif Basin of the Tell Atlas of Algeria, inducing NE-SW and E-W trending, 36-km-long of coseismic reverse faulting visible at the surface (Figure 1; Philip et Meghraoui, 1983). The Tell Atlas Mountains experienced several large reverse and thrust earthquakes (e. g., the 2003 Zemmouri earthquake) as attested by the focal (CMT) mechanisms shown in Figure 1. The 1980 earthquake destroyed the city of El-Asnam that was already severely affected by 1954 earthquake  $M_s 6.7$ . The prominent earthquake activity in northern Algeria is related to the convergent movement (at  $\sim 4$  to  $5$  mm/yr) of Africa towards Eurasia (Nocquet and Calais 2004; Serpelloni et al. 2007).

The 1980 coseismic surface ruptures at El Asnam revealed complex reverse faulting with sometimes thrust geometry and secondary normal faulting on a significantly folded hanging block (Yielding et al., 1981; Philip and Meghraoui, 1983). Detailed mapping of surface ruptures revealed about 6 m vertical slip along the railway line crossing the fault with an average 2.5 m uplift, and a maximum 1.5 m left-lateral slip and 2.1 m shortening as coseismic deformation (Ouyed et al., 1981; Philip and Meghraoui, 1983). These measurements were confirmed by the

maximum 6 m uplift obtained from the leveling line survey (Ruegg et al., 1982) and the total station survey of coseismic slip along the fault zone (Meghraoui and Doumaz, 1996).

The Chelif basin includes other parallel and comparable seismogenic faults and among them the Ténés-Abou El Hassan reverse fault responsible of the 1922 large earthquake (Mw 6.0; Aoudia and Meghraoui, 1995) and the Bou Kadir prominent fault scarp crossing the Chelif Basin (Meghraoui, 1988). The tectonic characteristics of these faults indicate a consistent NNW-SSE contraction movement during the late Quaternary with active folding.

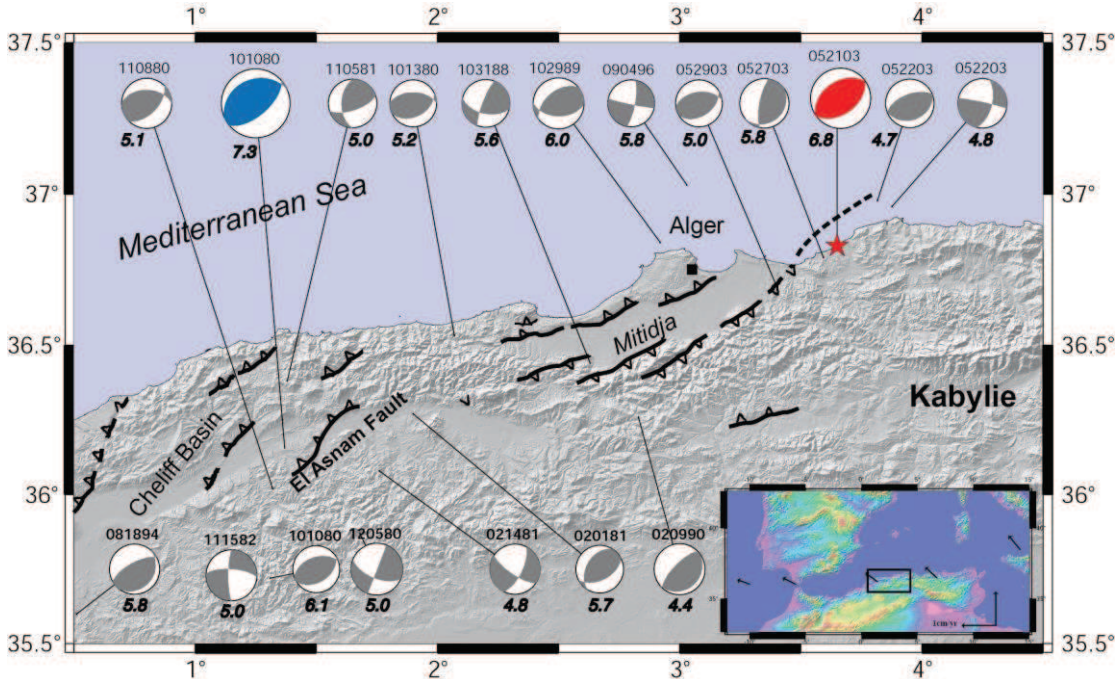


**Figure 1:** Seismotectonic setting of NW Algeria (Meghraoui, 1988). The El Asnam (Algeria) earthquake of 10/10/1980 ( $M_s = 7.3$ , blue CMT mechanism) occurred in the western Mediterranean, inducing NE-SW and E-W trending, 36-km-long of coseismic reverse faulting visible at the surface (Philip et Meghraoui, 1983). The red mechanism is the 2003 Zemmouri earthquake.



**Figure 2:** The El Asnam 10 October 1980 (Mw 7.3) surface rupture and ~ 5 m uplift on the flexural-slip faulting at the Sara El Maarouf region (Philip & Meghraoui, 1983).

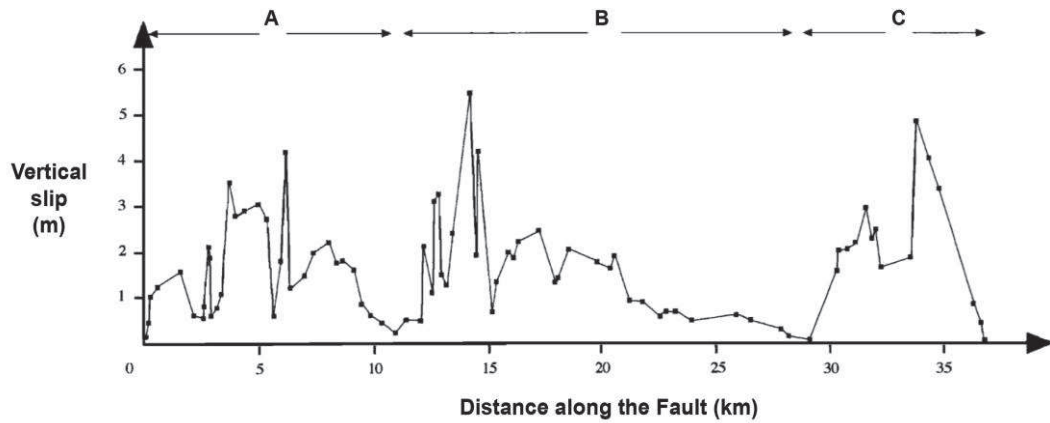


**Figure 3:** Vertical coseismic displacements in 1980 measured along El-Asnam fault with three segments A, B and C (Meghraoui et Doumaz., 1996).

### 3. InSAR Analyses:

We use conventional InSAR (Massonet et al., 1993) to detect significant surface changes across the fault zone. We produce 7 interferograms using ROI-PAC (Rosen et al., 2004). In addition, we apply DInSAR to refine the phase signal changes, use SRTM 3 arc-sec data to remove the topographic contribution from the resulting interferograms, and also the Delft ODR data from the Delft Institute for Earth-Oriented Space research (DEOS) for the orbital correction (Scharroo et al., 1998).

The figure 4 shows the interferograms with surface changes in cm ranging  $[-\lambda/2 \ \lambda/2]$  (ERS  $\lambda/2 = 2.83$  cm) between 1997 and 2000. The master SAR used to produce all the interferograms is 13-09-1998. Decorrelations due to atmospheric, orbital and topography errors are present in all the interferograms, except interferogram number 3 computed from the left (Figure 4) produced with 31-05-1998 (three months, the same season) we obtain a good correlation. To explain these results, knowing that between May and September the vegetation is the same. However, the change in the dialectical characteristics of the pixel after the first SAR image taken (first pass) is due to change in the vegetation cover including presence of water. In order to solve this problem (decorrelation), we choose to apply Multi-temporelle InSAR processing. The second generation on InSAR processing is called time series analysis. Focus on the correctoin of erros and decorrelation problems especially the temporal and geometric effects.

Both of Persistent Scatterer (PS) (Ferretti et al., 2001) and Small Baseline (SBAS) (Berardino et al., 2004) approaches of InSAR time series analysis were applied in this study. Figure 5, present both of PS connected SAR pairs Slave-Master (The same master for all

slaves) and SB (network) connection between the different SAR pairs. Circles indicate the SAR images, and the lines (connection between them) indicate the calculated interferogram. In addition, Using StaMPS (Hooper, 2008) a merged method for PS-SB is proposed. We use all the three methods, however we are interested in the merged method because it provides the best correlation and the biggest signal/noise ratio taking the advantages of both of PS and SB approaches.

The InSAR time series analysis shows that the El Asnam fault represents a major limit between two main tectonic blocks experiencing uplift to the NW and subsidence to the SE in the Tell Atlas of Algeria (Figure 6 and Figure 7). Figure 6 presents the mean LOS velocity in mm/yr obtained with the merged method reaching -14.3 mm/yr in the subsided block and +18.5 mm/yr in the uplifted block (Figure 6). In figure 6, we can see also the delimitation of the two blocks is indicated by the El Asnam fault location (zero LOS displacement).

Figure 7, is obtained according to a threshold used to classify the pixels into one of the two blocks according to their velocity value sign (i.e.: + with uplift block and - with subsided block). Subsided block (blue color) is situated in the right side of the fault and the uplifted block (red color) occupies the left part (the two fault compartment).

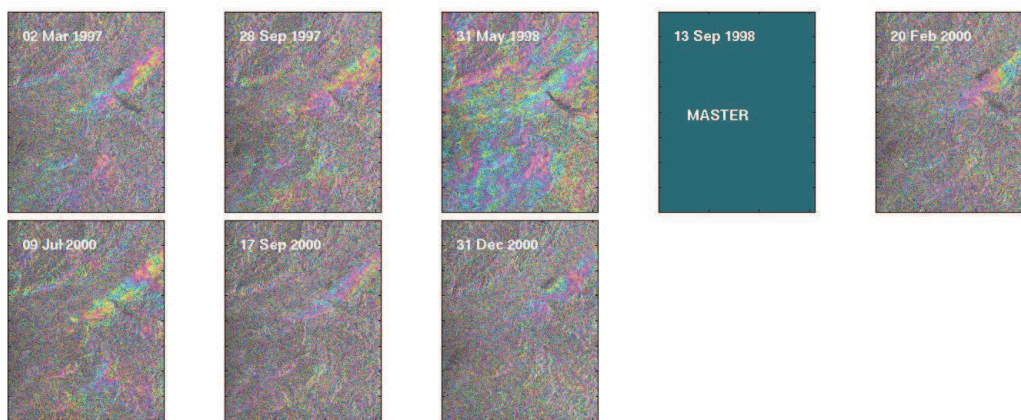


**Figure 4:** Conventional InSAR results produced using the 8 descending SAR images (one of 9 SAR images is not exploitable to measure the interferograms). We can clearly see that the biggest parts of these interferograms have a low signal/noise ratio. This is visible in the interferograms as decorrelations. In exception the third interferogram shows good correlation. Each color cycle ( $2\pi$ ) represents 2.83 cm.

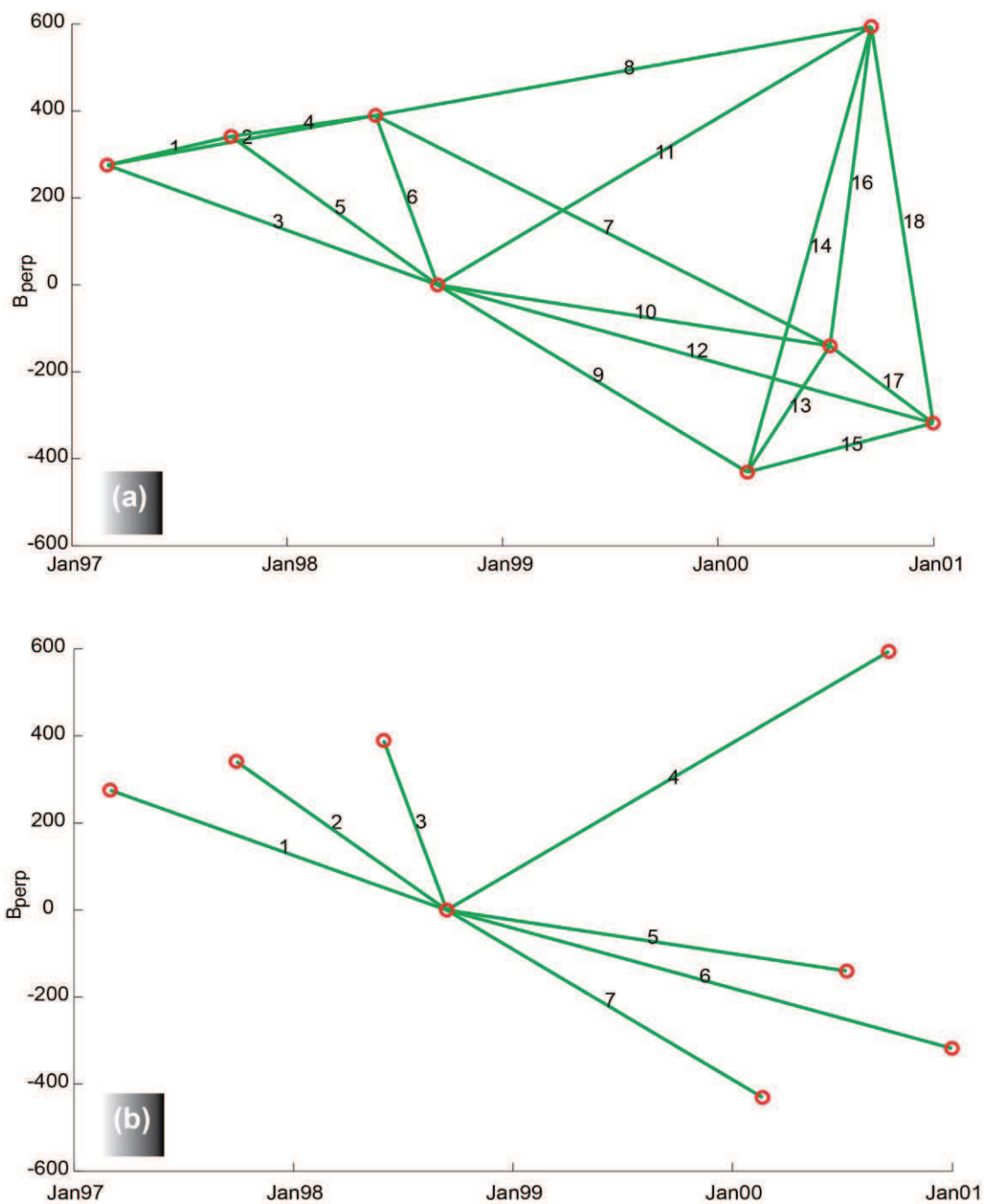


**Figure 5:** Both of Persistent scatterer and Small baseline methods used in this study. (a) The SB InSAR network used to calculate the interferograms for each SAR pairs (in red circles), the lines indicate the InSAR calculated between the tow connected SAR images. (b) The same Master SAR image used to calculate the differential interferograms is shown as the SAR image connected to all other SAR Slaves.

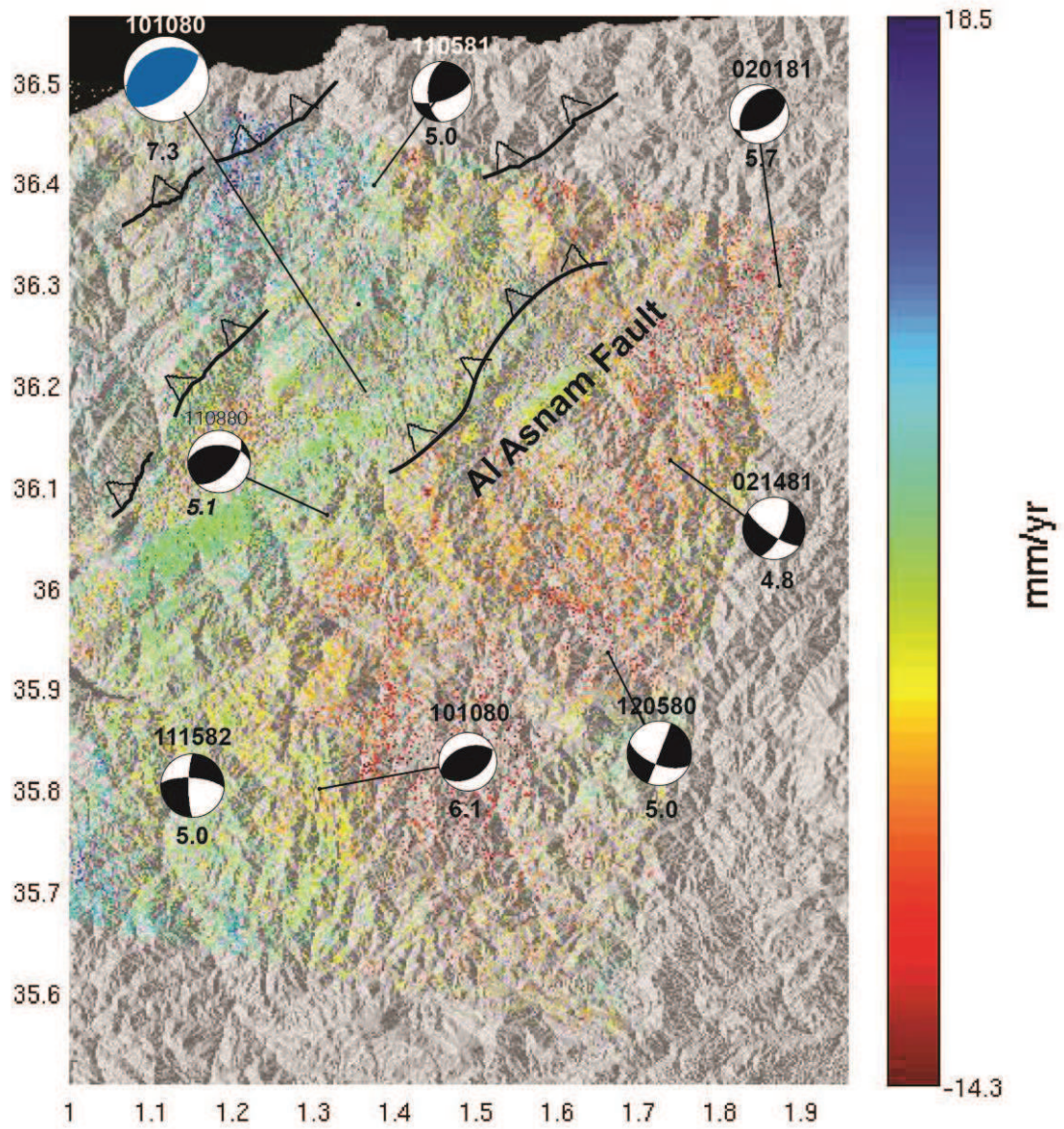


**Figure 6:** Mean velocity (mm/yr) obtained with the merged method of PS-SB showing that El Asnam fault (Mw 7.3; Bleu focal mechanism) separating two tectonic blocs showing is red (negative values) and blue (positive values) color indicates the velocity in mm/yr according to each scatterer direction in LOS. The focal mechanisms are from CMT catalogue.

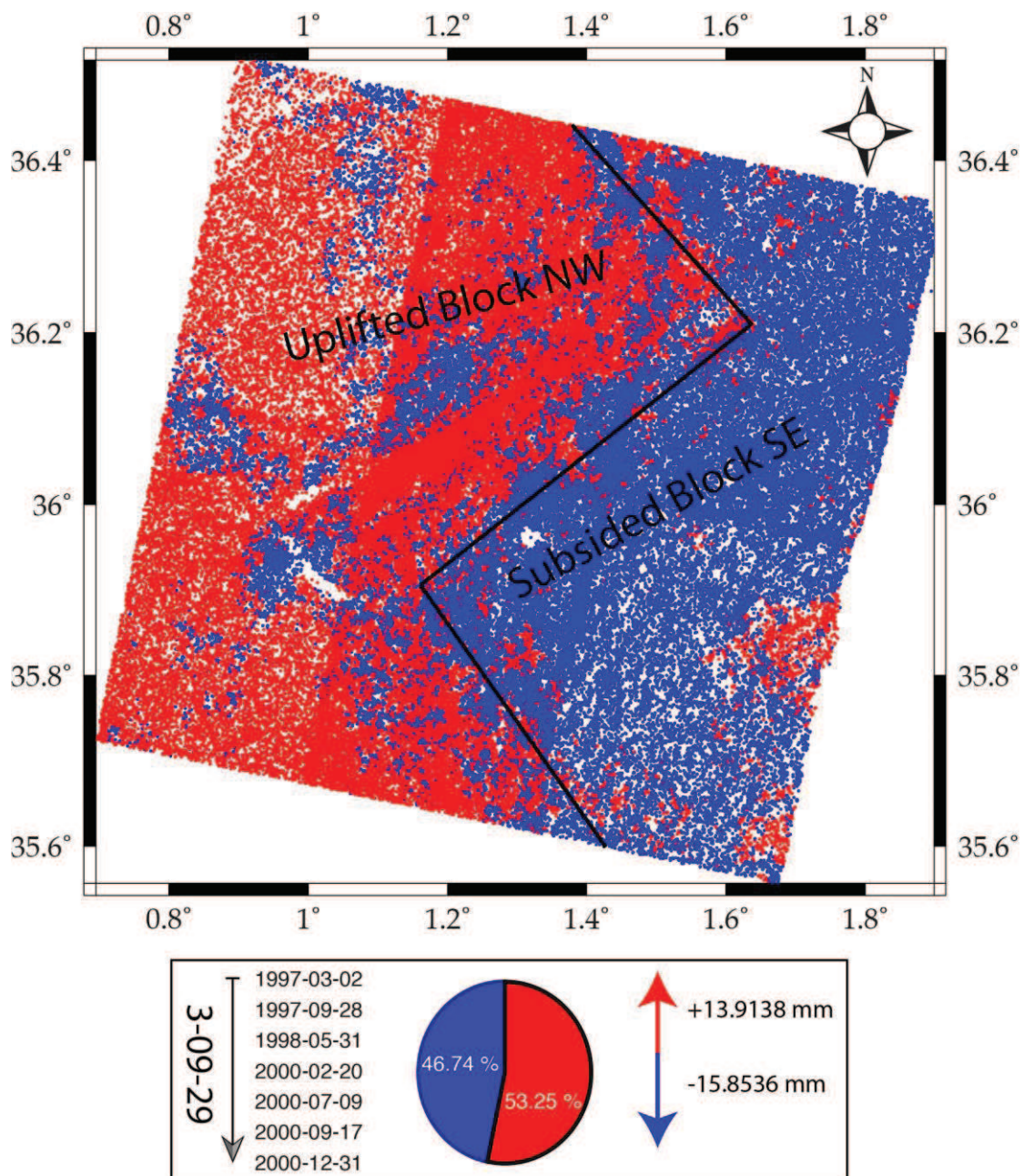


**Figure 7:** Mapping of the two blocks separating by El Asnam fault in correspondence with Figure 6. The uplifted block (red) is situated NW of the fault zone representing ~53 % of the map. The subsided block SE of the fault occupies ~47%. The average of each blocks is +13.9 mm/yr and -15.9 mm/yr respectively for the uplifted and the subsided blocks, for a total LOS cumulative slip of 60 mm in the uplifted bloc and ~ -50mm in the subsided bloc (and 11 cm LOS net slip) during three years across the El Asnam region.

The merged InSAR analysis and results are in agreement with previous geodetic and tectonic studies (Ruegg et al., 1982; Meghraoui and Doumaz, 1996) where the El Asnam coseismic faulting was revealed as a major limit between two main tectonic blocks in the Tell Atlas.

### **3.1 Chelif basin-scale deformation using time series analysis**

In this study, we cover a large region containing more than one active fault (Figure 6) in order to study the evolution in space and time of the postseismic displacement associated with the 1980 large earthquake. Five profiles indicating the time series and related surface deformation are selected based on the velocity values and distribution in the map (equal distance between the uplift and subsiding area, Figure 8). The distribution histogram of scatterer velocities give information about the clustering of scatterers according to their velocity and help in the selection of scatterers as a function of the maximum or the average displacement. Five time series extracted from selected five pixel scatterers (see numbers in Figure 8) show in Figure 9 the time evolution over three years with a positive or negative slope for regression line indicating the uplift and subsidence, respectively.

The cumulative postseismic (three years from 1997 to 2000) and perhaps comparable interseismic deformation across this tectonic boundary may explain the frequent earthquake occurrence in this region. This study of surface changes in the M7.3 El Asnam fault provides estimates of regional uplift and subsidence rates that may help in the earthquake hazard assessment along the plate boundary in North Africa (Figure 10). In three years of study, the cumulative displacement reaches 60 mm in the uplifted bloc and  $\sim -50$ mm in the subsided bloc.

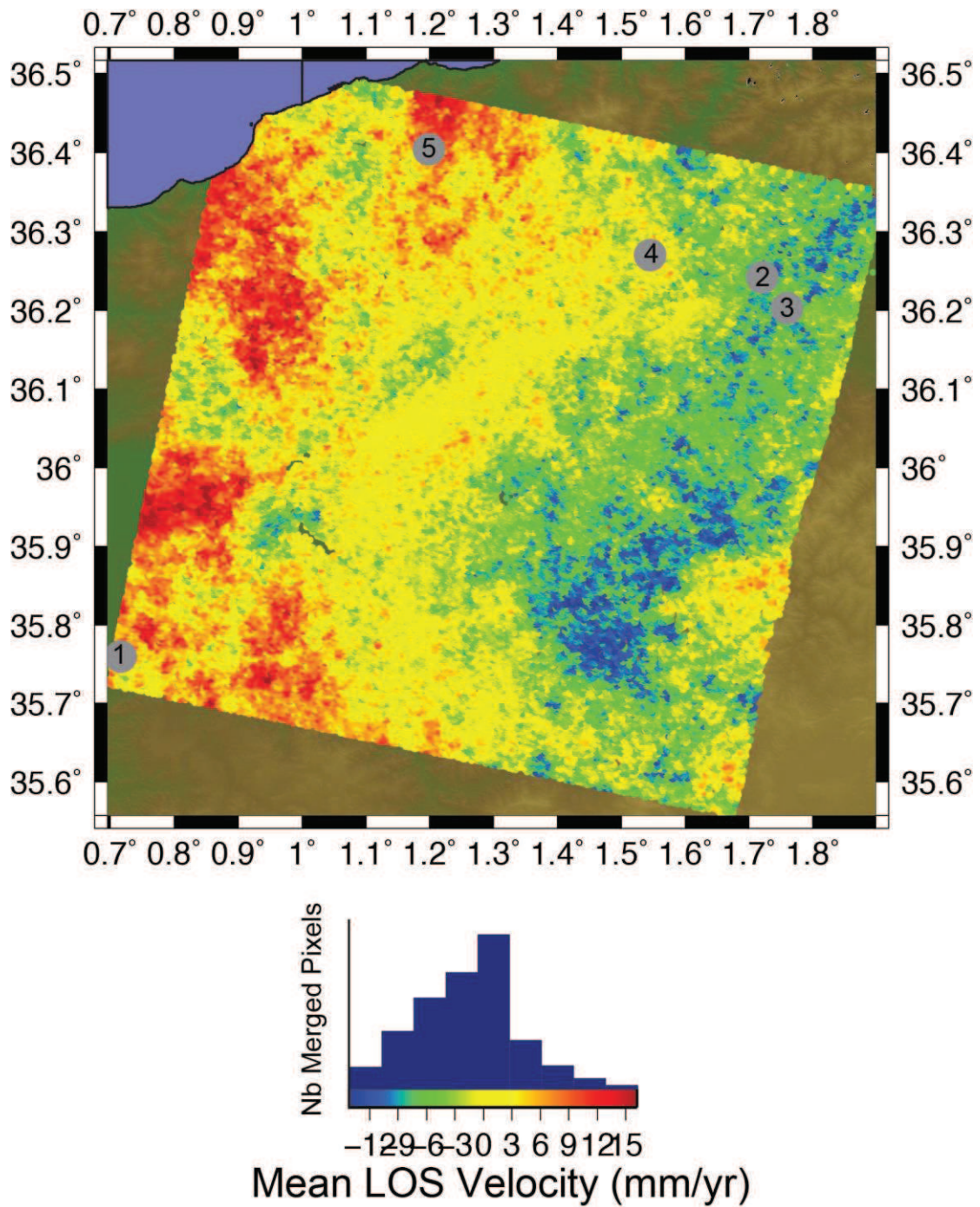


**Figure 8:** Mean LOS velocity map (mm/yr) from 1997 to 2000 showing the scatterer clustering in histogram according to their velocity. Five scatterers and their velocity changes are selected (see numbered circles) to show their evolution over time (see Figure 9).

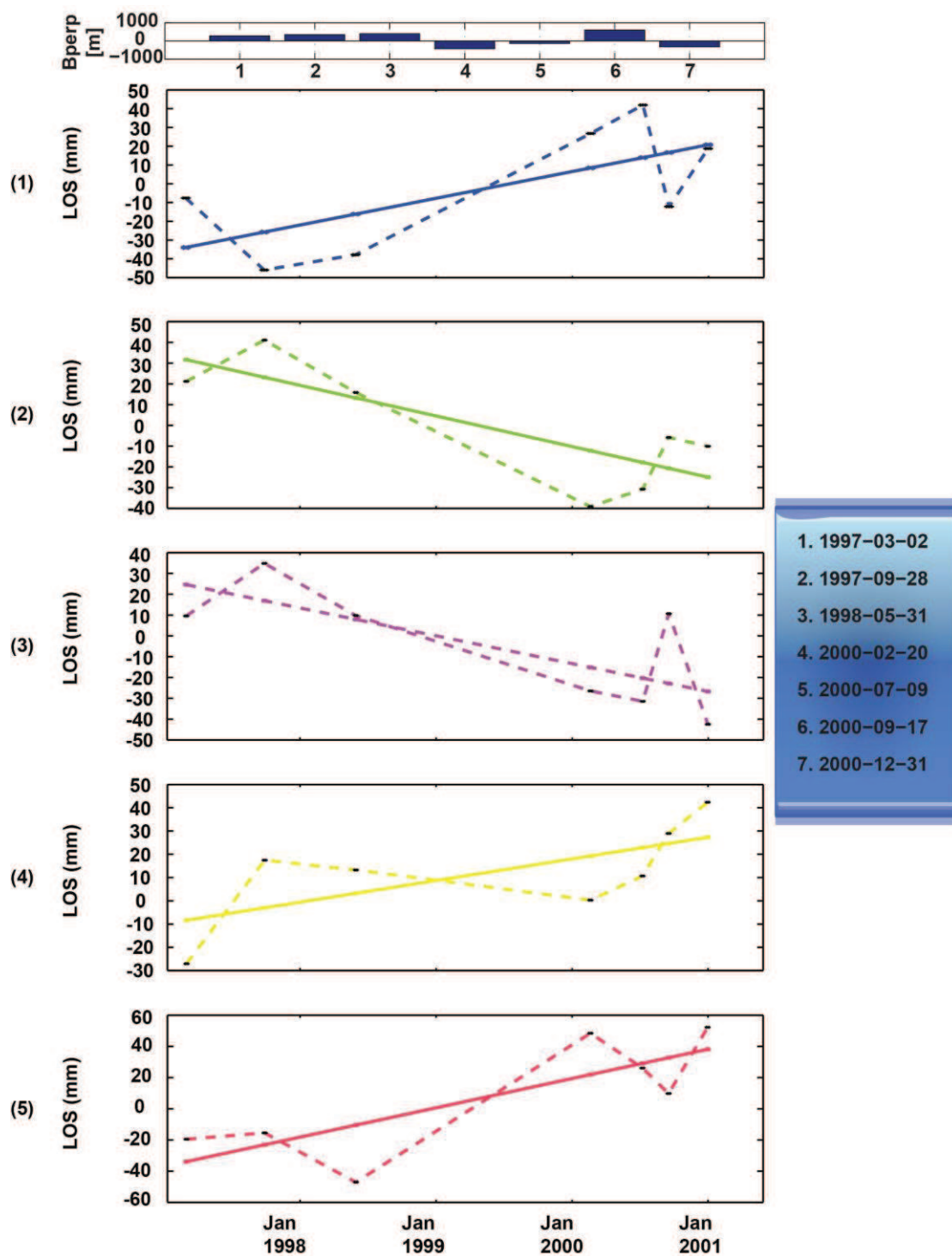
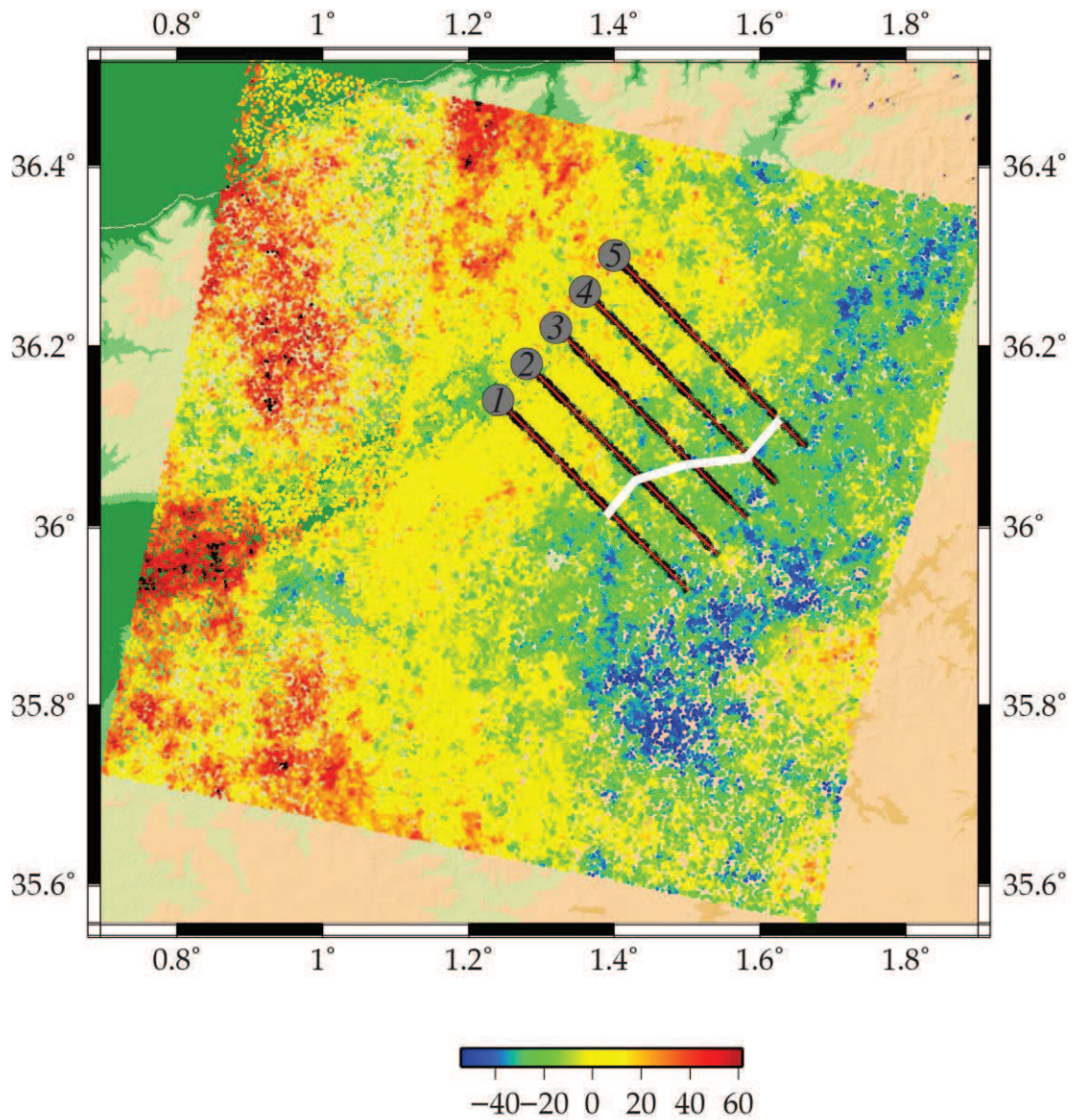


**Figure 9:** Profiles of the five selected scatterers from figure 8. Dashed lines indicate the time series and the continuous lines indicate the mean values of displacement rate.

The total ~11 cm cumulative LOS values of postseismic displacement appears to be fairly large compared with other regions of postseismic deformation. Numerous questions can be asked especially if the LOS signal did not contain any other component like topography.

In order to address this question, we compare the cumulative LOS signal with the SRTM (30'') topographic values. Hence, we select five profiles of cumulative displacement across the fault zone and the two blocs (Figure 10). The cumulative LOS signal is compared with the corresponding topographic value; we observe in Figure 11 that the LOS signal do not correlate with the topography values. In particular, profile number 3, we observe a sharp inflection from 1.4° to 1.45° longitude with a sudden change in the LOS ranges from ~+10 mm to -40 mm (with a total of 50 mm cumulative deformation along the profile) that can be explained as the transition from the uplifted block to the subsided block passing through a presumable 0 mm displacement and the El Asnam reverse fault tip location. The merged PS and SB method indicates the NW upthrown block and SE downthrown block assuming that 0 mm LOS value indicates the fault location.

In profile number 3, we observe from (1.4° to 1.45°) a sudden change in the LOS ranges from ~+10 mm to -40mm. which can be explained as we change from uplifted block to subsided block passing through 0mm (the fault location).



## Cumulative Displacement (mm)

**Figure 10:** Three years cumulative displacement (mm) in LOS. The total displacement reaches 60 mm in the uplifted bloc and  $\sim -50$ mm in the subsided bloc. The whiteline indicates the zone of deformation and location of inflexion obtained according to the maximum LOS changes between two neighbored pixels of the same profile (see also Figures 11).

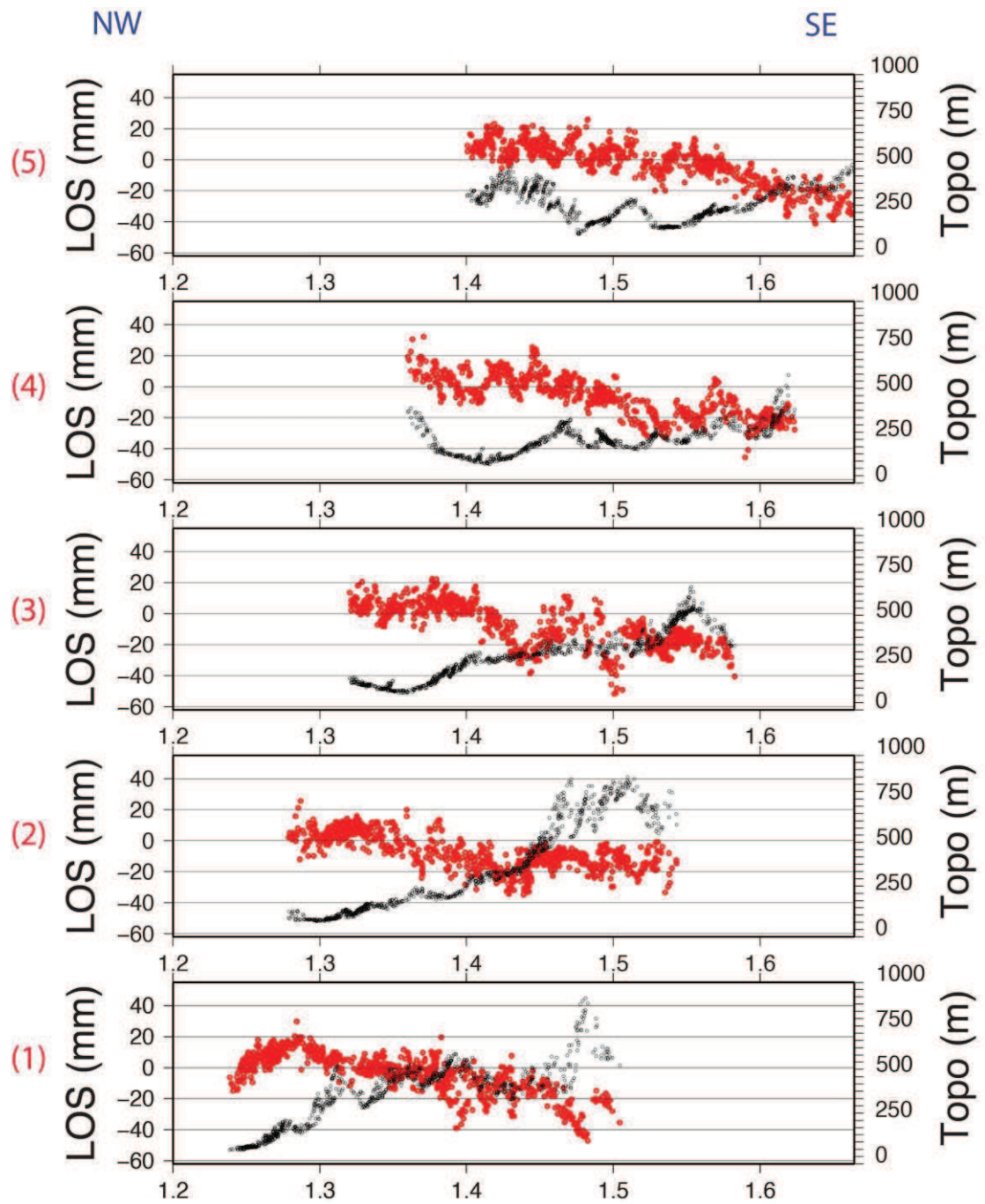


**Figure 11:** Five profiles of cumulative displacement (red dots) across the fault zone and the two blocs with topography in black. The merged PS and SB pixels indicate NW upthrow block where 0 mm pixel indicates the fault location.

## 4. Modeling:

The total postseismic deformation estimated at the Earth's surface during the observation period between 1997-2000 is modeled in an inverse approach using the Poly3Dinv software (Thomas, 1993). The deformation is modeled as a half-elastic plane space according to the fault characteristics as a strike-slip fault (lon, lat, dip, angle with the principle fault plan) that respects three segments 36 km NE-SW to E-W from the fault epicenter as describing in (Meghraoui et al., 1996). The fault-dipis chosen according to (Belabbes., 2008),  $54^\circ$ ,  $45^\circ$ , and  $30^\circ$  for the three segments respectively .

Poly3dinv use triangular elements for modeling fault plane with ( $1.28^\circ$  -  $1.77^\circ$  lon,  $36.0^\circ$  –  $36.3^\circ$  lat) in size encompassing El Asnam fault location area. We model the fault strain plane as triangular grids taking into account the merged PS-SB cumulative (three years) resulting file and there LOS sign and values (+/-) according to there spatial distribution using their UTM coordinates.

The model obtained by Poly3dinv is compared with the cumulative merged results (PS-SB) in order to validate or not the obtained model. The postseismic surface changes on the surface obtained with the modeling is compared with the InSAR results in term of faults location verifying for the cumulative merged as the max sudden changes between tow LOS of neighbored pixels values accorssing the fault subsided area and the uplifted one obtained with the profiles, and for the model it represents zeros postseismic values (figure 12).

We plot the obtained model with Poly3dInv with the cumulative merged PS-SB InSAR in order to measure the correlation between the obtained postseismic surface deformation from InSAR and thus from the model (figure 13).

(Lammali et al., 1997) propose a seismotectonic map of this region based on geological and seismological data and during the 1980 El Asnam earthquake they measured using a basic geodetically network the vertical movement along 40 km NE-SW thrust fault. The first geodetic network was buld in 1976, since 1986, they use also both of planematry and altimetry. There significan results are obtained witht the altimetric measurement of vertical movements with ( $5.1 \pm 1.9$  mm/yr) uplift of the NW block during 5 years of studies (1986 - 1991) and Sar El Maarouf was growing along the central postseismic slip rate of ( $9.6 \pm 1.4$  mm/yr).

The results obtained with InSAR of the postseismic displacement with a vertical companant comparable with (Lammali et al., 1997) results. The earthquake fault area limits two distinct zones. The positive (uplift) block have a LOS values reaching 30.4 mm cumulative displacement corresponding to 16.2 mm (uplift) on the hanging block and -14.2 mm

(subsidence) on the footwall block from 3 years from 1997 to 2000 of the covered period this study.

We then extract the vertical and horizontal components (uplift and NNW-SSE shortening) from the LOS and obtain 0.6 mm/yr and 0.4 mm/yr, respectively.

The model calculated fit with the cumulative merged PS-SB InSAR at 74.83 % (correlation factor  $R^2 \sim 0.75$ ) and the fit function that describe the similarity for each pixel chosen between InSAR surface deformation and the model distribution is:  $Y = 1.1 * X + 1.7$ .

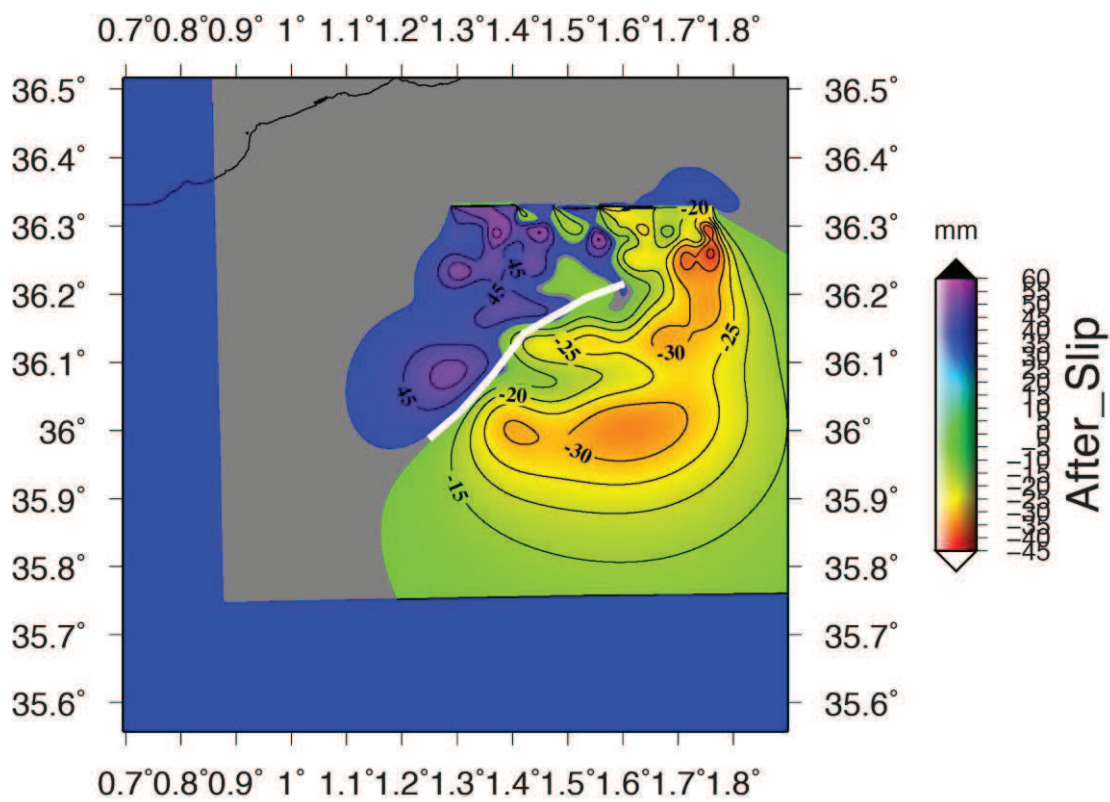


**Figure 12:** After slip model obtained with the Poly3d inversion using the merged PS-SB InSAR results. The white line indicates the fault location rapture after the obtained model along 36 km on the surface.

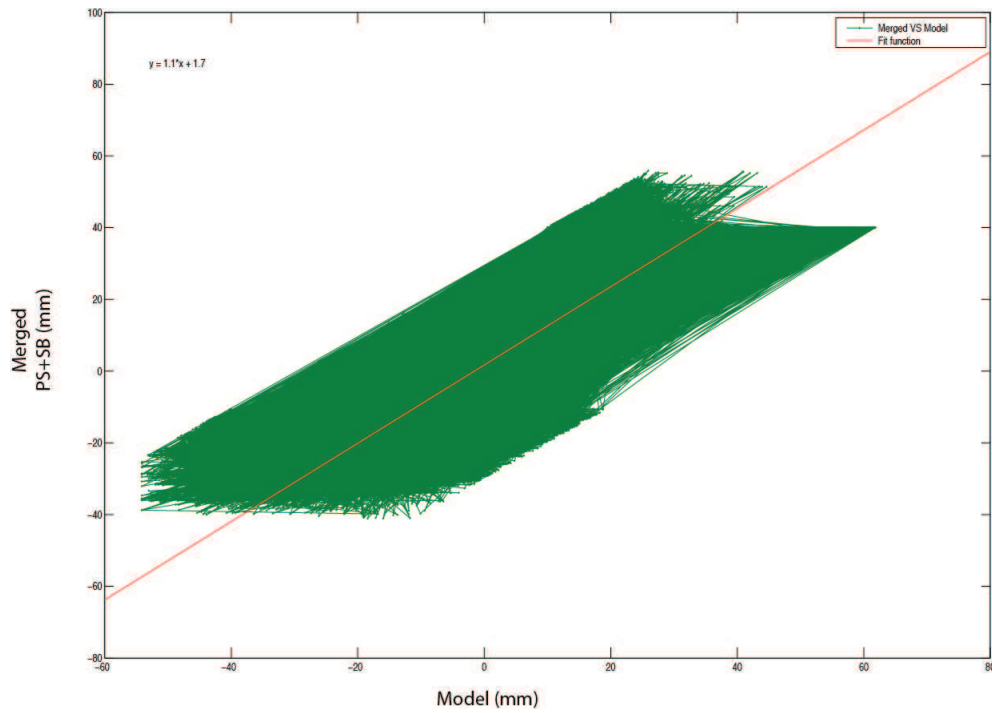


**Figure 13:** plot shows model versus the Merged PS-SB cumulative deformation results over the 3 years studies. The fitting line  $y = 1.1 * X + 1.7$  in red with percentage de correlation = 74.83 %.

## 5. Conclusion

9 ERS-SAR images recorded in C-band acquired between 1997 and 2000 have been processed using Stamps/MTI (Hooper, 2008) for advanced time series analysis.

The conventional InSAR using this data set shows big decorrelation in the resulting interferometry due to changes in ground cover of vegetation (seasons).

This study is based on the combination of two approaches for time series analysis of SAR images (PS and SB methods) incorporated in Stamps. The application of Persistent Scatterer (PS) and Small baseline (SB) approaches reveal significant surface changes across the El Asnam fault zone. Five NW-SE trending profiles across the fault zone show the cumulative LOS displacement versus the topography values on both sides of the fault. In all cases, the fault tip is located at zero-LOS value separating the tow blocks, the uplifted area (positive LOS) and the subsided area (negative LOS). The earthquake fault area limits two distinct zones, with LOS values reaching 30.4 mm cumulative displacement corresponding to 16.2 mm (uplift) on the hanging block and -14.2 mm (subsidence) on the footwall block.

We then extract the vertical and horizontal components (uplift and NNW-SSE shortening) from the LOS and obtain 0.6 mm/yr and 0.4 mm/yr, respectively (total of 1 mm/yr surface deformation). This study shows five time series from the merged results in different locations; the choice of PS to be plot is based on histogram value of Mean velocity.

One of the best explanations of this big postseismic rate is that the fault is still active and the fault strains are cumulate since 33 years, notate that the interseismic period between the first seismic of 1954 and the second of 1980 is 26 years in comparison with 33 years separating the second seism till now, helping to understand and predict the next seismic cycle.

## References:

Aoudia, A., Meghraoui, M., (1995), Seismotectonics in the Tell Atlas of Algeria : the Cavaignac (Abou El Hassan) earthquake of 25.08.1922 ( $M_s = 5.9$ ). *Tectonophysics*. 248, 263-276.

Belabbes, S., (2008) Caractérisation de la déformation active par l'Interférométrie Radar (InSAR): Failles sismiques aveugles et cachées de l'Atlas Tellien (Algérie) et du Rif (Maroc) le long de la limite des plaques Afrique-Eurasie. PhD thesis, EOST University Louis Pasteur, Strasbourg, France, 226 pp.

Berardino, P., G. Fornaro, R. Lanari, & E. Sansosti. (2002). A New Algorithm For Surface Deformation Monitoring Based On Small Baseline Differential SAR Interferograms, *IEEE Trans. Geosci. Remote Sens.* 40, 2375 – 2383.

Bezzeghoud M., Dimitrov D., Ruegg J.C., & Lamali K., (1995). Faulting mechanism of the El Asnam 1954 and 1980 earthquakes from modelling of vertical movement. *Tectonophysics*, 249, 249-266.

Dziewonski, A. M., T.-A. Chou and J. H. Woodhouse, ( 1981). Determination of earthquake source parameters from waveform data for studies of global and regional seismicity, *J. Geophys. Res.*, 86, 2825-2852. doi:10.1029/JB086iB04p02825.

Ekström, G., M. Nettles, and A. M. Dziewonski,. (2012) The global CMT project 2004-2010: Centroid-moment tensors for 13,017 earthquakes, *Phys. Earth Planet. Inter.*, 200-201, 1-9, 2012. doi:10.1016/j.pepi.2012.04.002.

Ferretti A., Prati C., Rocca F. (2001). Permanent Scatterers In SAR Interferometry, *IEEE Trans. Geosci. Remote Sens.* 39, 1, 8-20.

Hooper, A. (2008). A Multi-Temporal InSAR Method Incorporating Both Persistent Scatterer And Small Baseline Approaches, *Geophys. Res. Letters* 35, L16302, Doi:10.1029/2008GL034654.

Massonnet, D., & Feigl, K.L. (1998). Radar Interferometry And Its Application To Changes In The Earth's Surface. *Reviews Of Geophysics* 36, 441-500.

Meghraoui, M., & F. Doumaz. (1996). Earthquake-Induced Flooding And Paleoseismicity Of The El Asnam, Algeria, Fault-Related Fold. *Journal Of Geophysical Research*, 101, B8, 17,617-17,644.

Nocquet JM, Calais E (2004) Geodetic measurements of crustal deformation in the western Mediterranean and Europe, geodynamics of Azores–Tunisia. *Pure & Appl Geophys* 161:661–681, 0033-4553/04/030661-21. doi:10.1007/s00024-003-2468-z.

Ouyed et al., (1981) Seismotectonics of the El Asnam earthquake. *Nature* 292, 26 - 31 (02 July 1981); doi:10.1038/292026a0.

Philip, H. and Meghraoui, M., (1983). Structural analysis and interpretation of the surface deformations of the El Asnam earthquake. *Tectonics*, 2: 17-49.

Ruegg, J.C., Kasser, M., Tarantola, A., Lepine, J.C. and Chouikrat, B., (1982). Deformations associated with the El-Asnam earthquake of 10 October 1980: geodetic determinations of vertical and horizontal movements. *Bull. Seismol. Soc. Am*, 72(6): 2227-2244.

R. Scharroo and P. N. A. M. Visser,. (1998). Precise orbit determination and gravity field improvement for the ERS satellites, *J. Geophys. Res.*, 103, C4, 8113-8127,.

Serpelloni E, Vannucci G, Pondrelli S, Argnani A, Casula G, Anzidei M, Baldi P, Gasperini P (2007) Kinematics of the western Africa–Eurasia plate boundary from focal mechanism and GPS data. *Geophys J Int* 169:1180–1200. doi:10.1111/j.1365-246X.2007.03367.x

Sudhaus, H., and Jonsson, S., (2009). Improved source modelling through combined use of InSAR and GPS under consideration of correlated data errors: application to the June 2000 Kleifarvatn earthquake, Iceland *Geophys. J. Int.* 176, 389–404.

Thomas, A. L., (1993), POLY3D, A Three-Dimensional, Polygonal Element, Displacement Discontinuity Boundary Element Computer Program With Applications to

Fractures, Faults, and Cavities in the Earth's Crust, M.S. Thesis, Stanford University, Stanford, CA.

Wessel, P., & Smith H. F. (1998), New improved version of the Generic Mapping Tools Released, EOS Trans. AGU, 79, 579.

Wright, T.J., Lu, Z. & Wicks, C., (2003). Source model for the Mw 6.7, 23 October 2002, Nenana Mountain Earthquake (Alaska) from InSAR, *Geophys. Res. Lett.*, **30**(18), doi:10.1029/2003GL018014.

Bell, John W., Amelung, F., Ferretti, A., Bianchi, M. and Novali, F. (2008) Permanent scatterer InSAR reveals seasonal and long-term aquifer-system response to groundwater pumping and artificial recharge. *ATER RESOURCES RESEARCH*, VOL. 44, W02407, doi:10.1029/2007WR006152.

Calderhead, A.I., Therrien R., Rivera, A., Martel, R., Garfias, J. (2011) Simulating pumping-induced regional land subsidence with the use of InSAR and field data in the Toluca Valley, Mexico. *Advances in Water Resources*, VOL., 34., PP 83-97.

Singhroy, V.; Couture, R.; Alasset, P.-J.; Poncos, V. (2007) InSAR monitoring of landslides on permafrost terrain in Canada. *Geoscience and Remote Sensing Symposium. IGARSS. IEEE International*, vol., no., pp.2451-2454. doi: 10.1109/IGARSS.2007.4423338.

Riedel, B. and Walther A., (2008) InSAR processing for the recognition of landslides. *Adv. Geosci.*, 14, 189–194.

Ventisette, C., D., Ventisette1, E., Intrieri1, G., Luzi, N., Casagli, R., F., , and Leva, D. (2011) Using ground based radar interferometry during emergency: the case of the A3 motorway (Calabria Region, Italy) threatened by a landslide. *Nat. Hazards Earth Syst. Sci.*, 11, 2483–2495.

Yielding et al., (1981) Relations between surface deformation, fault geometry, seismicity, and rupture characteristics during the El Asnam (Algeria) earthquake of 10 October 1980. *Earth and Planetary, Science Letters*, 56, 287-304.





## **Chapter V**

# **Postseismic Surface Deformation Associated with the $M_w$ 6.4, 24 February 2004 Al Hoceima (Morocco) Earthquake using Time Series Analysis of SAR Images**



# 1. Introduction

We investigate six years (from 2004 till 2010) of postseismic surface displacement associated with the  $M_w$  6.4 of the 24 February 2004 Al Hoceima Morocco earthquakes. The postseismic displacement field is mapped using advanced Multi-temporelle synthetic aperture radar interferometry (InSAR) analysis based on the combination (merged) of both of Persistent Scatterer (PS) and Small Baseline (SBAS) of time series analysis approaches. 14 ERS-2 SAR images have been used in this study recorded in the C-band SAR sensor (5.6 cm wavelength) from the European Space Agency (ESA) acquired between 2004-06-06 and 2010-01-31.

Al Hoceima area is one of the most seismically active regions in Morocco with the Rif Mountains area because of their situation in the junction of two active plates (Figure 1); the Eurasia and Africa plates. Indeed, two biggest earthquakes token place at the Al Hoceima region and in the western Mediterranean, the first earthquake was on May 26, 1994 ( $M_w = 5.8$ ). Short time after this first event, in teen years, the second earthquake was on February 24, 2004 with the ( $M_w$  6.4) making this region one of the most active with high seismicity drawing the attention of numerous researchers all over the word. For this will, several studies have been done in El Hoceima region (Bezzeghoud et al., 1999; Çakir et al., 2006; Akoglu et al., 2006; Biggs et al., 2006; Tahayt et al., 2009) in order to understand the tectonic settings and explain the high seismicity in the region.

The seismotectonic characteristics of the earlier earthquake in 1994 are given by the study of Bezzeghoud et al. (1999). The authors resolve the focal solution based on 32 polarities of first motion data at teleseismic and regional distance. The obtained focal mechanism solution corresponds to a nearly vertical NNW-SSE trending, principal left-lateral strike-slip faulting with a normal component. The nodal fault plane is E-W oriented and dipping  $40^\circ$  to south.

Cakir et al. (2006) study the coseismic surface deformation of the Al Hoceima 24-02-2004 earthquake by SAR interferometry using Envisat SAR data. The results provide a clear distribution of fringes for ascendant and descendant image interferograms. The authors propose a modeling based on the inversion of InSAR results reflecting the fault characteristics; they show that the best fit (with minimum residuals between the model and data) corresponds to a NW-SE-trending, blind right lateral strike-slip fault and  $6.8 \cdot 10^{18}$  N.m. seismic moment, assuming 21-km-long, 16.5-km-deep and  $88^\circ$  NE dip as fault parameters.

(Biggs et al., 2006) combine radar interferometry with the aftershock relocation of the earthquake in order to recognize the orientation of primary fault plane of the  $M_w$  6.4 of the 24 February 2004 and 1994  $M_w$  6.0 Al Hoceima Morocco earthquakes. Faults plane used are NW-SE for 2004 aftershock and NE-SW for the 1994 earthquake.

Akoglu et al., (2006) provide a study on the surface deformation of both the 1994 to 2004 earthquake sequence, using Synthetic Aperture Radar Interferometry (InSAR) in order to characterize their seismic source parameters and to know the relationships between these two large earthquakes. The earthquake fault modeling using the inversion of surface deformation indicate that the 1994 earthquake is related to a N23°E trending, blind left-lateral fault, while the best fitted surface data of the 2004 earthquake correlate well with a N45° W trending, also blind right-lateral fault. The 1994 and 2004 fault geometries at depth show that both coseismic ruptures are blind and form an antithetic system. The authors also suggest that the 1994 earthquake induced a stress transfer and loaded the 2004 fault zone.

A recent work also describes the 24-02-2004 coseismic deformation in the Al Hoceima region using a combination between ENVISAT ASAR radar images and SPOT5 optical images (Tahayt et al., 2009). The authors also use a dislocation model in a half-space to extract the fault parameters assuming cross-fault mechanism. Their interpretation indicates the existence of a pair of blind faults associated with two subevents and assumes that the first fault is located at 500 m depth and the second is at 3 km depth.

In this chapter, I use the fault characteristics obtained from the InSAR analysis methods in order to identify the existence of a postseismic deformation and determine the associated faulting at the crustal level in the Al Hoceima region. The merged results (PS-SB) are used to enhance the signal and extract the ground deformation component from the line-of-sight (LOS) of the resulting interferograms. Although the earthquake area has a rather low coherency correlation between images, the multitemporal analysis of InSAR time series methods at pixel scale is powerful in term of small motion detection and selection of largest signal/noise ratio.

Using this combined method, I model the coseismic deformation and related strike-slip fault using the same fault parameters as in (Cakir et al., 2006) in order to compare and to validate the fault mechanism with previous results (Bezzeghoud et al., 1999; Çakir et al., 2006; Akoglu et al., 2006; Biggs et al., 2006; Tahayt et al., 2009). In addition, I compare my coseismic model with the postseismic cumulative ground deformation measured with InSAR to validate the model and to understand the origin of the postseismic transient deformation with respect to the tectonic setting of the Al Hoceima region.

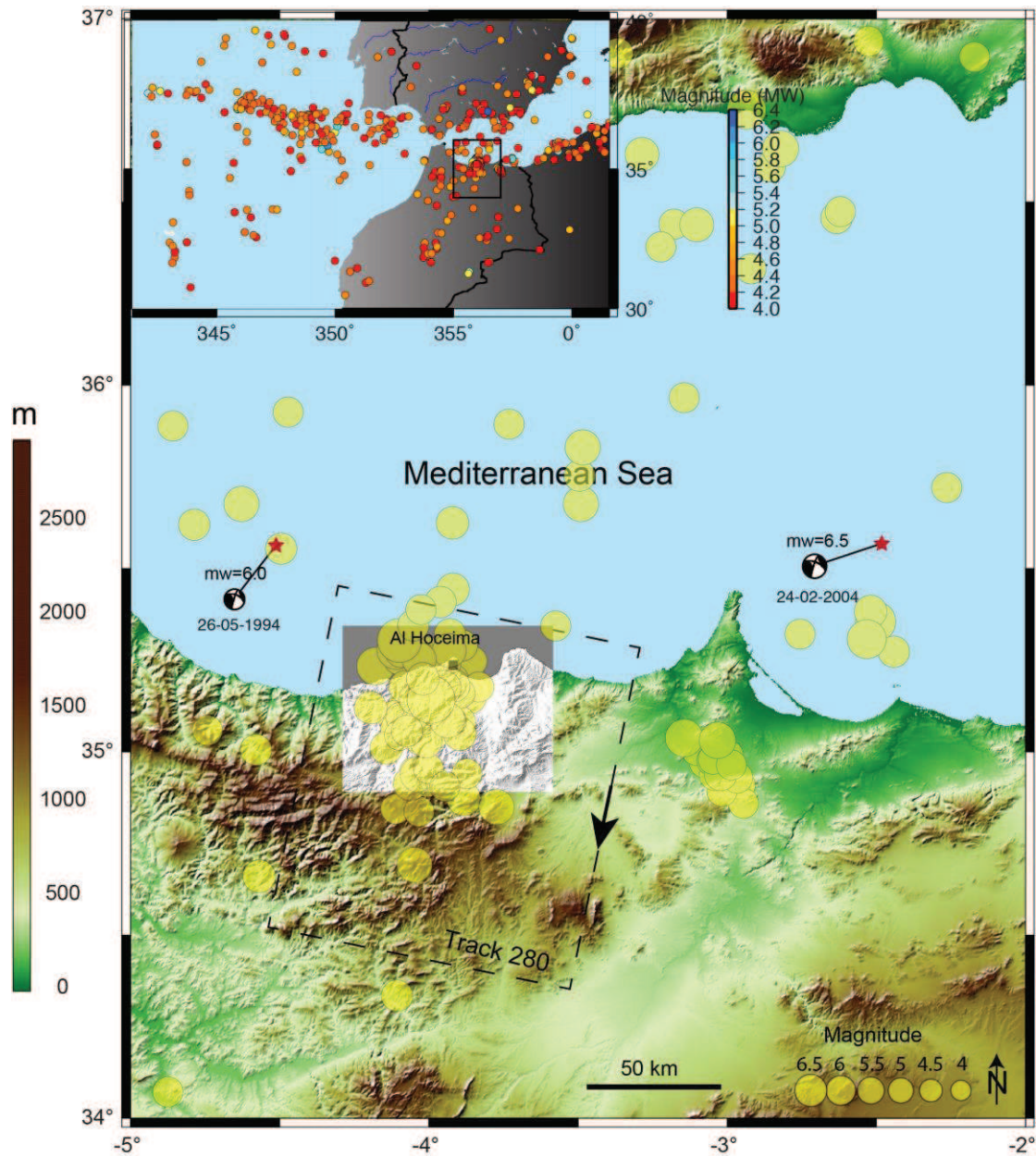


**Figure 1:** The seismicity along the Moroccan-Iberian section between the African-Eurasian plate boundaries. Yellow circles show earthquake epicenters for events with  $m_W \geq 4$  for the period 1990 to 2012 (USGS/NEIC data file <http://neic.usgs.gov>). Dashed line shows the satellite descending track number used for InSAR processing. The focal mechanism solutions are obtained from the Bezzeghoud et al., (2005).

## 2. InSAR Analysis

Two-pass InSAR method (Massonet et al., 1993) which is based on the measurement of phase change in an interferogram, comprise different sub-signals contributions including ground deformation, orbital effects, topographic errors and atmospheric delay that occurred between two satellite passes. The topographic contribution has been estimated and removed using a digital

elevation model (DEM) from the Shuttle Radar Topography Mission (SRTM) 3arc.sec (Farr and Kobrick, 200). Precise orbits (Sharroo and Visser, 1998) are used to estimate and remove the orbital delay from the phase signal.

We use ERS-2 radar images acquired in descending track after the 2004 earthquake to explore the postseismic deformation between 2004-06-06 and 2010-01-31 (Figure 2). StaMPS/MTI (Hooper, 2008) is used in this studys to measure the postseismic deformation. I applied both of Persistent Scatterer (PS) (ferritti, 2001) and Small Baseline (SB) (Bernardino et al., 2004) and Merged (Hooper, 2008) incorporated in StaMPS to retrieve the postseismic deformation.

Notice that StaMPS use ROI-PAC (Rosen et al., 2004) to focus the SAR images and Doris InSAR processing software (Kampes et al., 2003) to produce the interferograms. In addition, StaMPS allow to estrimate and remove the atmospheric and orbital error (AOE) from the Spatially-correltaed look angle (SCLA) from the Master SAR image in StaMPS processing steps (Hooper, 2008).

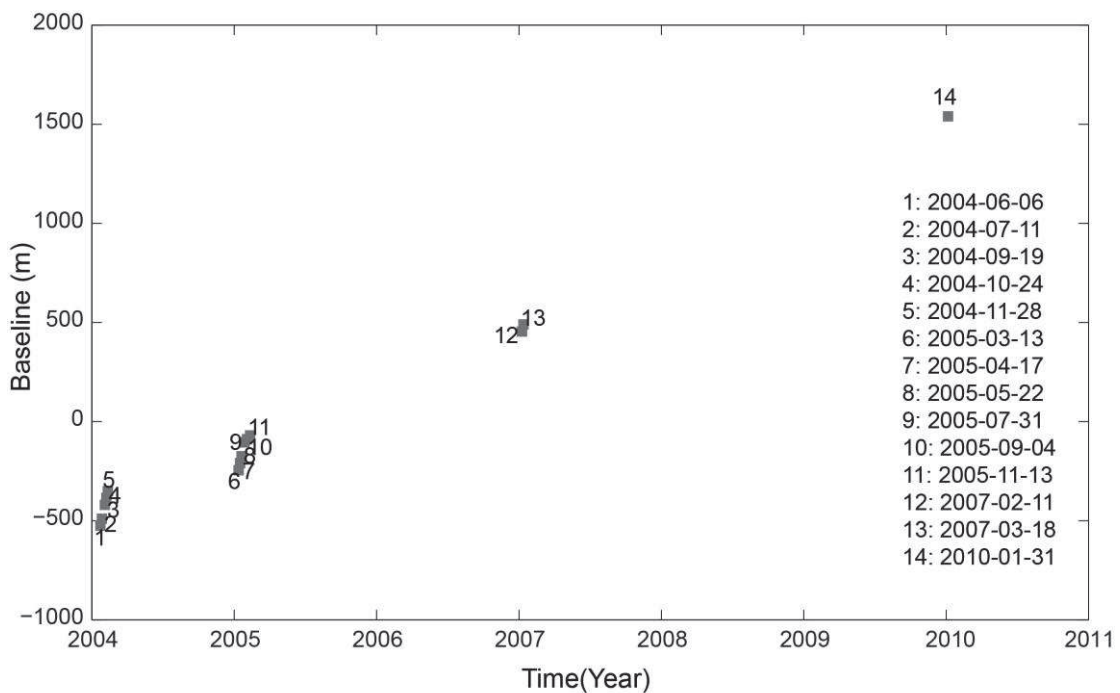


**Figure 2:** The 14 suitable SAR images used in this study plotted according to their baseline and their time of acquisition (right column). These SAR images are recorded on the track number 280 and in descending satellite view.

After applying each of Persistent Scatterer and Small Baseline algorithms alone, I combine them by using the merged method of StaMPS and obtain a mean LOS velocity ranging between - 6 to + 7 mm/yr of postseismic deformation (Figure 3).

In order to study the temporal component in term of time series distribution over the 6 years of postseismic deformation, I study the evolution of seven scatterers chosen according to their LOS value, their velocity sign (+/-) and their geolocation in the mapped surface displacement. Here, I also add the histogram of the mean velocity value that presents the density of scatterers distribution in the velocity map (Figure 3).

The time series of the 7 chosen Scatterers are plotted in Figure 4, where the blue symbols (star) and line indicate their displacement in the LOS direction and the red line indicates the displacement medium tendency in term of linear regression function ( $y = vt + c$ ) where  $v$  is the velocity,  $t$  the time and  $c$  is the initial displacement value at  $t_0$

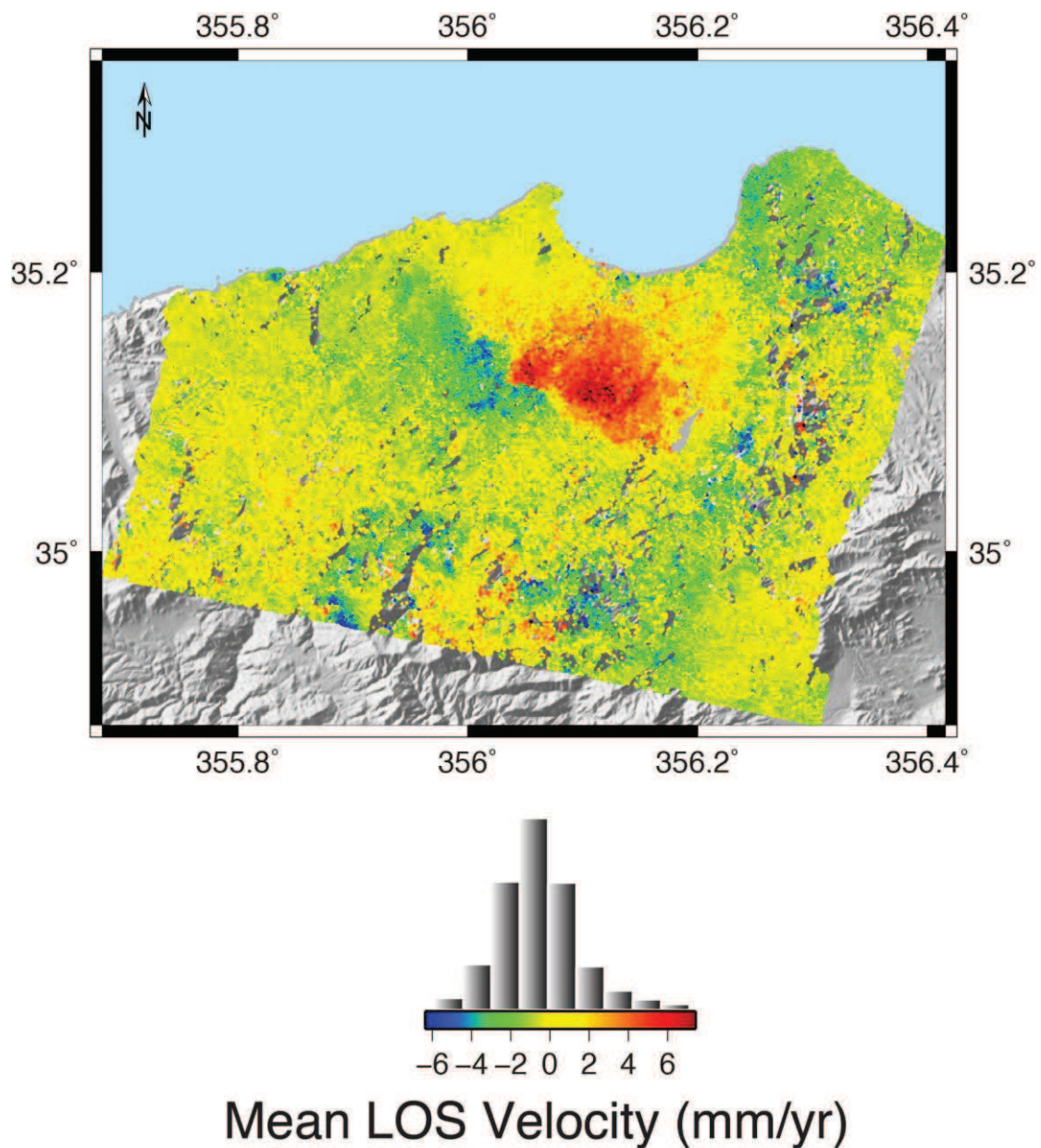


**Figure 3:** Mean LOS velocity of the postseismic deformation in (mm/yr) obtained after applying the merged method (Hooper, 2008). The histogram of the mean LOS velocity value indicates the density of scatterers distribution in the velocity map. We observe that the maximum velocity is located south of the fault zone and in agreement with the previous results of the 2004 coseismic deformation (Cakir et al., 2006).

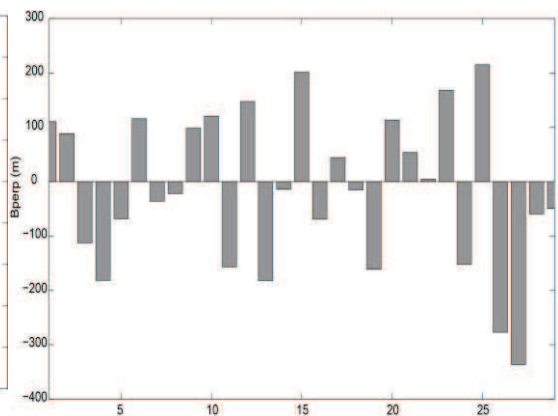
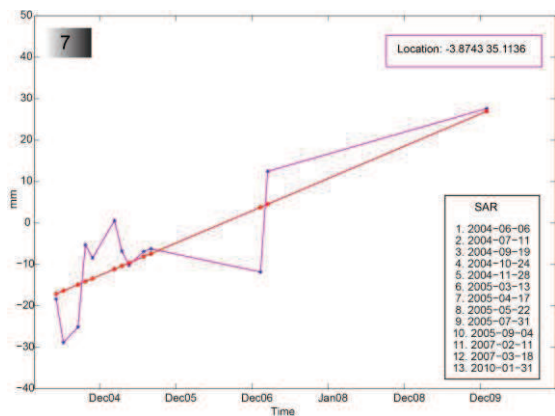
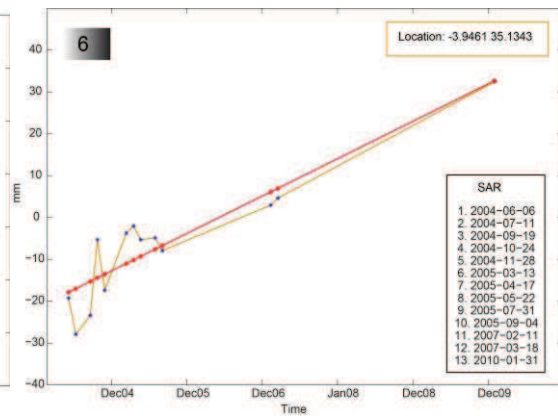
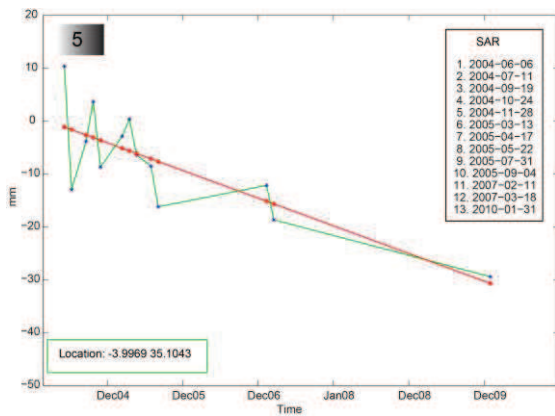
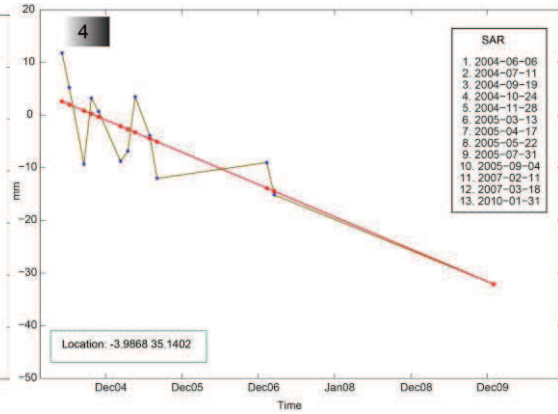
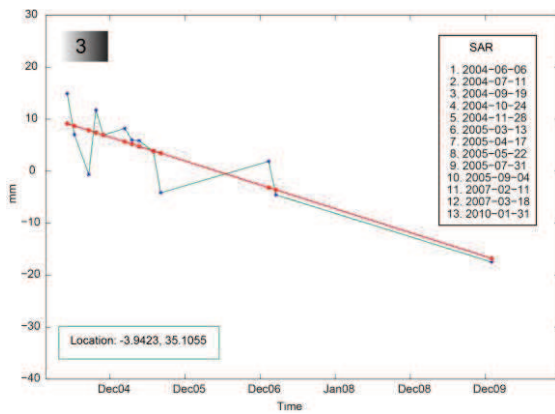
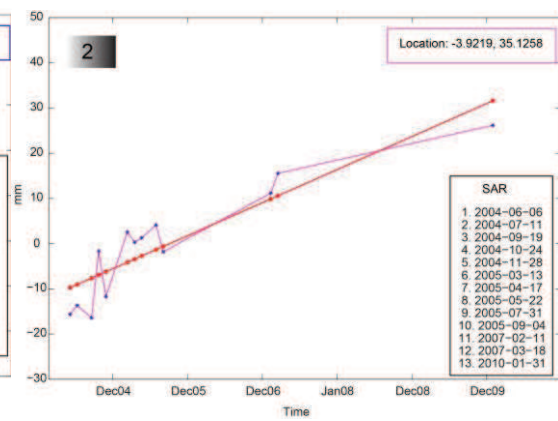
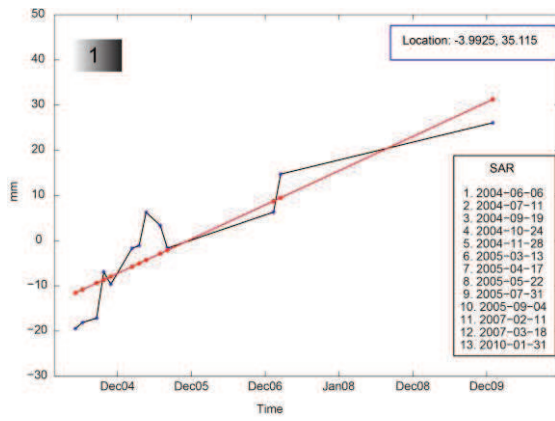
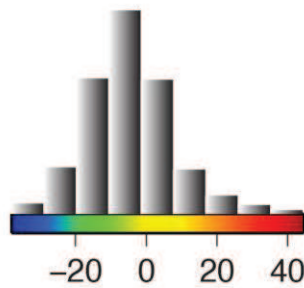
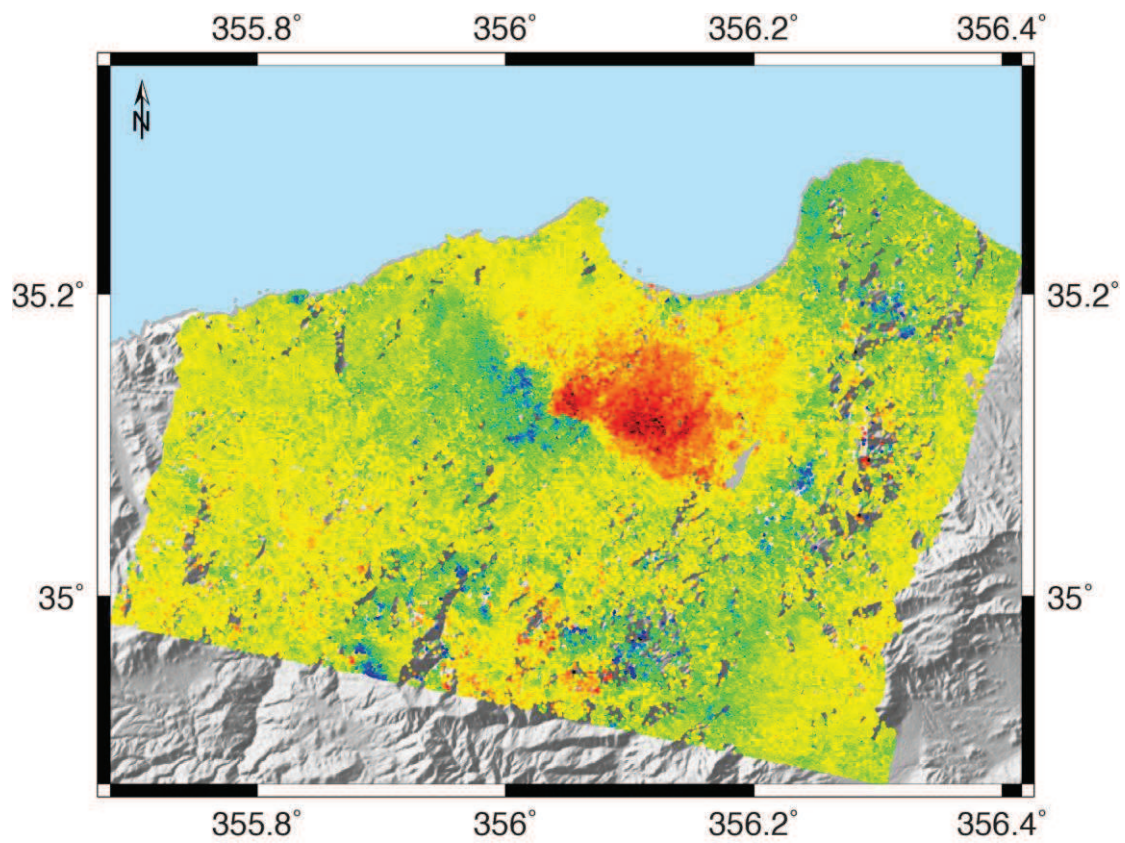


**Figure 4:** seven time series profiles of seven scatterers plotted from the merged mean velocity map to show the postseismic displacement of each scatterers location and with their evolution in time. The last figure indicates the perpendicular baseline distance between the differents SAR images aquisitions.

Using the merged mean LOS velocity map, I obtain six years of cumulative displacement with 54 mm maximum uplift and – 33 mm subsidence (Figure 5) located across the 2004 coseismic fault zone as described by Cakir et al. (2006). The cumulative postseismic displacement over the six years of studies is consistent with the characteristics of strike-slip fault mechanism. These results are analysed to obtain an inversion modeling solution of a fault slip at depth taking into account the related RMS.

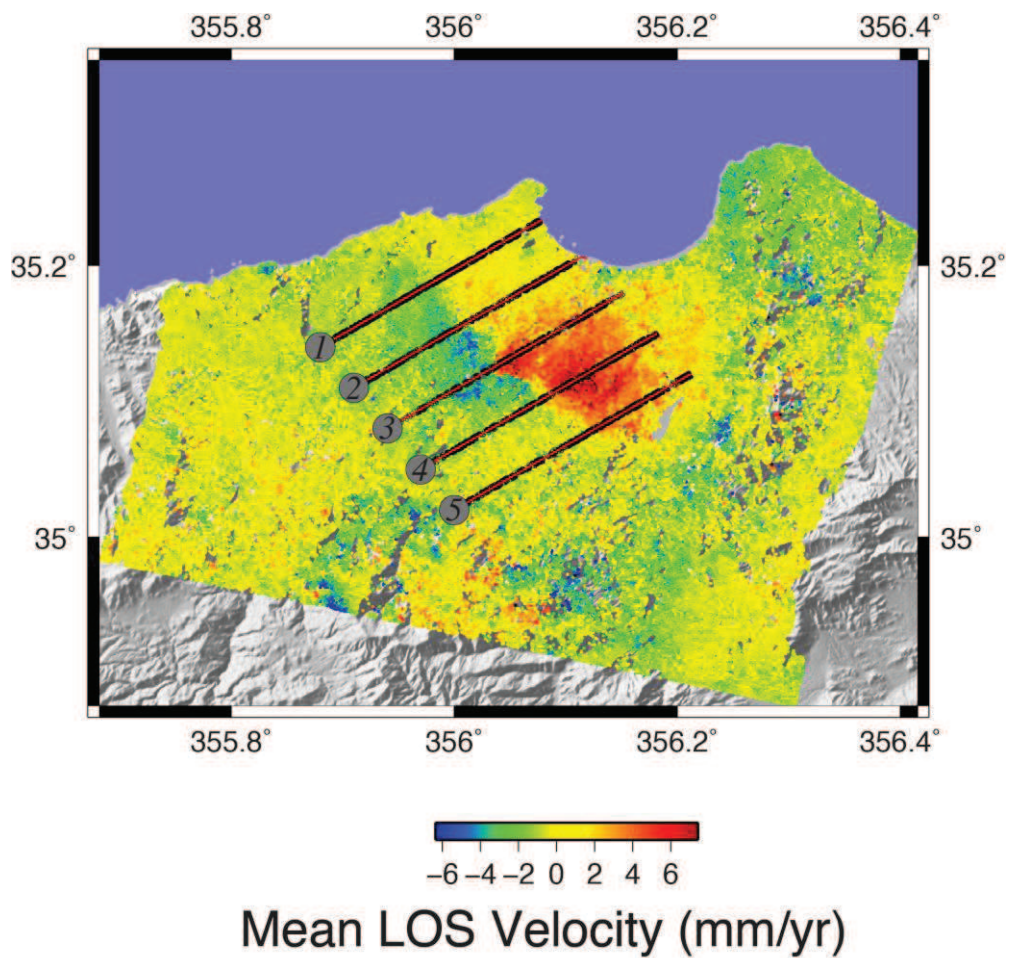
I use the mean LOS velocity map to plot 5 profiles crossing the fault tip with the N 45° direction (Figure 6a) in order to study the postseismic displacement over the fault region. In both side of the fault location (uplifted and subsided), we can see the immediate changes in the LOS values and sign going from one side to the other side. Which does the tip explain fault is located at zero-LOS and crossing this values the reflectors change in the term of direction toward or far from the satellite.

All the five profiles from 1 to 5 are plotted in the same figure (Figure 6b) in order to compere them in term of LOS value (mm) and in term of signal-shape. This tow information have big signification to help in tracing the fault trace (fault tip) location which is characterised by: a) zeros-LOS values, b) sudden and significant changes in LOS values of tow neighbours reflector from the same profile and c) the shape of the profile should have two local maximums in positive sign. (+ And -).

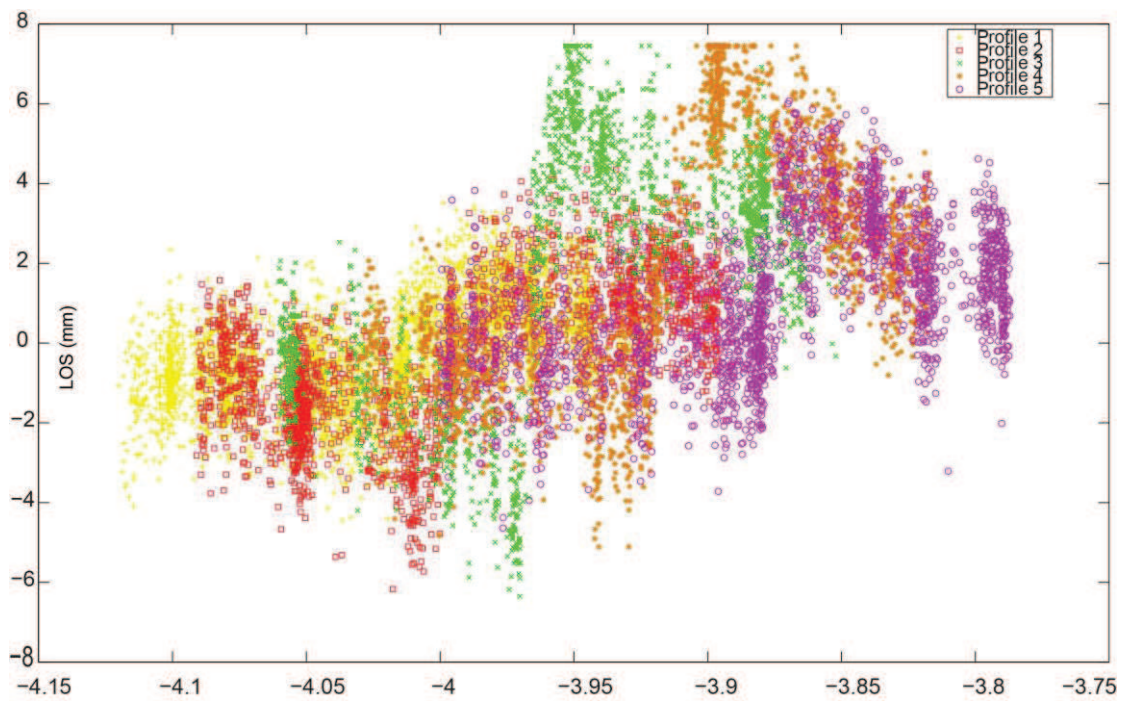


### Cumulative LOS Displacement (mm)

**Figure 5:** The cumulative LOS displacement en mm along the six year studies (2004-2010). Negative and positive scatterer values indict the direction on LOS (far from the satellite or close to the satellite). The LOS value ranges between [-33 to 54] mm.



(a)



(b)

**Figure 6:** (a) The N 45° five profiles plotted on the mean velocity map in order to study their velocity changes crossing the fault-zeros-LOS over the fault trace. This map is plotted on a shaded SRTM 3 arc.sec map. (b) All profiles from 1 to 5 plotted in the same figure in order to compare them in term of LOS value (mm) and shape of the signal have a big signification to trace the fault zeros LOS values.

In addition, the analysis of the mean LOS velocity changes in all the 5 profiles respecting the same LOS scale [-8 +8] mm helped to localize the fault trace according to the profile shape in zero-crossing area, as well the polynomial function that constraints the best fit of the scatterers LOS values (Table1; Figure 7). According to the 5 profiles, I determine the fault trace taking into account the zeros-LOS values with the profiles shape. Profile 1 gives the values of the zeros-LOS with the largest difference in the scatterers change between two scatterers neighbors. In profile 1, the best scatterers respecting this definition is located using the maximum between the absolute values of the difference between all the scatterers neighbors (see following equation):

$$Fault = \frac{Nbprofile}{1} \{Max (MeanVelo(1), \frac{N-1}{2} \{|MeanVelo(i) - MeanVelo(i + 1)|\})\} \quad (1)$$

The used polynomial function to identify the inflexion points from the LOS signal according the profile number is given by:

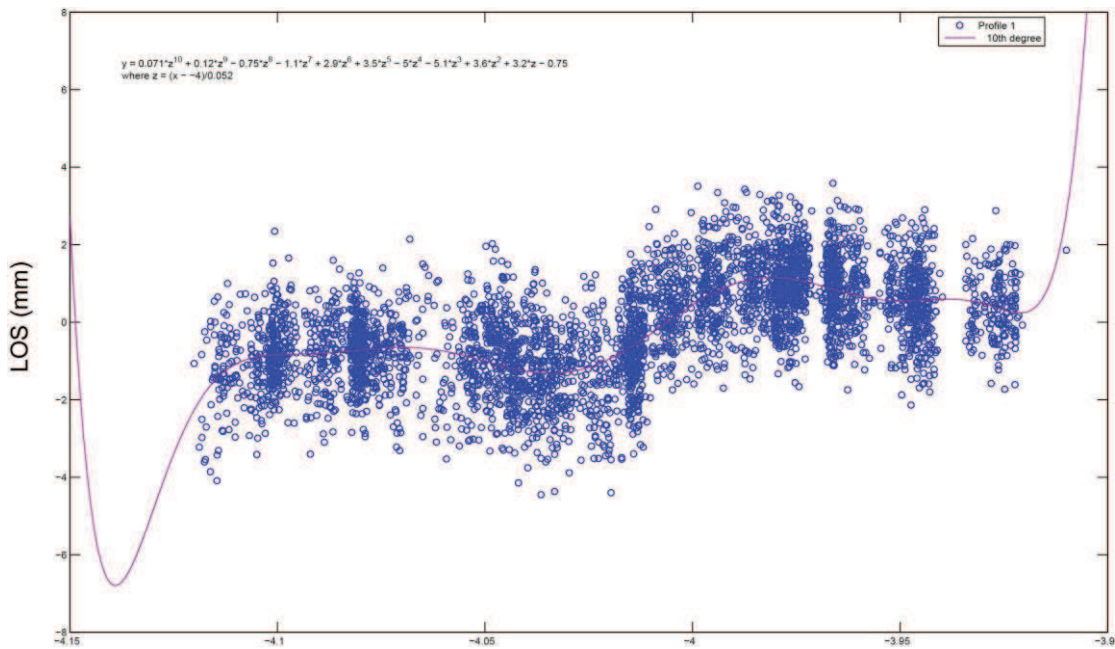
$$y = p_1 * z^{10} + p_2 * z^9 + p_3 * z^8 + p_4 * z^7 + p_5 * z^6 + p_6 * z^5 + p_7 * z^4 + p_8 * z^3 + p_9 * z^2 + p_{10} * z^1 + p_{11} \quad (2)$$

Profile	Location of zero LOS (Lon,Lat)	Polynomial Function	Amount of slip (subs+uplift)
1	(-4.21, 35.19)	$z = (x-\mu)/\sigma$	[-21,23]
		$\mu = -4.0165$	
		$\sigma = 0.052197$	
		Coefficients:	
		$p1 = 0.071151$	
		$p2 = 0.11585$	
		$p3 = -0.75209$	
		$p4 = -1.0544$	
		$p5 = 2.9051$	
		$p6 = 3.4926$	
		$p7 = -5.0271$	
2	(-3.99,35.18)	$z = (x-\mu)/\sigma$	[-32,30]
		$\mu = -3.9964$	
		$\sigma = 0.062464$	
		Coefficients:	
		$p1 = -0.17596$	
		$p2 = 2.3473$	
		$p3 = -1.3354$	
		$p4 = -12.73$	
		$p5 = 8.4031$	
		$p6 = 24.7$	
		$p7 = -13.217$	
$p8 = -21.02$			
$p9 = 7.2639$			
$p10 = 8.1333$			
$p11 = -1.2109$			

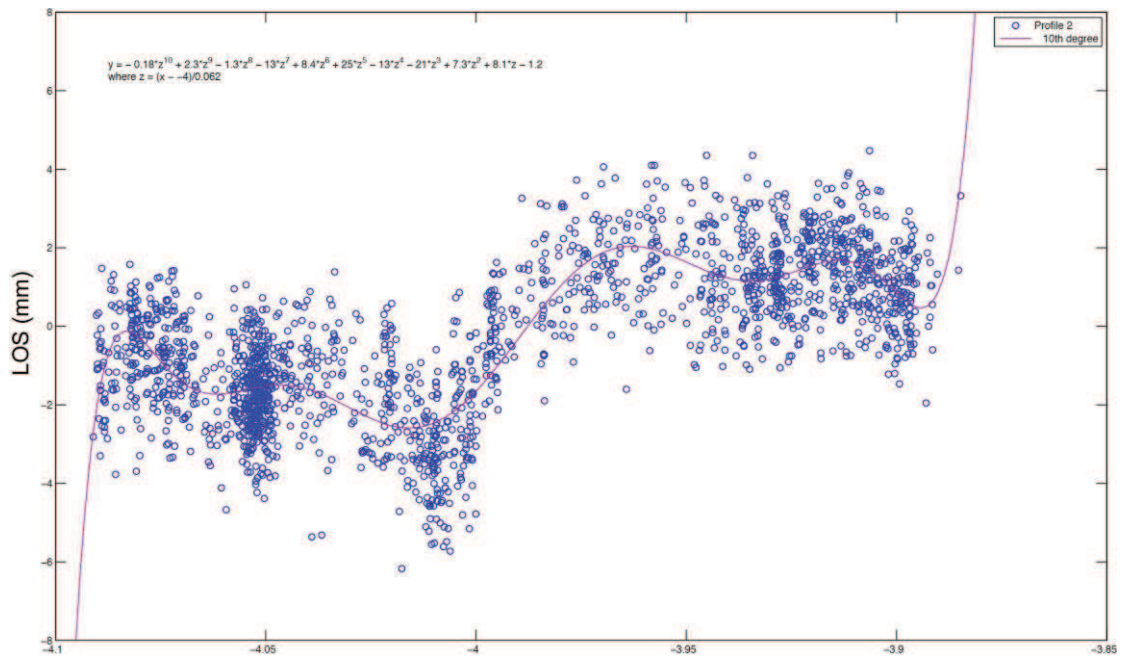
3	(-3.96,35.17)	$z = (x-\mu)/\sigma$ $\mu = -3.9469$ $\sigma = 0.056943$ Coefficients: $p1 = -1.0743$ $p2 = -0.75452$ $p3 = 9.9195$ $p4 = 4.8031$ $p5 = -33.554$ $p6 = -8.9836$ $p7 = 49.428$ $p8 = 2.8109$ $p9 = -29.075$ $p10 = 4.9203$ $p11 = 5.2829$	[-40,42]
4	(-3.92,35.15)	$z = (x-\mu)/\sigma$ $\mu = -3.9145$ $\sigma = 0.060433$ Coefficients: $p1 = 1.1273$ $p2 = 2.3828$ $p3 = -7.0906$ $p4 = -15.273$ $p5 = 16.3$ $p6 = 35.313$ $p7 = -16.42$ $p8 = -35.799$ $p9 = 5.5316$ $p10 = 15.309$ $p11 = 2.1213$	[-21,42]
5	(-3.87,35.14)	where $z$ is centered and scaled: $z = (x-\mu)/\sigma$	[-15,30]

$\mu = -3.8784$
$\sigma = 0.059892$
Coefficients:
$p1 = 0.32062$
$p2 = 0.49431$
$p3 = -3.0603$
$p4 = -4.6715$
$p5 = 9.5047$
$p6 = 13.965$
$p7 = -11.736$
$p8 = -16.502$
$p9 = 4.5869$
$p10 = 7.502$
$p11 = 1.1071$

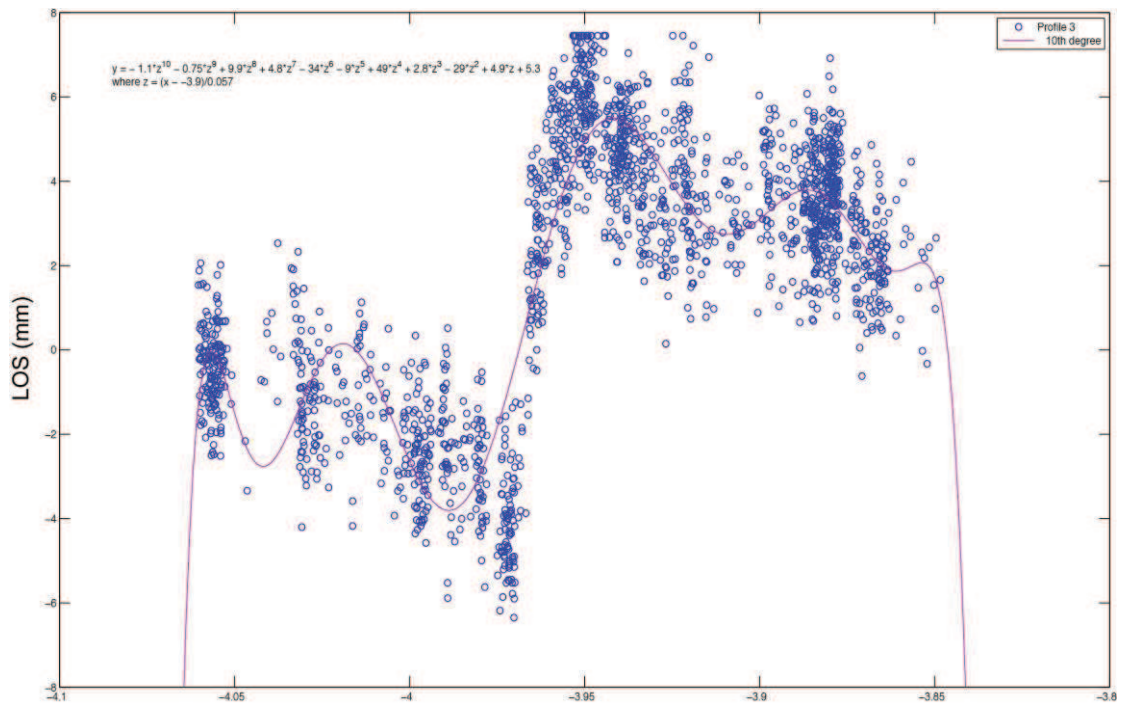
**Table 1:** The 10<sup>th</sup> degree polynomial functions used to describe the best fitting parameters values that embrace the profiles means velocity values associated with the postseismic events.



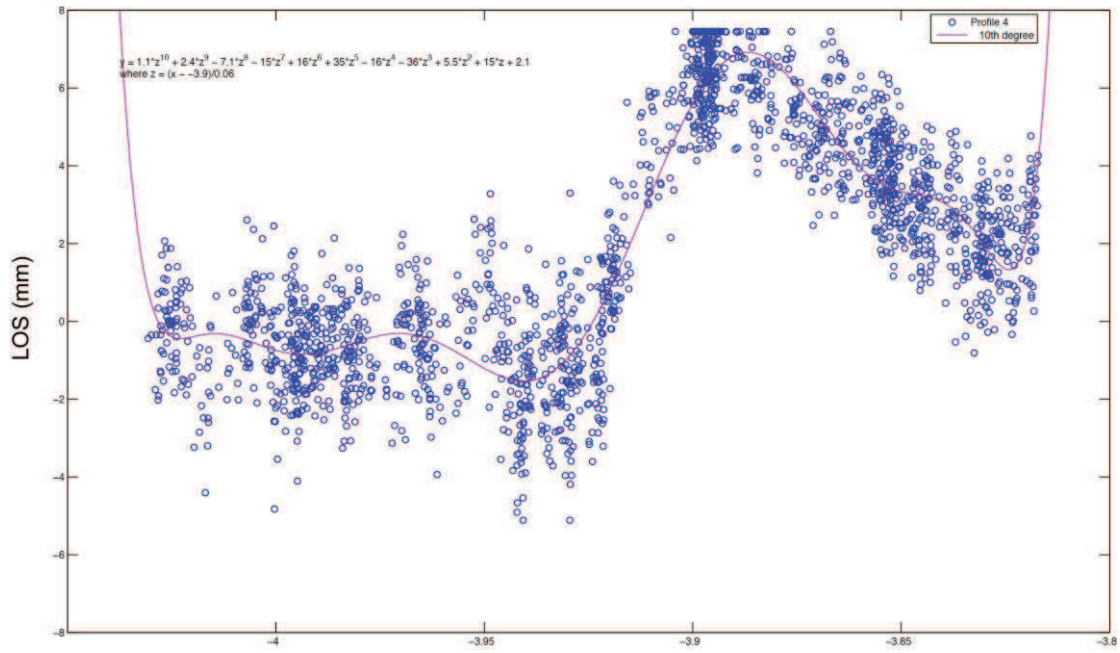
(a)



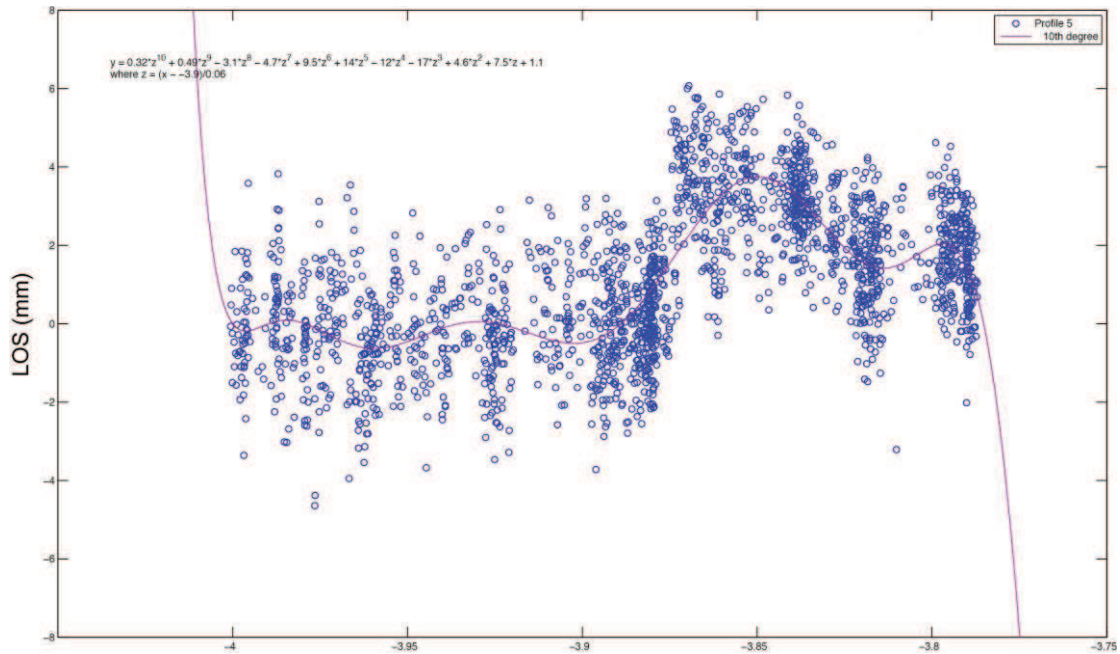
(b)



(c)



(d)



(e)

**Figure 7:** (a,b,c,d,e) for each profile, the recorded means velocity is plotted according to the profile geolocation; Blue circles indicate the scatterers LOS displacement in LOS direction (mm) and the red line indicate the polynomial fit function that express the scatterers values and distribution.

Figure 8 displays the results of the merged InSAR analysis with a sharp limit between two areas of postseismic surface deformation (mainly dark blue and red). It appears that the coseismic fault location according to Çakir et al. (2006) does not coincide with the presumable fault trace inferred either from the limit between the positive and negative displacements, or from profiles of Figure 9 (line n°2 in Figure 8). Indeed, ~ 6 to 8 km separate the coseismic fault and the postseismic trace. The existence of cross-faults at depth (pair of fault ruptures) as described in Tahayt et al. (2009) or a secondary branch from the 2004 rupture may explain the location of the postseismic displacements at the surface. Furthermore, in order to test the existence or not of topographic contribution in the final LOS signal, I also plot the cumulative displacement in LOS (mm) with the topography (Figure 9).

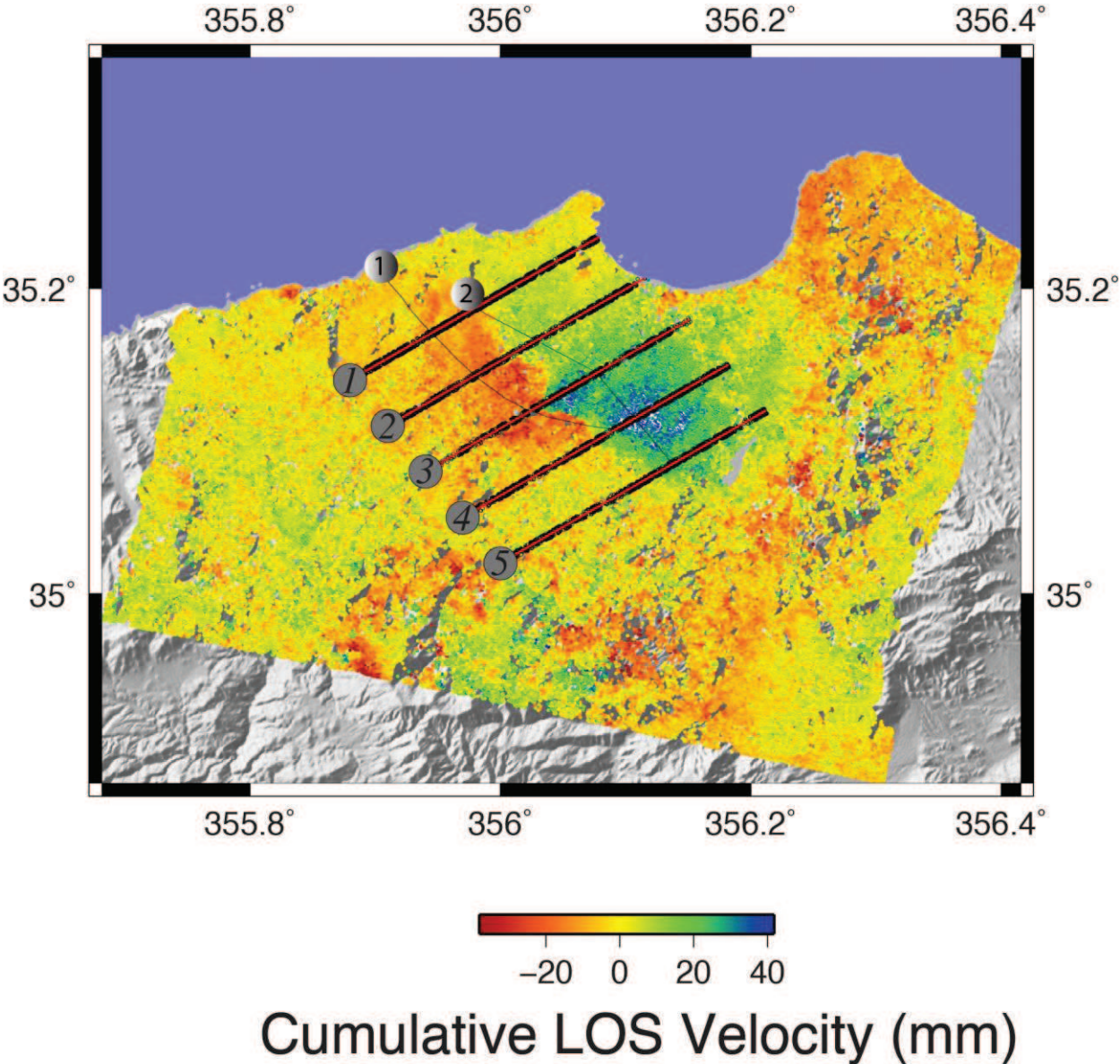


**Figure 8:** Merged InSAR results. The comparison between fault location according to (Çakir et al., 2006) and the fault trace located in this study ~ 8 km separate the faults trace witch can be explain by the existence of cross-fault (pair of fault raptures) as described in (Tahayt et al., 2009). The merged LOS signal shows a total maximum of 75 mm displacement (see also profile 3 in Figure 10).

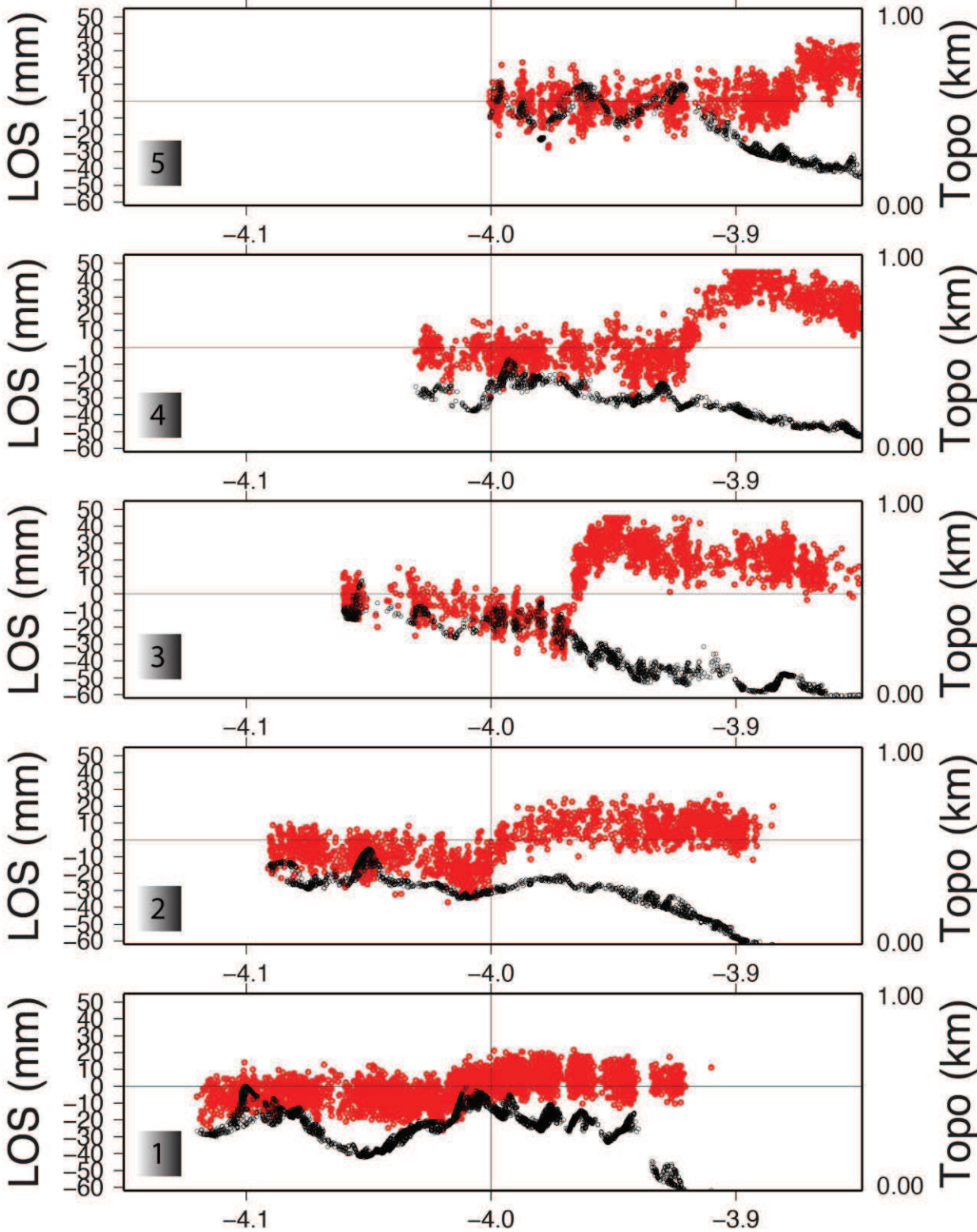


**Figure 9:** The comparison between the topography (black scatters) and the cumulative displacement in LOS (red scatters) indicates that from the shape of both signals, there is no correlation. The merged LOS signal shows a total maximum of 75 mm displacement.

I plot the fault location obtained from PS-SB merged method (Figure 8, line number 2) according to the maximum sudden change in LOS value from the 5 profiles and the fault location obtained with Cakir et al. (2006) using this Matlab code:

```
px5 = importdata('px5');
pos = 0;
maxx = 0;
diff = 0;
for i = 2:length(px5)
    diff = abs(abs(px5(i-1,4)) - abs(px5(i,4)));
    if (diff > maxx)
        maxx = diff;
        pos = i;
    end
end
px5(pos,1:2)
```

The difference between the two faults locations can reach ~8 km. I apply smoothing function in order to eliminate the dispersed values.

### **3. Modeling:**

I use the 3-D boundary element method Poly3Dinv base on the use of triangular dislocations in a linear-elastic and half-space elastic space. The fault surface is constructed respecting the triangular dislocation elements as a structure. I invert the cumulative merged PS-SB velocity file that gives a good coherence and a big signal/noise ratio. The fact that 2004 Al Hoceima fault rupture did not reach the surface add to the complexity of the interpretation of the surface deformation recorded by the InSAR.

I use the same model parameters as in Çakir et al. (2006; model 4B and 2A) and consider that the fault is NW-SE trending. The strike-slip distribution on the fault rupture is shown in Figure 10. The slip distribution obtained from the inversion of the postseismic deformation

shows a maximum of 3 cm (dextral strike-slip) at 8.5- km-depth. As in Cakir et al. (2006), the model in Figure 11 is obtained with fault parameters: Width = 16.5 km; Dip = 88° NE.

# strike-slip

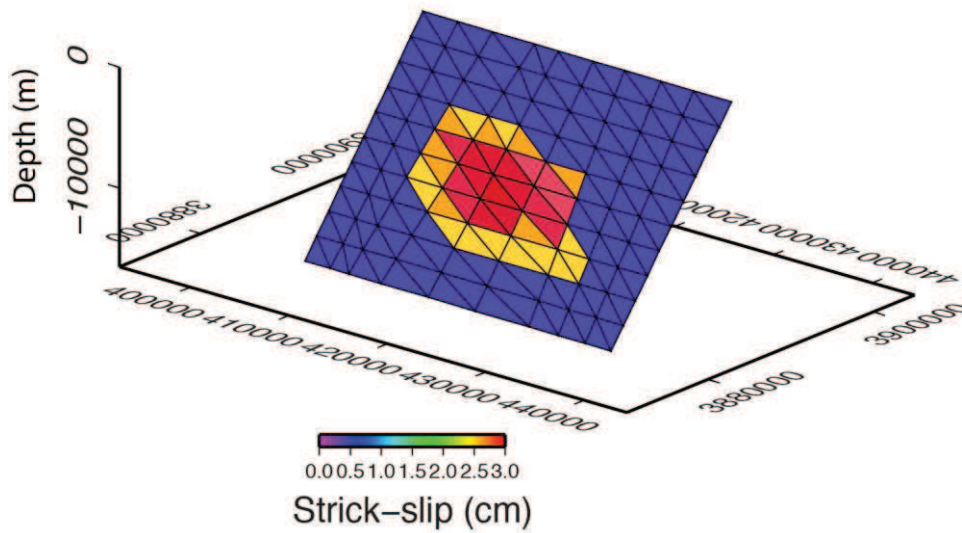


**Figure 10:** Strick slip distribution of the 2004 Al hoceima fault rupture.

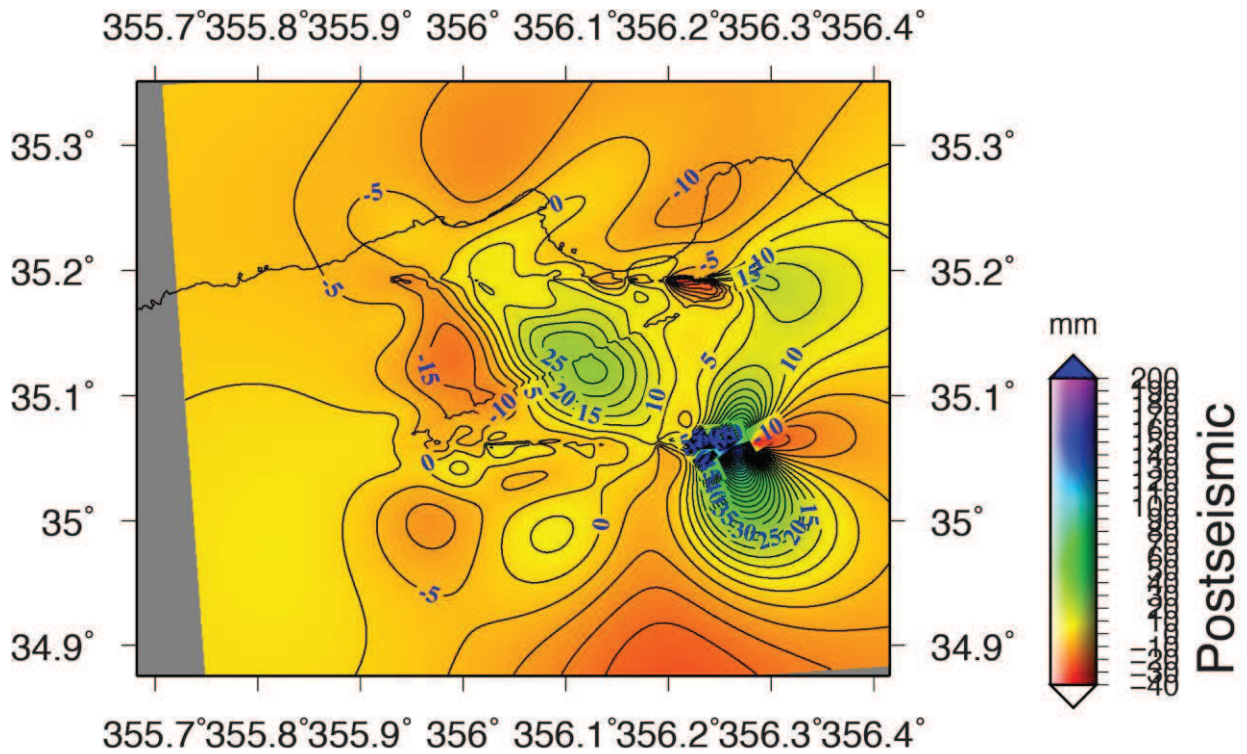


**Figure 11:** Postseismic model-1 obtained with parameters Width = 16.5 km; Dip = 88° NE).

## 4. Discussion and conclusion:

The MT-InSAR data from the ERS-2 satellite (2004 – 2010) reveals the existence of a significant surface deformation that reaches ~ 75 mm in the LOS direction. The merged InSAR results also provide an average LOS velocity ranging between -6 to 6 mm/yr. In comparison with the 2004 coseismic surface deformation and fault rupture modeled from InSAR study (Çakir et al., 2006), the maximum positive in cumulative displacement is located at the southeastern edge of the coseismic fault (Figure 8). The limit between the maximum and minimum subsided and uplifted postseismic deformation, respectively, does not coincide with the trace of the 2004 fault rupture. The ~6 to 8 km shift to the east indicates that the postseismic deformation at depth may occur on a fault section of the 2004 rupture but extends at the surface on a secondary fault branch. The model obtained by inversion on selected fault parameters in Figure 11 is consistent with the surface displacement obtained from MT-InSAR results.

## References:

- Akoglu, A. M., Çakir, Z., Meghraoui, M., Belabbes, S., El Alami, S. O., Ergintav, S., et al. (2006). The 1994–2004 Al Hoceima (Morocco) earthquake sequence: conjugate fault ruptures deduced from InSAR. *Earth and Planetary Sciences Letters*, 252, 467–480.
- Berardino, P., G. Fornaro, R. Lanari, & E. Sansosti. (2002). A New Algorithm For Surface Deformation Monitoring Based On Small Baseline Differential SAR Interferograms, *IEEE Trans. Geosci. Remote Sens.* 40, 2375 – 2383.
- Biggs, J., Bergman, E., Emmerson, B., Funning, G., Jackson, J., Parsons, B. & Wright, T., 2006. Fault identification for buried strike-slip earthquakes using InSAR: the 1994 and 2004 Al Hoceima, Morocco, earthquakes, *Geophys. J. Int.*, 166, 1347–1362.
- Çakir, Z., Meghraoui, M., Akoglu, A. M., Jabour, N., Belabbes, S., & Aït Brahim, L. (2006). Surface deformation associated with the  $M_w$  6.4, 24 February 2004 Al Hoceima, Morocco, earthquake deduced from InSAR: implications for the active tectonics along North Africa. *Bulletin of Seismological Society of America*, 96(1), 59–68.
- Harvard CMT (2005). Centroid Moment Tensor Project, On-line Catalog. <http://www.globalcmt.org/CMTsearch.html>

Ferretti A., Prati C., Rocca F. (2001). Permanent Scatterers In SAR Interferometry, IEEE Trans. Geosci. Remote Sens. 39, 1, 8-20.

Hooper, A. (2008). A Multi-Temporal InSAR Method Incorporating Both Persistent Scatterer And Small Baseline Approaches, Geophys. Res. Letters 35, L16302, Doi:10.1029/2008GL034654.

Massonnet, D., & Feigl, K.L. (1998). Radar Interferometry And Its Application To Changes In The Earth's Surface. Reviews Of Geophysics 36, 441-500.

NASA/SRTM (2005). SRTM3: Shuttle Radar Topography Mission digital topographic data. Version2, <ftp://e0srp01u.ecs.nasa.gov/srtm/version2/SRTM3/>

Rosen, P. A., S. Henley, G. Peltzer, and M. Simons (2004), Updated Repeat Orbit Interferometry Package Released, Eos Trans. AGU, 85(5), 47.

Scharroo, R., & Visser, P. (1998). Precise orbit determination and gravity field improvement for the ERS satellites. Journal of Geophysical Research, 103(C4), 8113–8127.

Simons, M., and P. A. Rosen (2007), Interferometric synthetic aperture radar geodesy, in Treatise on Geophysics, vol. 3 Geodesy , edited by G. Schubert, pp. 391– 447, Elsevier, Amsterdam.

Tahayt, A., Mourabit, T., Rigo, et al. (2009). The Al Hoceima (Morocco) earthquake of 24 February 2004, analysis and interpretation of data from ENVISAT ASAR and SPOT5 validated by ground-based observations. Remote Sensing of Environment 113 (2009) 306–316.

Thomas, A. L. (1993). POLY3D, A Three-Dimensional, Polygonal Element, Displacement Discontinuity Boundary Element Computer Program With Applications to Fractures, Faults, and Cavities in the Earth's Crust, M.S. Thesis, Stanford University, Stanford, CA.

Wessel, P., & Smith H. F. (1998), New improved version of the Generic Mapping Tools Released, EOS Trans. AGU, 79, 579.

## **General Conclusion**



In this thesis, I present the use of advanced InSAR processing methods applied to the study of mainly small surface deformation. Throughout the case-studies treated in this work, I use Persistent Scatterer (PS), Small Baseline (SB) and merged methods of MT-InSAR processing. The sub-millimeter accuracy of InSAR time series is exploited as an objective and application to geophysical issues in different areas with surface deformation. In comparison with conventional InSAR, uncertainties in the phase difference between two images taken at different times with different looking angle are mostly explored with the analysis of time series of SAR image data. The application of MT-InSAR to small surface deformation requires careful processing of interferograms due to the atmospheric delay, the topographic contribution and the orbital artifacts and related signal/noise ratio. The InSAR time series analysis takes advantage of the multi-temporal approach in order to constrain the physical parameters, enhance the final results in the study SAR images and obtain consistent interpretations of the related surface deformation.

This thesis highlights the use of InSAR time series analysis to measure different geophysical phenomenon and natural hazard events. This work addresses five different case-studies cases that include subsidence in a desert area, landslides in an urban area, and postseismic (and even perhaps interseismic) surface deformation associated with large and moderate earthquakes.

The surface displacement (sinkhole and subsidence) accessible using eight years (1992 to 2000) of SAR images is observed and measured in the Haoud Berkaoui oil field area. The accident occurred in 1978 and a large crater was formed with 320-m diameter and ~80-m depth at ~30 km from Ouargla, a city with a significant urban extension. The MT-InSAR shows a 64 km<sup>2</sup> subsidence area next to a 320-m-wide diameter sinkhole at the oil-well location. The surface deformation has average 1.5-mm/year subsidence and a model explains the dissolution collapse at depth. This partly man-made hazard may occur in other neighboring zones (OKN32) and generate further collapse of other oil wells in the same area.

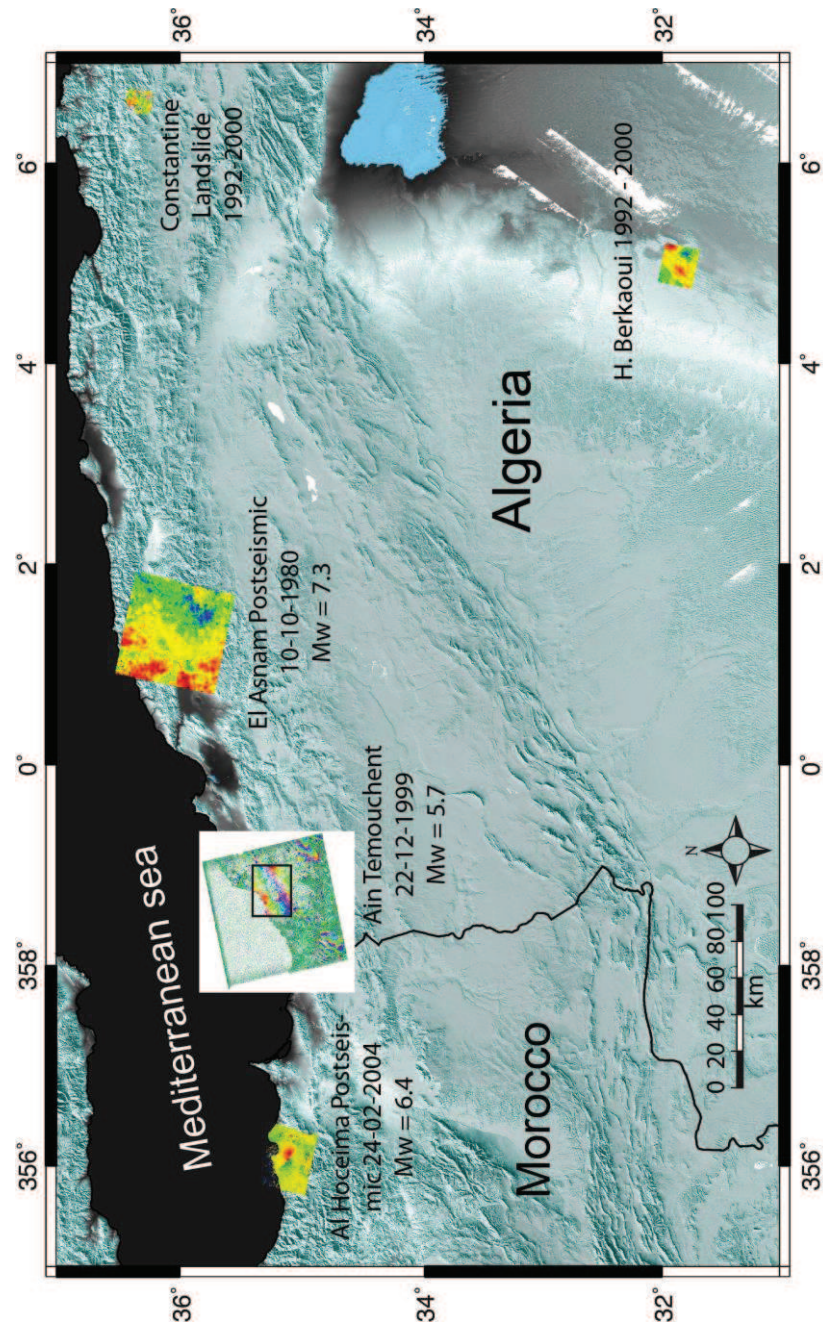


**Figure 1:** Studied sites with InSAR results of this thesis (plotted on shaded SRTM 3+). They show a subsidence at Haoud Berkaoui, landslides in the urban area of Constantine, and earthquake surface deformation at El Asnam, Ain Temouchent and Al Hoceima.

The monitoring of landslides by means of MT- InSAR analysis for eight years of data (SAR images) identifies prominent surface deformation in the Constantine urban Area (Northeast Algeria). Therefore, I use PS-SB and merged InSAR methods and obtain ~6.3 mm/yr from the combined (cumulative) rate of LOS deformation in the landslide area. In parallel, I developed

some aspects of the merged method and obtained  $\sim 3.15$  mm/yr velocity rate of individual landslide movement.

The use of open access GMTSAR (Generic Mapping Tools SAR; Sandwell, 2011) is tested for the InSAR analysis of the surface deformation associated with a moderate seismic event in northwest Algeria (Mw 5.7, 1999 AinTemouchent earthquake). GMTSAR was applied to the same data sets as in (Belabbes et al., 2009) and I added a new algorithm that counts automatically the number of fringes along with a new Graphical User Interface (GUI). Our new analysis of InSAR data reveals the existence of an additional fringe in the earthquake area, which indicates a total 14.3 cm LOS surface displacement.

The prominent 36-km-long surface displacement at the NE trending El-Asnam thrust fault (NW Algeria) responsible of two large earthquakes (Ms 6.7 in 1954 and Ms 7.3 in 1980) are also explored using PS and SB methods of time series analysis of SAR images from 1997 to 2000. Even nowadays, the InSAR results displays surface deformation where the El Asnam fault zone limits two tectonic blocks, with an uplifted (positive LOS) and a subsided area (negative LOS) of slow deformation reaching 30.4 mm cumulative displacement (over 4 years) covering the Chelif basin. The persistence of the surface deformation more than 40 years after the large Mw 7.3 earthquake is discussed in comparison with the seismic cycle of this plate boundary active zone in northern Algeria.

Similarly, the analysis of ERS SAR images from 2004 to 2010 in the area of the 1994 (Mw 5.9 and 2004 (M<sub>w</sub> 6.4) earthquakes at Al Hoceima (Morocco) shows a clear interferometric signal of surface deformation. A discrepancy in the location of the postseismic surface deformation indicates a complex fault structure with possible branching of seismic ruptures at depth. The characteristics and persistence of the cumulative  $\sim 87$  mm of 6 years postseismic deformation is discussed and a model of faulting geometry at depth is proposed to explain the relationships with the surface deformation.

The case-studies presented in this thesis show the use of remote sensing techniques and mainly PS and SB of the multi-temporal InSAR with some conceptual developments. Permanent Scatterer (PS) and Small Baseline (SB) SAR Interferometry aim to identify coherent radar targets presenting high phase stability over time (Ferretti et al., 2001) and/or in space (Hooper, 2008). Effective reflectors very often correspond to man-made (in city), with less effectiveness in non-urban areas. In order to overcome the limits of PS-InSAR and Small Baseline (SB) for time series analysis based on data-stacks of sets of interferograms, one should also take into account the information from distributed scatterers (DS) and not just from a single scatterer. As presented in this thesis, one way to do so is the combination of more than one algorithm (hybrid approach).

The monitoring of small surface deformation using the MT-InSAR approach may have decisive implications on the identification of natural hazards and mitigation of natural risks. The application of InSAR results may help in preventing natural risks in regions where urban areas have known a significant development of population growth. The advantage of MT-InSAR is in the understanding of spatial and temporal evolution of natural (or man-made) hazards in regions with limited field access.

## List of all references:

- Adam, N., Kampes, B., Eineder, M., Worawattanamateekul, J., and Kircher, M. (2003). The development of a scientific permanent scatterer system. In: ISPRS workshop. Inst. for Photogramm. and Geoinf., Hannover, Germany.
- Akoglu, A. M., Çakir, Z., Meghraoui, M., Belabbes, S., El Alami, S. O., Ergintav, S., et al. (2006). The 1994–2004 Al Hoceima (Morocco) earthquake sequence: conjugate fault ruptures deduced from InSAR. *Earth and Planetary Sciences Letters*, 252, 467–480.
- Akoglu, A. M., Çakir, Z., Meghraoui, M., Belabbes, S., El Alami, S. O., Ergintav, Çakir, Z., Meghraoui, M., Akoglu, A. M., Jabour, N., Belabbes, S., & Aït Brahim, L. (2006). Surface deformation associated with the  $M_w$  6.4, 24 February 2004 Al Hoceima, Morocco, earthquake deduced from InSAR: implications for the active tectonics along North Africa. *Bulletin of Seismological Society of America*, 96(1), 59–68.
- Akretche, S., Okbi, L. (1995). Historique de l'incident d'Okn 32, à la partie du nord du Sahara algérien, in Land subsidence, Proceedings of the land subsidence meeting, The Hague, IAHS Publ. 234 p.
- Amelung, F., Oppenheimer, C., Segall, P. and Zebker, H. (2000). Ground deformation near Gada 'Ale volcano, Afar, observed by radar interferometry. *Geophys. Res. Letters* 27(19): doi: 10.1029/2000GL008497. issn: 0094-8276.
- Aoudia, A., Meghraoui, M. (1995) Seismotectonics in the Tell Atlas of Algeria : the Cavaignac (Abou El Hassan) earthquake of 25.08.1922 ( $M_s = 5.9$ ). *Tectonophysics*. 248, 263-276.
- Alsop, G.I., and Marco, S. (2011). Soft-sediment deformation within seismogenic slumps of the Dead Sea Basin. *J. of Struct. Geology* 33, 433-457.
- Bawden, G., Thatcher, W., Stein, R.S., Hudnut, K.W., and Peltzer, G. (2011). Tectonic contraction across Los Angeles after removal of groundwater pumping effects, *Nature* 412, 812-815.
- Belabbes, S., (2008) Caractérisation de la déformation active par l'Interférométrie Radar (InSAR): Faillesismiques aveugles et cachées de l'Atlas Tellien (Algérie) et du Rif (Maroc) le long de la limite des plaques Afrique-Eurasie. PhD thesis, EOST University Louis Pasteur, Strasbourg, France, 226 pp.
- Belabbes S., Meghraoui M., Çakir Z., and Bouhadad Y., (2009) InSAR analysis of a blind thrust rupture and related active folding: the 1999 Ain Temouchent earthquake ( $M_w$  5.7. Algeria) case study. *Journal of Seismology* 13, 3, 421-432. Doi: 10.1007/s10950-008-9135-x.
- Bell, John W., Amelung, F., Ferretti, A., Bianchi, M. and Novali, F. (2008) Permanent scatterer

- InSAR reveals seasonal and long-term aquifer-system response to groundwater pumping and artificial recharge. *ATER RESOURCES RESEARCH*, VOL. 44, W02407, doi:10.1029/2007WR006152.
- Benaissa A., Cordary D., Giraud A. Les Mouvements de Terrain dans La Zone Urbaine de Constantine (Algerie) (1989). *Bulletin of the International Association of Engineering Geology*. N40.85-90.
- Benazzouz, M.T., 2002. Les Caractéristiques Géomorphologique Des Glissements De Terrain À Constantine (Algérie): Risques Et Aménagement. In: Proc. Symp. "Geomorphology: From Expert Opinion To Modeling", Strasbourg, France, April 2002, pp. 87-94.
- Berardino, P., G. Fornaro, R. Lanari, and E. Sansosti. (2002). A new algorithm for surface deformation monitoring based on small baseline differential SAR interferograms, *IEEE Trans. Geosci. Remote Sens.* 40, 2375 – 2383.
- Bernabé, Y., Mok, U., Evans, B. (2003). Permeability–porosity relationship in rocks subjected to various evolution processes. *Pure and Applied Geophysics* 160, 937–960.
- Bert M Kampes, Ramon F Hanssen, and Zbigniew Perski. (2003) Radar interferometry with public domain tools. In *Third International Workshop on ERS SAR Interferometry, 'FRINGE03'*, Frascati, Italy, 1-5 Dec 2003, page 6 pp.
- Bouraoui, S., Meghraoui, M., Bougdal, R., Monitoring Ground Deformation in the Haoud Berkaoui Oil Field (Sahara, Algeria) Using Times series Analysis of SAR Images. *Natural Hazards*, 2103.(Under review).
- Burgmann, R., Rosen, P. A., Fielding, E. J., (2000). synthetic aperture radar interferometry to measure earth's surface topography and its deformation. *Annual Reviews. Earth Planet.Sci.* 28:169-209.
- Bezzeghoud M., Dimitrov D., Ruegg J.C., & Lamali K., (1995). Faulting mechanism of the El Asnam 1954 and 1980 earthquakes from modelling of vertical movement. *Tectonophysics*, 249, 249-266.
- Bianchi, M., and Ferretti, A., (2006), Land deformation monitoring using satellite radar data processed with the Permanent Scatterers Technique (POLIMI PS Technique), *Tele-Rilevamento Europa*, 30 p., Milano.
- Biggs, J., Bergman, E., Emmerson, B., Funning, G., Jackson, J., Parsons, B. & Wright, T., 2006. Fault identification for buried strike-slip earthquakes using InSAR: the 1994 and 2004 Al Hoceima, Morocco, earthquakes, *Geophys. J. Int.*,166, 1347–1362.
- Çakir, Z., A. Barka, J-B.deChabalier, R. Armijo, B. Meyer. (2003). Kinematics of the November 12, 1999 (Mw=7.2) Düzce earthquake deduced from SAR interferometry, *Turkish Journal*

of Earth Sciences 12, 105-118.

- Çakir, Z., A. M. Akoglu, S. Belabbes, S. Ergintav, M. Meghraoui, (2005), Creeping along the Ismetpasa section of the North Anatolian Fault (Western Turkey): Rate and extent from InSAR, *Earth and Plan. Sci. Lett.* 238, 225-234.
- Cakir Z., Meghraoui M., Akoglu AM., Jabour N., Belabbes S., and Ait BL., (2006) Surface deformation associated with the Mw 6.4, 24 February 2004 Al Hoceima, Morocco, earthquake deduced from InSAR; implications for the active tectonics along North Africa. *Bull Seismol Soc Am* 96:59-68. Doi:10.1785/0120050108.
- Calderhead, A.I., Therrien R., Rivera, A., Martel, R., Garfias, J. (2011) Simulating pumping-induced regional land subsidence with the use of InSAR and field data in the Toluca Valley, Mexico. *Advances in Water Resources*, VOL., 34., PP 83-97.
- Chen, C. W., and H. A. Zebker (2000). Network approaches to tow-dimensional phase unwrapping: Intractability and two new algorithms, *J. Op. Soc. Am. A Op., Image Sci.*, 17(3), 401-414, doi:10.1364/JOSAA.17.000401.
- Carnec, C., Massonnet, D. and King, C. (1996). Two examples of the use of SAR interferometry on displacement fields of small spatial extent, *Geophys. Res. Letters* 23(24): doi: 10.1029/96GL03042. issn: 0094-8276..
- Castañeda, C., Gutiérrez, F., Manunta, M. and Galve, J.P. (2009). DInSAR measurements of ground deformation by sinkholes, mining subsidence and landslides, Ebro River (Spain), *Earth Surface Processes and Landforms* 34, 1562-1574.
- Closson, D., AbouKaraki, N., Klinger, Y. & Hussein, M.J. (2005). Subsidence Hazards Assessment in the Southern Dead Sea Area, Jordan, *Pure and Applied Geophysics*, 162, 2, 221-248, ISSN 0033-4553.
- Colesanti C., Le Mouelic, A., Bennani, M., Raucoules, D., Carnec, C., Ferretti, A. (2005). Detection of mining related ground instabilities using the Permanent Scatterers Technique – a case study in the east of France, *International Journal of Remote Sensing* 26, 1, 201-207,.
- Davidson D. L. and Lankford. J. (1983). Mixed-mode crack opening in fatigue, *Materials Science and Engineering* 60, 3, 225-229.
- Dziewonski, A. M., T.-A. Chou and J. H. Woodhouse, (1981). Determination of earthquake source parameters from waveform data for studies of global and regional seismicity, *J. Geophys. Res.*, 86, 2825-2852. doi:10.1029/JB086iB04p02825.
- Ekström, G., M. Nettles, and A. M. Dziewonski,. (2012) The global CMT project 2004-2010: Centroid-moment tensors for 13,017 earthquakes, *Phys. Earth Planet. Inter.*, 200-201, 1-9,

2012. doi:10.1016/j.pepi.2012.04.002.
- Farr, T. G., and Kobrick, J. (2007). The Shuttle Radar Topography Mission, *Rev. Geophys.* 45, RG 2004, doi : 10.1029/2005RG000183.
- Feuga, B. (2009). Les effondrements dus à l'exploitation du sel, *Geosciences* 9, 86-95.
- Ferretti, A., Prati, C., and Rocca, F. (2000). Nonlinear subsidence rate estimation using permanent scatterers in differential SAR interferometry. *IEEE Trans. on Geosci. Remote Sensing*, 38(5), 2202–2212.
- Ferretti A., Prati C., Rocca F. (2001). Permanent Scatterers in SAR Interferometry, *IEEE Trans. on Geoscience and Remote Sensing* 39, 1, 8-20.
- Frumkin, A., Magaritz, M., Carmi, I., and Zak, I. (1991). The Holocene climatic record of the salt caves of Mount Sedom, Israel, *The Holocene* 3, p. 191-200.
- Fu, L. L., and Holt, B. (1982). Seasat view oceans and sea ice with synthetic aperture radar. Tech. rept. Jet Propulsion Lab.
- Gabriel, A. K., Goldstein, R. M., and Zebker, H. A. (1989). Mapping small elevation changes over large areas, differential radar interferometry. *J. Geophys. Res.* 94 (B7), 9183-9191.
- Gibson, J. J. (2002). Short-term evaporation and water budget comparisons in shallow arctic lakes using non-steady isotope mass balance, *Journal of Hydrology* 264, 247-266.
- Goldstein, R. M., H. Engelhardt, B. Kamb, and R. M. Frolich. (1993). Satellite radar interferometry for monitoring ice sheet motion: Application to an Antarctic ice stream. *Science* 262, 1525-1530.
- Goldstein, R. M. (1995). Atmospheric limitations to repeat-track radar interferometry. *Geophys. Res. Lett.*, 22(18), 2517–2520.
- Goldstein, R. M., and C. L. Werner. (1998). Radar interferogram filtering for geophysical applications, *Geophys. Res. Lett.*, 25(21), 4035–4038.
- Gourmelen N., S.W. Kim, A. Shepherd, J.W. Park, A. Sundal, H. Bjornsson, F. Palsson (2011) Ice velocity determined using conventional and multiple-aperture InSAR, *Earth and Planet. Sci. Let.* 307 (1-2), pp. 156-160, 10.1016/j.epsl.2011.04.026.
- Guarnieri M., (2000) “*ScanSAR interferometric monitoring using the PS technique*”, ERS ENVISAT symposium (Gothenburg, Sweden), 12-22 October 2000.
- Guemache M. A., Chatelain J. L., Machane D., Benahmed S., Djadia L. (2011). Failure of landslide stabilization measures: The sidi Rached viaduct case (Constantine, Algeria). *Journal of African Earth Sciences.* 59. 349-358.
- Kampes, B. M., and Adam, N. (2005). STUN algorithm for persistent scatterer interferometry. In: FRINGE 2005 Workshop. European Space Agency.

- Kampes, B. M. (2006). Radar Interferometry: Persistent Scatterer Technique. First edn. P. O. Box 17, 3300 AA, Dordrecht, The Netherlands: Springer.
- Lanari, R., Mora, O., Manunta, M., Mallorqui, J. J., Berardino, P., and Sansosti, E. (2004). A small-baseline approach for investigating deformations on full-resolution differential SAR interferograms. *grs*, 42(7), 1377–1386.
- Hanssen, R. F. (2001). Radar Interferometry: Data interpretation and error analysis, Kluwer Academic Publishers, Dordrecht, 308 p.
- Harvard CMT (2005). Centroid Moment Tensor Project, On-line Catalog. <http://www.globalcmt.org/CMTsearch.html>
- Hilley G. E., Bürgmann, R., Ferretti, A., Novali F., and Rocca, F. (2004). Dynamics of Slow-Moving Landslides from Permanent Scatterer Analysis, *Science* 304, 1952-1955.
- Hocine F., Belhadj A. M., Ouarzeddine M., Haddoud A., and Belhadj A. A. (2008). Suivi des failles et du cratère de Haoud Berkaoui sud Algérie par images radar ERS1/ERS2, XIèmes Journées Scientifiques du Réseau Télédétection de l'AUF, 276-279, Madagascar.
- Hooper, A., Zebker, H., Segall, P., and Kampes, B. (2004). A new method for measuring deformation on volcanoes and other natural terrains using InSAR persistent scatterers. *Geophys. Res. Lett.*, 31, L23611.
- Hooper, A. J.,(2006) Persistent scatterer radar interferometry for crustal deformation studies and modeling of volcanic deformation, Ph.D. thesis, Stanford University, pp.
- Hooper, A. and Zebker, H. (2007). Phase Unwrapping in Three Dimensions with Application to InSAR Time Series, *J. Optical Soc. of America*. 24, 2737-2747.
- Hooper, A. (2008). A multi-temporal InSAR method incorporating both persistent scatterer and small baseline approaches, *Geophys. Res. Letters* 35, L16302, doi:10.1029/2008GL034654.
- Hooper, A. (2009). A Statistical-Cost Approach to Unwrapping the Phase of InSAR Time Series, Proceedings FRINGE Workshop, ESA-Frascati (Italy).
- A. Hooper (2012), A volcano's sharp intake of breath , *Nature Geosci.*, 5, 686-687, doi:10.1038/ngeo1584.
- Kampes, B. M., and Adam, N. (2005). STUN algorithm for persistent scatterer interferometry. In: FRINGE 2005 Workshop. European Space Agency.
- Kanamori, H. (1978). Quantification of Earthquakes, *Nature* 271, 411-414 doi:10.1038/271411a0.
- Lundgren, P., Usai, S., Sansosti, E., Lanari, R., Tesauro, M., Fornaro, G., and Berardino, P. (2001). Modeling surface deformation observed with synthetic aperture radar

- interferometry at Campi Flegreicaldera, *J. Geophys. Res.* 106, 19355–19366.
- Machane, D., Bouhadad, Y., Cheikhounis, G., Chatelain, J.-L., Oubaiche, E.H., Abbas, K., Guillier, B., Bensalem, R., (2008). Examples of geomorphologic and geological hazards in Algeria. *Nat. Hazards* 45, 295–308.
- Massonnet, D., Rossi, M., Carmona, C., Adragna, F., Peltzer, G., Feigl, K., and Rabaute, T. (1993). The displacement field of the Landers earthquake mapped by radar interferometry. *Nature*, 364, 138–142.
- Massonnet, D., and Feigl, K.L. (1998). Radar interferometry and its application to changes in the Earth's surface. *Reviews of Geophysics* 36, 441-500.
- Meghraoui, M., & F. Doumaz. (1996). Earthquake-Induced Flooding And Paleoseismicity Of The El Asnam, Algeria, Fault-Related Fold. *Journal Of Geophysical Research*, 101, B8, 17,617-17,644.
- Muller, J. R. and Martel S. J. (2000). Numerical Models of Translational Landslide Rupture Surface Growth, *Pure appl, geophys* 157, 1009-1038.
- NASA/SRTM (2005). SRTM3: Shuttle Radar Topography Mission digital topographic data. Version2, <ftp://e0srp01u.ecs.nasa.gov/srtm/version2/SRTM3/>
- Nikolaeva, E. and Walter, T. R. (2012) Comparison of InSAR two-pass and time series methods for analyzing landslides in central Georgia, Caucasus. *Geoscience and Remote Sensing Symposium (IGARSS), IEEE International.* 7573 – 7576. doi: 10.1109/IGARSS.2012.6351909.
- Nocquet JM, Calais E (2004) Geodetic measurements of crustal deformation in the western Mediterranean and Europe, geodynamics of Azores–Tunisia. *Pure & Appl Geophys* 161:661–681, 0033-4553/04/030661-21. doi:10.1007/s00024-003-2468-z.
- Ouyed et al., (1981) Seismotectonics of the El Asnam earthquake. *Nature* 292, 26 - 31 (02 July 1981); doi:10.1038/292026a0.
- Philip, H. and Meghraoui, M., (1983). Structural analysis and interpretation of the surface deformations of the El Asnam earthquake. *Tectonics*, 2: 17-49.
- Razon, B., (1999), L'effondrement d'un forage réalisé par Total en 1978 menace de polluer les eaux de Ouargla, l'un des plus anciens oasis sahariens. *Magazine Don Quichotte de la Mancha*, juillet-aout, Paris.
- Richman, D., (1971) Three dimensional azimuth-correcting mapping radar, Tech. rep., USA: United Technologies Corporation.
- Riedel B. and Walther A. (2008) InSAR processing for the recognition of landslides. *Adv. Geosci.*, 14, 189–194.

- Rosen, P. A., S. Hensley, H. A. Zebker, F. H. Webb and E. J. Fielding (1996). Surface deformation and coherence measurements of Kilauea Volcano, Hawaii, from SIR-C radar interferometry. *J. Geoph. Res.* 101(E10): 23,109-23,125.
- Rosen, P.A., Hensley, S., Joughin, I.R., Li, F.K., Madsen, S.N., Rodriguez, E., Goldstein, R. M. (2000). Synthetic Aperture Radar Interferometry, *Proc. IEEE*.
- Rosen, P. A., S. Henley, G. Peltzer, and M. Simons, (2004) Updated Repeat Orbit Interferometry Package Released, *Eos Trans. AGU*, 85(5), 47.
- Ruegg, J.C., Kasser, M., Tarantola, A., Lepine, J.C. and Chouikrat, B., (1982). Deformations associated with the El-Asnam earth- quake of 10 October 1980: geodetic determinations of vertical and horizontal movements. *Bull. Seismol. Soc. Am*, 72(6): 2227-2244.
- Ryder I; Parsons B; Wright TJ; Funning GJ (2007) Post-seismic motion following the 1997 Manyi (Tibet) earthquake: InSAR observations and modelling, *GEOPHYS J INT*, 169, pp.1009-1027. doi: [10.1111/j.1365-246X.2006.03312.x](https://doi.org/10.1111/j.1365-246X.2006.03312.x).
- Sandwell, D. T., and Price, E. J. (1998). Phase gradient approach to stacking interferograms. *J. Geophys. Res.*, 103(B12), 30183–30204.
- Sandwell, D., Mellors R., Tong X., Wei M., and Wessel P., (2011), Open radar interferometry software for mapping surface deformation, *Eos Trans. AGU*, 92(28), doi:10.1029/2011EO280002.
- Sandwell D., Mellors R., Tong X., Wei Matt., and Wessel P., (2011). GMTSAR: An InSAR Processing System Based on Generic Mapping Tools. UC San Diego: Scripps Institution of Oceanography. Retrieved from: <http://escholarship.org/uc/item/8zq2c02m>.
- Scharoo, R. and Visser, P. (1998). Precise orbit determination and gravity field improvement for the ERS satellites, *J. Geophys. Res.* 103, 8113–8127.
- Schmidt, D. A. & Burgman, R. (2003). Time-dependent land uplift and subsidence in the Santa Clara valley, California, from a large interferometric, synthetic aperture radar dataset, *J. geophys. Res.* 108, 8534–8543.
- Service de la carte géologique, Algérie. (1952). Carte géologique de l'Algérie (1 :500 000), Agence Nationale de la Géologie (ANGCM), Ministère de l'Énergie et des Mines, Alger.
- Serpelloni E, Vannucci G, Pondrelli S, Argnani A, Casula G, Anzidei M, Baldi P, Gasperini P (2007) Kinematics of the western Africa–Eurasia plate boundary from focal mechanism and GPS data. *Geophys J Int* 169:1180–1200. doi: [10.1111/j.1365-246X.2007.03367.x](https://doi.org/10.1111/j.1365-246X.2007.03367.x)
- Schmidt, D.A. and R. Bürgmann, (2003) Time dependent land uplift and subsidence in the Santa Clara valley, California, from a large InSAR data set, *J. Geophys. Res.*, 108(B9), 2416, doi:10.1029/2002JB002267.

- Sidle, R. C. and Ochiai, H. (2006) Landslides- Processes, Prediction and Land Use, AGU Books Board, Washington, 312 pp.
- Simons, M., Fialko, Y., and Rivera, L. (2002). Coseismic deformation from the 1999 msb 7.1 hector mine, California, earthquake as inferred from insar and gps observations. *Bull. Seism. Soc. Am.*, 92(4), 1390–1402.
- Simons, M., and P. A. Rosen (2007), Interferometric synthetic aperture radar geodesy, in *Treatise on Geophysics*, vol. 3 Geodesy, edited by G. Schubert, pp. 391– 447, Elsevier, Amsterdam.
- Singhroy V., Coutre R., Alasset P.-J. and Poncos V. (2007). InSAR monitoring of landslides on permafrost terrain in Canada, *Proc. IAGRS*, pp.2451 -2454.
- Smith, W. H. F., and Sandwell, D. T. (1997). Global sea floor topography from satellite altimetry and ship depth soundings. *Science*, 277,1, 956-1,962.
- Snieder, R.; Hubbard, S.; Haney, M.; Bawden, G.; Hatchell, P.; Revil, A., and DOE. (2007). Geophysical Monitoring Working Group, Advanced noninvasive geophysical monitoring techniques, *Annu. Rev. Earth Pl. Sc.* 35, 653-683,
- Sonatrach. (1995). Suivi de l'évolution de l'effondrement d'Okn 32. Rapports internes (1990, 1992, 1994, 1995), Division Ingénierie et Production, Direction Regional Haoud Berkaoui.
- Sonatrach. (1998). Le cratère d'effondrement du puits OKN 32, Service Technique, Rapport Puits 17, Division Ingénierie et Production, Direction Regional Haoud Berkaoui.
- Stramondo S., Cinti F. R., Dragoni M., Salvi S., and Santini S., (2002) The August 17, 1999 Izmit, Turkey, earthquake: new insights on slip distribution from dislocation modeling of DInSAR and surface offset, *Annals of Geophysics*, vol. 45, n.3/4, pp. 527-536, June/August 2002.
- Sudhaus, H., and Jonsson, S., (2009). Improved source modelling through combined use of InSAR and GPS under consideration of correlated data errors: application to the June 2000 Kleifarvatn earthquake, Iceland *Geophys. J. Int.* 176, 389–404.
- Tahayt, A., Mourabit, T., Rigo, et al. (2009). The Al Hoceima (Morocco) earthquake of 24 February 2004, analysis and interpretation of data from ENVISAT ASAR and SPOT5 validated by ground-based observations. *Remote Sensing of Environment* 113 (2009) 306–316.
- Thomas, A. L. (1993). POLY3D, A Three-Dimensional, Polygonal Element, Displacement Discontinuity Boundary Element Computer Program With Applications to Fractures, Faults, and Cavities in the Earth's Crust, M.S. Thesis, Stanford University, Stanford, CA.

- Thompson, A., J.M. Moran, and G.W. Swenson. (1986). *Interferometry and Synthesis in Radio Astronomy*, Wiley-Interscience, New York, 528 p.
- van der Kooij, M., Hughes, W., Sato, S., and Poncos, V. (2006). Coherent target monitoring at high spatial density, Examples of validation results, Eur. Space Agency Spec. Publ., SP-610.
- Ventisette, C., D., Ventisette1, E., Intrieri1, G., Luzi, N., Casagli, R., F., , and Leva, D. (2011) Using ground based radar interferometry during emergency: the case of the A3 motorway (Calabria Region, Italy) threatened by a landslide. *Nat. Hazards Earth Syst. Sci.*, 11, 2483–2495.
- Wessel, P. and Smith, H.F. (1998). New improved version of the Generic Mapping Tools Released, *EOS Trans. AGU79*, p. 579.
- Wright, T.J., Lu, Z. & Wicks, C., (2003). Source model for the Mw 6.7, 23 October 2002, Nenana Mountain Earthquake (Alaska) from InSAR, *Geophys. Res. Lett.*, **30**(18), doi:10.1029/2003GL018014.
- Yelles, C. AK., Djellit H., Beldjoudi H., Bezzeghoud M. and Buform E., (2004) The Ain Temouchent (Algeria) earthquake of December 22<sup>nd</sup>, 1999, geodynamique of Azeros-Tunisia. *Pure Appl. Geophys* 161:607-621. doi:10.1007/s00024-003-2465-2.
- Yielding et al., (1981) Relations between surface deformation, fault geometry, seismicity, and rupture characteristics during the El Asnam (Algeria) earthquake of 10 October 1980. *Earth and Planetary, Science Letters*, 56, 287-304.
- Yueping Y. Wamo Z. Yuping L. Jialong Z. Xiaochun L. (2010) Integration of GPS with InSAR to monitoring of the Jiaju landslide in Sichuan, China. *Landslides*.7:359–365 DOI 10.1007/s10346-010-0225-9.
- Werner, C., Wegmuller, U., Strozzi, T., and Wiesmann, A. (2003). Interferometric point target analysis for deformation mapping. Pages 4362–4364 of: *Proceedings of Geoscience and Remote Sensing Symposium, IGARSS '03*, vol. 7.
- Zhen Li, Xinwu Li, Huadong G., Huanyin Y. and Quan C. (2009). Sub-Canopy Soil Moisture Inversion Using Repeat Pass Shuttle Imaging Radar C Polarimetric Synthetic Aperture Radar Interferometric Data, *J. Appl. Remote Sens.* 3, 033553; Doi:10.1117/1.3256001.
- Zebker, H.A., and R.M. Goldstein. (1986). Topographic mapping from interferometric SAR observations, *J. Geophys.Res.* 91, 4993-5000.
- Zebker, H. A., and Goldstein, R. M. (1986). Topographic mapping from interferometric synthetic aperture radar observations. *J. Geophys. Res.*, 91(B5), 4993–5000.
- Zebker, H. A., and Villasenor, J. (1992). Decorrelation in interferometric radar echoes. *IEEE*

Trans. on Geosci. Remote Sensing, 30(5), 950–959.

Zebker, H. A., Rosen, P. A., Goldstein, R. M., Gabriel, A., and Werner, C. (1994). On the derivation of coseismic displacement field using differential radar interferometry : The Landers earthquake. J. Geophys. Res., 99, 19618–19634.

Zisk, S. H., (1972) A new, Earth-based radar technique for the measurement of lunar topography., Moon, 4 (3/4), 296 – 306.

## **APPENDIX**





**GMTSAR Processing: Application to the Surface  
Deformation of A Moderate Mw 5.7 Seismic Event  
(1999 Ain Temouchent Earthquake, Northwest  
Algeria)**

## Summary:

In this section, I apply and discuss the use of InSAR processing system called GMTSAR (Sandwell et al., 2011a; Sandwell et al., 2011b), which is based on the Generic Mapping Tools (GMT; Wessel et al., 1998). GMT is a freeware program used in GMTSAR program to filter and display the radar interferometry results and map the surface changes as described in the post-processing steps of GMTSAR processing package. I present here the processing of 7 C-band ERS SAR images from an earthquake area using GMTSAR and discuss the resulting interferogram (Table 2). In addition, I proceed with a comparison with the same data set processed with SARscape® and presented in (Belabbes et al., 2009). The final step in the GMTSAR processing system is producing the postscript and KML files to be visualized in a graphic interface or in Google Earth.

GMTSAR provides the possibility to easily process SAR images and access to the programming code, adding some filters for enhancing the final results. I will describe the GMTSAR 2-pass processing diagram as detailed in (Sandwell et al., 2011a) and present new interferograms resulting from the same SAR pairs presented in Belabbes et al. (2009). Finally, I present an automatic method that count the number of fringes and show 5 fringes (14.15 cm) as compared with the 4 fringes found manually in (Belabbes et al., 2009). In order to facilitate the use of GMTSAR (Shell based processing), I built two different graphical interface (GUI), with the first one based on the QtSDK C++ programming for Unix system and Mac OS, and the second implemented with the Java programming language which is portable and independent from the OS system type. These two GUIs versions are presented for ERS SAR processing images and will be generalized in the future for all types of radar images that can be processed with GMTSAR (Envisat, Radarsat, Alos-Palsar, Sentinel, ...).

# 1. Introduction

I study the coseismic surface displacement of the moderate seismic event (Mw 5.7) that occurred in Ain Temouchent (northwestern Algeria; (Figure 1)) using GMTSAR freeware program and the processing of SAR images to produce interferograms and map of surface changes. The moderate Mw = 5.7 and shallow earthquake occurred on December 22, 1999 at Ain Temouchent (Yelles et al., 2004; Belabbes et al., 2009) and caused a serious damage with 25 victims and visible damage to the buildings. This earthquake was located by different institutions yielding diverse epicenter locations, e.g., CRAAG [35.25°, -1.30°], USGS [35.32°, -1.28°], CSEM [35.23°, -1.39°], indicating the large error range in the seismological determination. The previous InSAR study of Belabbes et al. (2009) provides the area of maximum surface deformation (a few km southwest of Ain Temouchent city). The main shock focal mechanism solution indicates reverse faulting with a NE–SW trending ruptures consistent with the uplifted surface deformation (~11 cm) obtained from the coseismic interferogram and the use of the commercial SARscape software (Belabbes et al., 2009). Belabbes et al., 2009 calculate four interferograms and show the best interferogram with the shortest time interval and smallest baseline distance in order to have the best signal/noise ratio. From them, they give a model based on the analytical solution and Poly3Dinv program (Thomas et al., 1993). The phase unwrapping was not being produced due to the low coherence and difficulties, and then he used manual digitalized fringes. In all previous InSAR studies (Belabbes et al. 2009; Cakir et al., 2006; Stramondo et al., 2002) the authors used manual methods based on experience observation to count the number of fringes from the interferogram.

In this work, and in order to test GMTSAR I selected a pair of ERS-SAR data (Table 2) with short temporal and small baseline distance. All the 7 ERS-SAR images are recorded with the ascending orbit, track number 144 and frame number 697 (Figure 1). Several interferograms were calculated with different pairs combination (in total 9 interferograms were generated) and I present the best and suitable interferogram that illustrates the coseismic surface displacement and shows the best and clear fringes with good coherence and signal/noise ratio obtained between (ERS-2 25/11/1999 and ERS-2 13/04/2000; i.e. Table 2 with green background). The new interferogram measures five fringes and indicates an ellipse-shaped lobe that determines 14.15 cm peak line-of-sight displacement.

I present in the following the principles of GMTSAR and a description of the programming system necessary to obtain a SAR interferogram. The interferogram calculated

from a pair of ERS image analysis indicates the surface deformation and I implement a fringe counting method. Finally, I proceed with the analysis of interferogram and related uncertainties as obtained from GMTSAR, with a comparison with the surface deformation as obtained by Belabbes et al. (2009).

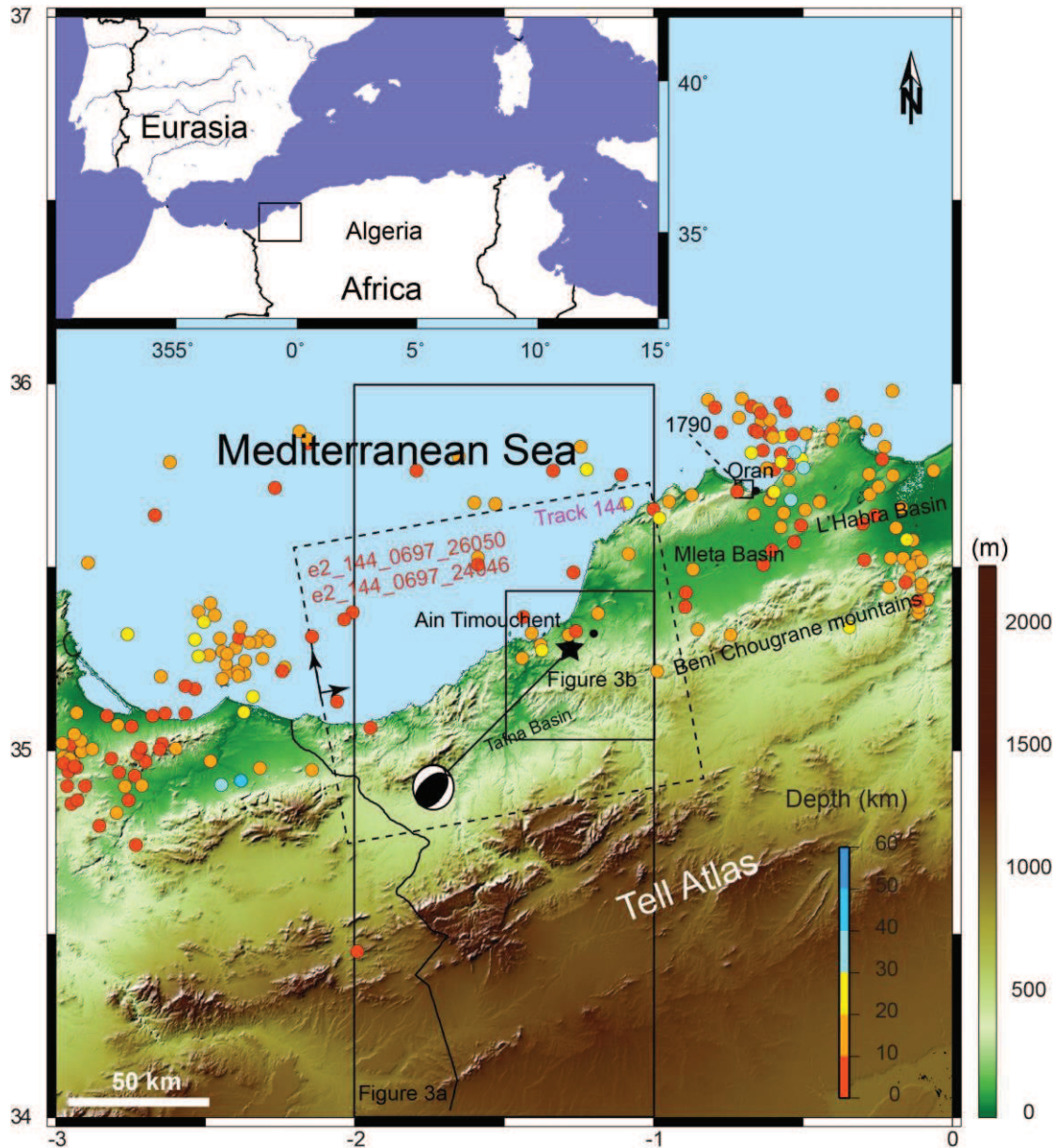


**Figure 1:** Seismotectonics of the Ain Temouchent earthquake area with shaded relief image from SRTM-3 are-sec data. The 1999 Ain Temouchent mainshock location (black star) is from CRAAG and the seismicity from the CNSS worldwide earthquake 1990-2012 catalogues. The square is from the main historical events from Belabbes et al. (2009). The focal mechanism solution of the 1999 Ain Temouchent (Mw 5.7) is shown from Global CMT. Dashed box shows the ERS SAR data frame (track 144) and the black arrows indicate the satellite flight direction (ascending) and the line of sight direction (towards east).

## 2. Seismotectonic Context

The Inter-Co-Post-Seismic deformations recorded in North Africa are caused by the cinematic of the barded plate between Africa and Eurasia. All the case of studies presents in this these are situated in the boundary regions (North of Algeria and Nort of Morocco) accepted Haoud Berkaoui, which represents Oil well accidental, caused by Human error, and Constantine Landslides, which is situated in region with low seismic activity. Figure 2, shows the seismicity of North Africa recorded between 1073 until 2013 from the NEIC database with events  $m_w \geq 4$ .

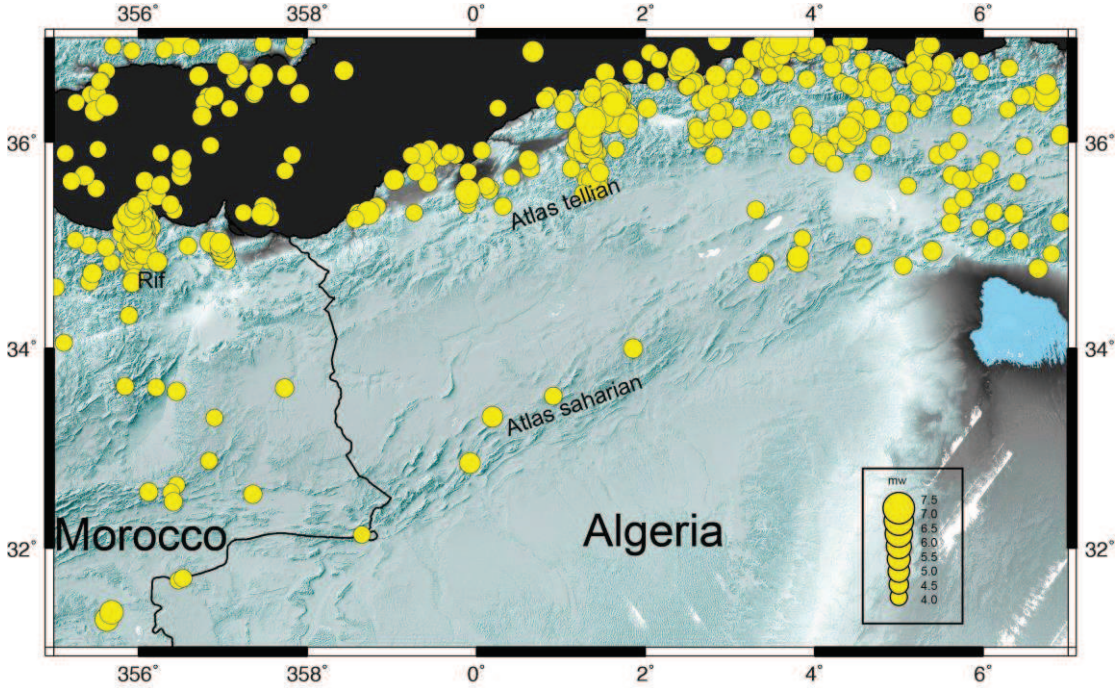


**Figure 2:** seismicity of the North Africa and the study area with  $M_w \geq 4$  recorded from 1973 and 2013 (data are from NEIC).

North Africa (south of the Mediterranean Sea) is situated on the junction of two plates, causing the high seismic activity of the region that explains the convergence between the North and south of the Eurasian and African plates from the Cretaceous.

The Figure 2 shows that the density of the seismicity is aligned on the northerner part of Africa and can be imitated by band of 100 km expressing the imitation of the Africa-Eurasian plates. The parameters of the plate movement can be determined with the geophysical measurement, as well as, the study of the faucal mechanism of the fault situated in the boundary between these two plates. Figure 3 and Figure 4, show the principal faults situated between the African and the Eurasia plates. Three of this big seismic event will be studied in this thesis: Al

Asnam, Ain Temouchent and Zemouri in the North of Algeria and Al Hoceima in the North of Morocco.

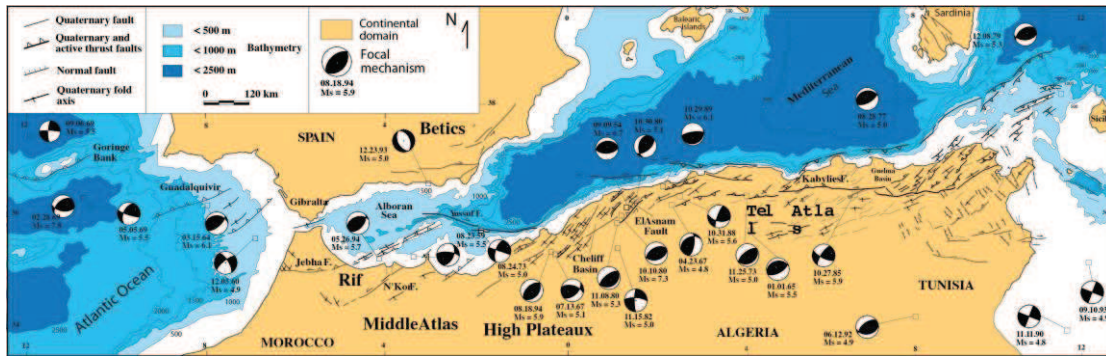


**Figure 3:** principal fault in North Africa and south European plates. The limitation of the tectonic plates and the principal faults mechanism are shown. Faulcal mechanisms are plotted using Global CMT.

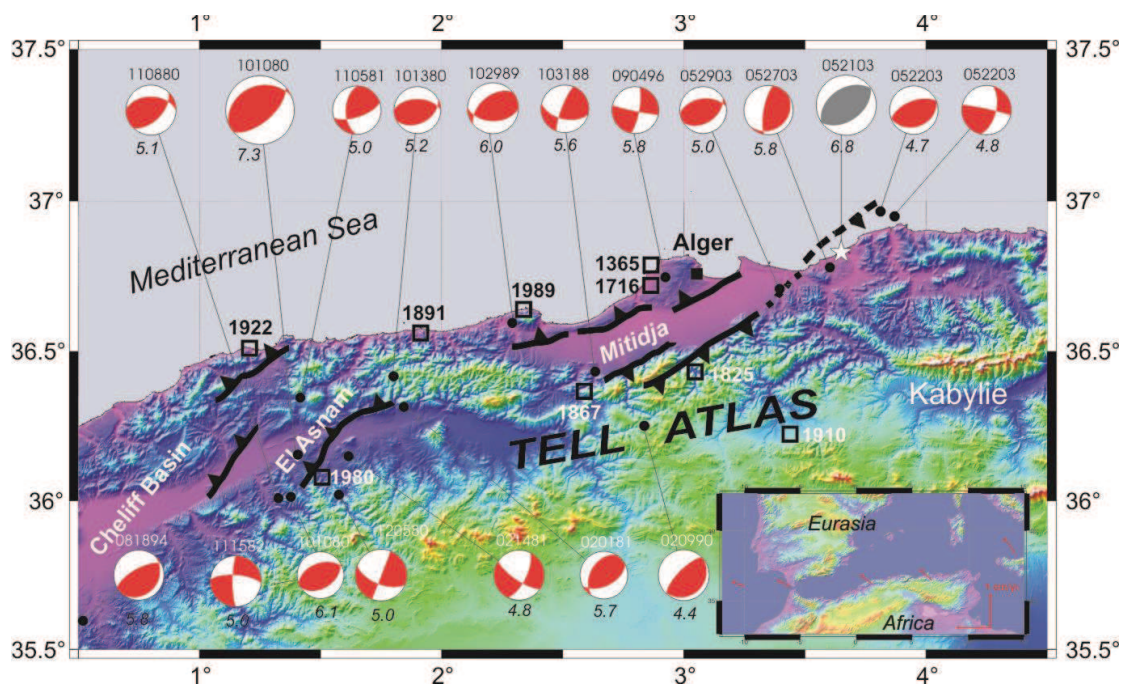


**Figure 4:** Morphotectonic map of Northwest Algeria with the principal faults ( $m_w > 4.0$ ). Focal mechanisms are plotted using the global CMT of the principal seismic activity after 1980 (Meghraoui, 1988). The speed of convergence between the Africa and Eurasia plates are in red arrows after the Nuvel-1A model (Argus et Gordon 1991).

The model Nuvel-1A proposed by (Argus et Gordon., 1991) is one of the best model used to explain the characteristics of the cinematic of plates on the three last million-years. Nuvel-1A is deriving from the Nuvel-1 model that is obtained with the inversion of 1122 data events situated in 22 plates limitations (boundary). In the North African region, the velocity of

convergence obtained from the model is 4 mm/yr at the Gibraltar and 5 mm/yr in North of Algeria.

Figure 5, present the events information in the study regions, The seismicity and faucal mechanism are presented together with  $m_w \geq 4$ . In this thesis, I will study three faults situated in the boundary of the African and Eurasian plates responsible of moderate earthquake (Al Asnam with 1980 Mw 7.3, Ain Temouchent 1999 Mw 5.7 and Al Hoceima 2004 Mw 6.4).

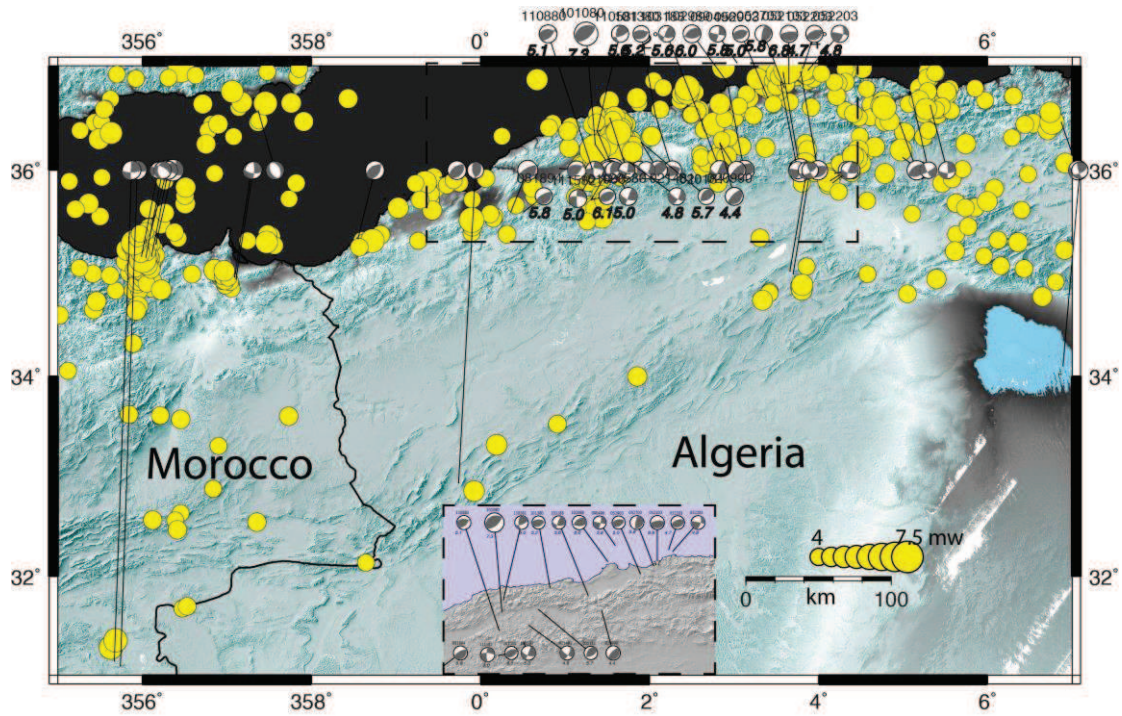


**Figure 5:** Seismicity of the North Africa with  $M_w \geq 4$  recorded from 1973 and 2013 (data are from NEIC) which is combined with the focal mechanisms plotted using the global CMT of the principal seismic activity recorded after 1980 (Meghraoui, 1988). Dashed rectangle shows zooms on the area of focal mechanism concentration (Al Asnam and Aint temouchent with Zemouri earthquakes)

### 3. GMTSAR systems

The open source and free package (GNU General Public License) InSAR processing system GMTSAR is written in c-code and csh scripts developed for InSAR processing (Sandwell et al., 2011a; Sandwell et al., 2011b). The method can start with preprocessing step from data recorded in radar coordinates (raw data), precise orbital information and the use of digital elevation model grid (DEM) for a given area as inputs for the system. The main system used to compute and generate the interferometric results from two SAR images in geographic coordinates (2-pass processing). The post-processing step consists in the GMT (Generic Mapping Tools) to map the results and show the different interferograms. GMTSAR has three main processing blocks as follows:

1. A preprocessor script for each satellite data type (ERS, Envisat, and ALOS) in order to convert the native recording format and orbital information into a generic format (preprocessing and focusing codes). Note that in case of ERS SAR images the system uses also 'getorb' program for orbital information.
2. The main part of the system, that allows the InSAR processing involving several 2-pass InSAR processing steps starting with the alignment of tracks of images and ending with the generation of the complex interferogram (phase difference, needs GMT and Netcdf).
3. A post-processor script, based on GMT to filter the interferogram and construct coherence phase gradient and line-of-sight displacement in both radar and geographic coordinates system. ("SNAPHU" software (Chen and Zebker, 2000) is used for phase unwrapping, and *grd2kml* script in order to prepare a *kml* file from gridding).

Two-pass processing method consists in common InSAR processing approaches that use two SAR images and a DEM (Digital Elevation Model) to produce the coseismic differential interferogram which is the result of multiplying the reference image by the complex conjugate of the repeat image and creating the complex InSAR result after subtracting the DEM values.

In the GMTSAR two-pass processing the system inputs are: The reference SAR image ([e2\_144\_0697\_24046.raw), the repeat SAR image (e2\_144\_0697\_26050.raw) and the digital elevation grid file. Notice that in the present study, the precise orbital information used for ERS is obtained with "getorb" software and the digital elevation grid (dem.grd) is generated from the [topex.ucsd.edu/gmtsar/demgen/](http://topex.ucsd.edu/gmtsar/demgen/) website. The hard part of the GMTSAR system is composed of the *xcorr* and the *phasediff* programs. *Xcorr* program takes as inputs two SLC files (focused single look complex image) in order to calculate the interferometric coherence between the Slave image

(repeat image) and the master image (reference image). Using the resulting correlation file, `phasediff` will calculate the interference between with the reference image as described in the taking into compt the topographic grid file (figure 6). The output files principally from this phase difference measuring, is real and image grid containing the real and the imaginary value of the inference process. In this step, the system has calculated the inteferogram, we can apply spatial filters or using GMT and also we can in this step introduce our filters in order to enhance the results. Unwrapping phase can be done using `snaphu`. The final step in the system processing consists of the geocoding of the resulting files and transforming the (x,y) coordinating system into the geological coordinating system. This processing step masked the phase values which are less than the given correlation threshold. Using GMTSAR open access software allow us to improve and make changes in all the processing steps by changing in the code or adding spatial filters in order to obtain the best signal/noir ration of the study case. InSAR Processing using GMTSAR system, the user should works in shell screen. In order to facilitate the analysis of the SAR data, there is a `process2pass` script describing all the processing steps starting from the preprocessing step until the generation of the final phase file and geocoding.

Not that GMTSAR package contain also codes for ScanSAR (Guarnieri et al., 2000) processing and able to perform time series analysis based on interferograms stacking (Sandwell et al., 2011a; Sandwell et al., 2011b). The complete syntax to process the ERS SAR images is:

```
P2p_ERS.csh e2_144_0697_24046 e2_144_0697_26050 config.ers.txt
```

The `/topo` directory should have `dem.grd` file and `/raw` directory should contain 4 files:

```
e2_144_0697_24046.dat
```

```
e2_144_0697_24046.ldr
```

```
e2_144_0697_26050.dat
```

```
e2_144_0697_26050.ldr
```

The processes step follows the diagram shown in (Figure 6).

## 4. InSAR data analysis:

InSAR is a remote sensing technique based on the emission/reception of height-frequency electromagnetic wave to generate sub-centimeter map of surface deformation or height resolution DEM from the radar wave differences (Hanssen, 2001). We use GMTSAR to process the same 7 C-band ERS-SAR ascending images of the European Space Agency (ESA) used before in (belabbes et al., 2009) for InSAR processing at the Ain Temouchent earthquake

area. With GMTSAR we follow the specific format of data: [e2\_144\_0697\_24046.raw e2\_144\_0697\_26050.raw] with: e2 : ERS-2 satellite type. 144: the track number. 0697: The Fram Number. 24046: The Orbital number.

The baseline parameters extracted from ERS-SAR images [e2\_144\_0697\_24046.PRM e2\_144\_0697\_26050.PRM] are indicated in Table 1.

Sat Track	Slave time	Bperp	xshift	yshift
E2 144	20001304	3024	-110.805529	-137.100194

**Table 1:** Baseline parameters from the two ERS-SAR pairs used in the generation of the suitable interferograms (see also Table 2).

The Bperp smallest distance information and the shortest time interval are the two parameters lead the chose of the suitable pairs from the SAR images having the shortest temporal distance and the smallest spatial baseline. The SRTM 3 arc second ( $\sim 90$  m; Farr and Kobrick, 2007) used to remove the topographic effect from the resulting interferograms, in addition the satellite precise orbits are from Delft University (Sharoo and Visser, 1998). The decorrelation due to the atmospheric delay cannot be removed using InSAR processing system and so it persists in the calculated interferometric (Figures 7a and 7b). The best-correlated interefogram is obtained with the 25/11/1999 as the reference SAR image and the 13/04/2000 as the repeat SAR image.

Satellite	Orbit number	Date	Track	Frame
ERS-1	41214	02/06/1999	144	697
ERS-2	29056	09/11/2000	144	697
ERS-2	24046	25/11/1999	144	697
ERS-2	12022	07/08/1997	144	697
ERS-2	25048	03/02/2000	144	697
ERS-2	26050	13/04/2000	144	697
ERS-2	11020	29/05/1997	144	697

**Table 2:** The 7 ERS-SAR images used in this study and processed with GMTSAR (green underline). The underlined 25/11/1999 and 13/04/2000 SAR products are the reference and repeat SAR images, respectively.

## 4.1 A new program for automatic fringe counting

Due to the small LOS signal in the maximum coseismic deformation area, it was not possible for Belabbes et al. (2009) to calculate the unwrapped phase. In addition, the ‘*snaphu*’ software alone is not able to calculate the unwrapped of the resulting phase. It was then necessary to perform a program in order to calculate the unwrapped phase of interferograms. After the production of an interferogram using GMTSAR (Figure 7), I have made a C-program to count automatically the number of fringes situated between two geographic points (Lon, Lat) showed with black dashed line in Figures 8a and 8c. The results for each Fringe-counter are shown as a histogram of variation ranges between  $[-\pi$  and  $\pi]$  for wrapped interferogram. The correct number of fringes corresponds to half of the total number of fringes counted in the histogram (I find 5).

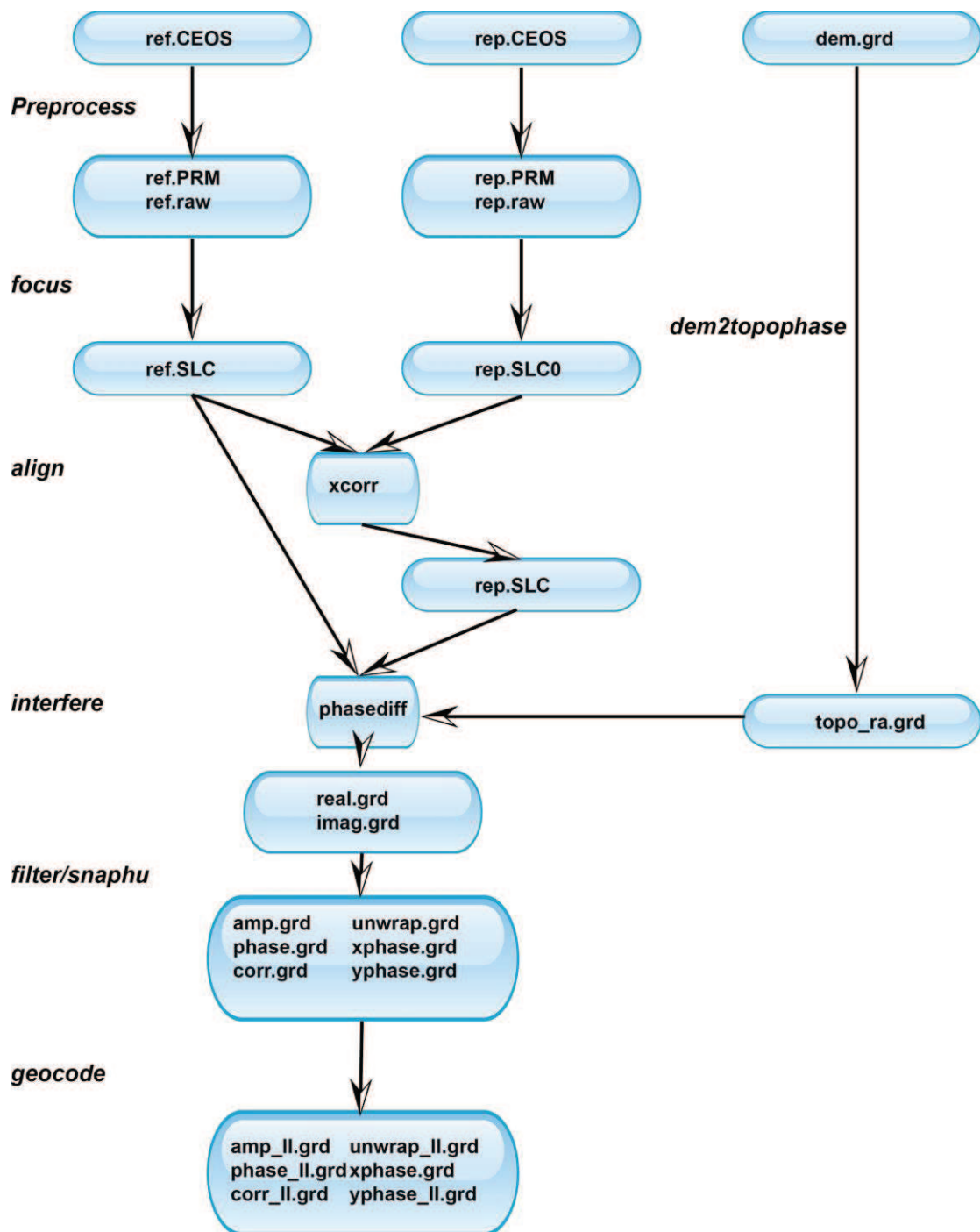


**Figure 6:** GMTSAR 2-pass processing diagram, the inputs are: reference SAR image, the repeat SAR image and the digital elevation grid file. The orbital data are used for ERS and a digital elevation grid (dem.grd), ending with geocoded grids of interferometric products.

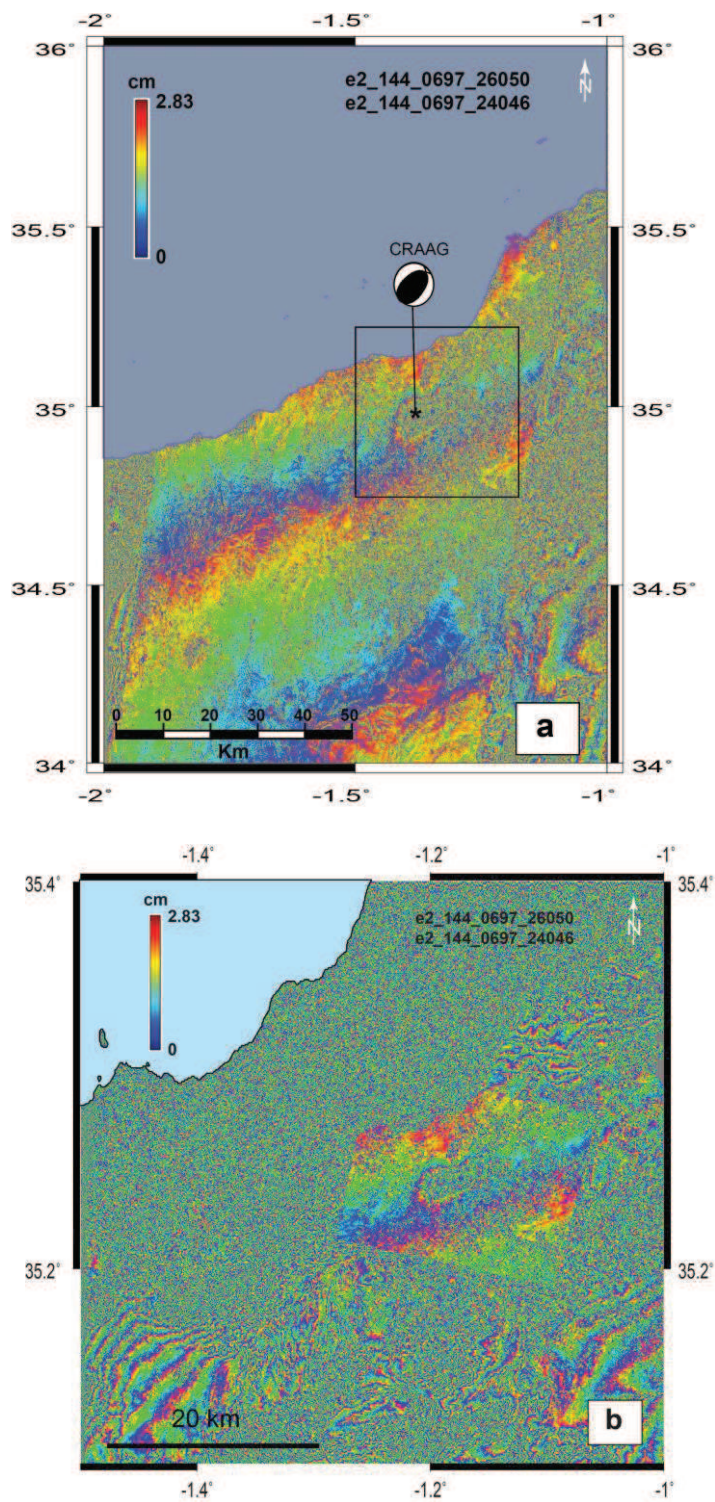


**Figure 7:** (a) ERS-2 coseismic interferogram of the 1999 Ain Temouchent earthquake.(b) Enlarged area of (a) showing an elliptical lobe with up to 11 cm deformation in LOS. The CMT focal mechanism and epicenter location are from USGS and CRAAG respectively.

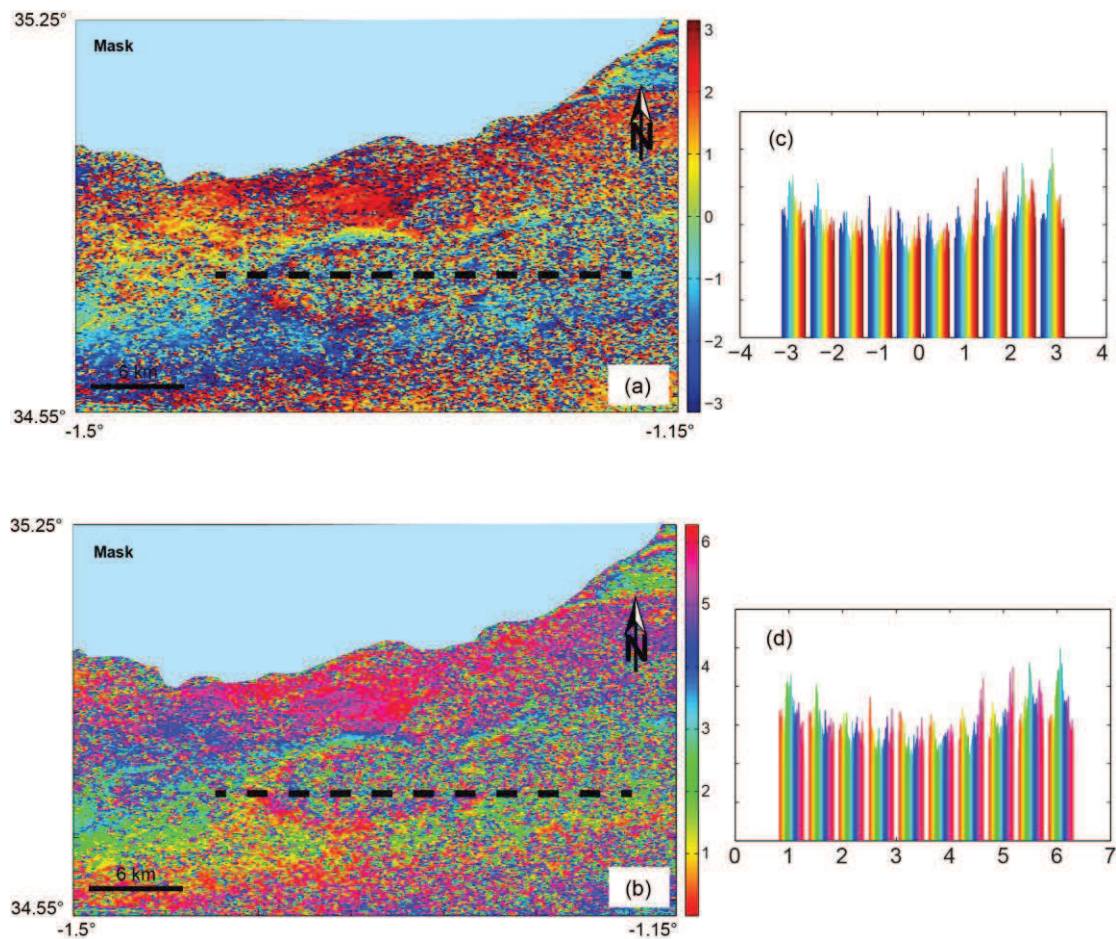


**Figure 8:** InSAR processing and automatic counting of fringes. (a) Wrapped interferogram  $[-\pi, \pi]$  and (b) the unwrapped interferogram  $[0, 2\pi]$ . (c, d) are automatic cycle change counting from the dashed line in a and across the coseismic deformation area. In comparison with the 4 fringes determined by Belabbes et al. (2009), both wrapped (a) and unwrapped (b) interferograms show the deformation area and InSAR lobes where we determined 5 fringes (14.15 cm slip in the line of sight) using our automatic method.

The unwrapped phase is lead by the information of the fringe numbers, the fringes shapes that are extracted automatically using the fringe contours than close the fringes lines contours using the mathematical morphology operator (erode and close). The dashed line traveling figure 8b, is used with the classification of each pixel situated between two fringes contours in the same class. Finally, this classes (2x the real number of fringes) are divid in two, according to the histogram (figure 8.b) and multiply the numer of the label associated to the fringe by all the pixel of the associated class. The resulting map image, will helps in the modeling. Using the unwrapped interferograms to guide the modeling processus, I applied the FFT to the signal with the (3 X 3) smoothing gaussian filter to obtaine the final synthetic model presents the best fringes visibility.

There are possibilities for implementation in other filters and include them with in GMTSAR processing. I developed and used my own spatial filter to enhance the final results of interferograms and also I developed a GUI in order to simplify the use of GMTSAR for non-familiar users with the c-shell programming of c-shell window as presented in (Figures 10a, 10b). I used the same configure file as presented with ERS processing example in GMTSAR samples.

## **4.2 A new Graphical User Interface (GUI) for GMTSAR**

I presented new version of GUI that allow user to set parameters needed for each processing step (Figure 11). This GMTSAR GUI is developed with Java and generated for all processing SAR images according to satellite type. The inputs of the main GUI are the three files that needed to be selected, the Master image, the slave image and the topographic file. The dialogue box (browsing) allows the selecting of each file in addition information box is also presented in the GUI aims to help the user how to process InSAR with GMTSAR (Figure 11b). Moreover, This GUI present five different windows used to set the processing parameters and needed for processing as Shown in (Figures 11c, 11d, 11e, 7f and 11g). The filtering window allows selecting filters in the GMTSAR\filters folder and also introducing our own filter.

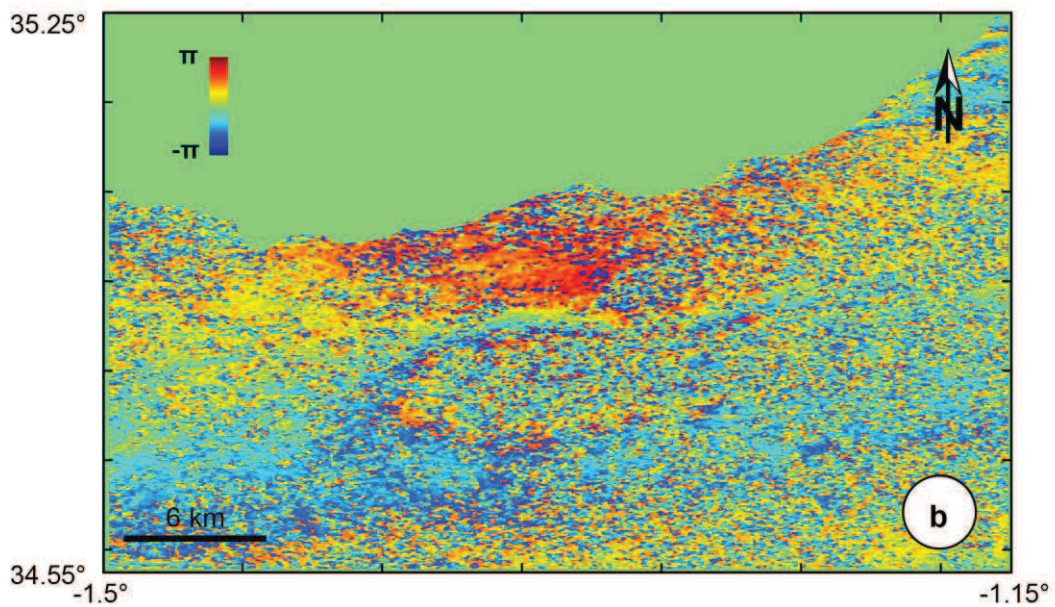
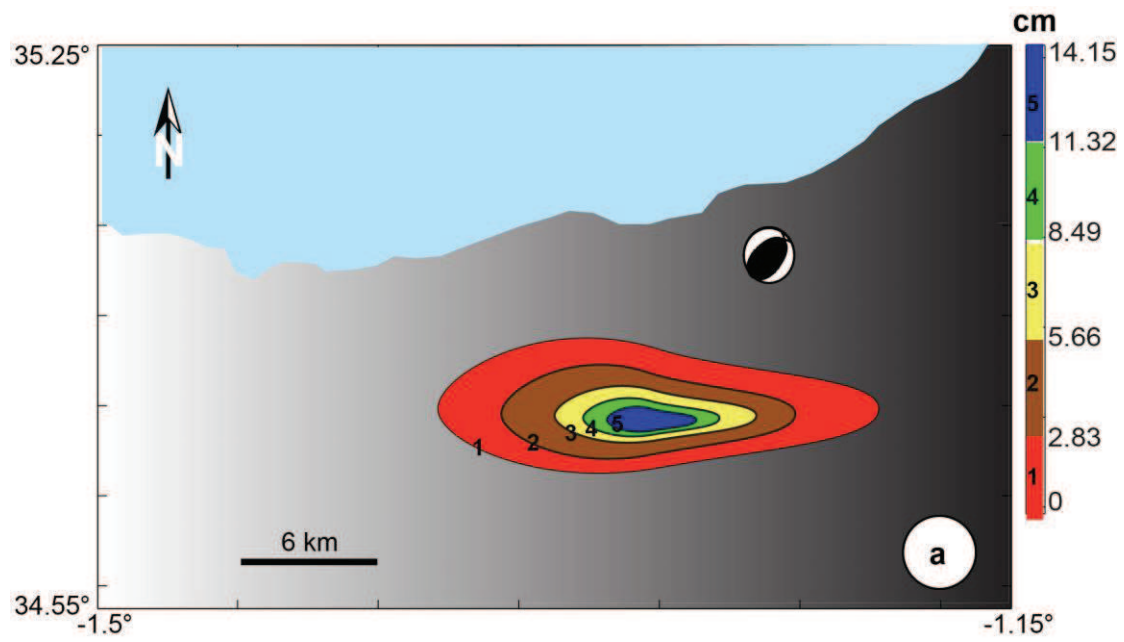


**Figure 9:** (a) Synthetic interferogram with GMT obtained with the filtered image of (b) and (b) the wrapped interferogram  $[-\pi + \pi]$  after applying 1) Fourier Transform of degradation, and 2) 3 X 3 Smoothing gaussian filter obtained from Matlab. I count 5 fringes (14.15 cm slip in the line of sight) with this automatic method.

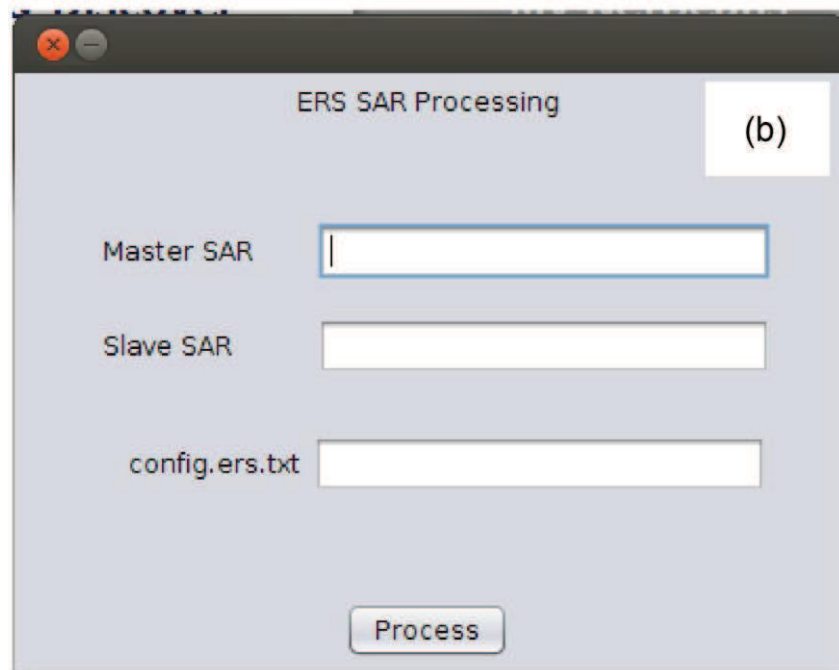
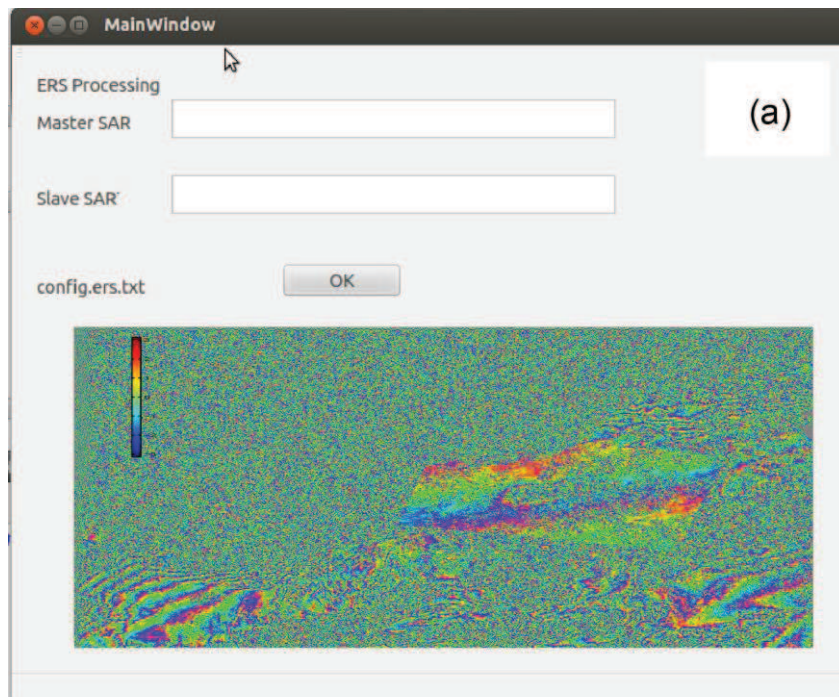


**Figure 10:** Graphical interface for GMTSAR ERS-SAR processing. (a) Using QtSDK C++ programming, (b) using NetBeans JDE Build for Java programming.

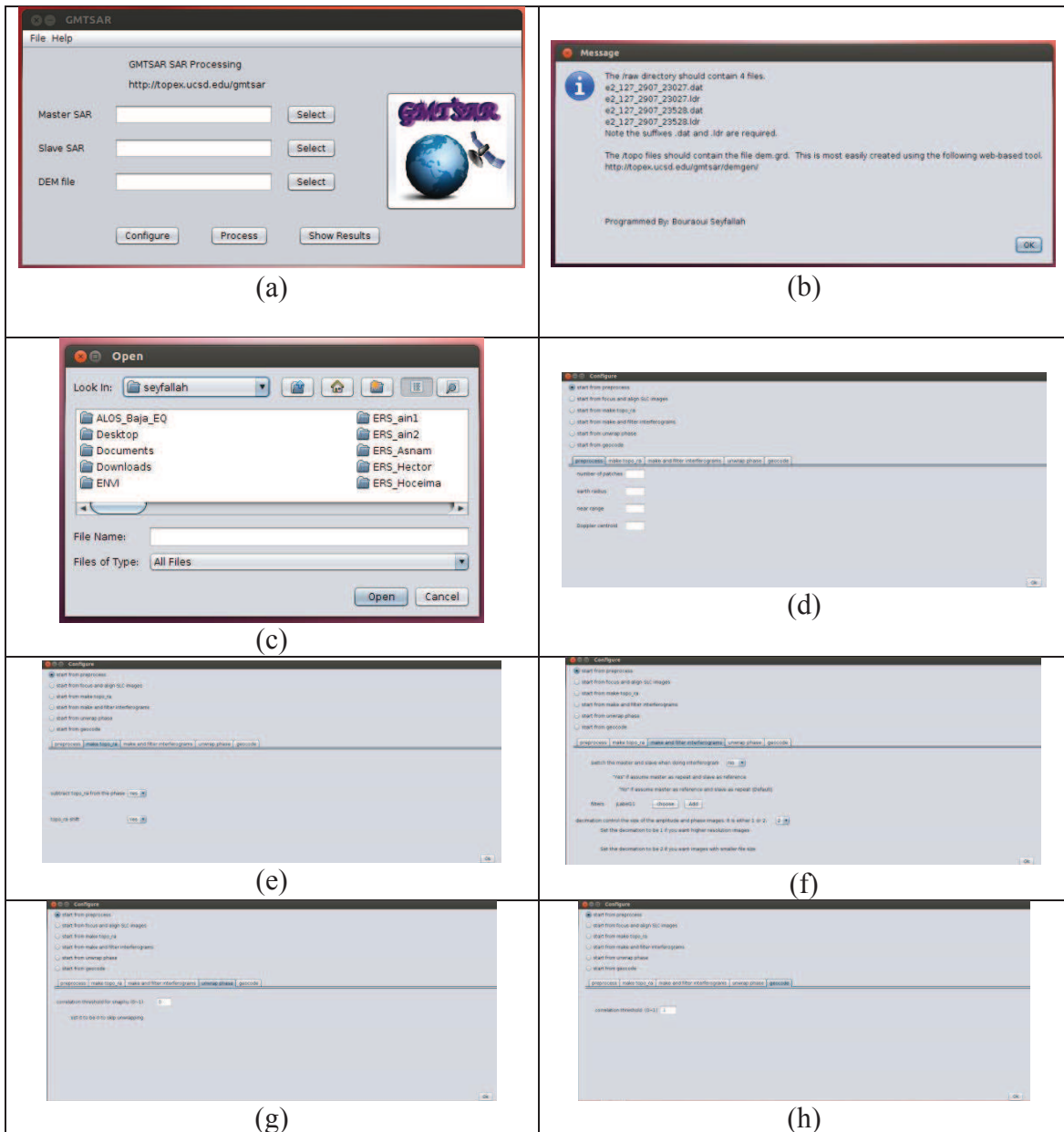


**Figure 11:** Graphical interface for GMTSAR SAR processing system developed with Java. (a) The main GUI indicates three files need to be selected, the Master image, the slave image and the topographic file. (b) Show the dialogue box allows selecting files with information box. (c) The configure window allow to chose the step from with the program will start processing (the default is preprocessing step 1).(d),(e),(f),(g) and (h) shows the how to set parameter for each processing step (Preprocessing, make Topography, Filters and Interferometry, unwrapping, Geocoding).

# 5. Conclusion:

Using GMTSAR to process SAR image providing from ERS-2 satellite, I obtain an interferogram of surface deformation associated with the 22-12-1999 Ain Temouchant earthquake. The GMTSAR processing added with automatic fringes counting and graphical interface (GUI) applied to a moderate-sized earthquake appear to be a powerful tool. With the automatic fringes counting program, I obtain 14.15 cm of displacement in the LOS direction. The difficulties in this study that since we have a small and discontinuous signal, Snaphu will not be able to measure the phase unwrapped.

(Figure 12) shows the final results from this study showing respectively the wrapped and the unwrapped interferogram after filtering and data geocoding.

Using formula introduced by (Kanamori, 1977) to calculate the magnitude of 22-12-1999 Ain Temouchant earthquake with the obtained unwrapped phase data, I obtained geodetic moment of  $6.2 * 10^{17}$  N m corresponding to  $M_w \sim 5.86$  in agreement with the previous studies of this earthquake.

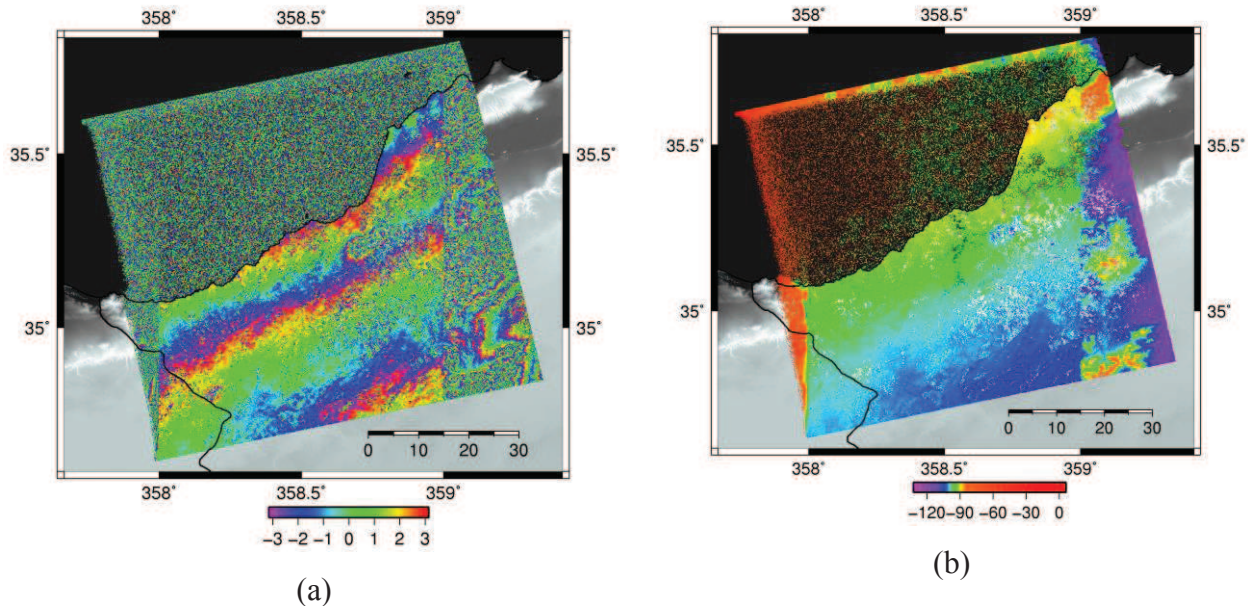


**Figure 12:** final InSAR results. (a) Wrapped phase. (b) Unwrapped phase.

## References:

- Belabbes S., Meghraoui M., Çakir Z., and Bouhadad Y., (2009), InSAR analysis of a blind thrust rupture and related active folding: the 1999 Ain Temouchent earthquake (Mw 5.7. Algeria) case-study. *Journal of Seismology* 13, 3, 421-432. Doi: 10.1007/s10950-008-9135-x.
- Cakir Z., Meghraoui M., Akoglu AM., Jabour N., Belabbes S., and Ait BL., (2006), Surface deformation associated with the Mw 6.4, 24 Februray 2004 Al Hoceima, Morocco, earthquake deduced from InSAR; implications for the active tectonics along North Africa. *Bull Seismol Soc Am* 96:59-68. Doi:10.1785/0120050108.
- Chen, C. W., and H. A. Zebker, (2000), Network approaches to tow-dimensional phase unwrapping: Intractability and two new algorithms, *J. Op. Soc. Am. A Op., Image Sci.*, 17(3), 401-414, doi:10.1364/JOSAA.17.000401.
- Farr, T. G., and Kobrick, J., (2007). The Shuttle Radar Topography Mission, *Rev. Geophys.* 45, RG 2004, doi : 10.1029/2005RG000183.
- Guarnieri M., (2000), “*ScanSAR interferometric monitoring using the PS technique*”, ERS ENVISAT symposium (Gothenburg, Sweden), 12-22 October 2000.
- Hanssen, R. F. (2001). *Radar Interferometry: Data interpretation and error analysis*, Kluwer Academic Publishers, Dordrecht, 308 p.
- Kanamori, H. (1978). Quantification of Earthquakes, *Nature* 271, 411-414 doi:10.1038/271411a0.
- Sandwell, D., Mellors R., Tong X., Wei M., and Wessel P., (2011a), Open radar interferometry software for mapping surface deformation, *Eos Trans. AGU*, 92(28), doi:10.1029/2011EO280002.
- Sandwell D., Mellors R., Tong X., Wei Matt., and Wessel P., (2011b). GMTSAR: An InSAR Processing System Based on Generic Mapping Tools. UC San Diego: Scripps Institution of Oceanography. Retrieved from: <http://escholarship.org/uc/item/8zq2c02m>
- Scharoo, R., and Visser, P., (1998) Precise orbit determination and gravity field improvement for the ERS satellites, *J. Geophys. Res.* 103, 8113–8127.
- Stramondo S., Cinti F. R., Dragoni M., Salvi S., and Santini S., (2002), The August 17, 1999 Izmit, Turkey, earthquake: new insights on slip distribution from dislocation modeling of DInSAR and surface offset, *Annals of Geophysics*, vol. 45, n.3/4, pp. 527-536, June/August 2002.
- Thomas, A. L., (1993), POLY3D, A Three-Dimentional, Polygonal Element, Displacement Discountinuity Boundary Element Computer Program With Applications to

Fractures, Faults, and Cavities in the Earth's Crust, M.S. Thesis, Stanford University, Stanford, CA.

Wessel, P., and Smith W. H. F., (1998), New improved version of Generic Mapping Tools released, EOS Trans. Amer. Geophys. U., vol. 79 (47), pp. 579.

Yelles, C. AK., Djellit H., Beldjoudi H., Bezzeghoud M. and Buform E., (2004), The Ain Temouchent (Algeria) earthquake of December 22<sup>nd</sup>, 1999, geodynamique of Azeros-Tunisia. Pure Appl. Geophys 161:607-621. doi:10.1007/s00024-003-2465-2.

I present in this section two articles published in the International Journal of Computer Science Issues (IJCSI) (Seyfallah BOURAOUI, 2011; Seyfallah BOURAOUI, 2013). In each of them, I present a new algorithm and method for optical remote sensing image processing. The first article details how to detect residential area in multispectral remote sensing images. In order to automatically detect and count the number of existing residential areas in remote sensing images. First of all, the system processed to the detection of known structures (Houses, Trees, Water-Body) that are surrounded by streets. The system hard is composed by adjacency graph and working with the principal of automaton language generator. The system is tested with SPOT 5 French Satellite images of the urban area of Strasbourg (la Robertsau). The system gives also a very clearly description of the residential area after processing with very height recognition rate.

In the second article, I present study of mount Saint-Michel bay using graph theory for the analysis of remote sensing SPOT 5 images. The system proposed is a combination of tow automatic classification methods well known in data mining. The system architecture composed by tow distinguishes classifications methods that are supervised method and unsupervised method (clustering). These two methods start the processing in the same time (run in parallel way) and using the same image in order to take advantage of these two methods of classifications. the final answer provide by the system is based on the graph matching algorithm of different patterns found by both of this two methods. Fourteen different classes of geographic land occupation were found in this study.

# A system to Detect Residential Area in Multispectral Satellite Image

## **Résumé:**

Dans cet article, nous proposons une nouvelle solution pour extraire des structures complexes présentes dans des images optiques de télédétection de haute résolution (HR). Nous proposons de représenter les formes trouvées et leurs relations à l'aide de graphe d'adjacence. Ils sont générés automatiquement à partir des images segmentées. Ainsi, les nœuds du graphe représentent les formes trouvées comme des maisons, des rues ou des arbres, tandis que les arcs décrivent la relation d'adjacence qui existe entre eux. Afin d'être invariant aux transformations tels que la rotation et mise à l'échelle des formes, l'extraction d'objets d'intérêt se fait par le biais de la combinaison de deux techniques: l'une basée sur la couleur du toit utile pour détecter les rectangles englobant ces maisons, tandis que l'autre est basée sur les notions de morphologie mathématique pour la détection des rues. Afin de reconnaître les zones résidentielles, un modèle décrit par un langage régulier est construit. La détection est réalisée par la recherche d'un chemin dans le graphe de voisinage de régions, qui peut être reconnue comme un mot appartenant au langage de description. Mon algorithme a été testé avec succès sur des images du satellite français SPOT 5 qui représente la zone urbaine de la Robertsau (Strasbourg; France) à des résolutions spatiales différentes.















# The Study of the Bay of Mount Saint-Michel by Using Graph Theory in the Analysis of Satellite Images

## Résumé:

Dans cet article, une nouvelle approche pour la cartographie basée sur le concept d'objet et de relations entre ces objets est proposée afin de tirer profit des deux méthodes de classification utilisées qui sont la classification supervisée et la classification non supervisée. D'une part, les objets obtenus après une classification supervisée sont représentés par un graphe modèle tenant en compte les relations voisinage. D'autre part, les objets obtenus après la classification non supervisée sont représentés par un graphe de donnée d'adjacence, ainsi que l'objectif est de mesurer l'adéquation entre ces deux graphiques afin d'améliorer les résultats de classification non supervisée en les associant avec ceux obtenus à partir de la classification supervisée. Cette étude a porté sur la baie côtière du Mont Saint-Michel, les données utilisées sont celles de SPOT 5 images satellitaires optiques.